SAPIENZA
UNIVERSITÀ DI ROMA

BDNF-dependent cerebellar alterations are associated with neurobiological abnormalities and autistic-like traits in a mouse model of cholesterol storage disorder

Faculty of **Medicine and Psychology**
Department of **Psychology**

PhD program in **Behavioral Neuroscience**
Curriculum **Psychobiology and psychopharmacology – XXXVIII cycle**

PhD Candidate **Greta Massa**

Supervisor **Prof.ssa Sonia Canterini**

Table of contents

Acknowledgements

This thesis was developed during my PhD in Behavioral Neuroscience, carried out at Sapienza University of Rome. Part of the experimental work was conducted during a research period abroad at the Instituto de Neurociencias de Alicante (CSIC-UMH), which provided an important scientific and personal contribution to this project.

I would like to express my sincere gratitude to my supervisor, Professor Sonia Canterini, for her scientific guidance and constant support throughout this work, which significantly contributed to my professional and personal growth.

I am also deeply grateful to Dr. Juan Antonio Moreno Bravo for hosting me in his laboratory during my research period in Spain and for his valuable suggestions, which remarkably enhanced the development of my PhD thesis. I would like to thank all the members of the host laboratory as well, for their insightful discussions and for creating a welcoming working environment. In particular, I thank Dr. Martina Riva for her help, availability, and for always keeping in touch even after my return to Italy.

Finally, I am grateful to all my colleagues and collaborators who contributed, directly or indirectly, to this project and made this journey both scientifically and personally enriching. In particular, I would like to thank Dr. Roberta Stefanelli for constantly looking after me and encouraging me to move forward.

Abstract

Niemann–Pick type C1 (NPC1) disease is an autosomal recessive lysosomal storage disorder caused by mutations in the *Npc1* gene, leading to defective intracellular cholesterol trafficking and widespread cellular dysfunction. Among the affected brain regions, the cerebellum exhibits the most pronounced pathology, characterized by progressive degeneration of Purkinje cells and ataxia. Although traditionally considered a neurodegenerative disorder, recent evidence from our group indicates that NPC1 also displays distinctive neurodevelopmental features, aligning it with the spectrum of neurodevelopmental disorders. Previous studies showed that *Npc1* deficiency disrupts *Sonic hedgehog* signaling during early postnatal cerebellar development, impairing granule cell (GC) proliferation. Several *Sonic hedgehog*-dependent processes also rely on brain-derived neurotrophic factor (BDNF) activity, which is likewise dysregulated in developing *Npc1*^{nmf164} mice, resulting in defective GC migration to the internal granule layer (IGL).

In the present work, we investigated whether altered neurotrophic signaling contributes to defective GC differentiation and synaptic connectivity, postnatal developmental processes that normally occur during the first weeks of life, leading to the emergence of behavioral abnormalities in adult *Npc1*^{nmf164} mice. We specifically addressed sex-related differences—an aspect previously overlooked—to delineate divergent molecular and behavioral trajectories in males and females following *Npc1* loss.

By integrating molecular, morphological, and behavioral approach, we demonstrate that *Npc1* loss severely impairs cerebellar maturation by persistently affecting BDNF–TrkB signaling and downstream PTEN–mTOR pathway. These alterations coincide with reduced levels of key synaptic proteins (Snap25, PSD95, Shank3, and Nlgn3) crucial for pre- and postsynaptic organization, excess immature dendritic spines particularly in *Npc1*^{nmf164} male mice, and decreased IGL volume, collectively indicating impaired differentiation and connectivity. Biochemical analyses revealed unchanged cerebellar GABA levels but elevated glutamine in *Npc1* mice, indicating altered glutamate–glutamine metabolism and an excitatory–inhibitory imbalance. Notably, these neurodevelopmental abnormalities manifested as sex-dependent behavioral alterations, with male *Npc1*^{nmf164} mice showing marked deficits in social interaction during adulthood, consistent with an *autistic-like* phenotype.

Overall, our findings demonstrate that *Npc1* deficiency disrupts neurotrophic signaling and GC synaptic maturation, leading to long-lasting alterations in cerebellar circuitry and social behavior. These effects exhibit a sex-dependent pattern, with males showing greater vulnerability to molecular, structural, and behavioral alterations than females. These results support the view that early cerebellar dysfunction—driven by impaired BDNF–TrkB signaling and altered synaptic organization—contributes to the emergence of autistic-like features in NPC1 disease, positioning the cerebellum as a critical hub linking lipid metabolism, neurotrophic regulation, and socio-emotional development.

Chapter I

Overview of Niemann-Pick disease

1.1 Niemann-Pick disease: definition, classification, and historical milestones

In 1914, the German pediatrician Albert Niemann reported the case of an infant presenting with hepatosplenomegaly, lymphadenopathy, jaundice, and neurological abnormalities, who died prematurely at 18 months of age (Niemann, 1914). Although Niemann noted certain similarities with Gaucher disease, it was only years later, in 1927, that the German pathologist Ludwig Pick analyzed tissues from infants with similar features and demonstrated that the disorder was distinct from Gaucher disease (Pick, 1927). Their pioneering contributions led to the introduction of the eponym *'Niemann-Pick disease'*, now used to describe a heterogeneous group of lysosomal storage disorders (LSDs), which may or may not involve the central nervous system (CNS) (Vanier, 2010).

A few decades later, in 1958, the American pediatric pathologist Sidney Farber and his collaborator Allan Crocker reported 18 cases of Niemann-Pick disease (NPD), highlighting the wide variability in age of onset and clinical features (Crocker and Farber, 1958). This heterogeneity prompted Crocker to propose a classification of the disease into four categories – types A, B, C, and D – based on age of onset, symptoms, and clinical and biochemical characteristics (Crocker, 1961).

According to this classification, **types A and B** represent neurovisceral forms of LSDs caused by mutations in the *sphingomyelin phosphodiesterase 1 (SMPD1)* gene, leading to reduced activity of the acid sphingomyelinase (ASM) enzyme (Kheder et al., 2013). ASM normally converts sphingomyelin (SM) into ceramide and phosphocholine (Mühle et al., 2013), and its deficiency results in SM accumulation within several organs (Schuchman and Wasserstein, 2015). In detail, **type A** is an infantile, severe disorder characterized by hepatosplenomegaly, hypotonia, profound CNS involvement, and rapid progression to death before three years of age (Sideris and Josephson, 2016). **Type B** is a milder variant, associated with hepatosplenomegaly, hyperlipidemia, and limited neurological impairment, while the survival of many patients into adulthood and respiratory compromise – absent in type A – appear as distinctive features (Wasserstein et al., 2004; von Ranke et al., 2016).

On the other hand, **types C and D** represent clearly distinct forms of NPD (Pentchev et al., 1980). Specifically, **type C** is a rare and heterogeneous disorder caused by mutations in the *NPC1* gene, which accounts for the vast majority of cases (~95%), or in the *NPC2* gene, accounting for the remaining ~5%. These mutations alter NPC1 and NPC2 proteins function, leading to systemic involvement, progressive neurodegeneration, cognitive decline, and cerebellar ataxia (Carstea et al., 1997; Loftus et al., 1997). Finally, **type D**, once considered a separate entity, is now recognized as an allelic variant of type C, and is characterized by CNS involvement and marked variability in both clinical presentation and disease course (Greer et al., 1998; Greer et al., 1999).

1.2 Focus on Niemann-Pick type C disease: epidemiology, clinical manifestations, diagnosis and treatment

The frequency of NPC disease has been estimated at approximately 1 in 120,000 live births (Park et al., 2021). Retrospective national studies conducted in Australia, the Netherlands, Portugal, the Czech Republic, France, and the United Arab Emirates have reported an annual incidence ranging from 0.35 to 2.20 per 100,000 live births (Vanier and Millat, 2003; Geberhiwot et al., 2018). More recent analyses, based on four independent exome sequencing or next-generation sequencing datasets, predicted a prevalence of about 1 in 92,000. These studies further suggested the existence of late-onset, underrecognized phenotypes, with an estimated incidence as high as 1 in 19,000–36,000 (Wassif et al., 2016).

Nevertheless, determining the true incidence and prevalence of NPC remains challenging, due to limited clinical knowledge of the disorder, combined with the difficulty of performing appropriate diagnostic assessment (Vanier and Suzuki, 1998). Therefore, many cases remain undiagnosed or are initially misdiagnosed, since the marked heterogeneity of NPC further complicates the diagnostic process (Ory, 2000).

The clinical presentation of NPC is extremely heterogeneous (**Figure 1B**), with the age of onset ranging from the perinatal period to adulthood (Vanier, 2010). Systemic manifestations usually appear first, preceding neurological, psychiatric, and cognitive symptoms (Dierks et al., 2009) (**Figure 1A**).

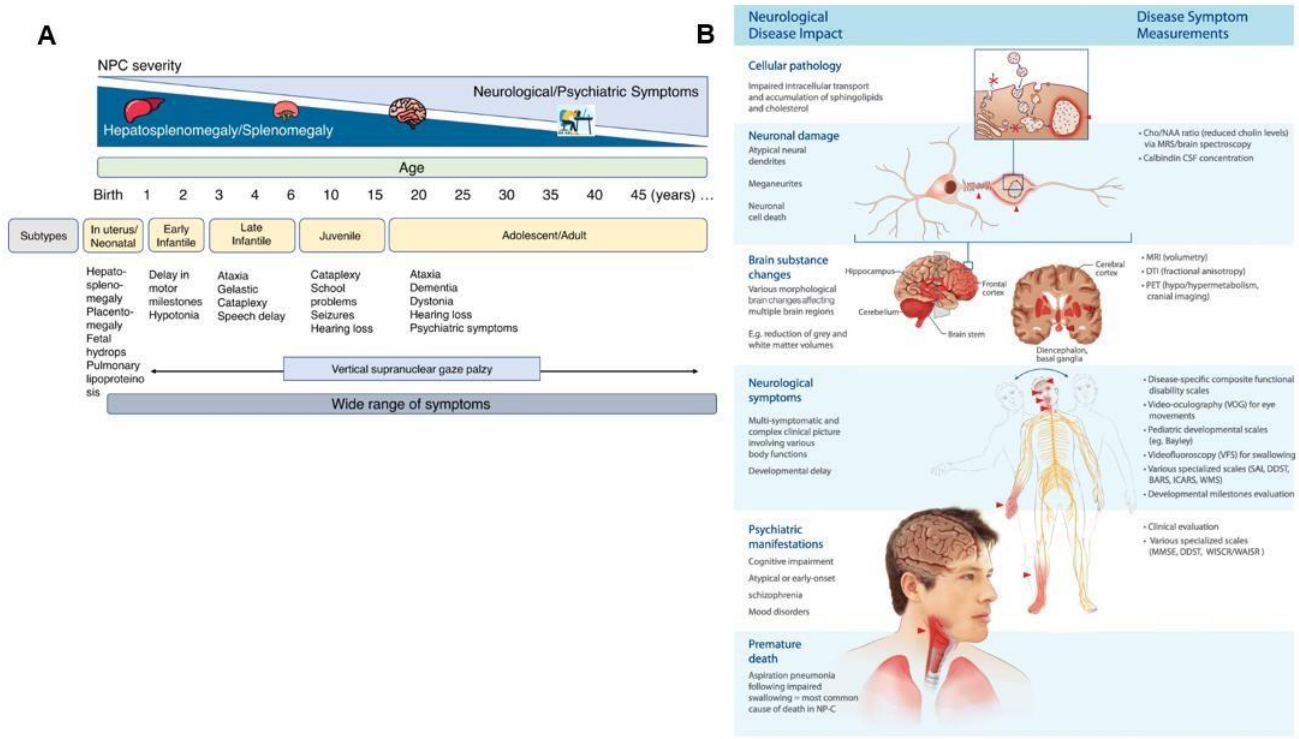

Figure 1. Schematic representation of NPC disease clinical manifestations. (**A**) The diagram shows the great phenotypic variation in NPC disease and within each subtype of it (adapted from Vanier 2015). (**B**) NPC disease is a neurovisceral condition with a wide range of biochemical and cellular/neuronal effects correlating with severity of neurological/psychiatric symptoms (Pineda et al., 2018).

NPC disease has been classified into five subgroups, based on the age of onset: pre/perinatal (shortly before and after birth), early infantile (2 months to 2 years), late infantile (2–6 years), juvenile (6–15 years), and adult (15 years and after) (Wraith et al., 2009).

1. **Pre/perinatal form.** This variant is characterized by hepatosplenomegaly leading to acute liver failure (Patterson et al., 2012). In most cases, this pronounced visceral involvement is associated with cholestatic icterus appearing within the first days of life (Wraith et al., 2009). Additional perinatal manifestations include fetal hydrops and ascites, both resulting from the accumulation of interstitial fluid in one or more fetal compartments (Spiegel et al., 2009). Although neurological symptoms are absent at this stage, the prognosis is poor, with death typically occurring around 6 months of age (Gumus et al., 2017).
2. **Early infantile form.** This form presents as a visceral–neurodegenerative disorder (Şeker Yilmaz et al., 2020). Pulmonary infiltration with foam cells, splenomegaly, hepatosplenomegaly, and/or prolonged neonatal jaundice are the most common systemic features (Geberhiwot et al., 2018). Neurological involvement usually appears between 2 months and 2 years, with delayed achievement of developmental motor milestones becoming evident around 8 months of age (Vite et al., 2008). Between the first and second year of life, patients may also exhibit mild cognitive regression, dystonia, and hypotonia (Vanier, 2010). The clinical course is typically aggressive, with rapid progression to ataxia, sporadic abnormal saccades, and dementia (Vanier, 2010; Mengel et al., 2013). Life expectancy does not exceed 5 years (Jahnova et al., 2014).
3. **Late infantile form.** This form is commonly characterized by clumsiness, gait disturbance, and impairment of fine motor skills, which may progress to cerebellar ataxia (Patterson, 2000). Other features include speech delay, neonatal cholestasis, and hepatosplenomegaly (Geberhiwot et al., 2018). A clinical hallmark of NPC, vertical supranuclear gaze palsy (VSGP), typically manifests with an early phase of delayed initiation of vertical saccades, followed by progressive slowing and eventual loss of these saccadic movements (Salsano et al., 2012; Mengel et al., 2013). Cognitive decline is often rapid and can be misinterpreted as a learning disability (Patterson, 2000). As cerebellar ataxia worsens, dysphagia, dysarthria, and dementia become apparent (Sarna et al., 2003; Walkley and Suzuki, 2004; Sitarska and Lugowska, 2019). In advanced stages, patients frequently develop spasticity, swallowing difficulties, and seizures (Berry-Kravis, 2021). Gelastic cataplexy, characterized by sudden loss of legs muscle tone in response to laughter or emotional stimuli, occurs in about half of patients (Sèvin et al., 2007). Approximately 25% of individuals with late infantile onset develop schizophrenia-like psychosis, with hallucinations and behavioral disturbances (Vanier et al., 1991; Walterfang et al., 2009). Life expectancy is generally limited, with death often occurring between 2 and 6 years of age (Geberhiwot et al., 2018; Patterson, 2000).

4. **Juvenile form.** Representing the most frequent and “classic” presentation of NPC, the juvenile form typically manifests with the first neurological symptoms between 6 and 15 years of age. Cognitive decline – including impaired school performance, language difficulties, and attention deficit hyperactivity disorder (ADHD) – is a common early feature, often accompanied by dystonia, dysarthria, dysphagia, cerebellar ataxia, and intellectual disability (Imrie et al., 2007). While psychiatric symptoms may also develop, VSGP is invariably present (Vanier, 2010; Evans and Hendriksz, 2017; Geberhiwot et al., 2018). Life expectancy is highly variable, with some patients surviving into their 30s (Wraith et al., 2009).
5. **Adult form.** The adult-onset form is rare and often underdiagnosed due to its wide clinical heterogeneity (Vanier, 2010). The disease course is generally slower than in juvenile forms and is frequently dominated by psychiatric manifestations, including psychosis, paranoid delusions, hallucinations, depressive syndromes, mood disorders, obsessive-compulsive behaviors, aggression, or schizophrenia-like syndromes (Shulman et al., 1995; Kawazoe et al., 2018). Neurological symptoms may include cerebellar ataxia, dysarthria, cognitive decline, and movement disorders such as dystonia, parkinsonism, or chorea, often accompanied by dysphagia (Sèvin et al., 2007). VSGP and hepatosplenomegaly may or may not be present in older patients. Life expectancy is highly variable (Davidson and Walkley, 2010).

The marked heterogeneity in systemic and neurological symptoms, along with the considerable variability in age of onset, complicates the clinical assessment of NPC, making timely diagnosis challenging and underscoring the need for specialized diagnostic tools to accurately detect the disease and guide patient care (Jiang and Ory, 2021). Over the years, a range of cellular, molecular, and genetic tests has been developed to improve diagnostic accuracy.

Among these, the **Filipin test** is considered one of the most sensitive and specific diagnostic tools for NPC disease (Vanier et al., 2016), widely used to label and quantify unesterified cholesterol in cells and tissues (Maxfield and Wüstner, 2012). Filipin is a macrolide polyene antibiotic, originally isolated from the bacterium *Streptomyces filipinensis* (Ammann and Gottlieb, 1955), binding to free cholesterol but not to esterified sterols. The hydrophobic interaction between Filipin and cholesterol is mediated by the presence of the 3β-OH group in the chemical structure of cholesterol molecule (**Figure 2**) (Norman et al., 1972).

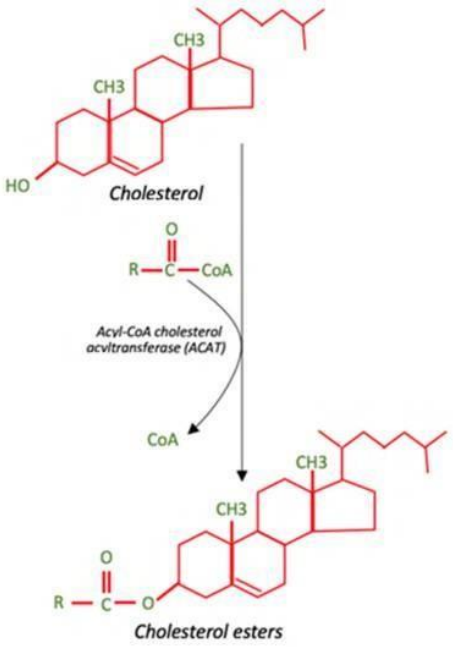

Figure 2. Chemical structure of cholesterol and cholesterol esters (Bruno et al. 2023).

For this reason, Filipin binds cholesterol in a 1:1 stoichiometry, forming a "Filipin-cholesterol" complex that localizes within the hydrophobic layer of biological membranes (Verkleij et al., 1973) (**Figure 3**). Upon binding, Filipin perturbs the plasma membrane (PM) lipid bilayer, therefore staining must be performed on fixed cells or tissues to prevent aggregation of the Filipin-cholesterol complexes (Robinson and Karnovsky, 1980).

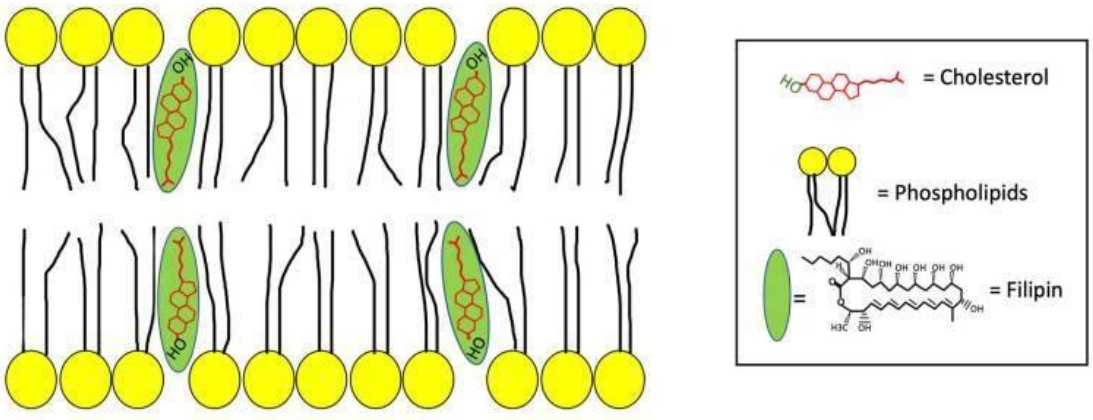

Figure 3. The binding of filipin to cholesterol in the plasma membrane (Bruno et al., 2023).

Over the past two decades, Filipin staining has been extensively used as a diagnostic marker for NPC disease (Patterson et al., 2012). In particular, fluorescent Filipin staining in cultured skin fibroblasts from NPC1 patients has revealed higher concentrations of unesterified cholesterol compared to controls, indicating altered intracellular cholesterol distribution and its accumulation within late endosome/lysosome (LE/Ly) compartments (Harzer and Kustermann-Kuhn, 2001; Canterini et al., 2017). Despite its long-standing use, the Filipin test has limitations. First, it requires cultured fibroblasts obtained via skin biopsy, making it an invasive, complex, and expensive

diagnostic procedure (Sitarska and Lugowska, 2019). Additionally, because cholesterol and lipid accumulation is a common feature of other LSDs – such as ASM deficiency and lysosomal acid lipase (LAL) deficiency – the test can yield false positives for NPC (Vanier and Latour, 2015). Although the Filipin test remains the diagnostic standard, NPC disease diagnosis is increasingly supported by the identification of disease-specific biomarkers, including oxysterols, glycosphingolipids, and bile acids (Fu et al., 2010; Mazzacuva et al., 2016; Polo et al., 2017), and by molecular analyses to detect *NPC1* and *NPC2* mutations, using Sanger sequencing or next-generation sequencing approaches (McKay Bounford and Gissen, 2014; Herbst et al., 2015).

To date, no definitive cure exists for NPC disease. However, over the years, several specific therapies have been developed with the aim of delaying symptom onset and progression, as well as improving patients' quality of life (Pérez-Poyato and Pineda, 2011). Given the heterogeneity of clinical manifestations, standard palliative treatments are often employed to alleviate specific symptoms, including seizures, dystonia, tremor, sleep disturbances, and mood or psychotic disorders (Patterson et al., 2012; Geberhiwot et al., 2018; Lad et al., 2019).

Previously approved for the treatment of other LSDs (Kuter et al., 2013), in 2009 the **Miglustat** (ZavescaTM; **N-butyldeoxynojirimycin**) was also approved in Europe and other countries as a targeted therapy for NPC disease (Lyseng-Williamson, 2014). Miglustat is a small, water-soluble iminosugar which inhibits glycosphingolipid synthesis by blocking the glucosylceramide synthase enzyme, thereby reducing lysosomal glycosphingolipid accumulation (Treiber et al., 2007). Clinical reports have demonstrated that Miglustat can cross the blood-brain barrier (BBB) and slow disease progression in both pediatric and adult patients, extending life expectancy (Zervas et al., 2001; Patterson et al., 2010; Bernardo et al., 2021). These protective effects found further confirmation in *in vivo* studies conducted on NPC animal models, showing reduced neuronal cholesterol accumulation, preservation of Purkinje cells (PCs), delayed onset of neurological symptoms, and prolonged survival (Lachmann et al., 2004; Jeyakumar et al., 2005; Pineda et al., 2018). However, side effects were also reported, including gastrointestinal disturbances such as diarrhea, flatulence, nausea, and less commonly, tremors and peripheral neuropathy (Papandreou and Gissen, 2016).

Another therapeutic strategy for NPC treatment involves the use of **histone deacetylase** (**HDAC**) **inhibitors** (Helquist et al., 2013). HDACs are enzymes that remove acetyl groups from histones, thereby regulating gene expression (Marks et al., 2003). By inhibition of HDAC and remodeling chromatin structure, inhibitors such as Vorinostat and Panobinostat, widely employed in various psychiatric and neurodegenerative disorders (Fischer et al., 2010), have been shown to increase *NPC1* gene expression and NPC1 protein activity in studies on human NPC1^{I1061T} fibroblasts. This resulted in reduced cholesterol accumulation within LE/Ly compartments (Munkacsi et al., 2011; Pipalia et al., 2011; Maceyka et al., 2013) (**Figure 4**).

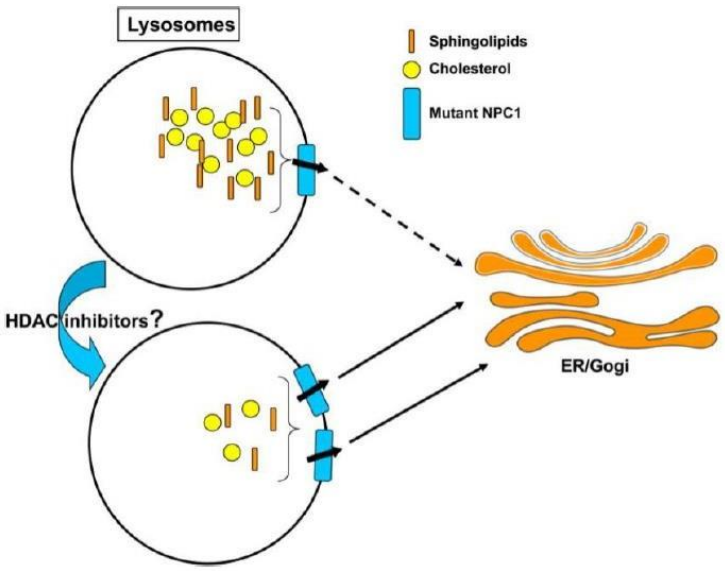

Figure 4. Mechanism of action of HDAC inhibitors. Numerous *in vivo* and *in vitro* studies demonstrated that HDAC inhibitors, blocking HDAC activity, increase NPC1 protein expression and correct cholesterol storage defects in mutant cells (Maceyka et al., 2013).

The most prevalent *NPC1* mutation, *I1061T*, causes protein misfolding, leading to endoplasmic reticulum (ER)-associated degradation and absence of NPC1 protein within LE/Ly compartments (Schultz et al., 2018). In this context, the use of **chemical chaperones** for LSDs treatment has largely increased (Balch et al., 2008). Chaperones are small molecules that bind to mutant proteins, enhancing their folding and stability (Perlmutter, 2002). Certain oxysterols, such as **25-hydroxycholesterol**, act as pharmacological chaperones (Fukuda et al., 2017). Studies on fibroblasts from patients carrying the *I1061T* mutation demonstrated that these molecules stabilize NPC1 protein by direct binding, and correct its localization and maturation, protecting it from degradation, ultimately alleviating cholesterol accumulation (Ohgane et al., 2014; Völkner et al., 2022).

End-product replacement therapy represents another approach, which aims to restore the final metabolites of the cholesterol biosynthetic pathway, appearing reduced in NPC disease (Madra and Sturley, 2010). Among these metabolites, the neurosteroid **allopregnanolone** (**ALLO**) has shown efficacy in the treatment of several neurological conditions (Griffin et al., 2004). ALLO is synthesized in the CNS from progesterone through specific enzymatic processes (Griffin and Mellon, 1999) and exerts neuroprotective effects across multiple neurodegenerative disorders, including Alzheimer's disease (AD), Parkinson's disease (PD), multiple sclerosis, and traumatic brain injury (Djebaili et al., 2004; Garay et al., 2007; Bourque et al., 2009; Irwin and Brinton, 2014). Reported mechanisms include reduction of neuroinflammation and apoptosis, promotion of neurogenesis and oligodendrogenesis, and improvement of cholesterol homeostasis (He et al., 2004; Chen et al., 2011; Adeosun et al., 2012).

Beyond its potential role in mood disorders, anxiety, depression, and diabetes mellitus, ALLO has also been proposed as a promising therapeutic option for NPC disease (Diviccaro et al., 2022)

(**Figure 5**). Several studies using knockout animal models of NPC demonstrated that a single neonatal administration of ALLO – whose levels are reduced in NPC – can delay the onset of neurological symptoms, enhance survival of both PCs and cerebellar granule cells (GCs), reduce cholesterol and ganglioside accumulation, attenuate neuroinflammation, and improve myelination, ultimately extending lifespan (Griffin et al., 2004; Ahmad et al., 2005; Liao et al., 2009).

Interestingly, the combination of ALLO with Miglustat has been shown to exert additive beneficial effects, particularly on motor performance in *Npc1* mouse models (Hovakimyan et al., 2013; Diviccaro et al., 2022). These findings underscore the therapeutic potential of ALLO, either alone or in combinatorial approaches, for the management of NPC disease.

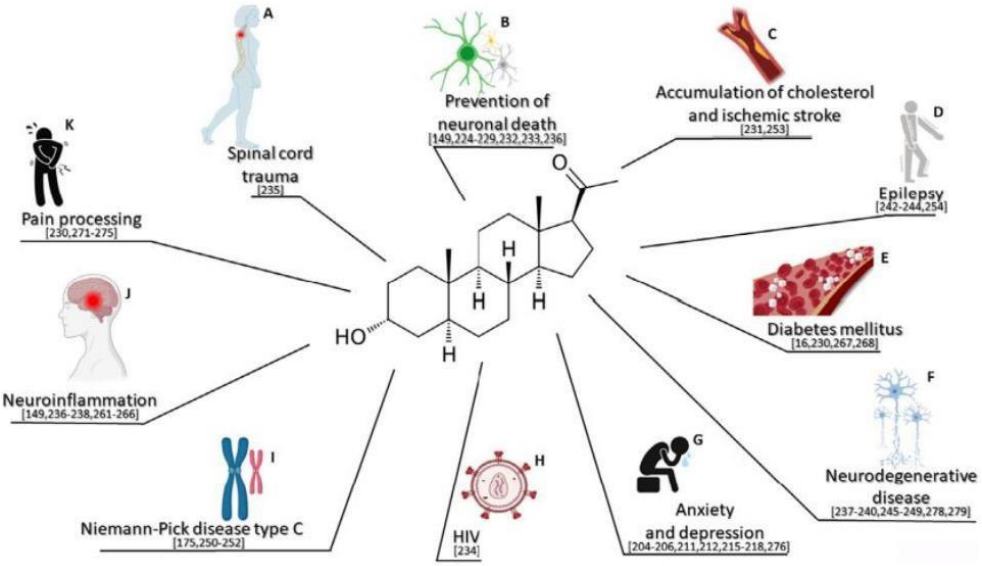

Figure 5. Allopregnanolone (ALLO) pleiotropic effects. ALLO is a neuroactive steroid that has been shown to exert neuroprotective effects in many pathological conditions. (**A**) ALLO has beneficial effects in spinal cord trauma; (**B**) prevents neuronal death; (**C**) prevents ischemic stroke, reducing cholesterol accumulation; (**D**) decreases epileptic seizures; (**E**) attenuates the damages induced by diabetes mellitus; (**F**) ameliorates symptoms of many neurodegenerative diseases; (**G**) exerts anxiolytic and anti-depressant effects; (**H**) protects against HIV-related neurotoxic effects; (**I**) exhibits protective effects in animal models of NPC disease; (**J**) reduces neuroinflammation; and (**K**) exerts analgesic effects (Diviccaro et al., 2022).

Finally, **cyclodextrins** (**CDs**) are widely used as delivery vehicles to improve the administration of poorly water-soluble and chemically unstable drugs (Gould and Scott, 2005). CDs consist of cyclic polysaccharides with a truncated cone-like shape, formed by α-(1–4) glycosidic bonds between glucopyranose units (Szejtli, 1998). Depending on the number of glucopyranose residues, CDs are classified into: α-CD (containing six units), β-CD (containing seven units) and γ-CD (composed of eight units) (Szejtli, 1998; Matencio et al., 2021) (**Figure 6**).

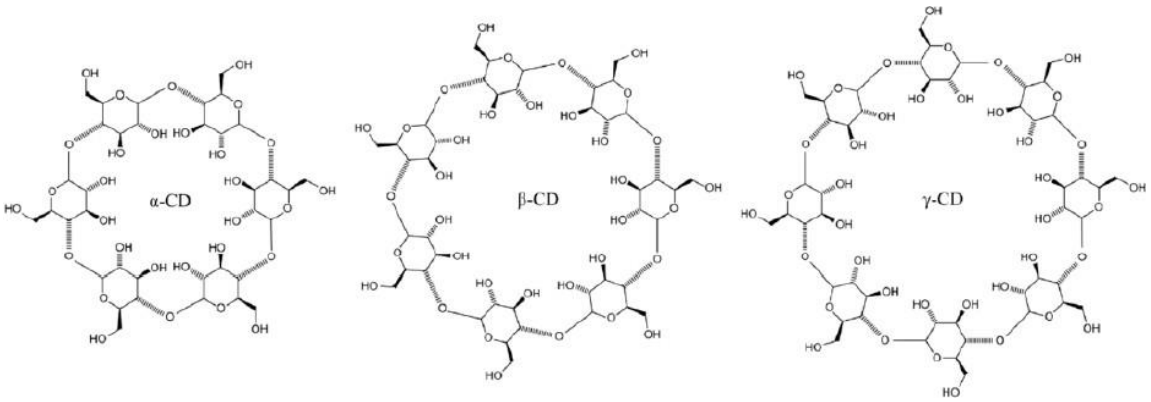

Figure 6. Chemical structure of cyclodextrins. CDs are cyclic oligosaccharides consisting of α-1,4-glucipyranose units. The most common forms are α-, β- and Y- CDs with six, seven and eight glucose units, respectively (Matencio et al., 2021).

CDs consist of a hydrophilic outer surface and a lipophilic central cavity, which confers high affinity for sterols (Tiwari et al., 2010). Indeed, they can bind cholesterol and extract it from cellular membranes (Zidovetzki and Levitan, 2007). Among them, **hydroxypropyl-β-cyclodextrin** (**HPβCD**) has been approved for the treatment of NPC disease (Yokoo et al., 2015). Preclinical studies have shown that the combined administration of Miglustat, HPβCD, and ALLO slows disease progression and reduces intracellular cholesterol accumulation in *Npc1* knockout mice (Hovakimyan et al., 2013). However, *in vivo* evidence suggests that HPβCD alone is primarily responsible for these therapeutic effects, since it has been demonstrated that a single dose administered to 7-day-old *Npc1* pups can increase cellular cholesteryl ester levels, suppress cholesterol synthesis, decrease inflammatory markers in both liver and brain, rescue cerebellar abnormalities, ameliorate neurodegeneration, and ultimately double lifespan (Madra and Sturley, 2010; Nusca et al., 2014; Caporali et al., 2016; Canterini et al., 2017; Kulkarni et al., 2018).

Although HPβCD crosses the BBB only poorly, it can reach LE/Ly compartments via pinocytosis, where it compensates for the loss of NPC1 and NPC2 function by catalytically shuttling cholesterol from LAL enzyme, directly to the limiting membrane of the lysosome (Rosenbaum and Maxfield, 2011). Once delivered to the luminal leaflet of the limiting membrane, cholesterol can spontaneously flip to the cytosolic leaflet and subsequently be redistributed to various cellular destinations (Maxfield and Menon, 2006) (**Figure 7**).

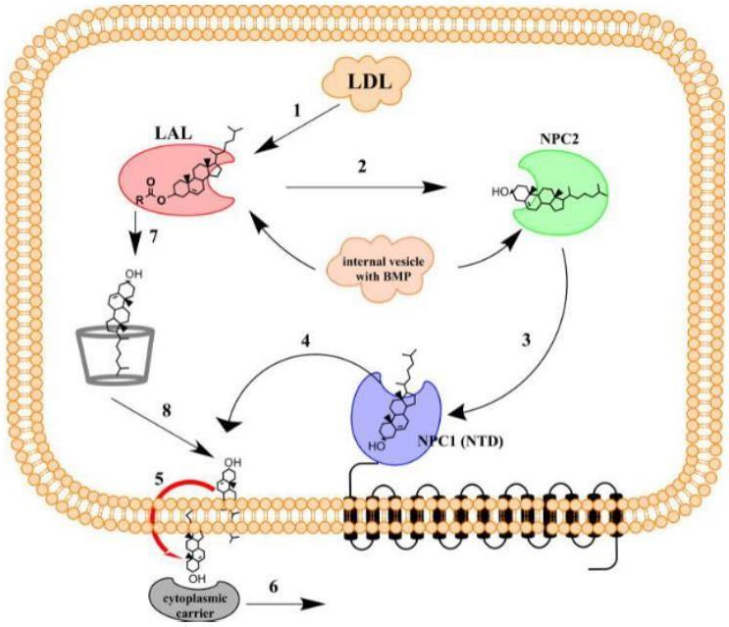

Figure 7. Schematic representation of HPβCD mechanisms of action. (**1**) In physiological conditions, LAL hydrolyzes cholesteryl ester; (**2**) the resulting free cholesterol is sequentially transferred to NPC2 and (**3**) NPC1 protein and (**4**) delivered to the luminal side of LE/Ly membranes. (**5**) Cholesterol can spontaneously flip to the cytosolic side and (**6**) then it can be carried to various destinations in the cell by cytoplasmic carriers. (**7**) In NPC disease, HPBCD can bind free cholesterol and (**8**) promote its efflux replacing the function of NPC1 and NPC2, bypassing steps 2-4 (Rosenbaum and Maxfield, 2011).

Clinical studies indicate that HPβCD treatment can slow disease progression in patients. However, because the compound does not effectively cross the human BBB, therapeutic protocols require prolonged high-dose intravenous infusions several times per week in addition to intrathecal injections to ensure CNS delivery. Importantly, significant side effects have been reported in both feline and murine models, including hearing loss and pulmonary toxicity (Helquist et al., 2013; Geberhiwot et al., 2018).

1.3 The genetic basis of NPC disease

NPC disease is a rare, inherited, autosomal recessive LSD (Guillemot et al., 2007; Vanier, 2013; Geberhiwot et al., 2018), caused by mutations in either the *NPC1* or the *NPC2* genes (Platt et al., 2014). Remarkably, patients carrying *NPC1* or *NPC2* mutations are phenotypically and biochemically indistinguishable (Dixit et al., 2011; Vanier et al., 2016).

1.3.1 *NPC1* and *NPC2* genes: spectrum of mutations

In 1997, the *NPC1* gene was identified and mapped to chromosome 18q11 (Carstea et al., 1997). It spans approximately 56 Kb and comprises 25 exons encoding the NPC1 protein (Morris et al., 1999; Vanier and Millat, 2003).

NPC1 is a large (~180 kDa) transmembrane glycoprotein localized in LEs/Lys membranes (Higgins et al., 1999; Sleat et al., 2004), playing a crucial role in the trafficking of low-density

lipoprotein (LDL)-derived cholesterol from LE/Ly compartments (Cruz et al., 2000; Wiegand et al., 2003). It consists of 1,278 amino acids (aa) containing a signal sequence (1–24 aa), thirteen transmembrane domains (TMDs) and three large luminal hydrophilic loops: the amino-terminal domain (25–264 aa, NTD), the middle luminal domain (371–615 aa, MLD), and the C-terminal domain (855–1098 aa, CTD) (Davies and Ioannou, 2000) (**Figure 8**).

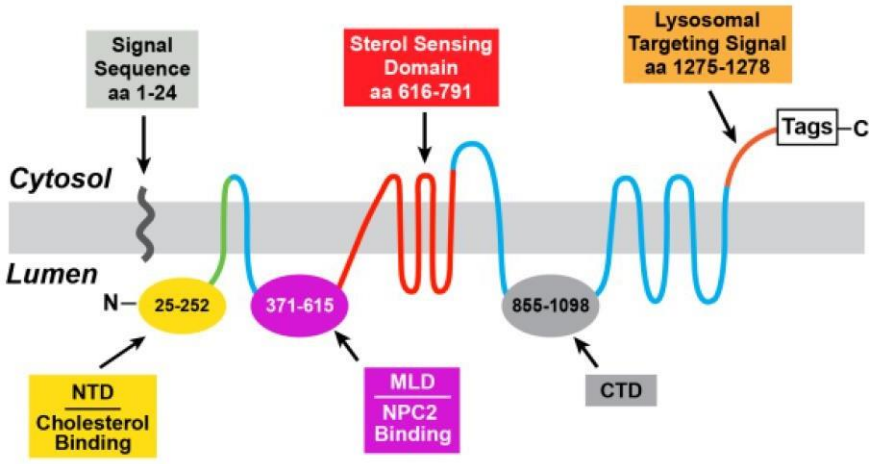

Figure 8. Structure of human NPC1 protein. NPC1 protein comprises a signal sequence, 13 transmembrane helices, 3 large hydrophilic domains (NTD, MLD and CTD), a sterol-sensing domain (SSD) and a C-terminal tail (Trinh et al., 2018).

The NTD, connected to the first TMD through a proline-rich region, contains multiple cysteine residues and a leucine zipper motif (Infante et al., 2008). Both the NTD and the transmembrane sterol-sensing domain (616–791 aa, SSD) function as cholesterol-binding sites (Ohgami et al., 2004; Lu et al., 2015). The SSD, located between the MLD and CTD of NPC1, shares ~30% sequence identity with the SSDs of 3-hydroxy-3-methylglutaryl-coenzyme A reductase (HMGR) enzyme, the sterol cleavage-activating protein (SCAP), and the Sonic Hedgehog (Shh) receptor Patched (Ptc) (Davies and Ioannou, 2000). Mutations in the SSD impair cholesterol export from LE/Ly compartments (Millard et al., 2005). The MLD serves as the binding site for NPC2 (Deffieu and Pfeffer, 2011; Li et al., 2016), while the CTD contains a cysteine-rich loop and finger motifs involved in protein–protein interactions (Lu et al., 2015). The NPC1 protein structure also includes a C-terminal tail containing dileucine motifs, which are essential for directing the protein to LEs/Lys (Fukuda et al., 1988; Ioannou, 2000) (**Figure 8**).

The *NPC2* gene, also known as *HE1*, is located on chromosome 14q24.3, spans approximately 13.5 Kb, and contains 5 exons encoding the NPC2 protein (Naureckiene et al., 2000). NPC2 is a small (~14.5 kDa) glycoprotein of 132 amino acids localizing to the lumen of LEs/Lys (Vanier and Millat, 2004). This soluble protein contains a 19-amino-acid signal sequence, a proline-rich region (PVPFPIP), six cysteine residues, and three N-glycosylation sites (Friendland et al., 2003). Crystallographic studies identified four evolutionarily constrained regions (ECR A, B, C, and D), which are essential for NPC2 function (Ko et al., 2003). Human NPC2 shares ~80% sequence identity with its bovine counterpart (Nielsen et al., 2011). Structurally, the protein consists of seven

β-strands stabilized by three disulfide bonds, forming an immunoglobulin-like β-sandwich fold (Ko et al., 2003) (**Figure 9**).

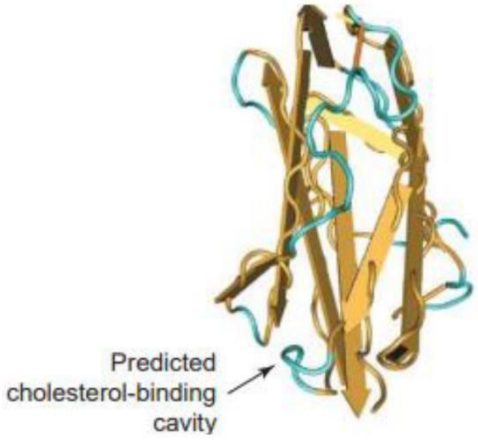

Figure 9. Structure of bovine NPC2 protein. NPC2 protein structure shows an immunoglobulin-like fold and multiple cholesterol-binding pockets (in light blue) (Ioannou, 2005).

To date, more than 400 disease-causing mutations in the *NPC1* gene have been described (Shammas et al., 2019). Among these, approximately 62% are missense mutations, 7% nonsense mutations, 13% small insertions, and 12% splicing mutations, while ~3% and 2% correspond to complex alleles and gross deletions/duplications, respectively (Carstea et al., 1997; Dardis et al., 2020) (**Figure 10A**). More than one-third of mutations occur within the cysteine-rich luminal loop of NPC1, primarily between amino acid residues 927–958 (Vanier and Millat, 2003). The most frequent mutations include I1061T, P1007A, and G992W (Bountouvi et al., 2017) (**Figure 10B**).

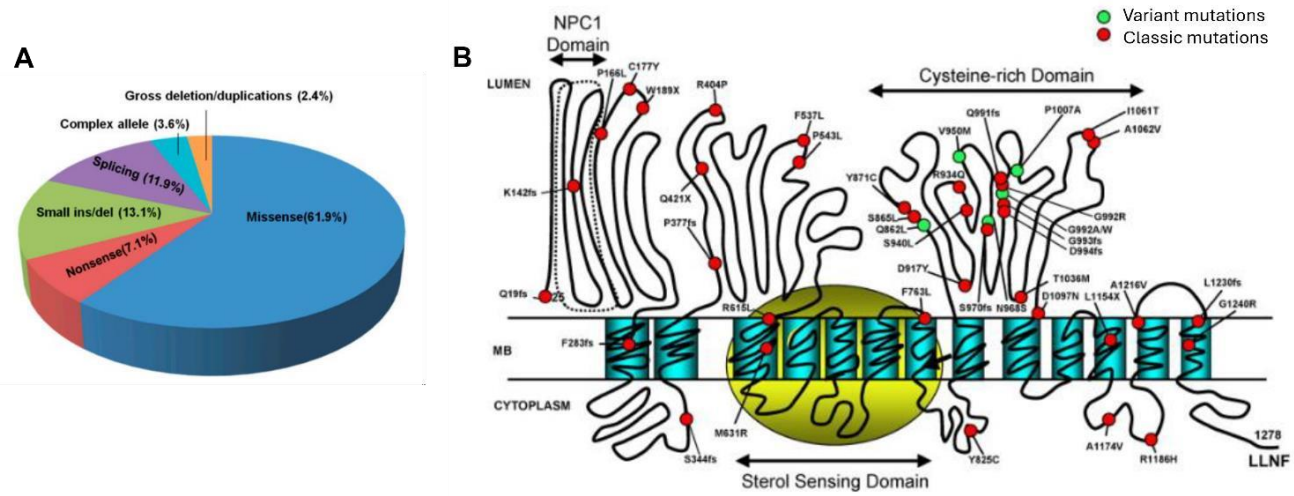

Figure 10. Identification and distribution of the most frequent human NPC1 mutations. (**A**) The pie chart represents the percentage of mutations occurring in the *NPC1* gene, most of which are missense and nonsense mutations (Dardis et al., 2020). (**B**) About 400 mutations are described in *NPC1* gene, although distributed in different regions of NPC1 protein, about one third of mutations occur within the cysteine-rich luminal loop and are associated with a classic biochemical form (red dots) or with a variant biochemical form (green dots) (Millat et al., 2005).

The I1061T mutation is an isoleucine-to-threonine missense mutation at position 1061, found in 20% of Western European patients and related to severe cholesterol-trafficking alterations ("classic biochemical phenotype"), corresponding to the juvenile neurological onset form (Millat et

al., 1999; Millat et al., 2005). It is also predominant in patients from the Spanish-American isolate, Southern Colorado and New Mexico (Ribeiro et al., 2001).

The P1007A mutation, a point mutation in exon 20 of the NPC1 protein, is most frequently detected in Europe and, together with G992W, which is typical of Nova Scotia, is responsible for a mild impairment of cholesterol trafficking in NPC1 patients ("variant biochemical phenotype") and correlates with adult neurological onset forms (Greer et al., 1999; Bauer et al., 2002; Tarugi et al., 2002; Vanier and Millat, 2003; Millat et al., 2005). In addition, more than 50 *NPC1* polymorphisms have been described, the most common being *Y129Y*, *H215R*, *P237S*, *I642M*, *I858V*, *N931N* and *R1266Q* (Kaminski et al., 2002).

Mutations in the *NPC1* gene generate different protein phenotypes, which differ in their intracellular trafficking and localization and in the severity of symptoms (**Table 1**) (Shammas et al., 2019). Three different NPC1 protein phenotypes were identified:

- **ER-located *NPC1* mutants**. This first group comprises *V378A, R404Q, H510P, Q775P, M1142T, G1162V, N1156S, L1244P, R1186H* and *I1061T* mutations, resulting in sequestration of the NPC1 protein within the ER.
- **Mutants revealing trafficking delay along the secretory pathway**. In this case, the trafficking of NPC1 protein from the ER is slower than that of the wild-type (*wt*) protein. This defective trafficking is due to *M631R, G1162A, C1168Y* and *D874V* mutations.
- **Mutants with *wt*-like trafficking pattern**. This last group refers to *L1213F, P1007A, V950M* and *D948Y* mutations, which result in NPC1 lysosomal localization similar to *wt*.

Number	Mutation	Processing	Biochemical Phenotype	Clinical Phenotype	Cell line
1	P1007A	Wt-like	Mild	Adult	Homozygous
2	D948Y	Wt-like	ND	ND	ND
3	L1213F	Wt-like	ND	Juvenile	Heterozygous with Y1088C
4	V950M	Wt-like	Mild	Adult	Homozygous
5	M631R	Partial trafficking	Severe	ND	Homozygous
				Late infantile	Heterozygous with I1061T
6	D874V	Partial trafficking	Severe	No neurological symptoms	Homozygous
7	C1168Y	Partial trafficking	Severe	Late infantile	Homozygous
8	G1162A	Partial trafficking	Severe	ND	Homozygous
9	V378A	ER block	Severe	Adult without neurological symptoms	Heterozygous with I1061T

10	R404Q	ER block	Severe	ND	Homozygous
					Heterozygous with D874V
11	H510P	ER block	Severe	Late infantile	Homozygous
12	Q775P	ER block	Severe	Severe infantile	Homozygous
					Heterozygous with N1156S
13	I1061T	ER block	Severe	Juvenile	Homozygous
			Mild	Juvenile	Heterozygous with P1007A
			Mild	Adult	Heterozygous with V950M
14	M1142T	ER block	Severe	ND	Heterozygous with G248V
15	N1156S	ER block	Mild	ND	Homozygous
			Severe	Juvenile	Heterozygous with I1061T
16	G1162V	ER block	Severe	ND	Heterozygous with I1061T
17	R1186H	ER block	Severe	ND	Homozygous
				ND	Heterozygous with N1156S
18	L1244P	ER block	ND	Late infantile	Heterozygous with P1007A

Table 1. Classification of NPC1 protein phenotypes. Different protein phenotypes, due to different *NPC1* mutations, differ in their intracellular trafficking and localization leading to a wide range of symptoms (Adapted from Shammas et al., 2019).

Regarding the *NPC2* gene, about 20 mutations have been identified, including 15 missense/nonsense mutations, 3 small deletions and 2 splicing mutations (McKay Bounford and Gissen, 2014). The most frequent is the nonsense mutation *E20X*, associated with a severe biochemical and clinical phenotype (Verot et al., 2007). Among the missense mutations occurring in *NPC2*, the most common are *V39M* and *C99R*, resulting in the adult onset of neurological symptoms and in the severe neonatal/infantile disease form, respectively (Klünemann et al., 2002; Vanier and Millat, 2004) (**Figure 11**).

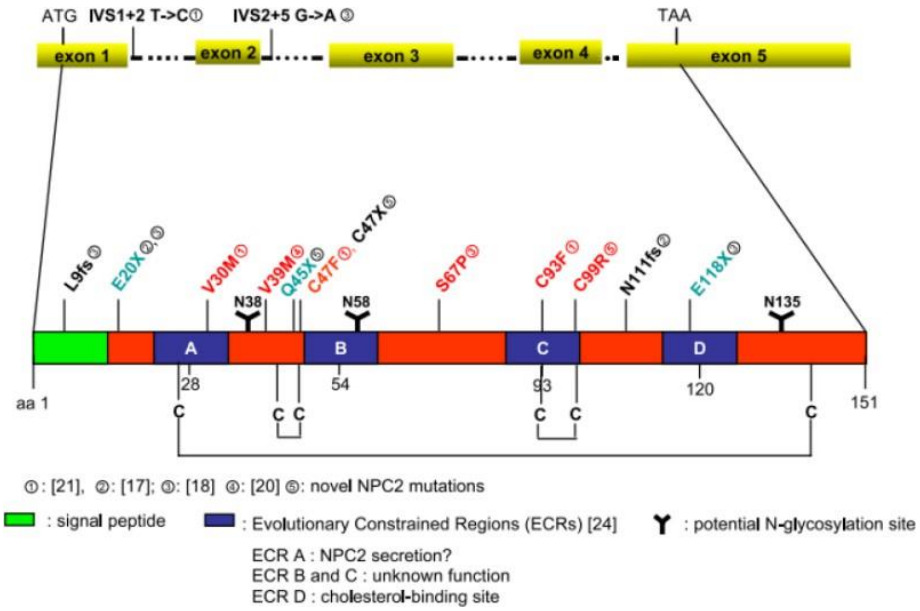

Figure 11. Localization of *NPC2* mutations. About 5% of NPC patients present mutations in the *NPC2* gene. To date, 20 mutations leading to a truncated protein have been described (Vanier and Millat, 2004).

1.3.2 The role of NPC1 and NPC2 proteins in intracellular cholesterol trafficking

The brain contains about 25% of the total body cholesterol, making it the most cholesterol-rich organ in the human body (Björkhem and Meaney, 2004). In the CNS, cholesterol represents an essential structural component of the PM and plays a crucial role in several key processes, including neuronal development, synaptic vesicle release, neurite outgrowth, synapse formation, and synaptic plasticity (Koudinov and Koudinova, 2001; Fünfschilling et al., 2012; Zhang and Liu, 2015).

Cholesterol does not cross the BBB, therefore it must be synthesized locally, both during development and in adulthood (Jurevics and Morell, 1995; Berghoff et al., 2021). Astrocytes represent the main source of cholesterol in the brain, supplying it to neurons (Dietschy and Turley, 2004). In astrocytes, cholesterol is synthesized by HMGR enzyme and packaged with Apolipoprotein E (ApoE) into small high-density lipoprotein (HDL)-like particles (Boyles et al., 1989; Herz and Bock, 2002). Eventually, astrocytes secrete the ApoE–cholesterol complexes through the ATP-binding cassette transporter A1 (ABCA1), so that neurons can uptake the complexes via members of the LDL receptor family (Brown and Goldstein, 1986; Benarroch, 2008). Following clathrin-mediated endocytosis, the complexes are delivered to LEs/Lys, where cholesterol esters are hydrolyzed by LAL (Pfrieger, 2003; Herz, 2009). Free cholesterol is then exported from the LEs/Lys compartments through a mechanism mediated by NPC1 and NPC2 proteins (Maxfield and Menon, 2006; Storch and Xu, 2009) (**Figure 12**).

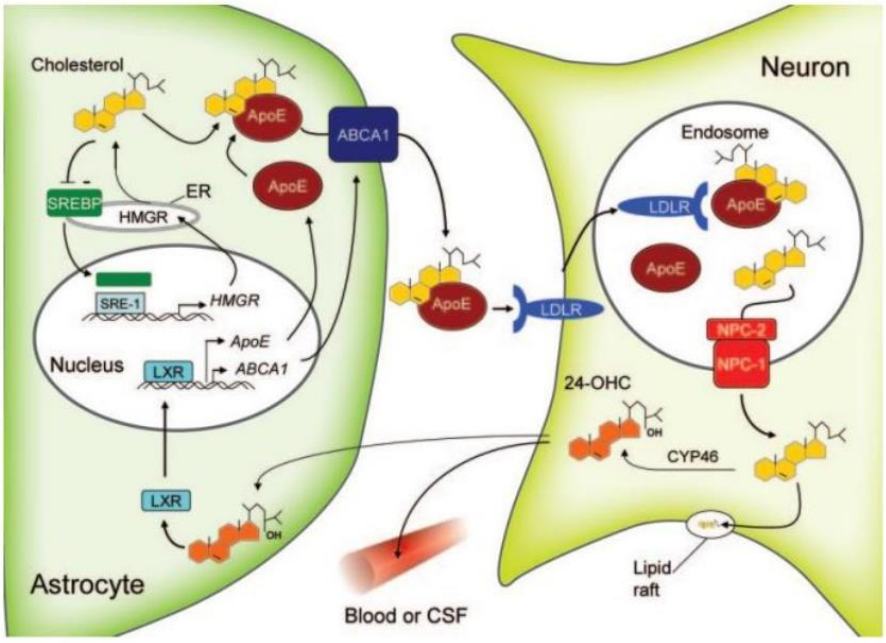

Figure 12. Cholesterol metabolism in CNS. In the CNS astrocytes are the main source of cholesterol, which is synthesized in the ER by HMGR enzyme. This latter is regulated by the sterol-regulated element binding protein (SREBP) which, in turn, binds to the sterol-regulated element 1 (SRE-1). Synthesized cholesterol binds ApoE, forming an ApoE-cholesterol complex, secreted via ABCA1 and internalized into the neuron by the LDLR family. In neurons, the complex is hydrolyzed, and free cholesterol binds to NCP2 and NPC1 proteins, mediating its efflux from LE/Ly compartments. The unesterified cholesterol is then transported to ER and PM, by sterol transfer proteins. Within the brain, cholesterol is mainly eliminated via its oxidation to 24-hydroxy cholesterol (24-OHC), catalyzed by membrane protein cytochrome P450 (CYP) enzymes (Benarroch, 2008).

In recent years, a mechanistic model describing how NPC1 and NPC2 proteins cooperate to mediate cholesterol egress from LEs/Lys has been proposed (Long et al., 2020). In this model, endocytosed cholesterol binds to the sterol transfer protein NPC2 within the lumen of LEs/Lys, with a 1:1 stoichiometry (Xu et al., 2007). NPC2 subsequently delivers the unesterified cholesterol to the NTD of NPC1, located in the limiting membrane. This interaction induces a conformational change in NPC1-NTD, which reorients – likely in a vertical alignment – to form an internal hydrophobic tunnel within the NPC1 protein. This tunnel enables the transfer of cholesterol from the NTD to the SSD (Long et al., 2020). Once transferred, NPC1 inserts cholesterol into the LE/Lys membrane, where it rapidly flips toward the cytosolic leaflet. From there, cholesterol is transported to the ER and PM via sterol transfer proteins (Benarroch, 2008; Infante et al., 2008; Du et al., 2011; Long et al., 2020). Thus, NPC1 and NPC2 function cooperatively to facilitate cholesterol export from LEs/Lys, playing an essential role in maintaining cholesterol homeostasis (Frolov et al., 2003; Kwon et al., 2009; Pfeffer, 2019) (**Figure 13**).

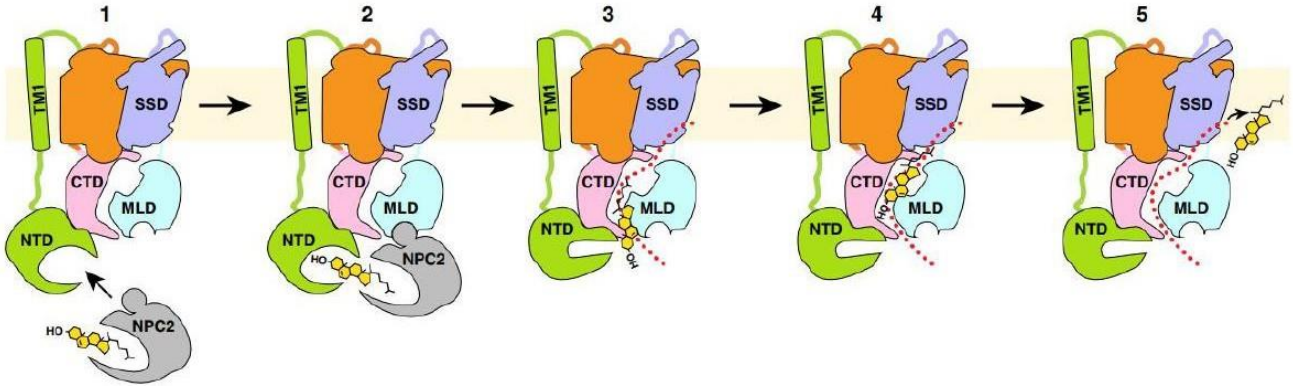

Figure 13. Mechanism of action of NPC1 and NPC2 proteins in mediating cholesterol efflux from LEs/Lys. NPC2 binds cholesterol with high affinity and transfers it to the N-terminal domain (NTD) of NPC1 (1). This interaction induces a conformational change in NPC1-NTD (2), which reorients to create an internal hydrophobic tunnel, enabling cholesterol transfer through NPC1 (3–4). Cholesterol is then released from LEs/Lys and transported to the ER and PM (5) (Long et al., 2020).

1.4 Neuropathological mechanisms in NPC1 disease

As already mentioned, in NPC disease, mutations in the *NPC1* or *NPC2* gene cause misfolding and reduced functionality of the corresponding proteins (Sokol et al., 1988), leading to cholesterol sequestration within LEs/Lys (Hawes et al., 2010). The resulting impairment in cholesterol trafficking is associated with a marked reduction of cholesterol content in the PM and ER, ultimately leading to widespread cholesterol dyshomeostasis (Peake and Vance, 2010; Cariati et al., 2021) (**Figure 14**).

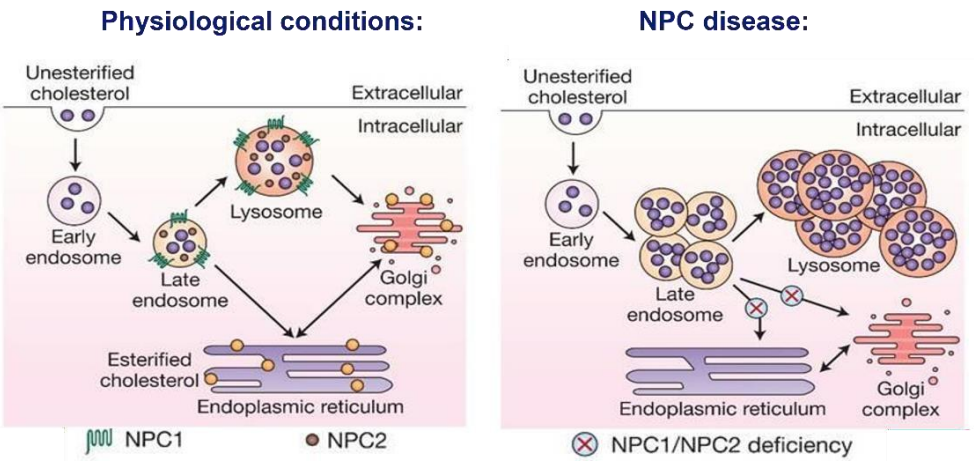

Figure 14. Cholesterol trafficking defects in NPC disease. Under physiological conditions, NPC1 and NPC2 proteins mediate the egress of endocytosed cholesterol from LE/Ly compartments. Free cholesterol is transported, by sterol transfer proteins, to ER and PM where it will undergo an esterified process. In NPC disease, defects in either of two cholesterol-binding proteins lead to a cholesterol accumulation within LEs/Lys and a consequent imbalance of PM and EM cholesterol contents (Adapted from Cariati et al., 2021).

The reduced activity and functionality of both proteins underlies several neuropathological processes (Shen et al., 2012; Vázquez et al., 2012; Fiorenza et al., 2018). In addition to defects in cholesterol efflux from LE/Ly compartments, alterations in endo-lysosomal trafficking have been reported (Zhang et al., 2001; Chen et al., 2008). Retrograde transport of endo-lysosomes from the cell periphery to the perinuclear region is mediated by motor proteins such as dynein, which drives organelles toward the minus end of microtubules located in the perinuclear area (Granger et al., 2014; Reck-Peterson et al., 2018). Dynein recruitment to endo-lysosomal compartments depends on the small GTPase Rab7 and the cholesterol-binding protein ORP1L (Vihervaara et al., 2011). In NPC1 disease, the excessive endo-lysosomal cholesterol accumulation induces a conformational change in ORP1L, which – through interaction with Rab7 – promotes dynein association with endo-lysosomes (Zhang et al., 2001; Rocha et al., 2009). As a consequence, endo-lysosomes remain anchored at the microtubule minus ends near the perinuclear region, become immobilized, and fail to fuse with early endosomes (Lebrand et al., 2002; Takahashi and Kobayashi, 2009). Moreover, it has been suggested that high endosomal cholesterol content, as observed in NPC disease, inhibits the activity of Rab4, a GTPase regulating membrane recycling from early endosomes, leading to delayed and abnormal membrane recycling (Mohrmann et al., 2002; Choudhury et al., 2004).

Several studies have implicated defective autophagic flux in NPC1 disease (Pacheco and Lieberman, 2008; Lieberman et al., 2012; Elrick and Lieberman, 2013; Fiorenza et al., 2018). Autophagy is an intracellular degradation pathway responsible for removing misfolded proteins and damaged organelles and is essential for maintaining cellular homeostasis (Glick et al., 2010). The process begins with the formation of autophagosomes, which fuse with LEs to generate amphisomes. These latter, in turn, fuse with Lys to form autolysosomes, where the cargo is degraded (Berg et al., 1998; Yang and Klionsky, 2009). *In vitro* and *in vivo* studies have demonstrated that cholesterol accumulation in NPC1 disease is associated with impaired autophagy (Ishibashi et al.,

2009; Sarkar et al., 2013; Vanier, 2015). Consistently, an increase in the steady-state number of autophagosomes and LEs has been observed, likely due to defects in their degradation, resulting in impaired amphisome formation in NPC1 mutant cells (Sarkar et al., 2013; Maetzel et al., 2014; Meske et al., 2014). The defective fusion of autophagosomes with LEs has been attributed to abnormalities in both the recruitment and assembly of the SNARE complex on LEs, thereby impairing amphisome formation (Vanier, 2015). As a consequence, autophagosome maturation into autolysosomes is hindered, leading to delayed clearance of autophagic cargo and progressive accumulation of autophagic vacuoles within the Lys of NPC1-deficient cells (Elrick et al., 2012; Ordonez et al., 2012).

Both endocytosis and autophagy are processes that rely on calcium (Ca^{2+}) release from Lys (Wu et al., 2009; Bootman et al., 2018). In addition to the described anomalies in these two essential pathways, NPC1-deficient cells exhibit decreased Ca^{2+} levels in LE/Ly compartments, resulting in reduced Ca^{2+} release. Furthermore, as observed in other LSDs, altered ER Ca^{2+} homeostasis has been reported, due to an imbalance in ER cholesterol content (Ginzburg et al., 2004; Lloyd-Evans et al., 2008; Shen et al., 2012).

Cholesterol, glycosphingolipid, and other lipid accumulation in NPC1 disease profoundly affects mitochondrial function (Yu et al., 2005; Vázquez et al., 2012; Liedtke et al., 2022). The excess of mitochondrial cholesterol described in *Npc1* mice is responsible for alterations in mitochondrial morphology and function (Kennedy et al., 2014; Torres et al., 2017). In particular, mitochondria of *Npc1* mutant mice appear reduced in size, length, and width compared to those of *wt* mice, accompanied by a decreased mitochondrial membrane potential and ATP synthase activity, increased lactate levels, enhanced respiration, and diminished antioxidant capacity. These alterations culminate in an overall increase in reactive oxygen species (ROS) production, which in turn causes oxidative stress (Yu et al., 2005; Koh et al., 2006; Klein et al., 2011; Visentin et al., 2013; Woś et al., 2016; Wheeler and Sillence, 2020).

The neuropathology of NPC1 disease includes diffuse cerebral and cerebellar atrophy, neuronal degeneration, neuroaxonal dystrophy, and demyelination (Sèvin et al., 2007; Evans and Hendriksz, 2017). Notably, NPC1 disease is also referred to as "*Juvenile Alzheimer's Disease*", since it shares two key pathological hallmarks: amyloid plaques and neurofibrillary tangle deposition (Love et al., 1995; Pacheco et al., 2009; Saito et al., 2022). Studies on postmortem AD brain samples have shown that in juvenile/adult patients, *NPC1* gene mutations induce endosomal amyloid β accumulation and tau protein hyperphosphorylation, leading to neurofibrillary tangle formation and contributing to neurodegeneration (Esposito et al., 2019; Saito et al., 2022).

The most vulnerable neuronal populations are cerebellar PCs, basal ganglia, and thalamus, whereas hippocampal and cortical regions are affected later (Pressey et al., 2012; Walterfang et al.,

2013). The massive loss of PCs is the prominent feature of NPC1 disease, resulting in progressive ataxia and motor impairment (Higashi et al., 1993; Sarna et al., 2003; Martin et al., 2019). Several *in vivo* studies have demonstrated that PC degeneration occurs along an anterior-to-posterior gradient (Ko et al., 2005). Specifically, PC death begins in the first four cerebellar lobes, corresponding to the anterior zone, and then progresses posteriorly (Sarna et al., 2003; Elrick et al., 2010). PCs undergo programmed necroptosis (Cougnoux et al., 2018), in which the release of damage-associated molecular patterns (DAMPs) and proinflammatory cytokines recruits microglia, promoting the phagocytosis of damaged cells (Heckmann et al., 2019).

For a long time, several studies argued and demonstrated a cell-autonomous degeneration of PCs (Ko et al., 2005; Elrick et al., 2010). However, Kavetsky and colleagues highlighted the contribution of activated microglia to degeneration. Using *Npc1*$^{nmf164/nmf164}$ mice, they found that in the cerebellar molecular layer (ML), neuroinflammation and subsequent microglia activation occur earlier than in *wt* mice, and precede PC degeneration. Specifically, they observed that before significant PC loss – which typically occurs between the 8th and 12th postnatal week – microglia are already activated around the 4th postnatal week in *Npc1* mutant mice, where they contact PC dendrites. Interestingly, microglia activation increases as PC death progresses and coincides with dendritic degeneration in the ML. To further investigate the role of microglia, the authors fed *Npc1*$^{nmf164/nmf164}$ mice a Western diet enriched with saturated fats, cholesterol, and sugars, which induced an inflammatory response and enhanced microglial activation. They demonstrated that this treatment leads to stronger microglial activation and increased engulfment of PCs, resulting in accelerated and more severe PC degeneration, thus proving that microglia actively contribute to PC death (Kavetsky et al., 2019).

1.5 Murine models of NPC1 disease

Over the years, several animal models have been developed to study the molecular and cellular mechanisms underlying NPC1 disease. Among these, the most commonly used experimental models include cat, zebrafish, fruit fly, nematode, yeast, and mouse (Lopez and Scott, 2013) (**Table 2**).

Species	Name	Affected gene	Mutation (cDNA position)	Outcome	Strain of origin
Feline	*NPC1*	*Npc1*	c.2864G>C	p.Cys955Ser (C955S)	N.A.
Feline	*NPC2*	*Npc2*	c.82 + 5G>A	p.Gly28_Ser29ins35 (G28_S29ins35) retention of 105 bp in the mature mRNA leading to an in-frame insertion of 35 aa between residues 28 and 29 of NPC2 protein	N.A.

Murine	*Npc1*$^{nih(m1n)}$	*Npc1*	824 bp of MaLR retrotransposon-like DNA replacing 703 bp of *wt* genomic sequence	Frameshift + premature stop codon (null allele)	BALB/c
Murine	*Npc1*^{smp}	*Npc1*	c.2911 + 3 A>C	p.Val971GlyfsTer31 (V971GfsTer31) cDNA retains 43 bp of intron 19 shifting the reading frame, replacing p.Val 971 for a Gly, adding 30 novel residues followed by a stop codon	C56BL/Ks
Murine	*Npc1*$^{pf/pf}$	*Npc1*	c.604C>G; c.607-608TT>GC	p.Pro202Ala; Phe202Ala (P202A/F203A)	C57BL/6
Murine	*Npc1*^{nmf164}	*Npc1*	c.3163A>G	p.Asp1005Gly (D1005G)	C57BL/6
Murine	*Npc1*$^{tm(I1064T)Dso}$	*Npc1*	c.3179T>C + loxP sites flanking exons 14-20	p.Ile1064Thr (I1064T)	C57BL/6
Murine	*Npc1*^{imagine}	*Npc1*	c.1554-1009G>A	Inclusion of 194 bp pseudoexon in intron 9 resulting in a premature stop codon	C57BL/6
Murine	*Npc1*^{pioneer}	*Npc1*	c.1920delG	p.His641ThrfsTer2 (H641TfsTer2) frameshift replacing p.His641 with Thr and resulting in a premature stop codon two residues downstream	C57BL/6
Murine	*Npc2*^{tm1Plob}	*Npc2*	Insertion into intron 2 resulting in splice junction mutation	Hypomorphic allele (decrease in correctly spliced *Npc2* mRNA)	BALB/c or mixed
Murine	*Npc1 ASO*	*Npc1*	N/A	Antisense-mediated knockdown of hepatic *Npc1*	BALB/c

Table2. Genetic features of the main animal models of NPC1 disease. The table shows the main mouse models used to study NPC1 disease. The most used mouse models are circled in red (Adapted from Fog and Kirkegaard, 2019).

1.5.1 *Npc1*^{nih} (*Npc1*^{m1n}) mouse strain

The *Npc1*^{nih} mouse model, maintained on a BALB/c background, was first described by Pentchev in 1980 (Pentchev et al., 1980). This model was generated using a mouse retroposon that inserts 1,100 base pair (bp) of DNA, causing an 800 bp deletion in the *Npc1* gene, resulting in a complete knockout of *Npc1* and total absence of Npc1 protein (Loftus et al., 1997) (**Table 2**). Compared to other NPC1 mouse models, *Npc1* knockout mice display early disease onset and rapid progression, leading to death before 90 days of age (Morris et al., 1982). The disorder in *Npc1* null mice resembles the late-infantile form of human NPC1 disease, recapitulating several clinical features, including unesterified cholesterol accumulation, hepatosplenomegaly, cerebellar ataxia, and progressive neurodegeneration (Nusca et al., 2014; Fog and Kirkegaard, 2019).

Additionally, *Npc1*^{nih} mice exhibit weight loss, axonal swelling, gliosis, cognitive decline, motor impairment, reduced muscular strength, tremors, and, by 6 weeks of age, pronounced PC loss (Võikar et al., 2002). However, certain human hallmarks, such as neurofibrillary tangles and β-amyloid deposits, are not observed (Walkley et al., 2004; Fog and Kirkegaard, 2019). The *Npc1*^{nih} strain also shows marked demyelination due to a reduced number of mature oligodendrocytes (Takikita et al., 2004). Since cholesterol is a major component of myelin, it is unsurprising that cholesterol dyshomeostasis is accompanied by myelin defects (Hussain et al., 2019).

1.5.2 *Npc1*^{spm} mouse strain

The *Npc1*^{spm} mouse model, maintained on a C57BL/Ks background, carries a point mutation in the third base of intron 19, which, as in *Npc1*^{nih} mice, results in a null *Npc1* allele (Sarna et al., 2003) (**Table 2**). This mutation, known as sphingomyelinosis (hence the acronym spm), causes a deficiency of the sphingomyelinase enzyme, leading to SM accumulation in multiple organs (Miyawaki et al., 1982). Affected mice, similarly to *Npc1*^{nih} mice, exhibit weight loss around 7 weeks of age, hepatosplenomegaly, PC degeneration, and cognitive decline, ultimately progressing to death between 12 and 14 weeks of life (Miyawaki et al., 1986).

1.5.3 *Npc1*$^{nmf164/nmf164}$ mouse strain

In 2012, Jackson Laboratory generated a novel mouse model, *Npc1*$^{nmf164/nmf164}$ (hereafter *Npc1*^{nmf164}) on a C57BL/Ks background (Maue et al., 2012). This model carries a point mutation resulting in a single aa substitution (D1005G) in the Npc1 protein, changing aspartate to glycine at position 1005 (Fog and Kirkegaard, 2019) (**Table 2**). The mutation occurs in the cysteine-rich luminal loop of Npc1 protein, between the 8th and 9th transmembrane domains, a region where approximately one-third of human mutations are located (Vanier, 2010). This single bp change causes reduced levels of Npc1 protein and impaired functionality (Maue et al., 2012).

Npc1^{nmf164} mice recapitulate the human juvenile form of NPC1 disease, which represents the majority of human cases, sharing many key features, including cholesterol and sphingolipid accumulation, hepatosplenomegaly, cognitive decline, and PC degeneration leading to cerebellar ataxia (Morris et al., 1982). In contrast to *Npc1*^{nih} mice, pronounced PC degeneration in *Npc1*^{nmf164} mice occurs between postnatal day 60 and 90 (PN60–PN90), with few PCs remaining by PN90 (Maue et al., 2012). Unlike knockout mice, these mice do not display a marked loss of myelin (Maue et al., 2012); however, a reduction in myelin basic protein (MBP) expression and impaired myelination due to inhibited oligodendrocyte maturation has been observed (Caporali et al., 2016).

The *Npc1*^{nmf164} model mimics later-onset, slower, and milder forms of human NPC1 disease, recapitulating many biochemical, pathological, and behavioral features (Caporali et al., 2016; Kulkarni et al., 2018), making it a valuable tool for investigating the molecular and cellular mechanisms underlying NPC1 pathogenesis. However, a significant limitation of this model is the

low percentage of homozygous offspring obtained from crossing heterozygous mice (Maue et al., 2012; Fog and Kirkegaard, 2019).

1.5.4 Evaluation of motor and cognitive deficits in *Npc1* mutant mice

Over the years, several *in vivo* studies have investigated the effects of cholesterol dyshomeostasis on motor and cognitive performance, since the main clinical features of NPC1 disease are cerebellar ataxia and cognitive decline (Heitz et al., 2017; Martin et al., 2019). Most behavioral assessments have been conducted on *Npc1*$^{nmf164/nmf164}$ and *Npc1*^{nih} mouse models.
Using *Npc1*$^{nmf164/nmf164}$ mice on a BALB/cJ background, it was demonstrated that during tasks requiring coordination and balance (e.g., ascending a ladder, crossing a narrow bridge, suspension on a wire), pups from PN10 displayed a significant delay in the acquisition of complex motor skills compared to *wt* littermates (Caporali et al., 2016). Furthermore, when tested with the Vertical Screen, Balance Beam, and Coat Hanger tasks – aimed at evaluating motor performance – adult *Npc1*$^{nmf164/nmf164}$ mice exhibited severe motor deficits after PN30, coinciding with the onset of PC degeneration (Võikar et al., 2002; Maue et al., 2012; Caporali et al., 2016).

Regarding *Npc1*^{nih} mice, maintained on a BALB/cJ background, motor impairment appeared earlier, between the 4th and 6th week of age, as assessed through behavioral tests, such as Gait Analysis, Rotarod, Balance Beam, Coat Hanger, and Open Field tests (Smith et al., 2009; Maue et al., 2012; Kirkegaard et al., 2016).

In addition to motor dysfunction, deficits in learning and hippocampal-dependent memory consolidation have been observed in both models (Võikar et al., 2002; Oddi et al., 2019). Specifically, *Npc1*^{nih} mice displayed cognitive impairments at PN50–PN51, as measured by the Spatial Water Maze task (Võikar et al., 2002; Fog and Kirkegaard, 2019). Similarly, in *Npc1*$^{nmf164/nmf164}$ mice on a C57BL/6J background, the evaluation of cognitive performance using the Elevated Plus Maze and Spatial Novelty Discrimination tests revealed perseverative behavior and learning and memory deficits starting from PN55 (Oddi et al., 2019). Interestingly, *Npc1* mutant mice also exhibited reduced anxiety compared to *wt* animals, likely reflecting a lack of adaptive ability to distinguish safe from unsafe situations, as a consequence of cognitive impairment (Oddi et al., 2019).

Chapter II

Focus on the cerebellum

2.1 Macro- and micro-architecture of the cerebellum

2.1.1 Large-scale neuroanatomy of the cerebellum

The term *cerebellum* derives from the Latin diminutive of *cerebrum*, literally meaning "little brain", reflecting both its anatomical proximity to and morphological resemblance with the brain.
The cerebellum represents a fundamental component of the CNS, specifically of the rhombencephalon or hindbrain, and is located in the posterior cranial fossa, beneath the occipital and temporal lobes of the cerebral cortex (D'Angelo, 2018; van Essen et al., 2018), where it constitutes the dorsal wall of the fourth ventricle (Iulianella et al., 2019).

From a macro-anatomical perspective, the mammalian cerebellum, characterized by a distinctive oval shape, mirrors the structural organization of the brain. Its **gray matter** (**GM**) is primarily arranged into two principal compartments: an external one represented by the highly folded **cerebellar cortex**, and an internal one composed of three pairs of **deep cerebellar nuclei** (**DCN**) – dentate, interposed (consisting of globose and emboliform nuclei), and fastigial – embedded within the **subcortical white matter** (**WM**) (Gilmore et al., 2009; Manto and Oulad Ben Taib, 2010; Farini et al., 2021). Notably, neurons of the DCNs represent the sole output of the cerebellum (Ito et al., 1984; Manto and Oulad Ben Taib, 2010). In parallel, the cerebellum also exhibits a medio-lateral organization, comprising a central **vermis** and two **paravermial** regions that connect the two lateral **hemispheres** (Larsell, 1970; Sillitoe and Joyner, 2007) (**Figure 15**).

Two deep transverse fissures divide the cerebellar cortex into three main lobes: the primary fissure separates the **anterior** from the **posterior lobe**, while the posterolateral fissure separates the posterior from the **flocculonodular lobe** (Sotelo and Wassef, 1991; Sillitoe and Joyner, 2007; Roostaei et al., 2014). In addition, more superficial fissures further subdivide these three lobes into ten **lobules** (I–X) arranged along the rostro-caudal axis, which can be further divided into **sub-lobules** or **folia**, giving the cerebellar surface its characteristic onion-like appearance (Voogd and Glickstein, 1998; Glickstein et al., 2009; Lin et al., 2020). Each transverse lobule encompasses a central portion in the vermis along with the adjacent two lateral segments in the hemispheres (Roostaei et al., 2014). (**Figure 15**).

Although anatomically the cerebellum is divided into three major transverse lobes, its functional organization is primarily segregated along the longitudinal axis: the **vestibulocerebellum**, corresponding to the flocculonodular lobe; the **spinocerebellum**, constituted by the vermis and paravermial zones; and the **cerebrocerebellum**, consisting of the two lateral hemispheres (Ramnani, 2006; Stoodley and Schmahmann, 2010) (**Figure 15**).

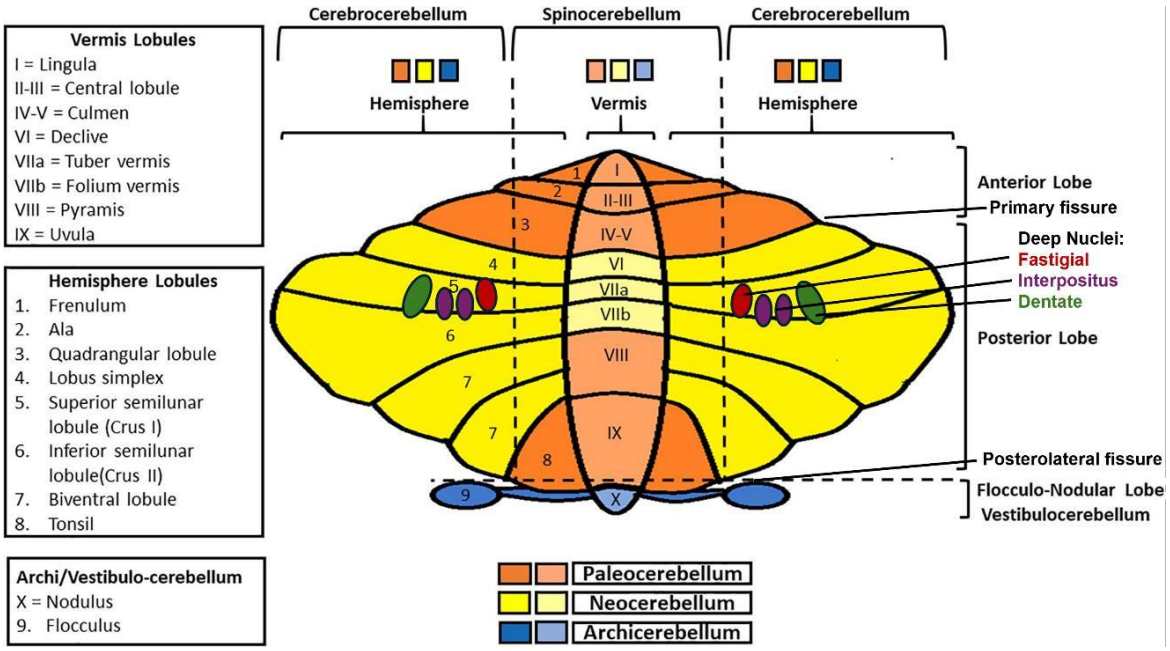

Figure 15. Schematic representation of cerebellar gross anatomy. Anterior-posteriorly, the cerebellum presents three lobes (anterior, posterior, and flocculo-nodular), each one further divided into lobules (I-X). Medio-laterally, it is composed of a central part (the vermis), and two lateral ones (cerebellar hemispheres). Functionally, it is divided into three different regions: the spinocerebellum formed by the vermis and paravermial zones, so-called since it communicates with the spinal cord; the cerebrocerebellum constituted by the most lateral zones of the hemispheres, in connection with the cerebral cortex; and finally, the vestibulocerebellum, corresponding to the flocculo-nodular lobe (adapted from Amore et al., 2021).

2.1.2 Cerebellar cortex cytoarchitecture and microcircuitry

Despite its morphological and molecular complexity, the mammalian cerebellar cortex is remarkably homogeneous from a histological perspective and is organized into three distinct layers, arranged above the WM: the **internal granular layer** (**IGL**), the **Purkinje cell layer** (**PCL**), and the **molecular layer** (**ML**) (Palay and Chan-Palay, 1974; Ramnani, 2006; Sillitoe and Joyner, 2007; Apps et al., 2018; Iulianella et al., 2019) (**Figure 16**).

The **IGL**, the innermost layer, is densely packed with **GCs** – small excitatory glutamatergic neurons that represent about 80% of all cerebellar neurons (Herculano-Houzel et al., 2006) – together with inhibitory **Golgi cells** (**GoCs**) and excitatory **unipolar brush cells** (**UBCs**), the latter more recently recognized as glutamatergic interneurons (Palay and Chan-Palay, 1974; Sillitoe and Joyner, 2007). GC dendrites receive excitatory input from **mossy fibers** (**MFs**), the second major afferent system of the cerebellar cortex, which originate from multiple brainstem nuclei (Wu et al., 1999; Fink et al., 2006; Green and Wingate, 2014). MFs form synapses with both GC dendrites and GoC axons, creating highly organized synaptic structures within the IGL known as cerebellar **glomeruli** (Farini et al., 2021; De Schutter, 2002; Mapelli et al., 2014). Each glomerulus integrates excitatory glutamatergic inputs (MF–GC and MF–GoC contacts) with inhibitory GABAergic synapses (GoC–GC), making it the primary station of afferent signal processing within the cerebellar cortex (Camuso et al., 2022). Although MFs primarily innervate GCs, the information they convey reaches PCs indirectly via GC axons projecting into the ML, where they bifurcate into **parallel fibers** (**PFs**) and synapse onto PC dendrites (Valle et al., 2001; Voogd et al., 2003) (**Figure 16**).

The **PCL**, the intermediate layer, hosts the cell bodies of PCs, **Bergmann glia** (**BG**), and **candelabrum cells** (**CCs**) (Laine and Axelrad, 1994; Iulianella et al., 2019). PCs are large GABAergic neurons whose dendrites extend into the ML, while their axons traverse the IGL and project all processed cerebellar cortical output to the DCN within the subcortical WM, thereby constituting the sole efferent pathway of the cerebellar cortex (Stoodley and Schmahmann, 2010; Leto and Rossi, 2012). The DCN, in turn, send excitatory projections to various supratentorial and brainstem targets (Allen and Tsukahara, 1974; Heck and Sultan, 2002). Within the PCL, PC bodies are flanked by BG soma, representing the main glial component of the cerebellum (Wang et al., 2012). Finally, CCs, another class of inhibitory interneurons, are interspersed among PC bodies and contribute to local circuit modulation (Ambrosi et al., 2007) (**Figure 16**).

The **ML**, the outermost layer, contains the fan-shaped dendritic arbors of PCs, the bifurcating axons of GCs forming T-shaped PFs, and two main types of inhibitory interneurons: **stellate cells** (**SCs**) and **basket cells** (**BCs**) (Fox and Barnard, 1957; Straub et al., 2020; Kim and Augustine, 2021). Each PF forms excitatory glutamatergic synapses on the dendrites of numerous PCs (Hibi and Shimizu, 2012). Within this layer, PC dendrites are also innervated by glutamatergic **climbing fibers** (**CFs**), an extracerebellar afferent projection originating in the inferior olive. In the mature cerebellum, each PC is innervated by a single CF (Schilling et al., 2008; Cerminara et al., 2015). In addition to excitatory inputs, PCs in the ML also receive inhibitory input from BCs and SCs, which modulate PC activity through synapses onto dendritic arbors and the soma, respectively (Leto and Rossi, 2012; Brown et al., 2019) (**Figure 16**).

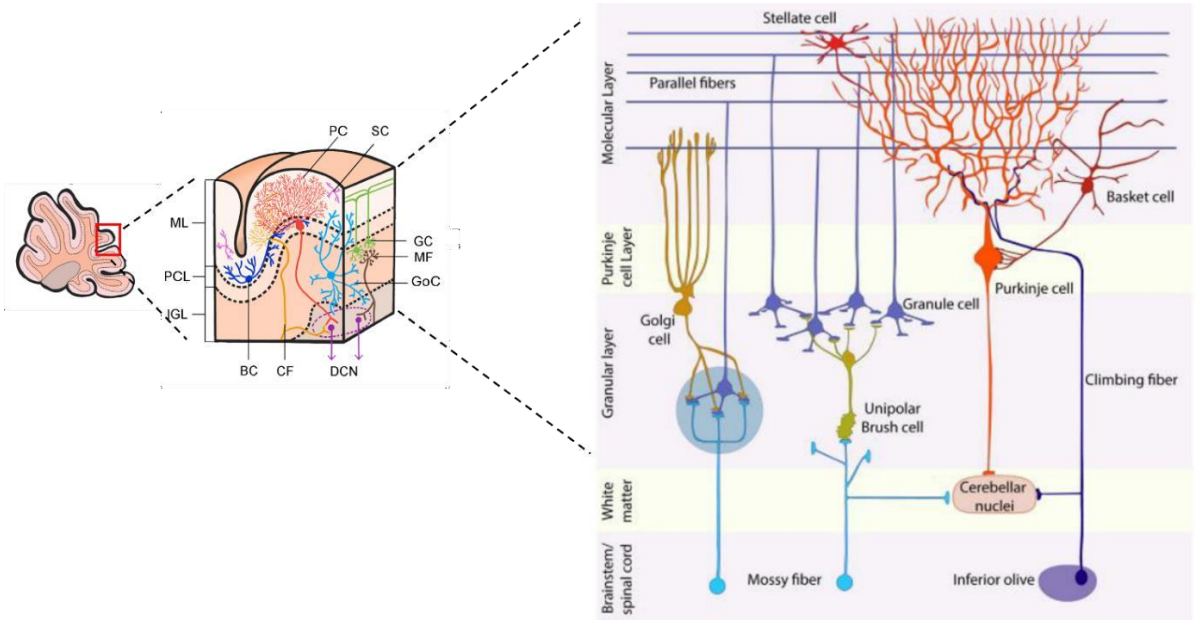

Figure 16. Schematic representation of the cerebellar cortex cytoarchitecture. The adult mammalian cerebellar cortex is organized into three distinct layers: the outermost ML containing the dendritic arbors of PCs, the BCs and SCs (two types of inhibitory interneurons) which form synapses on PC bodies and dendrites, respectively; the intermediate PCL hosting the PC bodies, which integrate all afferent inputs and, through their axons, transmit the processed information to

the DCNs, thereby serving as the principal efferent output of the cerebellum; and, finally, the innermost IGL containing GABAergic GoCs together with glutamatergic UBCs and GCs, whose axons ascend into the ML, where they bifurcate to form PFs, establishing synapses with PCs, inhibitory interneurons, and GoC dendrites. Two main types of glutamatergic afferents innervate the cerebellar cortex: CFs, originating from the inferior olive, and MFs, arising from brainstem nuclei and the spinal cord. In the adult cerebellum, each PC is innervated by a single CF, whereas MFs form complex synaptic structures, known as glomeruli, by contacting GC dendrites and GoC axons (adapted from Consalez et al., 2021).

2.2 Postnatal development of the cerebellum

The development of the CNS is an extremely complex and tightly regulated process that encompasses fundamental stages such as neurogenesis, neuronal differentiation, migration, and neural circuit organization (Hatten, 1999; Suzuki and Sato, 2014; Perry et al., 2017; Rahimi-Balaei et al., 2018). During neurogenesis – the initial phase of CNS organogenesis – neurons originate within the neuroepithelium, a proliferative layer of the neural tube that ultimately gives rise to the brain and spinal cord (Hollyday, 2001; Haubensak et al., 2004; Paridaen and Huttner, 2014). These newly generated cells then migrate to their final destinations, where they assemble into highly organized networks (Frith et al., 2024; Saade and Martí, 2025).

The cerebellum represents a paradigmatic model of such development, because of its highly ordered laminar architecture and its prolonged postnatal maturation. Indeed, human cerebellar development begins in the first trimester of pregnancy and continues up to two years after birth (van Essen et al., 2020). For example, maturation of PCs in humans is particularly protracted, being completed only by the end of adolescence, at 18–20 years (Haldipur et al., 2019), meanwhile GCs cease proliferating by about nine months of age (Gelpi et al., 2013), and ML inhibitory interneurons, UBCs and SCs, originate postnatally from a neurogenic niche in the **perspective white matter** (**PWM**) (Huang et al., 2007).

However, much of our current understanding of cellular and molecular maturation of cerebellar components derives from rodent models, especially mice (Marzban et al., 2015; Consalez et al., 2021). While in humans proliferation, migration and differentiation of cerebellar neurons unfold over several years (Sotelo et al., 2004; Butts et al., 2014), in mice these processes occur within the first postnatal weeks (Tsekhmistrenko, 2001; Haldipur et al., 2019). In murine development, cerebellar formation begins around **embryonic day 9** (**E9**), when the cerebellar primordium emerges as a neuroepithelial swelling of the rostral lip of the fourth ventricle, and extends through the third postnatal week, during which foliation – the shaping of the characteristic fissures and lobes – and hemispheric expansion are completed (Goldowitz and Hamre, 1998; Wingate, 2005; Leto et al., 2016; Consalez et al., 2021; Farini et al., 2021).

Cerebellar development relies on the coordinated contribution of distinct progenitor domains. Two principal germinal zones – the **ventricular zone** (**VZ**) and the **rhombic lip** (**RL**) – generate the diverse neuronal and glial populations that will form the cerebellar cortex and DCN (Martinez et al., 2013). From these embryonic compartments arise the main cerebellar cell types, including PCs,

GCs, interneurons, and BG, which undergo precise temporal sequences of proliferation, migration, and differentiation to establish the mature trilaminar architecture of the cerebellar cortex (Ben-Arie et al., 1997; Hashimoto and Mikoshiba, 2003; Sultan et al., 2003; Machold and Fishell, 2005; Wang et al., 2005; Leto et al., 2006; Englund et al., 2006) (**Figure 17**).

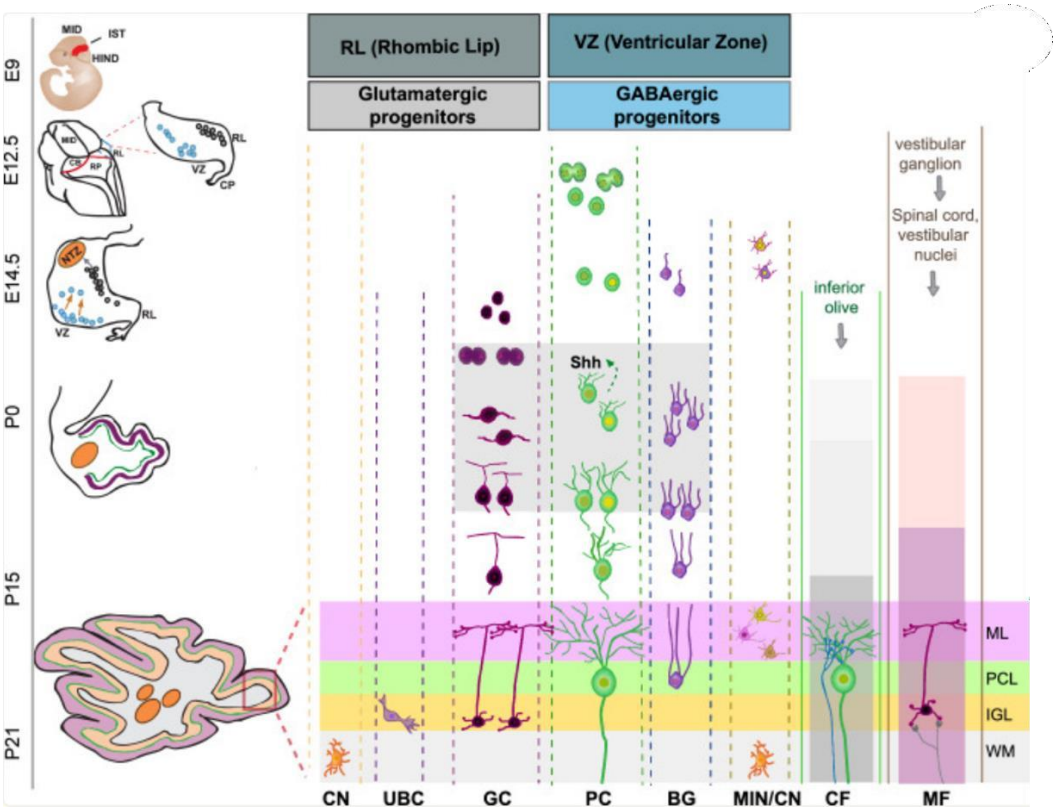

Figure 17. Spatiotemporal representation of mouse cerebellar development. On the left side is represented a schematic timeline of cerebellar neurogenesis from E9 to PN21. VZ progenitors (turquoise) and RL progenitors (gray) migratory trajectory is indicated by arrows (E14.5). On the right side is represented cerebellar histogenesis. From the RL, glutamatergic precursors give rise to neurons of DCN, UBCs and GCs, while GABAergic precursors from the VZ differentiate into PCs, BG, ML interneurons and inhibitory neurons of DCN. CFs (from inferior olive) and MFs (from vestibular ganglion/spinal cord) forming synaptic connections with PCs and with GCs respectively are also shown. PCs release Shh mitogenic factor, stimulating GC precursors proliferation in the EGL. The migration of cerebellar cells toward their final destination is indicated by dashes (Farini et al., 2021).

2.2.1 Purkinje cells, Bergmann glia and interneurons

PCs and DCN interneurons are the first cell types to be generated in the cerebellum (E 10.5–E13) (Miale and Sidman, 1961; Carletti and Rossi, 2008). In mice, between E10.5 and E12.5, glutamatergic precursors originating from the caudal RL give rise to the excitatory projection neurons of the DCN, which migrate toward the nuclear transitory zone beneath the pial surface (Ben-Arie et al., 1997; Machold and Fishell, 2005). Shortly thereafter, between E11 and E16.5, the VZ generates PCs (E11–E13), BG (E13–E14), and GABAergic interneurons – GoCs, SCs and BCs – of the cerebellar cortex (E13.5–E16.5) (Hashimoto and Mikoshiba, 2003; Sultan et al., 2003; Leto et al., 2006) (**Figure 17**).

Starting from E13 PC progenitors exit the cell cycle and migrate radially toward the cerebellar plate, where postmitotic PCs transiently assemble into a multilayered arrangement (Altman and

Bayer, 1978). Notably, during migration, PCs display a simple bipolar morphology, characterized by an apical leading process and a trailing axon (Rahimi-Balaei et al., 2015). Around **postnatal day 0** (**PN0**), they undergo extensive morphological remodeling, and between PN4 and PN5 begin to align into a single monolayer (Sotelo and Dusart, 2009). Lastly, from PN6 to PN8, PCs extend multiple short neurites that progressively branch into a highly ramified dendritic arbor, acquiring their typical planar, fan-shaped morphology by the end of the third postnatal week (Cerminara et al., 2015) (**Figures 17 and 18**).

In parallel, after originating within the VZ, BG precursors migrate toward the developing PCL until PN7. These specialized astrocytes mature during the second and third postnatal weeks, undergoing marked morphological and cytoskeletal remodeling to extend long radial fibers spanning the ML (Yamada and Watanabe, 2002; Marazziti et al., 2013). BG play a pivotal role in guiding neuronal migration – particularly that of GCs – and in regulating PC synaptogenesis and maintenance (Nguyen et al., 2013; Xu et al., 2013) (**Figures 17 and 18**).

Lastly, starting from E16.5, cerebellar interneurons, including GoCs, UBCs, and SCs (also originating from VZ-derived progenitors), begin their migration toward their final destinations. In particular, GoCs migrate radially toward the IGL, whereas UBCs and SCs follow a tangential route to reach their definitive positions within the ML (Zhang and Goldman, 1996; Hibi and Shimizu, 2012; Marzban et al., 2015) (**Figures 17 and 18**).

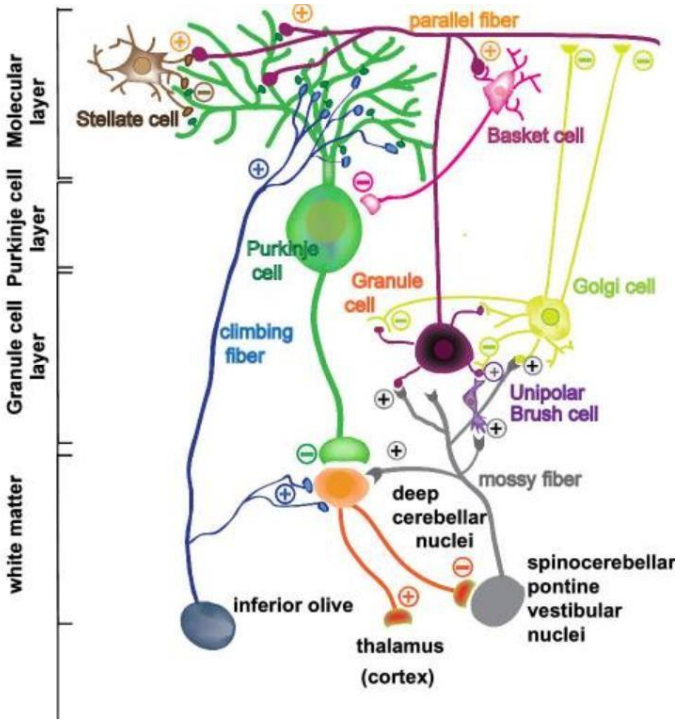

Figure 18. Schematic representation of the cerebellar circuitry organization. ML hosts PCs dendritic tree synaptic connections with PFs (from GCs), GABAergic SCs, and BC interneurons. In turn, PCs project their axon toward the WM connecting with the DCN. GC activity within the IGL is modulated by the GABAergic GoCs and UBCs, while the excitatory afferent fibers reaching the cerebellar cortex are constituted by MFs (from brainstem nuclei and spinal cord) and CFs (from the contralateral inferior olive), which control GC and PCs activity, respectively, through connections with UBCs or directly (Farini et al., 2021).

2.2.2 Granule cell differentiation and synaptic integration

GC and UBC precursors originate from the **rostral RL** between E12.5 and E17.5, giving rise to the glutamatergic lineage of the cerebellar cortex (Wang et al., 2005; Englund et al., 2006) (**Figure 17**). Thereafter, newly generated GC precursors migrate tangentially to form the **external granular layer** (**EGL**), a transient secondary proliferative zone located just beneath the pial surface (Xu et al., 2013; Nakashima et al., 2015; Consalez et al., 2021; Tam et al., 2021). The EGL is organized into two distinct compartments: an outer proliferative zone containing cycling GC precursors, and an inner zone composed of postmitotic differentiating GCs (Chédotal, 2010; Furuichi et al., 2011). During the first three postnatal weeks, GC precursors proliferate vigorously within the EGL to generate postmitotic GCs, which after cell-cycle exit beginning in the first postnatal week, migrate radially along BG fibers toward the IGL, where they complete differentiation by approximately PN30 (Pisu et al., 2005; Espinosa and Luo, 2008; Nguyen et al., 2013; Xu et al., 2013; Rahimi-Balaei et al., 2015). This continuous process leads to the progressive thinning and eventual disappearance of the EGL, coinciding with the establishment of the mature three-layered cerebellar cortex (**Figures 17 and 18**).

In parallel, the afferent circuitry of the cerebellum begins to assemble during embryogenesis. MFs and CFs — the two principal excitatory inputs — originate around E11–E12 and E14–E15, respectively (Paradies and Eisenman, 1993; Sillitoe, 2016). MFs derived from the vestibular ganglion are the first to reach the cerebellum, followed by those arising from the vestibular nuclei and spinal cord (Farini et al., 2021) (**Figure 17**). These early afferent connections provide a structural scaffold for subsequent synaptic refinement and the maturation of functional cerebellar circuits (Cajal, 1995; Hashimoto and Kano, 2013) (**Figures 17 and 18**).

2.2.3 Molecular regulation: Sonic hedgehog and brain-derived neurotrophic factor signaling

The definitive murine cerebellar architecture is established around PN16, when the laminar and synaptic organization of circuits becomes fully consolidated (Sillitoe & Joyner, 2007). The precise temporal and spatial coordination of proliferation, differentiation, migration, and synaptogenesis within the cerebellum is governed by the interplay between morphogenetic signaling pathways – originating from distinct brain regions – and local transcriptional programs (Wang and Zoghbi, 2001; Varjosalo and Taipale, 2008; Farini et al., 2021).

Among these, **Shh**, a secreted glycoprotein belonging to the Hedgehog family, is expressed by PCs starting at late embryonic stages (E18.5), and continues to act throughout early postnatal life as key mitogenic and morphogenetic factor, driving BG and GC precursor proliferation within the EGL (Wechsler-Reya and Scott, 1999; Lewis et al., 2004; Huang et al., 2010; Haldipur et al., 2012; Men et al., 2015; De Luca et al., 2016; Chen et al., 2022; Wang et al., 2022). Beyond its proliferative effects, Shh also promotes inhibitory interneuron differentiation and orchestrates the structural

organization of cerebellar cortical layers (Huang et al., 2010, De Luca et al., 2016; Consalez et al., 2021; Farini et al., 2021).

The Shh signaling cascade is initiated by ligand binding to the PM receptor **Patched1** (**Ptch1**), a 12-transmembrane-domain protein that, in the absence of Shh, constitutively inhibits **Smoothened** (**Smo**), a G-protein-coupled receptor-like protein (Roberts et al., 2016; Gong et al., 2018; Carballo et al., 2018; Qian et al., 2019; Petrov et al., 2021). Upon Shh binding, Ptch1-mediated repression is released, allowing Smo to translocate into the **primary cilium**, a specialized cellular organelle serving as a signaling hub (Wang et al., 2009; Goetz et al., 2009; Wilson et al., 2009). Activated Smo triggers the dissociation of the Gli transcription factors (**Gli1**, **Gli2**, and **Gli3**) from their cytoplasmic inhibitor **Suppressor of Fused** (**SuFu**), thereby enabling their nuclear translocation (Tukachinsky et al., 2010; Humke et al., 2010; Pak and Segal, 2016) (**Figure 19**). Once in the nucleus, Gli1 and Gli2 act as transcriptional activators, whereas Gli3 functions mainly as a repressor, together regulating the expression of Shh target genes involved in cell proliferation and differentiation, including *NMyc*, *Cyclin D1*, and *Gli1* itself, the latter providing a positive feedback loop (Oliver et al., 2003; Corrales et al., 2004; Lin et al., 2017).

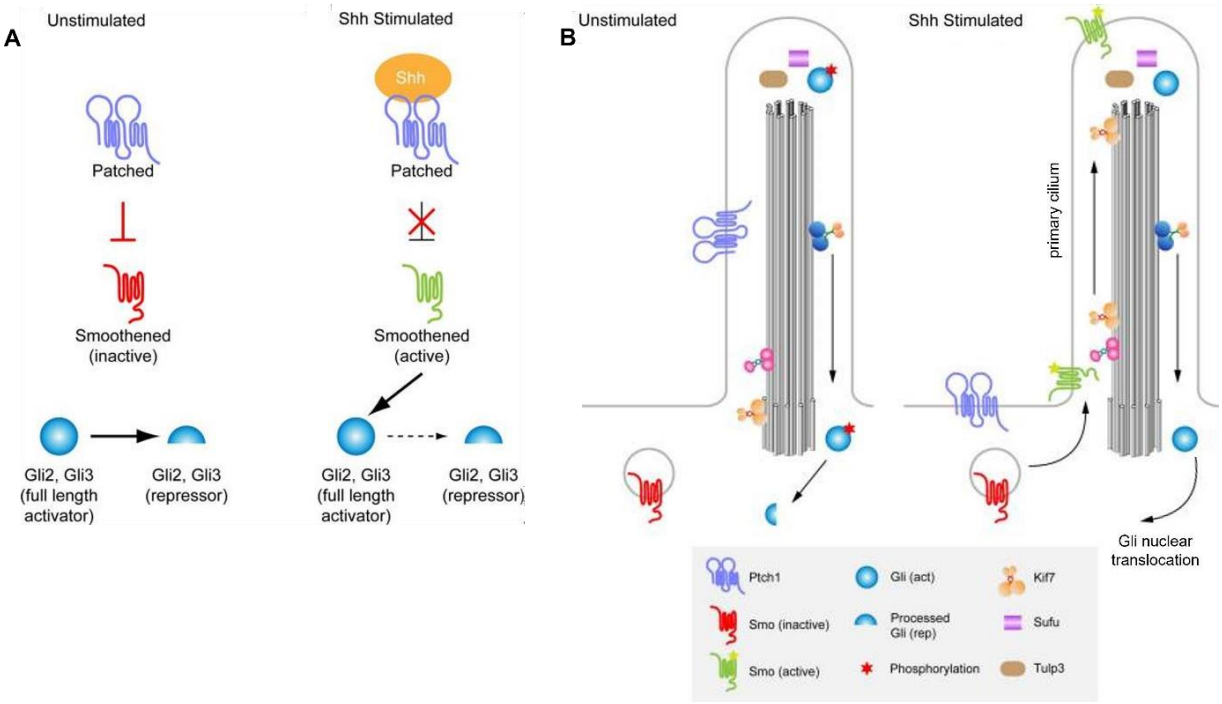

Figure 19. The vertebrate Sonic Hedgehog pathway. (**A**) Schematic representation of Shh signaling pathway. In the absence of Shh, Ptch1 receptor prevents Smo protein activation. In this state, full length Gli2 and Gli3 are proteolytically processed into a smaller repressor form. Upon Shh binding to Ptch1, the inhibition on Smo is relieved and full-length Gli proteins are activated, blocking Gli repressors production. (**B**) Schematic representation of Shh signaling at the primary cilium. In the absence of Shh, Ptch1 is enriched in primary cilia and Smo is not. Sufu and Gli are present at the cilia tip, promoting the proteolytic processing of Gli3 to its transcriptional repressor form (red star), causing repression of Shh target genes. Whereas, upon Shh binding to its receptor, Ptch1 moves out of the ciliary axoneme. In parallel, Smo is enriched in primary cilia and promotes Gli proteins activation. Activated Gli proteins are transported out of the cilium to turn on Shh target gene expression in the nucleus (adapted from Goetz et al., 2009).

In the developing cerebellum, Shh signaling exerts a dual and temporally regulated role: it first acts as a potent mitogen for GC precursors in the EGL – driving their rapid proliferation, essential

for GC population expansion and progressive cerebellar foliation – and concurrently, it influences the differentiation of inhibitory interneurons, including BCs and SCs, while promoting BG proliferation, which in turn provide the radial scaffold necessary for the inward migration of postmitotic GCs toward the IGL (Wechsler-Reya and Scott, 1999; Corrales et al., 2004; Huang et al., 2010; Men et al., 2015; De Luca et al., 2016).

Moreover, Shh signaling regulates the radial organization of the cerebellar cortex by modulating PC alignment and BG fiber maturation, ensuring proper formation of the ML and IGL. The coordination between Shh-mediated GC proliferation and BG-guided migration is therefore essential to establish the laminated architecture of the cerebellar cortex (Corrales et al., 2004; Rahimi-Balaei et al., 2018; Farini et al., 2021). Indeed, given its broad influence, disruption of Shh signaling results in severe cerebellar morphogenetic defects, including reduced foliation, impaired layer formation, and aberrant synaptic connectivity (Corrales et al., 2006).

In concert with Shh, **brain-derived neurotrophic factor** (**BDNF**) exerts multifaceted roles in neuronal survival, migration, and synaptic maturation (Lindholm et al., 1993; Chen et al., 2016; Camuso et al., 2022).

At molecular level, BDNF is synthesized in the ER as pre-pro-BDNF (Seidah et al., 1996; Lu, 2003). Following endoproteolytic cleavage, it is converted to pro-BDNF in the Golgi apparatus (Mowla et al., 2001; Yang et al., 2014) and subsequently undergoes post-translational processing to yield the mature active form (mBDNF) (Greenberg et al., 2009; Foltran and Diaz, 2016; Mizui et al., 2016). Once secreted, pro-BDNF and mBDNF, bind to distinct PM receptors, triggering diverse intracellular cascades with opposing biological effects (Je et al., 2013; Sasi et al., 2017; Camuso et al., 2022). Specifically, mBDNF exerts neuroprotective effects, through high-affinity binding to the **tropomyosin kinase receptor B** (**TrkB**) (Rodriguez-Tèbar and Barde, 1988; Chao and Hempsted, 1995; Zaccaro et al., 2001). Its interaction with TrkB receptor elicits receptor dimerization and autophosphorylation of its intracellular tyrosine residues (Chao, 2003;Huang and Reichardt, 2003; Minichiello, 2009; Philippidou et al., 2011). TrkB activation **induces receptor dimerization and autophosphorylation** of intracellular tyrosine residues. The resulting **pTrkB** complex is internalized via endosomes and activates three main downstream signaling pathways (Sandhya et al., 2013; Panja and Bramham, 2014):

- the phosphatidylinositol 3-kinase (**PI3K**)–serine/threonine kinase 1 (**AKT**) pathway, promoting neuronal proliferation, survival, and differentiation by inhibition of the two pro-apoptotic transcription factors **Bax and BAD** (the BCL2-associated agonist of cell death) (Kaplan and Miller, 2000; Cantley, 2002; Tsuruta et al., 2002; Chen et al., 2017; Kowiański et al., 2018);
- the **Ras**/mitogen-activated protein kinase (**MAPK**)/extracellular signal-regulated kinase (**ERK**) pathway, regulating protein synthesis during neuronal differentiation via transcription factor **CREB phosphorylation** (Skaper, 2008; Semaan et al., 2015);

- the phospholipase C-gamma **PLC-γ** pathway, activating inositol triphosphate receptor (**IP3R**)-mediated Ca^{2+} release from internal stores and triggering **CaMKII** and protein kinase C (**PKC**) activation (Cunha et al., 2010; Gonzalez et al., 2016). The activation of the PLC-γ cascade also culminates in CREB phosphorylation, facilitating the transcription of genes involved in neuronal survival, differentiation, and synaptic plasticity (Minichiello et al., 2002; Chao, 2003; Camuso et al., 2022) (**Figure 20**).

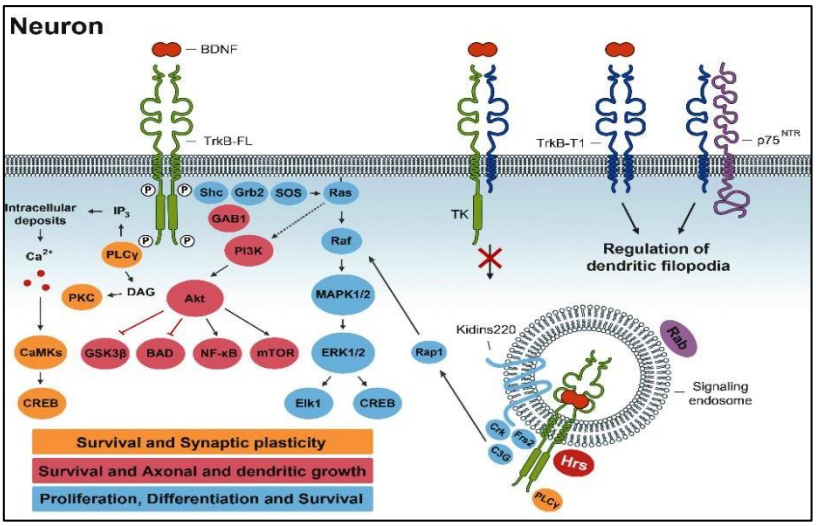

Figure 20. Schematic representation of intracellular signaling cascades activated by pro-BDNF and m-BDNF receptors. BDNF binding to full-length receptor TrkB (green), leads to receptor dimerization and autophosphorylation of intracellular tyrosine residues, triggering three different signaling pathways: **MAPK/ERK** (blue) crucial for neuronal proliferation, differentiation and survival; **PI3K / Akt** (red) involved in survival and axonal/dendritic growth; and **PLC-γ** (orange) involved in neuronal survival and synaptic plasticity. pro-BDNF, instead, interacts with high affinity to $p75^{NTR}$ receptor/sortilin complex (violet and blue) to perform its proapoptotic function, by the activation of apoptotic signaling pathways, such as JNK. pro-BDNF can also bind with low-affinity to TrkB receptor, activating signaling cascades involved in neuronal survival (Camuso et al., 2022).

Conversely, pro-BDNF binds to the **low-affinity neurotrophin receptor p75** (**$p75^{NTR}$**), a member of the tumor necrosis factor receptor family (Chao and Bothwell, 2002). Its activation requires recruitment of the co-receptor **sortilin**, triggering apoptotic signaling cascades, involving c-Jun N-terminal kinase (**JNK**) and **caspase-3/9** activation (Baker and Reddy, 1996; MacPhee and Barker, 1997; Roux and Barker, 2002; Nykjaer et al., 2004; Anastasia et al., 2013; Notaras and van den Buuse, 2019). Nevertheless, pro-BDNF–$p75^{NTR}$/sortilin complex can also activate **Ras homolog gene family member A** (**RhoA**), a small GTPase involved in neuronal survival and growth cone dynamics (Teng et al., 2005; Kowiański et al., 2018; Eggert et al., 2021) (**Figure 20**).

In addition to these pathways, activation of the **mechanistic target of rapamycin** (**mTOR**) pathway is increasingly recognized as a key downstream effector of BDNF–TrkB signaling (Slipczuk et al., 2009). Following BDNF binding, TrkB autophosphorylation activates the PI3K–Akt axis, which in turn recruits **mTOR complex 1** (**mTORC1**) to promote local protein synthesis at dendrites and synapses, supporting dendritic growth and cytoskeletal remodeling (Kumar et al., 2005; Jaworski et al., 2005) (**Figure 21**). Recent findings indicate that BDNF–TrkB signaling endosomes can travel

from axons to the soma, coordinating mTOR activation and global protein translation required for neuronal differentiation and maturation (Moya-Alvarado et al., 2023). Moreover, concurrent activation of NMDA and TrkB receptors has been shown to enhance mTORC1 recruitment to lysosomes, linking synaptic activity with TrkB-dependent translational control (Khamsing et al., 2021). Finally, evidence from cerebellar GCs further supports the direct role of mTOR in neurite outgrowth (Okada et al., 2011; Zhan et al., 2014). Altogether, these findings highlight mTOR as a central integrator of neurotrophic and activity-dependent signals essential for neuronal differentiation and synaptic development.

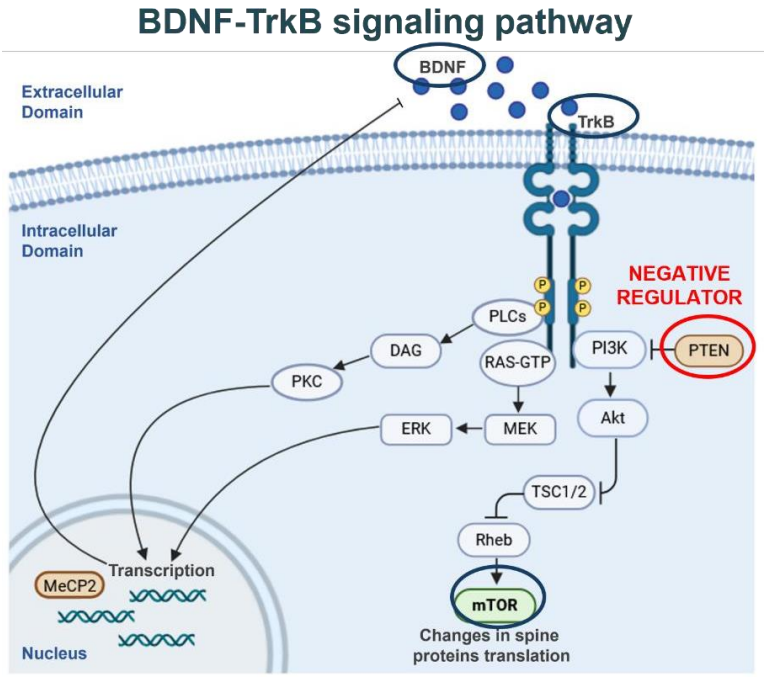

Figure 21. Schematic representation of mTOR activation upon BDNF binding to TrkB receptor (Image created by Biorender).

Through these signaling mechanisms, BDNF controls multiple developmental processes within the cerebellum. It acts as a chemotactic cue for GCs, guiding their migration along BG processes through a concentration gradient toward the IGL (Chen et al., 2016; Camuso et al., 2022). Upon reaching their destination, GCs release BDNF in an autocrine manner, reinforcing local signaling (Zhou et al., 2007).

BDNF is also required for the structural refinement of CF–PC synapses (Chen et al., 2016). At early postnatal stages (PN3), each PC receives multiple CF inputs, but by the third postnatal week only one is maintained through BDNF-dependent synaptic pruning (Hashimoto and Kano, 2005; Fiorenza et al., 2022). Disruption of this process, as observed in BDNF-deficient mice, results in persistent multiple CF–PC synapses and ataxic phenotypes, impairing motor coordination (Camuso et al., 2022). In addition to synapse pruning, BDNF promotes the assembly and stabilization of cerebellar **glomeruli**, where MFs form excitatory connections with GCs and GoCs, by enhancing the recruitment of scaffold proteins (e.g. gephyrin) and adhesion molecules (e.g. contactin-1),

facilitating postsynaptic receptor clustering, essential for synaptic stability and transmission efficiency (Chen et al., 2016; Camuso et al., 2022).

Together, the coordinated activity of Shh and BDNF signaling ensures the correct temporal progression of neurogenesis, the spatial arrangement of cortical layers, and the establishment of precise cerebellar circuitry. Disruption of either pathway profoundly alters synaptic organization, leading to motor and cognitive impairments typical of several neurodevelopmental and neurodegenerative disorders (Ismail and Shapiro, 2019; Camuso et al., 2022).

2.3 Physiology and functions of the cerebellum

The cerebellum is connected to the brainstem via three pairs of peduncles – inferior, middle, and superior – through which all cerebellar afferents and efferents travel to reach their respective targets (**Table 3**). The **middle cerebellar peduncle**, the largest of the three, is composed almost exclusively of pontocerebellar fibers, arising from the contralateral pontine nuclei and conveying signals from the cerebral cortex (Voogd and Glickstein, 1998; Apps and Garwicz, 2005; Ramnani, 2006). Medial to it lies the **inferior cerebellar peduncle**, which contains the restiform body, primarily afferent, and the juxtarestiform body, mainly efferent (Voogd and Glickstein, 1998). Lastly, the **superior cerebellar peduncle** consists predominantly of efferent fibers originating from the dentate and interposed nuclei, and, to a lesser extent, from the fastigial nucleus (D'Angelo & Casali, 2013; Roostaei et al., 2014).

Beyond their anatomical roles, cerebellar peduncles serve as critical conduits for bidirectional communication between the cerebellum and multiple brain regions, including the cerebral cortex, brainstem nuclei, and spinal cord, integrating motor, sensory, and cognitive information (Bostan and Strick, 2018). Such extensive connectivity underlies cerebellum contribution not only to motor coordination and learning, but also to higher-order processes such as cognition and affect regulation (Ramnani, 2006; D'Angelo & Casali, 2013).

Peduncle	Tracts	Distribution	Laterality	Location of Cell Bodies
Cerebellar Afferents				
Inferior	Olivocerebellar tract	Cerebellar cortex and deep cerebellar nuclei	Contralateral	Inferior olivary nucleus
	Vestibulocerebellar tract	Flocculonodular lobe, caudal uvula, and fastigial nucleus	Ipsilateral	Vestibular nuclei and vestibular ganglion
	Posterior spinocerebellar tract	Lower extremity regions of the	Ipsilateral	Clarke column

		cerebellar cortex and nuclei		
	Cuneocerebellar tract	Upper extremity and trunk regions of the cerebellar cortex and nuclei	Ipsilateral	Cuneate and external cuneate nuclei
	Rostral spinocerebellar tract	Upper extremity and trunk regions of the cerebellar cortex and nuclei	Ipsilateral	Intermediate zone and horn of the cervical enlargement
	Reticulocerebellar tract	Cerebellar hemispheres and vermis, along with fastigial and interposed nuclei	Bilateral	Lateral reticular nucleus of the medulla oblongata
	Trigeminocerebellar tract	Related somatotopic regions of the cerebellar cortex and nuclei	Ipsilateral	Trigeminal nucleus
Middle	Pontocerebellar tract	Neocerebellar cortex and dentate nucleus	Contralateral	Pontine nuclei
Superior	Anterior spinocerebellar tract	Lower extremity regions of the cerebellar cortex and nuclei	Ipsilateral	Clarke column
Cerebellar Efferents				
Inferior	Cerebellovestibular tract	Vestibular nucleus	Ipsilateral	Fastigial nucleus, vermis, and vestibulocerebellar cortex
Superior	Cerebellorubral fibers	Red nucleus	Contralateral	Dentate and interposed nuclei
	Cerebellothalamic fibers	Ventrolateral thalamic nucleus	Contralateral	Dentate and interposed nuclei
	Uncinate fasciculus	Vestibular, pontomedullary reticular, and thalamic nuclei	Contralateral	Fastigial nucleus
	Nucleo-olivary tract	Inferior olive	Contralateral	Deep cerebellar nuclei

Table 3. Major cerebellar afferents and efferents (Roostaei et al., 2014).

As already mentioned, three major functional regions of the cerebellum can be distinguished based on the distribution of afferent and efferent connections: the **vestibulocerebellum**, the **spinocerebellum**, and the **cerebrocerebellum** (Ramnani, 2006; Stoodley and Schmahmann, 2010;

Kandel and Schwartz, 2013). This tripartite division reflects cerebellum integration of vestibular, spinal, and cortical inputs, allowing for fine-tuned control of balance, posture, coordination, and motor learning (Voogd and Glickstein, 1998; Ito, 2006).

The **vestibulocerebellum**, receives **vestibular inputs** via the inferior cerebellar peduncle, both directly from the ipsilateral vestibular nerve – the only primary afferents that project directly to the cerebellum – and indirectly from the vestibular nuclei (superior, medial, and inferior) (**Table 3**). It also integrates **visual information** conveyed from the pretectal area of the midbrain and the visual cortex (Ito, 1993; Angelaki and Cullen, 2008; Roostaei et al., 2014). Notably, its distinctive feature is that the vestibulocerebellum sends its outputs directly to the vestibular nuclei, thereby bypassing the deep cerebellar nuclei (**Table 3**) (Ito, 1993; Angelaki and Cullen, 2008; Roostaei et al., 2014).

Functionally, the medial vestibulocerebellum regulates **axial musculature** by modulating vestibular nuclei activity, while the lateral vestibulocerebellum contributes to smooth pursuit **eye movements** and to the coordination of eye and head movements through its influence on the medial vestibular nuclei (Ito, 1991; Voogd et al., 2012; Roostaei et al., 2014). A central mechanism mediated by this circuitry is the **vestibulo-ocular reflex** (**VOR**), which counter-rotates the eyes during head motion to stabilize retinal images. Adaptive modulation of the VOR is crucial for maintaining visual stability during locomotion and relies on the functional integrity of the flocculus and paraflocculus (Ito, 1998; Ito, 1993; Lisberger, 2021). Notably, VOR adaptation has long served as a model system for investigating the neural basis of cerebellar-dependent **motor learning** (Broussard et al., 2011).

The **spinocerebellum** receives extensive direct and indirect **somatosensory information** from the trunk and limbs through its connections with the spinal cord, from the head and face via trigeminal nuclei, and from visual and auditory systems (Manni and Petrosini, 2004; Apps and Hawkes, 2009; Stoodley and Schmahmann, 2010; Roostaei et al., 2014; Stoodley and Schmahmann, 2018). Via the inferior cerebellar peduncle, **proprioceptive inputs** from the lower and upper extremities are conveyed by the posterior spinocerebellar and cuneocerebellar tracts, respectively, whereas efference copies of spinal motor discharges from lower and upper limbs are transmitted by the anterior and rostral spinocerebellar tracts (**Table 3**) (Bosco and Poppele, 2001; Manni and Petrosini, 2004; Roostaei et al., 2014; Stoodley and Schmahmann, 2018).

Within the spinocerebellum, somatotopic maps of the body are organized in a highly conserved manner: the vermis receives inputs from the trunk and proximal limb regions, while the paravermis processes inputs from the distal limbs, forming multiple fractured somatotopies that allow parallel processing of sensorimotor information (**Figure 22**) (Manni and Petrosini, 2004; Apps and Hawkes, 2009; Roostaei et al., 2014).

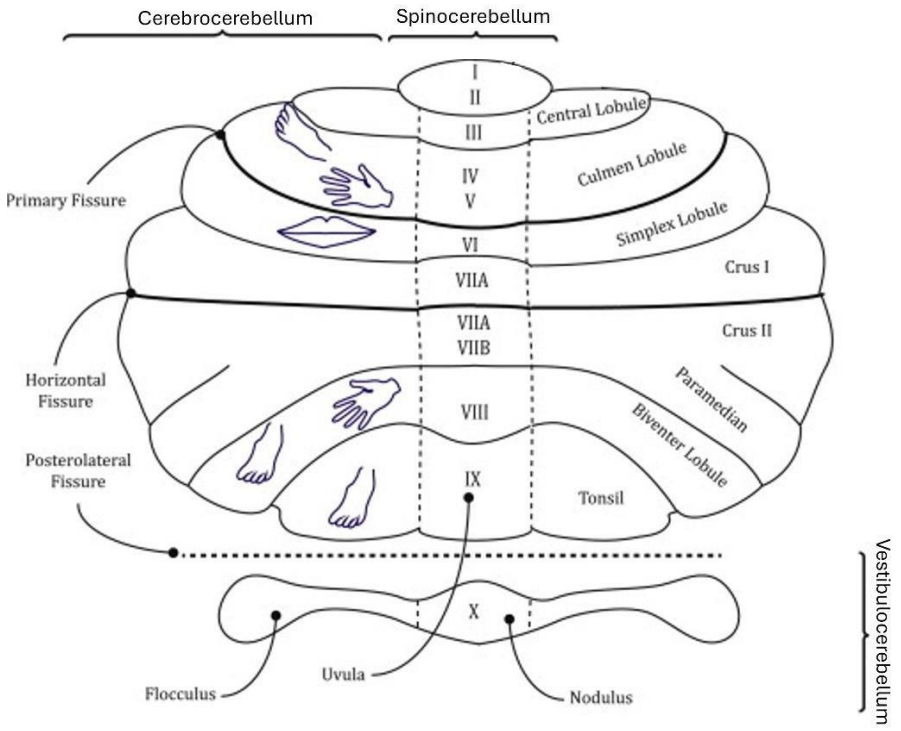

Figure 22. Representation of cerebellar somatotopy. Unfolded view of the cerebellar cortex showing fissures and lobules, along with cerebellar somatotopy (left cerebellum only) (adapted from Roostaei et al., 2014).

PCs in the vermis project to the fastigial nuclei, which in turn send efferent projections through both the superior and inferior cerebellar peduncles, thereby modulating **vestibulospinal** and **reticulospinal** pathways (**Table 3**), which regulate **axial** and **proximal musculature**, critically contributing to **posture**, **equilibrium**, and **gait stability** (Voogd and Glickstein, 1998; Apps and Garwicz, 2005). In contrast, PCs in the paravermis project to the interposed nuclei, which send outputs via the superior cerebellar peduncle to the magnocellular division of the red nucleus and to the ventrolateral thalamus, thereby influencing **rubrospinal** and **corticospinal activity** (**Table 3**), which refine **distal limb coordination** and **precision movements** (Thach et al., 1992; Middleton and Strick, 2001; Kelly and Strick, 2003).

Therefore, the spinocerebellum is thought to continuously compare planned motor commands (efference copies) with incoming sensory feedback, adjusting motor outputs in real time to minimize error and ensure smooth movement execution (Ito, 1993; Kandel and Schwartz, 2013**;** Ito, 2005). Moreover, converging evidence supports its role in implementing an **internal forward dynamic model** – a computational mechanism that allows the cerebellum to predict the sensory consequences of motor commands and generate timing signals for **movement correction** (Wolpert et al., 1998; Ito, 2005; Shadmehr & Krakauer, 2008; Imamizu and Kawato, 2012; Lisberger, 2021). Through these mechanisms, the spinocerebellum translates a desired endpoint into a sequence of precisely timed muscle activations, while predicting the future position of limbs during ongoing movement based on sensory and proprioceptive feedback (Wolpert et al., 1998; Ito, 2005; Shadmehr & Krakauer, 2008).

The **cerebrocerebellum**, is the largest and phylogenetically newest region of the cerebellum, which has undergone remarkable expansion in humans in parallel with higher-order association areas of the neocortex (Herculano-Houzel, 2010; Balsters et al., 2014). Its afferents arise exclusively from the cerebral cortex, particularly from parietal, premotor, and prefrontal regions, via relay neurons in the pontine nuclei, forming the **cortico-ponto-cerebellar pathway** (**Table 3**) (Kelly and Strick, 2003; Roostaei et al., 2014; Gao et al., 2018).

Outputs from the lateral hemispheres are transmitted through the dentate nuclei, whose axons project to the contralateral ventrolateral thalamus and the parvocellular division of the red nucleus (**Table 3**). Thalamic projections subsequently target the premotor and primary motor cortices, contributing to **movement planning and initiation**, whereas neurons of the parvocellular red nucleus send inputs to the inferior olivary nucleus, completing a closed **cerebrocerebellar feedback loop** that supports **adaptive motor learning and error correction** (Thach et al., 1992; Kelly and Strick, 2003; Ito, 2005; Roostaei et al., 2014; Gao et al., 2018).

Lesions of the cerebrocerebellum produce ataxic dysmetria, delayed initiation of movement, irregular timing of sequential motor acts, and impaired motor planning – consistent with its role in predictive control of movement (Kandel and Schwartz, 2013).

In addition, growing evidence implicates the cerebrocerebellum in higher **cognitive and affective domains**, including working memory, language processing, and executive functions, which will be discussed in later sections (Schmahmann, 2019; Rudolph et al., 2023).

2.3.1 Cerebellar contribution to cognitive and social functions

Traditionally associated with motor coordination and control, the cerebellum is now recognized as a key structure in cognitive, affective, and social processing (Farini et al., 2021; Rudolf et al., 2023; Van Overwalle et al., 2024). As early as the 19th century, pioneering work by the Italian anatomist Luigi Rolando suggested a link between the cerebellum and motor functions. Indeed, for more than a century, its role was considered strictly motoric, primarily in relation to disorders such as ataxia, dysarthria, and oculomotor dysfunctions, which manifest as impairments in balance, coordination, and fine motor control (Glickstein et al., 2009; Koziol et al., 2014; Nodera and Manto, 2014).

In recent decades, a major paradigm shift has occurred, driven by the rediscovery of historical evidence, new theoretical models, and anatomical data, all highlighting cerebellar involvement in non-motor domains, including social cognition (Schmahmann, 2019; Van Overwalle et al., 2020; Van Overwalle et al., 2024). Social cognition encompasses core relational abilities, such as mentalization and mirroring – the capacity to attribute mental states, intentions, and beliefs to others, and the capacity to understand others' actions and emotions, respectively (Van Overwalle et al., 2020; Van Overwalle et al., 2024).

Recent studies have demonstrated that the cerebellum, particularly its posterior lobe regions Crus I and Crus II, plays a crucial role in **theory of mind** (**ToM**) processes, including the observation of actions, the inference of others' intentions, and the processing of complex social information (Van Overwalle et al., 2015; Van Overwalle et al., 2019; Heleven et al., 2019). ToM is essential for understanding others' thoughts and emotions and is tightly linked to the capacity to learn, communicate, and integrate within social and cultural contexts (Olson et al., 2023). The cerebellar contribution to these domains is thought to rely on the generation of internal predictive models, a computational mechanism long recognized in motor control but now extended to behavioral and social sequences (Van Overwalle et al., 2019). The prevailing hypothesis proposes that the cerebellum supports the understanding and learning of social action sequences, facilitating social cognition by enabling the brain to predict and adapt to future or ongoing social interactions (Van Overwalle et al., 2019; Heleven et al., 2019). This predictive function is particularly relevant when interpreting false beliefs or hidden intentions. Notably, neuroimaging studies using **dynamic causal modeling** (**DCM**) have identified functional connectivity between Crus I/II, the **temporo-parietal junction** (**TPJ**), and the **medial prefrontal cortex** (**mPFC**), outlining a cerebello-cerebral network involved in social mentalizing (Van Overwalle et al., 2020; Ma et al., 2023; Pu et al., 2023; Haihambo et al., 2025;).

Clear evidence of cerebellar involvement in cognitive and emotional regulation is also represented by the **cerebellar cognitive affective syndrome** (**CCAS**), observed in patients with cerebellar lesions (Schmahmann and Sherman, 1998). This syndrome is characterized by executive, linguistic, and visuospatial deficits, as well as personality and affective changes, including emotional blunting, disinhibition, and socially inappropriate behavior (Schmahmann and Sherman, 1998; Manto and Mariën, 2015; Schmahmann, 2019; Olson et al., 2023). CCAS patients often show marked difficulties in recognizing emotions from subtle cues in ToM tasks, such as in the Reading the Mind in the Eyes Test (RMET), while performing relatively better in verbal or narrative-based tasks (Beuriat et al., 2022; Olson et al., 2023). Recent meta-analyses have confirmed that the cerebellum – especially lobule VI and Crus I/II – is consistently activated during the processing of emotional and rewarding stimuli, suggesting a role in modulating attention toward socially salient cues (Van Overwalle, 2015; Pierce et al., 2023). Emotional processing and social cognition appear to recruit overlapping cerebellar areas, supporting the notion of a shared cerebellar representation for social and affective domains (Van Overwalle, 2015).

At the neuroanatomical level, the cerebellum is embedded in a network of reciprocal connections with the PFC, limbic system, amygdala, insula, and hippocampus (Yu and Krook-Magnuson, 2015; D'Angelo, 2018; Jung et al., 2022). The cerebellar vermis and Crus I/II in particular are thought to modulate emotional responses and social–affective behaviors (D'Angelo & Casali, 2013). Supporting evidence from animal models further demonstrates that activity in Crus regions is critical for regulating social behavior in rodents (Van Overwalle, 2024).

From a developmental perspective, cerebellar maturation follows a trajectory similar to that of the cerebral cortex: sensorimotor regions mature early, whereas posterior cognitive regions – such as Crus I/II – develop at later stages (Kipping et al., 2013, Kipping et al., 2017; Tikoo et al., 2025). This timing suggests that the cerebellum may play a particularly important role early in life, when cortical networks are still being established. The interaction between cerebellum and cerebral cortex contributes to the organization of neural networks underlying implicit learning, language, and affective regulation (De Smet et al., 2013). Accordingly, early cerebellar damage can hinder the maturation of these abilities, resulting in clinical phenotypes resembling **autism spectrum disorders** (**ASDs**) or psychotic disorders, underscoring cerebellum role not only in observable behavior but also in the internal mechanisms underpinning social interaction (Olson et al., 2023; Elandaloussi et al., 2023; Kong et al., 2024). For instance, following surgical resection of cerebellar tumors, approximately one-fourth of pediatric patients develop posterior fossa syndrome, characterized by transient mutism, emotional lability, and disturbances in social behavior, often accompanied by irritability, social withdrawal, or inappropriate affective responses (Lanier and Abrams, 2017; Schmidt et al., 2023).

2.4 The cerebellum and neurodevelopmental disorders

The expanded functional view of cerebellar role in higher-order cognitive and affective processes – beyond motor functions – has led to increasing recognition its contribution to a wide spectrum of **neurodevelopmental disorders** (**NDDs**), including ASD, **attention-deficit/hyperactivity disorder** (**ADHD**), and intellectual disability (Shevelkin et al., 2014; Stoodley, 2016). Early cerebellar damages – whether genetic, inflammatory, or environmental – during critical postnatal windows can result in long-lasting disruptions of cerebro-cerebellar circuits that underlie cognitive and social behavior (Wang et al., 2014; Stoodley and Limperopoulos, 2016).

As mentioned, the cerebellum exhibits a protracted postnatal developmental trajectory, characterized by extensive neuronal precursors proliferation, synaptic refinement, and maturation of local circuitry (Sudarov and Joyner, 2007; Hibi and Shimizu, 2012). This makes it particularly vulnerable to early-life perturbations. Abnormal cerebellar morphogenesis has been consistently reported in neurodevelopmental disorders, especially within the posterior vermis and Crus I/II lobules, regions that form closed-loop circuits with the prefrontal cortex and limbic areas (Wang et al., 2014; Stoodley, 2016; Stoodley and Limperopoulos, 2016). Structural MRI studies have shown reduced cerebellar volume and altered connectivity patterns in individuals with ASD and ADHD (Amaral et al., 2008; Fetit et al., 2021), supporting the hypothesis that cerebellar dysfunction may impair the timing and prediction mechanisms essential for complex cognition and adaptive behavior (Ito, 2005; D'Angelo & Casali, 2013).

From a cellular perspective, alterations in PCs have been identified as a consistent hallmark across several NDDs (Kern, 2003; Reith et al., 2013; Spisák et al., 2019). Reduced PC number and dendritic arborization, accompanied by aberrant synaptic pruning and impaired inhibitory signaling, have been observed in both postmortem ASD brains and animal models (Kern, 2003; Reith et al., 2013; Spisák et al., 2019). In mice, PC-specific deletion of genes such as Tsc1, Pten, or Shank2, all implicated in ASD, leads to social deficits, repetitive behaviors, and altered synaptic plasticity (Reith et al., 2013; Kloth et al., 2015; Peter et al., 2016). These findings support the notion that the cerebellum, and specifically PC output, modulates the maturation of prefrontal circuits through reciprocal cerebro-cerebellar interactions during development (Badura et al., 2018; Kelly and Strick, 2003).

Emerging data further implies neurotrophic and neuroinflammatory signaling pathways in cerebellar vulnerability to developmental disorders. Dysregulation of BDNF and its receptor TrkB, critical regulators of cerebellar synaptogenesis and dendritic differentiation, has been reported in ADHD, ASD and intellectual disability (Tsai, 2003; Hashimoto et al., 2006; Wang et al., 2019). Moreover, genetic disruption of BDNF-TrkB signaling specifically in PCs leads to impaired dendritic maturation and deficits in motor learning and social behavior (Carter et al., 2002; Ohira et al., 2004). Concurrently, microglial activation and increased levels of pro-inflammatory cytokines within the cerebellum have been described in both ASD patients and mouse models, suggesting that chronic low-grade neuroinflammation may exacerbate synaptic dysfunction during critical developmental stages (Vargas et al., 2005; Rose et al., 2012; Pangrazzi et al., 2022; Cerilli et al., 2024).

Collectively, these findings support the hypothesis that cerebellar dysfunction acts not merely as a secondary consequence of broader cortical pathology, but as a primary driver in the pathogenesis of NDDs. Through its widespread projections to associative cortical areas and subcortical nuclei, the cerebellum contributes to temporal coordination, prediction, and error-based learning – fundamental processes for adaptive cognition and social behavior (Koziol et al., 2014; Diedrichsen et al., 2019). Understanding the mechanisms by which cerebellar circuits interact with cerebral networks during early development may therefore offer new therapeutic avenues for targeting cognitive and behavioral impairments in NDDs.

2.5 The cerebellum and Niemann–Pick type C1 disease

The cerebellum is particularly vulnerable to NPC1 disease, especially during postnatal development, when the demand for cholesterol is at its peak (Caporali et al., 2016; Fiorenza et al., 2022; Lucarelli et al., 2023). Cholesterol plays a fundamental role in supporting key developmental processes such as cell proliferation, neuronal migration, synaptogenesis, and myelination (Goritz et al al., 2005; Huang et al., 2007; Mathews and Appel, 2016). During the first three postnatal weeks, the mouse cerebellar cortex undergoes profound structural and functional changes that depend on

the tightly coordinated maturation of GCs, PCs, and glial elements (Huang et al., 2007). In this context, loss of NPC1 function profoundly impairs normal cerebellar maturation, with prominent effects on GCs and PCs (Caporali et al., 2016; Fiorenza et al., 2022; Lucarelli et al., 2023).

In *Npc1*^{nmf164} mice, a significant reduction in GC number and overall lobular volume has been reported, resulting from the premature exit of GC progenitors from the cell cycle (Nusca et al., 2014; Caporali et al., 2016; Lucarelli et al., 2023). The scarcity of GCs within the IGL negatively affects PC survival and firing properties, reduces glomerular size and synaptic connectivity, and alters the differentiation of inhibitory interneurons, such as BCs and SCs (Caporali et al., 2016; Fiorenza et al., 2022; Lucarelli et al., 2023). Moreover, BG, which respond to Shh signaling, display an aberrant differentiation pattern in NPC1-deficient mice, impairing neuronal migration, dendritogenesis, and synaptogenesis (Caporali et al., 2016; Fiorenza et al., 2022).

These structural and functional abnormalities translate into a delay in the acquisition of complex motor skills, despite preserved basic locomotion and normal sensorimotor reflexes. This observation indicates that vestibular, tactile, and proprioceptive systems, as well as descending motor pathways, remain largely functional (Caporali et al., 2016; Fiorenza et al., 2022). In contrast, fine motor control, which relies on the coordinated activity of cerebellar circuits enabling real-time movement correction and long-term adaptation underlying motor learning, is markedly impaired (Caporali et al., 2016; Fiorenza et al., 2022).

A key feature of cerebellar pathology in NPC1 is the disruption of synaptic input to PCs (Caporali et al., 2016). Abnormalities in afferent signaling from interneurons and mossy fibers, together with defective synaptic compartmentalization mediated by BG processes, lead to dysfunctional PC firing and consequent motor deficits (Caporali et al., 2016). Additionally, both the formation and functional maturation of MF–GC synapses are compromised and associated with reduced expression of BDNF and its receptor TrkB during early postnatal stages (Lucarelli et al., 2023). Since PCs receive BDNF from GCs, the reduction of BDNF levels observed in PCs can be attributed to the decreased GC population (Lucarelli et al., 2023).

Cerebellar myelination, another process critical for efficient synaptic transmission, is also disrupted in NPC1. In *Npc1*^{nmf164} mice, oligodendrocyte maturation is defective, leading to reduced expression of **myelin basic protein** (**MBP**) and early demyelination detectable from PN11, particularly along PC axons (Caporali et al., 2016; Fiorenza et al., 2022). Studies in both *Npc1*^{nih} and *Npc1*^{nmf164} models have documented a progressive loss of PCs following an anterior-to-posterior gradient, accompanied by dendritic and axonal alterations (Fiorenza et al., 2022). Before degeneration, PCs display swollen axons and abnormal dendritic varicosities, and their death appears to originate in the dendritic compartment — a pattern reminiscent of other cerebellar neurodegenerative conditions such as spinocerebellar ataxia (Fiorenza et al., 2022; Baudry et al., 2003).

The heightened cerebellar vulnerability can also be explained by defective Shh signaling, which is tightly linked to cholesterol metabolism. The covalent attachment of cholesterol to Shh (cholesteroylation) is critical for its stability, distribution, and biological activity (Canterini et al., 2017; Fiorenza et al., 2022). In NPC1 deficiency, reduced cholesterol availability prevents proper Shh activation, thereby impairing the proliferation of both neuronal progenitors and BG, leading to persistent morphological and functional abnormalities (Canterini et al., 2017; Fiorenza et al., 2022).

Cerebellar impairment occurs within a broader neuroanatomical context involving the thalamus, cerebral cortex, basal ganglia, and hippocampus, consistent with the functional interconnection of these regions through cerebello-thalamo-cortical loops (Fiorenza et al., 2022). Glial alterations, including astrocytic and microglial activation, both precede and accompany cerebellar neurodegeneration (Rava et al., 2022; Fiorenza et al., 2022).

Finally, the altered expression and localization of BDNF and TrkB in *Npc1*^{nmf164} mice suggest that NPC1 deficiency disrupts the molecular mechanisms underlying neuronal migration and terminal differentiation (Lucarelli et al., 2023). Cholesterol accumulation may also trigger compensatory responses, such as increased BDNF levels at MF terminals, but these mechanisms appear insufficient to prevent progressive degeneration (Lucarelli et al., 2023).

In conclusion, NPC1 deficiency triggers a cascade of molecular, cellular, and circuit-level alterations that selectively compromise cerebellar development and function. Together, these findings underscore the central role of cholesterol homeostasis and Shh–BDNF signaling in maintaining cerebellar integrity and provide insight into how metabolic disturbances can disrupt neurodevelopmental trajectories leading to ataxia and cognitive dysfunction. Thus, the cerebellum emerges as a critical site where the metabolic failure of NPC1 and alterations in cellular lipid homeostasis translate into disrupted developmental signaling, synaptic disorganization, and progressive neurodegeneration.

Chapter III

The research project

3.1 Background and aims

As described in Chapters I and II, NPC1 disease is an autosomal recessive LSD that profoundly disrupts intracellular cholesterol trafficking (Peake and Vance, 2010), triggering metabolic and cellular dysfunctions primarily affecting the CNS (Pineda et al., 2018).

The main neuropathological hallmark of NPC1 is the prominent cerebellar involvement, with progressive degeneration of PCs, leading to cerebellar ataxia — one of the most consistent clinical symptoms across disease variants (Vanier et al., 1991; Elrick et al., 2010; Martin et al., 2019). Owing to overlapping pathological features, such as cholesterol dyshomeostasis, amyloid plaque deposition, neurofibrillary tangle accumulation, and widespread neuroinflammation, NPC1 has also been referred to as "*juvenile Alzheimer's disease*" (Nixon, 2004; Pacheco et al., 2009; Borbon et al., 2012; Saito et al., 2022). Moreover, defects in oligodendrocyte differentiation and consequent myelination have been reported in both NPC1 patients and knockout mouse models (Takikita et al., 2004; Yan et al., 2011).

Although traditionally classified as a neurodegenerative disorder, recent studies from our group have revealed distinct neurodevelopmental features in NPC1 pathophysiology, aligning it more closely with neurodevelopmental syndromes (Nusca et al., 2014; Caporali et al., 2016; Canterini et al., 2017; Dragotto et al., 2019). Accordingly, loss of NPC1 function profoundly affects postnatal cerebellar development, primarily by impairing Shh signaling during the critical window of GC precursor proliferation, resulting in aberrant cerebellar morphogenesis and subsequent PC degeneration (Nusca et al., 2014; Caporali et al., 2016; Canterini et al., 2017).

In addition, many Shh-regulated developmental processes also depend on BDNF trophic action, essential for GC migration, differentiation, and synaptogenesis (Zhou et al., 2007; Camuso et al., 2022). Several studies have demonstrated that Shh activation induces BDNF expression and release (Bond et al., 2013; Delmotte et al., 2020), linking morphogenetic and neurotrophic regulation of cerebellar development. BDNF signaling through its high-affinity receptor TrkB activates intracellular cascades, including PI3K–AKT–mTOR, which regulate neuronal survival, cytoskeletal remodeling, and synaptic plasticity (Camuso et al., 2022). Recent data from our laboratory demonstrated that *Npc1*^{nmf164} mice — reproducing the late-onset and slowly progressive form of human NPC1 (Maue et al., 2012) — exhibit reduced expression of BDNF and abnormal polarization and subcellular localization of the pTrkB receptor in cerebellar GCs during early postnatal life, leading to defective migration towards the IGL (Lucarelli et al., 2023). These findings indicate that the altered crosstalk between cholesterol metabolism and BDNF–TrkB signaling in *Npc1*^{nmf164} mice interferes with proper GC migration and downstream signaling pathways.

GCs – the most abundant neuronal population of the cerebellum (Herculano-Houzel et al., 2010) – form the principal excitatory network and provide input to PCs via PFs (Valle et al., 2001). Therefore, developmental alterations in GCs are expected to profoundly impact cerebellar circuit formation and, consequently, higher-order behaviors such as cognitive, emotional and social processes, which have been increasingly associated with cerebellar function (Stoodley and Schmahmann, 2010; Van Overwalle et al., 2020).

Building on this evidence, here we hypothesize an abnormal differentiation program of *Npc1*^{nmf164} GCs, representing not simply a developmental variation, but rather a key factor underlying defective synaptic maturation within the IGL. While our previous work demonstrated reduced Shh-driven GC proliferation in the EGL, and impaired BDNF-TrkB-driven GC migration (Caporali et al., 2016; Canterini et al., 2017; Lucarelli et al., 2023), the subsequent differentiation fate of these neurons upon reaching the IGL remains unclear. In particular, it is to be determined whether GCs are able to properly establish functional synaptic contacts and integrate within the local circuitry. Indeed, disruptions in these processes are likely to interfere with the fine-tuning of excitatory–inhibitory balance in local microcircuits, ultimately weakening the integrity of cerebellar connectivity. Over time, such alterations may lead to enduring changes in cerebellar output, with downstream effects on higher-order brain functions. Given the well-established role of the cerebellum in cognitive and socio-affective processes (Stoodley and Schmahmann, 2010; Van Overwalle et al., 2020), these developmental disturbances may provide a mechanistic explanation for lasting impairments in cerebellar-dependent behaviors, which could eventually culminate in social difficulties.

Moreover, growing evidence highlights sex as a major biological variable influencing neurodevelopmental trajectories and vulnerability to brain disorders (Werling and Geschwind, 2013; McCarthy et al., 2017). Yet, sex-dependent mechanisms have not been systematically investigated in NPC1. Therefore, the present study was designed to investigate the molecular, structural, and behavioral consequences of altered BDNF–TrkB signaling during key-stages of cerebellar development in the *Npc1*^{nmf164} mouse model, with a specific focus on sex-related differences.

Specifically, we aimed to: (**i**) characterize the molecular cascades downstream of BDNF–TrkB activation, with particular emphasis on PTEN–mTOR signaling, a pathway known to regulate cell growth and synaptic plasticity; (**ii**) analyze pre- and postsynaptic proteins and cell-adhesion molecules essential for synaptic structural organization and circuit stabilization; (**iii**) assess the morphology of GC dendritic spines to detect potential alterations in synaptic architecture; (**iv**) measure levels of glutamate and GABA metabolism to evaluate potential imbalances in excitatory-inhibitory neurotransmission; (**v**) explore GC-driven regional vulnerability, reflected in volumetric changes in the cerebellar IGL; (**vi**) examine social behavior across developmental stages, to determine whether the convergence of several developmental alterations within the cerebellum is associated with behavioral phenotypes preceding overt neurodegeneration.

3.2 Materials and methods

3.2.1 Animals

Wild-type (*wt*) and *Npc1*^{nmf164} mice were used in all experiments. *Npc1*^{nmf164} mice, on a BALB/cJ background (Charles River Laboratories, Italy), carrying a single point mutation (*D1005G*) in the *Npc1* gene, were generated through heterozygous breeding, although the yield of homozygous mutants is typically low (Maue et al., 2012; Fog and Kirkegaard, 2019).

All animals were housed in our animal facility in compliance with Sapienza University guidelines. Mice were kept under a 12-hour light/dark cycle at a constant temperature (21°C ± 1), with food and water available *ad libitum*. Animals were group-housed (maximum 5 per cage) and provided with nesting and housing materials for environmental enrichment. All experimental protocols were approved by the Italian Ministry of Health and conducted in accordance with Italian Legislative Decree 26/2014 and European Directive 2010/63/EU. Every effort was made to minimize animal suffering.

3.2.2 Genotyping

Genotypes and sexes were determined by Polymerase Chain Reaction (PCR) followed by restriction enzyme digestion, as previously described (Maue et al., 2012). Genomic DNA was extracted from tail snips (0.2cm), incubated at 98°C for 1 hour in 75µL of lysis solution (25mM NaOH, 0.2mM disodium EDTA, pH 8), followed by a neutralization phase performed by adding 75µL of neutralization solution (40mM Tris-HCl, pH 5.5) (Truett et al., 2000). 1µL of the resulting DNA solution was used for PCR amplification (Thermal Cycler T100, Bio-Rad), using the following primer pairs:

GENE	FORWARD PRIMER	REVERSE PRIMER	COMPANY
NPC1	GGGTAAACAGAGGCCTCAGG	TAAACCGTGTCTCTGCCCTAG	Bio-Fab Research
SRY	TTGTCTAGAGAGCATGGAGGGCCATG TCAA	CCACTCCTCTGTGACACTTTAGCCCTC CGA	Bio-Fab Research

The thermal cycling conditions for *Npc1* gene were as follows:

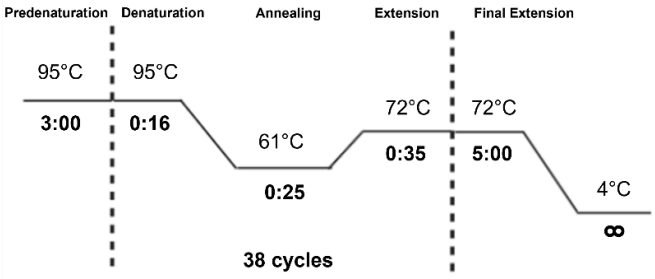

Thereafter, PCR products were incubated at 37°C for 1 hour with the restriction enzyme Eco91I (*BstEII*) (Thermo Fisher Scientific, #ER0391, Massachusetts, USA), which cuts only the mutant G allele, generating two fragments of 481 and 173 bp. This allows the detection of the A-to-G point mutation responsible for the *Npc1*^{nmf164} phenotype (Maue et al., 2012).

To determine sex, the *Sex-determining Region Y* (*Sry*) gene – located on the distal short arm of the Y chromosome and essential for male sex determination (Fechner, 1996) – was amplified generating a 273 bp product present only in males, according to the following protocol:

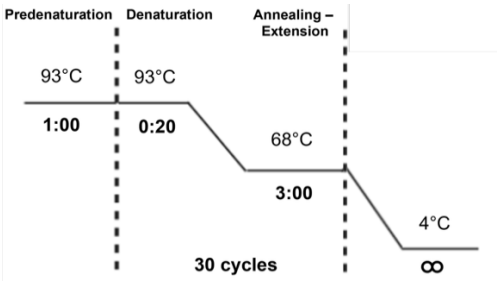

3.2.3 RNA preparation and quantitative Real-Time PCR of BDNF-related signaling molecules

Total RNA was extracted from PN11, 30 and 60 male and female *wt* and *Npc1*^{nmf164} cerebella, using the Total RNA Purification Plus Kit (Norgen Biotek Corp., Ontario, Canada) (Canterini et al., 2017). Reverse transcription was performed using Oligo(dT) and OneScript Plus Reverse Transcriptase reagents (cat. G236, ABM) in a 15-minute reaction at 50°C, followed by a 5-minute enzyme inactivation step at 85°C.

Quantitative real-time PCR (qRT-PCR) was conducted in triplicate/duplicate using 1µL of cDNA with SensiFAST SYBR Mix (Meridian Bioscience Inc., Cincinnati, OH, USA) on a QuantStudio™ 3 Real-Time PCR Detection System (Applied Biosystems by ThermoFisher Scientific). All primers were designed and validated using Primer-BLAST (NIH), and specificity was confirmed through melting curve analysis and amplified product electrophoresis in 2% agarose gels. In this study the following primer sequences were used:

Gene	FORWARD PRIMER	REVERSE PRIMER	COMPANY
BDNF	CATAAGGACGCGGACTTGTACA	AGACATGTTTGCGGCATCCA	Bio-Fab Research
TrkB	GGGCTTATGCCTGCTGGTCTT	TCCGGGTCAACGCTGTTAGGTT	Bio-Fab Research
PTEN	TGGGGAAGTAAGGACCAGAG	GGCAGACCACAAACTGAGGA	Bio-Fab Research
mTOR	GACACCATGAACCATGTCC	CCGGCTCAGGTCATAGAG	Bio-Fab Research
Snap25	GGATGAGCAAGGCGAACAAC	AGCTTGTTACAGGGACACACA	Bio-Fab Research
Shank3	ACGAAGTGCCTGCGTCTGGAC	CTCTTGCCAACCATTCTCATCAGTG	Bio-Fab Research
Nlgn3	GAAGATGGATCCGGCGCTAA	ACGATGACGTTGCCGTAACT	Bio-Fab Research
Gapdh	TGTGTCCGTCGTGGATCTGA	TTGCTGTTGAAGTCGCAGGAG	Bio-Fab Research

Amplification was performed using the following protocol: 50°C for 5 minutes, 95°C for 2 minutes, followed by 40 cycles of 95°C for 5 seconds and annealing at 60–64°C for 15-30 seconds, depending on the primer pair.

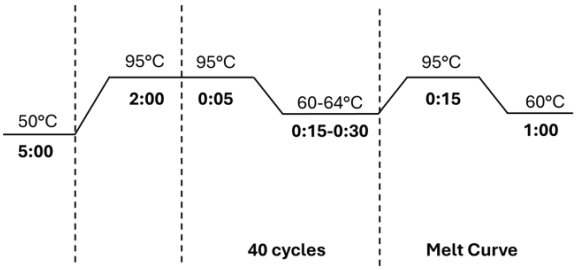

Relative gene expression levels were calculated using the 2^−DeltaDeltaCt (ΔΔCt) method (Livak and Schmittgen, 2001) and normalized to the expression of *Gapdh* RNA as the housekeeping gene (Canterini et al., 2017; Dragotto et al., 2019). Quantitative data were analyzed using three-way ANOVA, with between-subject factors genotype (2 levels: *wt* and *Npc1*^{nmf164}), sex (2 levels: male and female), and age (3 levels: PN11, PN30, PN60).

3.2.4 Protein extract preparation, subcellular fractionation and Western Blot analysis of cerebellar synaptic proteins

PN11, 30 and 60 *wt* and *Npc1*^{nmf164} mice were euthanized by decapitation, and brains were removed and stored at − 80°C. For subcellular fractionation, cerebellar tissues were homogenized using a glass-glass Potter homogenizer in 0.32M ice-cold sucrose Buffer A, containing 1mM $NaHCO_3$, 1mM $MgCl_2$, 1mM HEPES, 1mM NaF (Sigma-Aldrich, Milan, Italy), and protease/phosphatase inhibitors (Santa Cruz Biotechnology, USA; 1:100). Homogenates were first centrifuged at 1,000 × g for 10 minutes at 4°C. The resulting pellet (P1), containing nuclei and debris, was discarded, while the supernatant (S1) was centrifuged at 10,000 × g for 15 minutes at 4°C to obtain the crude synaptosomal fraction (P2). The supernatant (S2), representing the cytosolic fraction, was discarded. P2 pellets were resuspended in Buffer B, containing 75mM KCl, 1mM HEPES, 1% Triton X-100 (Sigma-Aldrich, Milan, Italy), and inhibitors (1:100), then ultracentrifuged at 47,000 rpm for 1 hour at 4°C using an Optima L-100K ultracentrifuge (Beckman Coulter). The supernatant (S3), referred to as the Triton Soluble Fraction (TSF), was stored at −80°C. The final pellet (P3), containing postsynaptic densities and referred to as the Triton Insoluble Fraction (TIF), was resuspended in Buffer C composed of 1mM HEPES and inhibitors (1:100), sonicated, and stored at −80°C (**Figure 23**) (Buccarello et al., 2018).

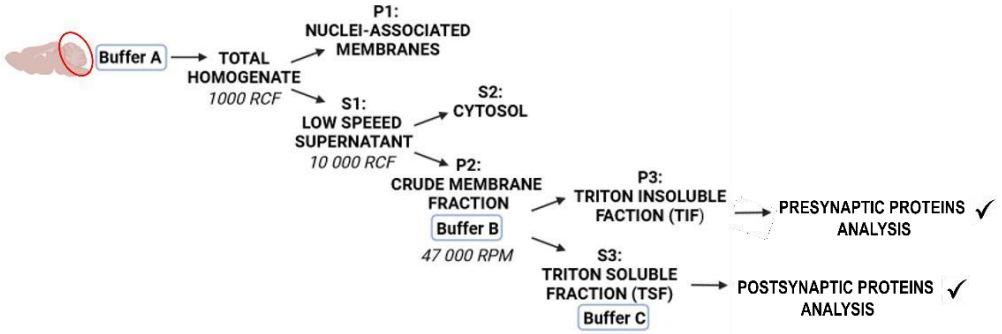

Figure 23. Subcellular fractionation procedure. PN11, 30 and 60 cerebella were homogenized in Buffer A and centrifuged at 1000 RCF at 4°C. The supernatant (S1) was then centrifuged at 10,000 RCF at 4°C. The resulting crude membrane fraction (P2) was resuspended in Buffer B and ultracentrifuged at 47,000 rpm obtaining the Triton soluble

fraction (TSF) and Triton insoluble fraction (TIF). The latter was resuspended in Buffer C, sonicated, and stored to -80°C until processing (Image created by BioRender).

For total protein extraction, instead, cerebellar tissues were homogenized in ice-cold RIPA buffer (Sigma-Aldrich, Milan, Italy) supplemented with protease and phosphatase inhibitors (SERVA Electrophoresis GmbH, Germany; 1:10,000). After 30 minutes on ice, samples were centrifuged at 12,000 × g for 15 minutes at 4°C. The pellets were discarded while supernatants were collected and stored at −80°C for further use (Canterini et al., 2013).

Total protein concentrations were determined using the Bradford colorimetric assay (SERVA, #P220101, Germany) and processed using Western blot analyses. In detail, extracted proteins were separated, according to their molecular weight, by SDS-polyacrylamide gel electrophoresis (SDS-PAGE) (homemade: 30% Acrylamide/Bis solution, 1.5M Tris-HCl pH 8.8, 20% SDS, TEMED, and 10% APS; Sigma-Aldrich, Milan, Italy), following standard protocols (Canterini et al., 2013). After electrophoretic migration, proteins were transferred onto polyvinylidene fluoride (PVDF) membranes (GVS, #1212639; Sanford, ME, USA). Membranes were then blocked for 1 hour at room temperature (RT) in either 3% bovine serum albumin or 5% non-fat dried milk (PanReac AppliChem, ITW Reagents) diluted in Tris-buffered saline with 0.1% Tween-20 (TBS-T) (Sigma, Milan, Italy). Blots were incubated overnight at 4°C with primary antibodies diluted in their respective blocking buffers, as previously described (Canterini et al., 2013). The following antibodies were used:

Antibody	SPECIES RAISED	COMPANY	DILUTION
Syntaxin 1A	Rabbit polyclonal	GeneTex, #GTX113559; Prodotti Gianni, Milan, Italy	1:3000
Snap25	Rabbit polyclonal	GeneTex, #GTX113839; Prodotti Gianni, Milan, Italy	1:3000
Vamp2	Rabbit polyclonal	GeneTex, #GTX133241; Prodotti Gianni, Milan, Italy	1:3000
Drebrin	Rabbit polyclonal	Invitrogen, #PA5-34725; Milan, Italy	1:1000
Shank3	Mouse monoclonal	Invitrogen, #MA5-27601; Milan, Italy	1:1000
PSD95	Mouse monoclonal	Enzo Life Sciences Inc., #ADI-VAM-PS002; NY, USA	1:250
Neuroligin1	Mouse monoclonal	Synaptic Systems, #129-111; Germany, EU	1:1000
Neuroligin2	Rabbit polyclonal	Synaptic Systems, #129-203; Germany, EU	1:1000
Neuroligin3	Rabbit polyclonal	Synaptic Systems, #129-113; Germany, EU	1:1000
β-actin	Mouse monoclonal	Elabscience, # E-AB-48018; North America, USA	1:5000

The following day, membranes were incubated 1 hour at RT with horseradish peroxidase (HRP)-conjugated secondary antibodies, specific for mouse IgG (Cell Signaling Technology, Danvers, MA, USA) or rabbit IgG (Cytiva, USA), diluted in TBS-T, according to the producer's instructions. Chemiluminescent detection was performed using the WesternBright Sirius Chemiluminescent Detection Kit (Advansta), and signals were acquired using an iBright 1500 Imaging System (Invitrogen) (Canterini et al., 2013). Densitometric analysis of immunoreactive bands was carried out using ImageJ Fiji software (latest version). The intensity of each band was

normalized to the β-actin signal intensity as the housekeeping protein. Quantitative data were analyzed using two-way ANOVA, with between-subject factors genotype (2 levels: *wt* and *Npc1*^{nmf164}) and age (3 levels: PN11, PN30, PN60).

3.2.5 Immunofluorescence detection of cerebellar synaptic proteins

For histological analyses, PN60 male and female *wt* and *Npc1*^{nmf164} mice were deeply anesthetized via intraperitoneal injection of xylazine (20mg/kg) and ketamine (34mg/kg), then transcardially perfused with 4% paraformaldehyde (PFA; Sigma, Milan, Italy) in 0.1M phosphate-buffered saline (1X PBS; 137mM NaCl, 2.7mM KCl, 10mM Na_2HPO_4, 1.8mM KH_2PO_4, pH 7.4). After isolation, brains were post-fixed overnight in 4% PFA at 4°C, followed by cryoprotection in 30% sucrose in 1X PBS. Collected brains were then embedded in Surgipath FSC22 Frozen Section Embedding Medium (Leica Biosystems, Wetzlar, Germany) and sagittally sectioned at 20µm thickness using a CM1900 cryostat (Leica, Milan, Italy). Sections were mounted onto Superfrost Plus microscope slides (Thermo Scientific, Germany) as previously described (Palladino et al., 2017).

For immunofluorescence, cerebellar sections were fixed in 4% PFA in 1X PBS, washed three times for 5 minutes in 0.05M NH_4Cl in 1X PBS, and rinsed three times in 1X PBS. Sections were then incubated overnight at 4°C with primary antibodies diluted in a blocking/permeabilization solution composed of 0.2% Triton X-100 (Sigma, Milan, Italy) and 3% fetal bovine serum (FBS; EuroClone, Milan, Italy) in 1X PBS. The following antibodies were used: anti-SNAP25 (polyclonal, GeneTex #GTX113839; Prodotti Gianni, Milan, Italy) and anti-SHANK3 (monoclonal, Invitrogen #MA5-27601; Milan, Italy). After primary antibody incubation, sections were washed three times in 1X PBS for 5 minutes each, then incubated for 1 hour at RT with Alexa Fluor 555-conjugated secondary antibodies specific for mouse IgG or rabbit IgG (Invitrogen, Milan, Italy; 1:500 in 1X PBS). Nuclei were counterstained with Hoechst (Sigma-Aldrich, USA; 1:10,000 in 1X PBS) for 15 minutes, followed by three additional PBS washes. Finally, sections were mounted using Fluoromount Aqueous Mounting Medium (Sigma-Aldrich, USA) and stored at −20°C. Immunofluorescence signals from cerebellar fields were visualized and using a TCS SP5 laser scanning confocal microscope (Leica Microsystems, Mannheim, Germany).

3.2.6 Golgi-staining and morphological analysis of cerebellar granule neuron dendritic spines

PN11, 30, and 60 male and female *wt* and *Npc1*^{nmf164} mice were deeply anesthetized and transcardially perfused with 0.9% NaCl (Sigma, Milan, Italy) in double-distilled water (ddH_2O). Following isolation, brains were processed using the Golgi-Cox staining protocol, as previously described (Di Segni et al., 2017). Brains were protected from light and immersed for 7 days at RT in a solution containing 1% potassium dichromate ($K_2Cr_2O_7$), 1% mercuric chloride ($HgCl_2$), and 0,8% potassium chromate (K_2CrO_4) (Sigma, Milan, Italy) in ddH_2O. After impregnation, brains were

cryoprotected in a 30% sucrose solution in 1X PBS and stored at 4°C for 1 week. Thereafter, 200µm thick sagittal sections were cut using a vibratome (S1000, Leica, Milan, Italy), mounted on gelatin-coated microscope slides, developed using a 3:1 ammonia and 5% sodium thiosulfate solution, and dehydrated by an ethanol series (70%, 90%, 100%). Finally, sections were mounted with Eukitt mounting medium (Electron Microscopy Sciences, Hatfield, PA, USA) and stored in the dark at RT.

GCs in the IGL were visualized using an Olympus BX53 microscope equipped with a 100x oil-immersion objective lens (numerical aperture 1.25) and identified based on their characteristic small somata and short dendrites with claw-shaped endings (Lucarelli et al., 2023). For histological analyses, 10-25 neurons exhibiting complete Golgi impregnation and intact dendritic arbors were selected from different cerebellar sections obtained from 2-3 animals per experimental group. GC dendrites and their spines were manually traced using Neurolucida software (version 8.0, MBF Bioscience, Williston, VT, USA). Dendritic spine density was quantified as the ratio between the total number of spines and the total dendritic length ($Spine\ density = \frac{N_{Spines}}{L_{Dendrite}} (Spine/\mu m)$) (Tortolani et al., 2025). In addition, dendritic spines were classified into different types based on spine head width (W) and neck length (L), following previously established criteria (Risher et al., 2014): filopodia (L > 2 µm), long thin (L = 1–2 µm), thin (L < 1 µm), stubby (L:W ≈ 1), and mushroom (W > 0.6 µm) (**Figure 24**). This classification was used for the detailed morphological characterization of GC dendritic spines.

Obtained data were statistically evaluated using three-way ANOVA, with between-subject factors genotype (2 levels: *wt* and *Npc1*^{nmf164}), sex (2 levels: male and female), and age (3 levels: PN11, PN30, PN60).

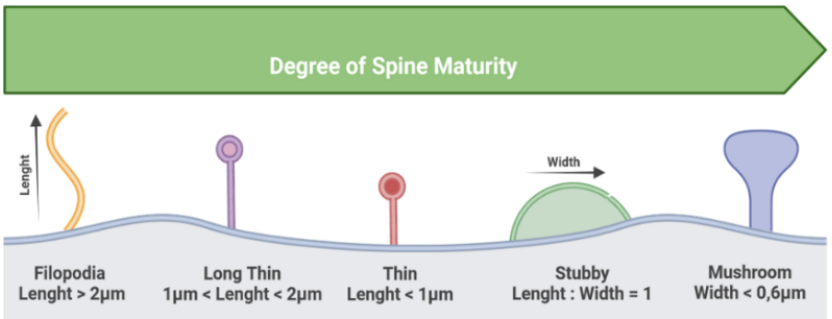

Figure 24. Dendritic spine types and maturity level. Spine maturity progresses (from left to right) from long filopodia type structures (**yellow**) to wide-headed mushroom spines (**blue**), as indicated by the green arrow. Morphological characteristics of spines are listed below each type (Image created by BioRender – adapted from Risher et al., 2014).

3.2.7 High-Performance Liquid Chromatography quantification of amino acid neurotransmitters and metabolites

PN30 male and female *wt* and *Npc1*^{nmf164} mice were euthanized by decapitation, and brains were removed and stored at − 80°C. Bilateral micro punches of cerebellar cortex were obtained, using a stainless-steel tube of 1.0mm inside diameter and stored at − 80°C until analysis.

On the day of the assay, frozen samples were homogenized in 0.05M $HClO_4$. The homogenates were centrifuged at 14,000 rpm for 20 min at 4°C. The resulting pellets were weighed, and aliquots of the supernatant were used to determine local γ-aminobutyric acid (GABA) and glutamine tissue levels using a High-Performace Liquid Chromatography (HPLC) system (Alliace, Waters Corporation, Milford, MA), as previously described (Puglisi-Allegra et al., 2000; Andolina et al., 2011).

GABA and glutamine concentrations (pg/20 µL) were determined in separate runs using the HPLC system coupled with a fluorescence detector (474 Model, Waters Corporation, Milford, MA). For derivatization, 30µL of each sample were mixed with 50µL of freshly prepared o-Phthaldialdehyde (OPA)/2-mercaptoethanol reagent and allowed to react for 2 minutes (Lindroth and Mopper, 1979; Rea et al., 2005). Subsequently, 50µL of the reaction mixture were injected and separated on a mobile phase containing 70mM disodium hydrogen phosphate (Na_2HPO_4), 400µM EDTA, 0.15% tetrahydrofuran (THF), and 26% methanol (all from Sigma-Aldrich, Milan, Italy). The pH of the mobile phase was adjusted with orthophosphoric acid and optimized separately for each analyte (pH 4.9 for GABA and pH 3.85 for glutamine).

Calibration curves were generated using external standards of GABA and glutamine at known concentrations (10^{-4} M), and all sample peak heights were normalized to these standards. Data are reported as total amount of analyte per 20 µL of extract (ng/20 µL), normalized to the weight of the corresponding tissue pellet. Data were statistically analyzed using two-way ANOVA, with genotype (2 levels: *wt* and *Npc1*^{nmf164}) and sex (2 levels: male and female) as between-subject factors.

3.2.8 Whole-brain iDISCO+ tissue clearing, 3D reconstruction and volumetric analysis of cerebellar lobules

PN15 male and female *wt* and *Npc1*^{nmf164} mice were deeply anesthetized and transcardially perfused with 4% PFA (Sigma-Aldrich, Milan, Italy) in 1X PBS. Harvested brains were post-fixed overnight in 4% PFA at 4 °C, then transferred to a 0.1% sodium azide (NaN_3) solution in 1X PBS to prevent microbial contamination.

Samples were processed using the iDISCO+ immunolabeling and clearing protocol with minor adjustments (Belle et al., 2017). Briefly, whole brains were dehydrated at RT through methanol series (20%, 40%, 60%, 80% and 100% twice; 1h per step) in 1X PBS, followed by overnight incubation under gentle agitation in a 66% dichloromethane (DCM; Sigma-Aldrich, USA) and 33% methanol solution. Samples were then bleached overnight at 4 °C in 5% hydrogen peroxide (H_2O_2) in 100% methanol. The following day, brains were rehydrated at RT through descending methanol concentrations (80%, 60%, 40%, 20%) and washed in 1X PBS. Tissue permeabilization was then performed for 2 h at RT in PTx.2 buffer, containing 0.2% Triton X-100 (Sigma-Aldrich, USA) and 0.1% NaN_3 in 1X PBS. Samples were subsequently incubated for 2 days at 37°C under agitation in a permeabilization solution composed of 80% PTx.2, 20% DMSO, 2.3% glycine (Sigma-Aldrich,

USA), and 0.1% NaN_3. For nuclear staining, samples were protected from light, incubated for 7 days at RT under continuous rotation into a solution containing TO-PRO (1:1000; Thermo Fisher Scientific) diluted in 1X PBS, then washed five times in 1X PBS (1 h each).

Following staining, all tissue-clearing steps were performed at RT, inside a chemical fume hood. Brains were dehydrated again through methanol series (20%, 40%, 60%, 80%, 100% twice), followed by a 3 h incubation under gentle rotation in 66% DCM/33% methanol. Subsequently, samples underwent delipidation by incubation in 100% DCM for 30 minutes under continuous rotation. Finally, brains were immersed overnight in dibenzyl ether (DBE; Sigma-Aldrich, USA) for optical clearing. The following day cleared samples were transferred to individual light-protective glass vials and stored at RT (Belle et al., 2017; Habart et al., 2023).

3D imaging was performed as previously described (Belle et al., 2017). Image acquisition was carried out using an Ultramicroscope CDC Olympus MVX10 (Olympus, Japan) equipped with ImspectorPro software (LaVision BioTec). The light sheet was generated by a 640 nm laser (Coherent Sapphire Laser, LaVision BioTec). A binocular stereomicroscope (MVX10, Olympus) equipped with a 2× objective (MVPLAPO, Olympus) was operated at 0.8× magnification. Samples were placed in a quartz imaging chamber (LaVision BioTec) filled with DBE and illuminated laterally by the laser beam. Images were captured at a step size of 7µm. All TIFF files were exported in 16-bit format. Subsequently, image stacks were converted to .ims format using ImarisFileConverter, and three-dimensional reconstructions were manually generated in Imaris x64 software (version 8.0.1; Bitplane, Oxford Instruments) with the “Surface” and “Mask” tools.

For quantitative volumetric analysis, only one cerebellar hemisphere was analyzed for each sample, starting from the midline sagittal division, as no hemispheric differences have been reported in this model (Maue et al., 2021). The hemisphere was subdivided into vermis and hemisphere proper, and individual lobules were grouped according to functional domains (anterior, central, and posterior) (**Figure 25A**). Since only nuclear labeling was performed, reconstruction was restricted to the densely packed IGL, which was clearly distinguishable at a low magnification. Each lobule group was subsequently pseudo-colored for visualization (**Figure 25B**). Final 3D images and animations were produced using the “Snapshot” and “Animation” tools.

Volumes (µm³) of the IGL were automatically extracted using the Imaris “Surface Statistics*”* module. Absolute IGL volumes were used both to assess global size differences between groups and calculate ΔVolumes ($\Delta V_{\text{individual}} = \frac{V_{Npc1nmf164} - mean\, V_{wt,same\ sex}}{mean\, V_{wt,same\ sex}} - 1$). Volumetric data were analyzed separately for each lobular group, using two-way ANOVA, with genotype (2 levels: *wt* and *Npc1*^{nmf164}) and sex (2 levels: male and female) as between-subject factors. ΔVolumes were compared separately for the vermis and the hemispheres, using repeated-measures one-way ANOVA, with between-subject factor sex (2 levels: male and female), and within-subject factor lobular group (4 levels: anterior, central, posterior, nodular).

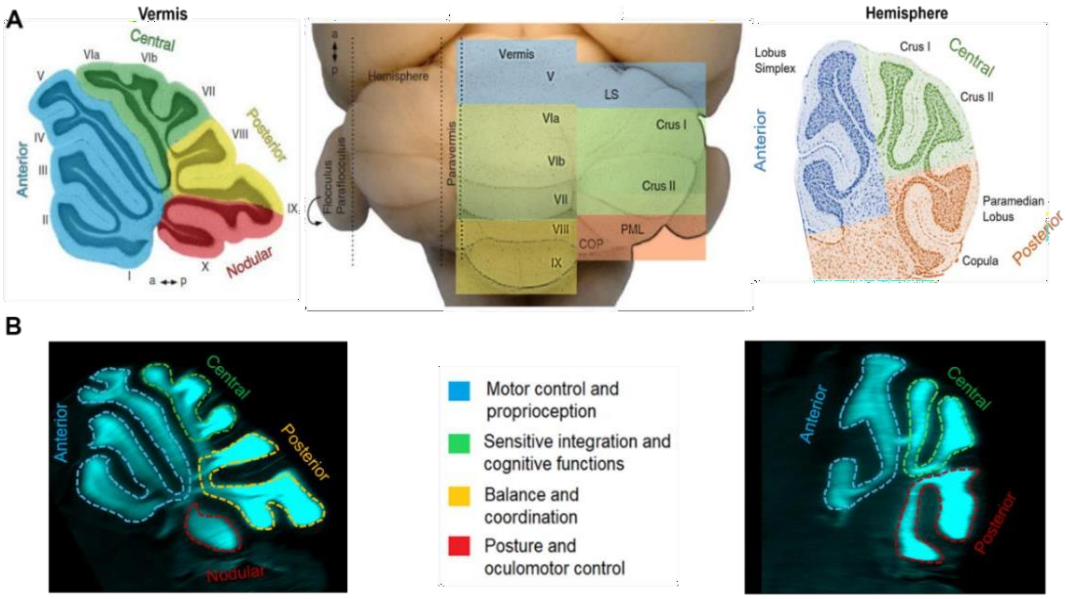

Figure 25. Analysis of cerebellar lobules. (**A**) Schematic representation of sagittal sections from mouse cerebellum in both the vermis (**left**) and hemisphere (**right**), illustrating the anterior–posterior lobular segmentation according to functional domains, each identified by a distinct color: anterior lobules (**blue**), involved in motor control and proprioception; central lobules (**green**), associated with sensory integration and cognitive processing; posterior lobules (**yellow**), essential for balance and coordination; and nodular lobules (**red**), contributing to posture and oculomotor control (adapted from White and Sillitoe, 2013). (**B**) Representative sagittal views of iDISCO-cleared cerebella stained with the nuclear marker TO-PRO, showing the distinguishable IGL in both the vermis (**left**) and hemisphere (**right**), and Imaris x64 reconstructions of segmented lobules color-coded according to their corresponding functional domains.

3.2.9 Behavioral procedures

The development of social behavior was evaluated in PN8 and 30 *wt* and *Npc1*^{nmf164} littermates, prior to the onset of motor deficits in mutant mice (Maue et al., 2012), through UltraSonic Vocalizations (**USVs**) and the Social Interaction Test (**SIT**), whereas coping strategies were only investigated in PN30 *Npc1*^{nmf164} and *wt* mice, using the Tail suspension test (**TST**). Both male and female mice were tested to assess potential sex differences. All behavioral testing was conducted between 11:00 AM and 3:00 PM, following a one-hour habituation period in the testing room. To eliminate olfactory cues, all equipment was thoroughly cleaned with 70% ethanol in between trials.

3.2.9.1 UltraSonic Vocalizations recordings

On PN8, a maximum of four male and female *wt* or *Npc1*^{nmf164} pups per litter were selected for behavioral testing. To perform USVs recordings, after one hour of habituation, the mother was removed from the litter and placed into a clean cage, while the pups were left in the home cage, positioned on a warming plate (35°C ± 2) to prevent hypothermia. Each pup was individually placed into a glass container (5cm in length and height), which was then positioned inside a sound-attenuated chamber. Spontaneous vocalizations were recorded during 5-minutes sessions, while the room temperature was maintained at 22°C ± 1 as previously described (Fiori et al., 2015) (**Figure 26**). Each pup was weighed immediately after the recording session.

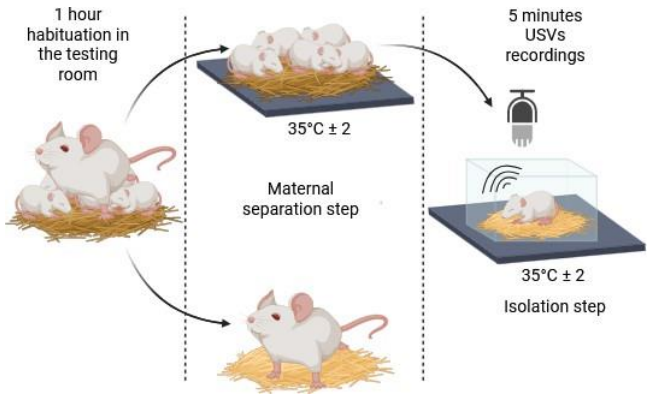

Figure 26. Schematic representation of the USV recording procedure. For USV measurement, a litter of 6 or 7 pups was separated from their mother and was kept in a stainless-steel cup at 33–37°C on a hot plate. Thereafter, each pup was isolated from its littermates and placed in another stainless-steel cup at 33–37°C for 5 min. A microphone was set above the cup in a sound-attenuated chamber, for immediate recording of the pup's USVs. After USV recording, each pup was placed back in the cage with the mother (Image created by BioRender).

USVs were captured using an UltraSoundGate CM16 condenser microphone (Avisoft Bioacoustics, Berlin, Germany), sensitive to frequencies ranging from 15 to 180kHz and with a flat frequency response (66dB) between 25 and 140kHz. The microphone was positioned 1cm above the container and connected to a computer via an UltraSoundGate USB Audio device. Acoustic data were recorded as 16-bit WAV files at a sampling rate of 250,000Hz. Sound files were analyzed using SasLab Pro software (version 4.40; Avisoft Bioacoustics). A fast Fourier transformation (FFT) was applied with the following parameters: 512 FFT-length, 100% frame, Hamming window, and 75%-time window overlap. Spectrograms were generated with a frequency resolution of 488Hz and a time resolution of 0.512ms. USVs were detected using a threshold-based automatic detection algorithm with a 20ms hold time. Signals below 30kHz were filtered out to reduce background noise. Manual corrections were made by an experienced user prior to automatic parameter extraction. The total number of calls emitted within the 5-minute period was quantified. In addition, qualitative parameters of ultrasonic emission were analyzed, including the average peak amplitude (dB) and average peak frequency (kHz) (D'Amato et al., 2011; Fiori et al., 2015). Obtained data were analyzed by two-way ANOVA, with between-subject factors genotype (2 levels: *wt* and *Npc1*^{nmf164}) and sex (2 levels: male and female).

3.2.9.2 Social Interaction Test

The SIT was conducted on PN30 male and female *wt* and *Npc1*^{nmf164} mice to evaluate social interaction (Kaidanovich-Beilin et al., 2011). Animals were placed in a grey Plexiglas rectangular apparatus (60cm × 40cm × 24cm) consisting of a central chamber connected with two lateral chambers. During the 10-minute habituation trial, two identical empty transparent Plexiglas cylinders (8 cm in diameter) were positioned in the two lateral chambers, while each mouse was placed in the central chamber and allowed to freely explore the entire apparatus. Following habituation, the 10-minute sociability trial was performed by placing an age- and sex-matched conspecific (used as a

social stimulus) and a plastic tube (used as a neutral stimulus) inside the two transparent cylinders located in the two lateral chambers (**Figure 27**). The placement of subjects and objects was alternated between trials to avoid location or side bias across subjects and groups (Cinque et al., 2012; Fiori et al., 2015).

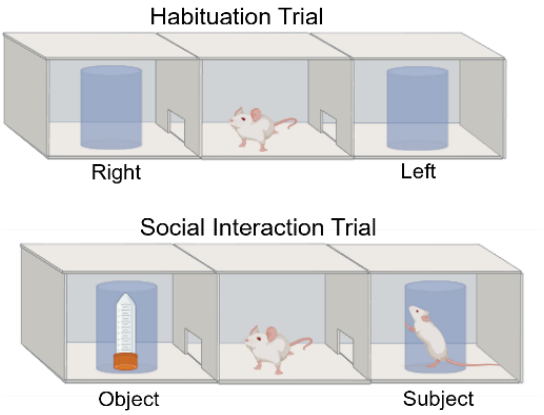

Figure 27. Schematic representation of the SIT procedure. During the 10-minutes habituation trial, each tested mouse was placed in the central chamber and allowed to freely explore the testing apparatus. The time spent in each chamber (**left**, **right**) during the habituation phase was recorded. In the sociability trial, an age- and sex-matched conspecific and an object were placed alternatively into one of the holding cups. The tested mouse was reintroduced into the central chamber of the apparatus, and the time spent in each of the two lateral chambers (**object**, **subject**), as well as the time spent directly sniffing the social stimulus were measured during a 10-minutes session (Image created by BioRender).

Both sessions were video recorded using EthoVision XT software (Noldus, the Netherlands), a computerized video tracking system. During the habituation trial, velocity and distance traveled by animals were automatically measured, to investigate motor variables. During the sociability trial, the percentage of time spent by the experimental subject in each lateral chamber, as well as the time spent sniffing each cylinder was manually scored by a trained observer, blind to the experimental conditions (Fiori et al., 2015).

The time spent exploring each chamber/stimulus, both in the habituation and sociability sessions, were analyzed by repeated-measures two-way ANOVA, with between-subject factors genotype (2 levels: *wt* and *Npc1*^{nmf164}) and sex (2 levels: male and female), and one within-subject factor (chamber, 2 levels: subject *vs* object). Whereas, velocity and distance moved during the habituation session were analyzed by two-way ANOVA, with between-subject factors genotype (2 levels: *wt* and *Npc1*^{nmf164}) and sex (2 levels: male and female).

3.2.9.3 Tail suspension test

The TST is commonly used to evaluate depressive-like behaviors (Can et al., 2012). This test assumes that the animal will actively try to escape from a stressful situation, but as time passes by, the animal will switch from vigorous struggling behavior to increasing immobility. In this context, long immobility phases are interpreted as a pro-depressive phenotype (Teegarden, 2012).

For TST, each PN30 male and female *wt* and *Npc1*^{nmf164} mouse was placed into a three-walled rectangular apparatus (60cm × 60cm × 20cm) with a suspension bar (1cm × 1cm × 60cm)

positioned on the top of the box. Animals were individually suspended by the tail at 60cm above the floor, using an adhesive tape positioned < 1cm from the tip of the tail (Yan et al., 2015) (**Figure 28**).

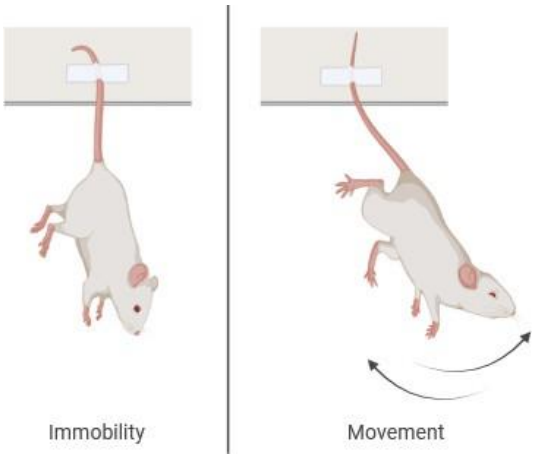

Figure 28. Schematic representation of the TST procedure. PN30 mice were suspended by the tail on a bar using an adhesive tape. Behavioral performances were recorded for 10 minutes, and the duration of immobility was manually scored and interpreted as a measure of depressive-like behavior (Image created by BioRender).

Behavioral performances were recorded for 10 minutes, by a digital camera placed in front of the apparatus. Duration of immobility – defined as the period when the animals stopped struggling for ≥ 1s – was manually scored by a trained observer blind to the experimental conditions, using EthoVision XT software (Noldus, TheNetherlands) (Lo Iacono et al., 2021). The immobility time was analyzed by two-way ANOVA, with between-subject factors genotype (2 levels: *wt* and *Npc1*^{nmf164}) and sex (2 levels: male and female).

3.2.10 Statistical analysis

All statistical analyses were performed using GraphPad Prism 8.0 (GraphPad Software, Inc., San Diego, CA, USA) or SuperANOVA (Abacus Concepts, Berkeley, CA, USA). Prior to analysis, all datasets were tested to verify compliance with ANOVA assumptions. Normality of data distribution was assessed using the Shapiro–Wilk test. Quantitative data were analyzed using one-way, two-way, or three-way ANOVA, with between-subject factors genotype (2 levels: *wt* and *Npc1*^{nmf164}), sex (2 levels: male and female), and age (3 levels: PN11, PN30, PN60), as appropriate. Post-hoc comparisons were performed using Tukey's multiple comparisons test or Fisher's least significant difference (LSD) test. When only a main effect of genotype was detected, Student's *t*-tests were conducted to compare *wt* and *Npc1*^{nmf164} mice at each age, or regardless of sex. Statistical significance was set at $p < 0.05$. All data are presented as mean ± SEM.

3.3 Results

3.3.1 *Npc1*^{nmf164} mice display sex- and age-dependent alterations in the BDNF-TrkB signaling pathway during cerebellar postnatal development

BDNF plays a crucial role in the CNS by modulating key neurodevelopmental processes at both pre- and postsynaptic sites, supporting neurogenesis as well as dendritic spine formation and maturation (Cirulli et al., 2004; Bramham and Messaoudi, 2005; Erickson et al., 2010; Edelmann et al., 2014; Lin et al., 2018; Camuso et al., 2022). Consequently, alterations in the BDNF-TrkB signaling cascade during critical developmental windows have been associated with dysregulation of intracellular pathways and to the onset of several NDDs (Gonzales and LaSalle, 2010; Tilot et al., 2015). Our previous studies have reported reduced cerebellar levels of BDNF and its TrkB receptor during postnatal development of *Npc1*^{nmf164} mice (Lucarelli et al., 2023). To expand upon these findings, here we examined sex-dependent differences in the expression of BDNF–TrkB signaling components (**Figure 1**). Specifically, by qRT-PCR we quantified mRNA levels of *BDNF* and *TrkB*, along with downstream effectors, including the mechanistic target of rapamycin (*mTOR*) and its negative regulator phosphatase and tensin homolog (*PTEN*), in cerebellar extracts from male and female *wt* and *Npc1*^{nmf164} mice at PN11, PN30 and PN60.

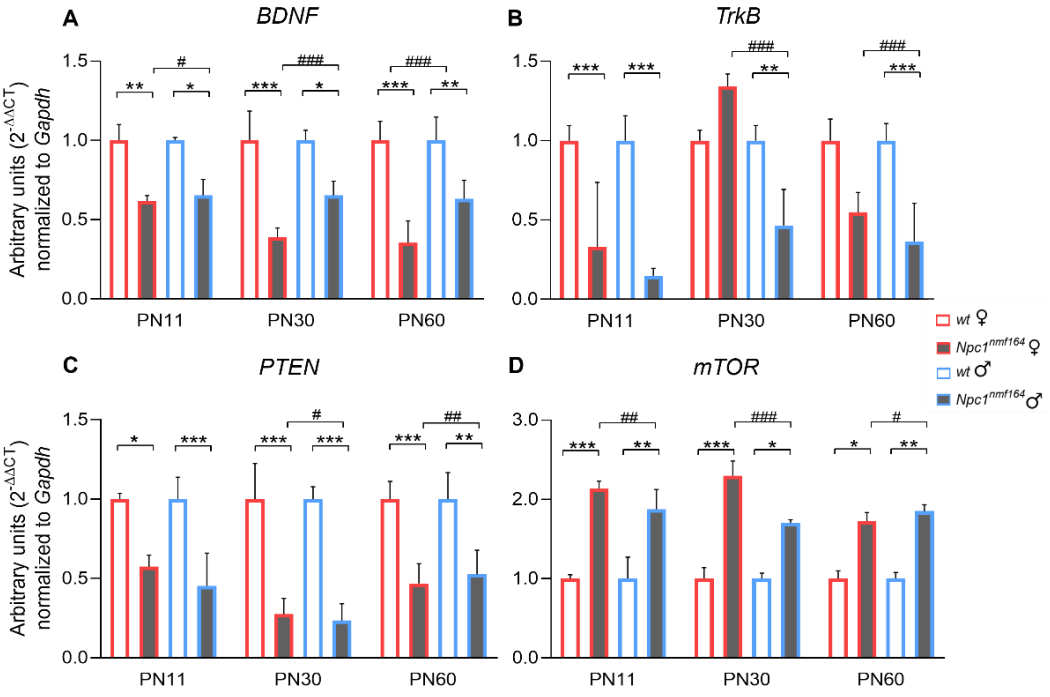

Figure 1. Analysis of the BDNF-TrkB signaling pathway in the postnatal developing cerebellum of male and female *wt* and *Npc1*^{nmf164} mice. Relative qPCR quantification of (**A**) *BDNF*, (**B**) *TrkB*, (**C**) *PTEN*, and (**D**) *mTOR* mRNA levels in the cerebellum of male (♂ **blue contour**) and female (♀ **red contour**) *wt* (**white bars**) and *Npc1*^{nmf164} (**grey bars**) mice at PN11, PN30, and PN60. Data are presented as fold change relative to *wt* (mean = 1). Histograms represent the mean 2^-ΔΔCt of biological replicates normalized to *Gapdh*. Error bars indicate SEM (n = 3 per group). Statistical analyses were performed on ΔCt values (target Ct – *Gapdh* Ct) using three-way ANOVA (genotype × sex × age), followed by Tukey's post hoc test for multiple comparisons. Statistical significance is indicated on the graphs (*p < 0.05; **p < 0.01; ***p < 0.001). * indicates comparisons between genotypes (*wt*, *Npc1*^{nmf164}); # indicates comparisons between sexes (male, female). **Note:** Age-related comparisons (PN11, PN30, PN60) were analyzed and reported in **Supplementary Tables 1–4.**

At PN11, qRT-PCR analysis revealed that *Npc1*^{nmf164} mice of both sexes already exhibited significantly reduced *BDNF*, *TrkB*, and *PTEN* cerebellar transcript levels, together with a concomitant increase in *mTOR*, compared to *wt* controls, indicating an early disruption of the BDNF-TrkB signaling pathway, consistent with our previous findings (Lucarelli et al., 2023). At PN30, the reduction in *BDNF* and *PTEN* and the upregulation in *mTOR* persisted in both male and female mutants, consistent with the well-established role of PTEN as a negative regulator of mTOR. In contrast, *TrkB* expression displayed a sex-specific pattern, with a significant decrease in male *Npc1*^{nmf164} mice and a slight, non-significant increase in female mutants relative to *wt*. By PN60, both sexes exhibited significant reductions in *BDNF*, *TrkB*, and *PTEN*, alongside elevated *mTOR* levels, indicating a persistent alteration of intracellular signaling downstream of TrkB (**Figures 1A**–**D**). Across all time points, sex-dependent differences in *Npc1* mutants were generally in the same direction (increase or decrease), with the exception of *TrkB* at PN30, showing a sex-specific divergence (**Figures 1A**–**D**). Finally, within the *Npc1*^{nmf164} group, age-related trends were observed: *BDNF* levels tended to decrease with age, whereas its expression increased during *wt* development, as expected (Maisonpierre et al., 1990; Lindholm et al., 1997); *PTEN* decreased from PN11 to PN30 and then partially recovered at PN60, and *mTOR* levels increased between PN11 and PN30 in females but decreased in males, with the opposite trend emerging by PN60 (statistical significance reported in supplementary tables 1–4).

These results indicate a dynamic modulation of the BDNF-TrkB pathway during postnatal cerebellar development, with early alterations persisting and partially diverging between sexes over time.

3.3.2 Developmental dynamics of synaptic protein expression during cerebellar development in *Npc1*^{nmf164} mice

The BDNF-mTOR pathway plays a central role in regulating the synthesis of proteins involved in synaptic function, structure, and plasticity (Kelleher et al., 2004; Jaworski and Sheng, 2006; Richter and Klann, 2009; Hoeffer and Klann, 2010). Dysregulation of mTOR has been widely associated with several NDDs (Winden et al., 2018; Thomas et al., 2023), as its activity and downstream effector influences dendritic arborization, spine morphology, and synaptic plasticity in post-mitotic neurons (Jaworski and Sheng, 2006; Hoeffer and Klann, 2010). Therefore, based on the abnormalities observed in *Npc1*^{nmf164} mice, and considering the importance of cholesterol homeostasis for membrane integrity and synaptic vesicle dynamics, we next assessed whether these molecular changes affect the expression of key synaptic proteins in the developing cerebellum.

To this end, we analyzed selected pre- and postsynaptic proteins, playing distinct functional roles at the synapse, in cerebellar extracts from *wt* and *Npc1*^{nmf164} mice at PN11, PN30, and PN60. In this set of experiments, however, samples were not distinguished by sex, since subcellular fractionation procedures (see Materials and Methods, section 3.2.4) typically yield only limited

amount of material. To ensure sufficient sample availability, males and females were therefore pooled for these analyses. This approach also aligns with the 3Rs principle as it allowed minimizing the number of animals used.

As shown in **Figure 2**, Western blot analyses were performed to evaluate the levels of presynaptic components of the Soluble N-ethylmaleimide-sensitive factor activating protein receptor (SNARE) complex, in order to assess presynaptic integrity. The SNARE complex – comprising Syntaxin 1A, Vesicle-associated membrane protein 2 (Vamp2), and Synaptosomal-associated protein 25 (Snap25) – is localized in both vesicular and target membranes and is essential for vesicle docking and membrane fusion in synaptic transmission (Yoon and Munson, 2018) (**Figure 2A**).

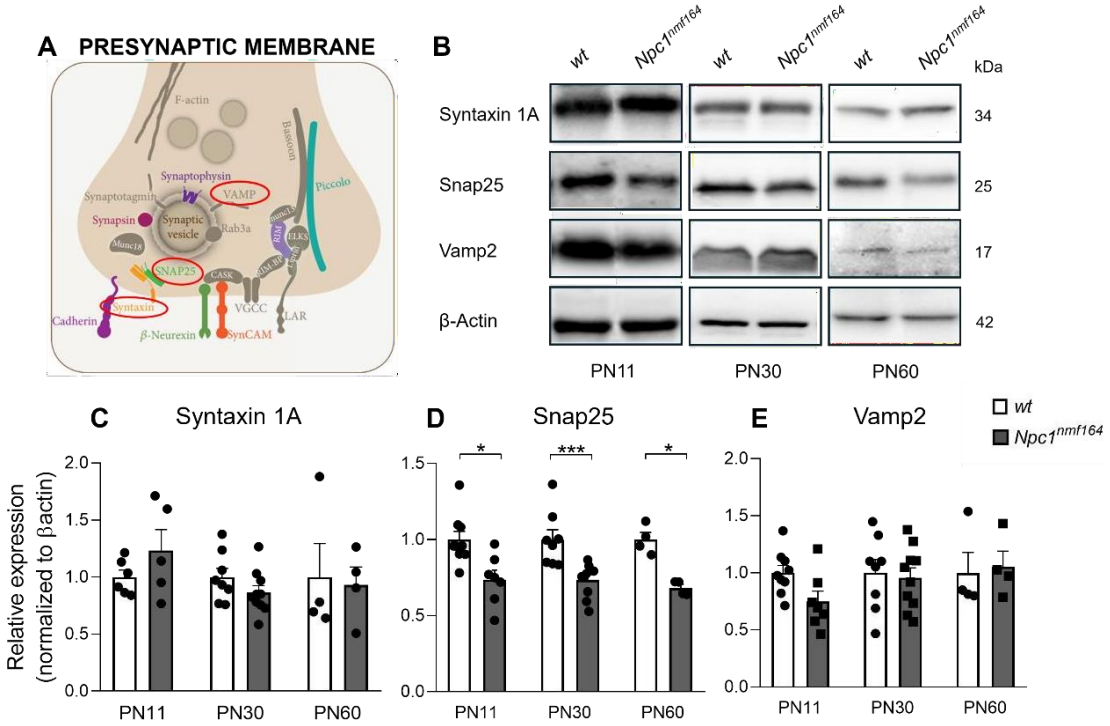

Figure 2. Analysis of presynaptic protein expression levels in the postnatal developing cerebellum of *wt* and *Npc1*^{nmf164} mice. (**A**) Schematic representation of SNARE proteins localization at presynaptic terminals. (**B**) Representative immunoblots of SNARE protein levels in *wt* and *Npc1*^{nmf164} cerebella at increasing timepoints. Densitometric quantification of (**C**) Syntaxin 1A, (**D**) Snap25, and (**E**) Vamp2 in the cerebellum of *wt* (**white bars**) and *Npc1*^{nmf164} (**grey bars**) mice at PN11, PN30, and PN60. Data are presented as fold change relative to *wt* (mean = 1). Each point of the scatter plot represents a biological replicate normalized to β-Actin (target intensity/β-Actin intensity). Error bars indicate SEM (n ≥ 4 per group). Statistical analyses were performed on normalized ratios (target/β-Actin) using two-way ANOVA (genotype × age), followed by Fisher's post hoc test for multiple comparisons. When only a main effect of genotype was detected, *t*-tests were also conducted to compare *wt* and *Npc1*^{nmf164} mice at each age. Statistical significance is indicated on the graphs (*p < 0.05; **p < 0.01; ***p < 0.001). * indicates comparisons between genotypes (wt, *Npc1*^{nmf164}). **Note:** Age-related comparisons (PN11, PN30, PN60) were analyzed and reported in **Supplementary Tables 5–6.**

Our results revealed that Snap25 protein levels were significantly reduced in the cerebellum of *Npc1*^{nmf164} mice compared to *wt* controls at all developmental stages analyzed. In contrast, Syntaxin 1A and Vamp2 levels did not show significant differences between genotypes (**Figures 2C–E**). Additionally, analysis of age-related effects revealed that Snap25 expression increased from PN11 to PN30 and subsequently declined at PN60, regardless of genotype. Conversely, Vamp2

levels exhibited a progressive age-dependent increase in both *wt* and *Npc1*^{nmf164} mice (statistical significance reported in supplementary tables 5–6).

Given the emerging evidence that alterations in the molecular components of the postsynaptic density (PSD) region contribute to the pathogenesis of NDDs (de Bartolomeis et al., 2014; Ulu et al., 2024), we next examined the expression of selected postsynaptic markers (**Figure 3**). These included Shank3 and Drebrin, two actin-binding scaffolding proteins involved in dendritic spine organization and dynamics (Luna et al., 1997; Aoki et al., 2005; Wan et al., 2021); and PSD95, a major postsynaptic scaffold protein that stabilizes N-methyl-D-aspartic acid (NMDA) and α-amino-3-hydroxy-5-methyl-4-isox-azoleproprionic acid (AMPA) receptors at excitatory synapses (Coley and Gao, 2018; Xie et al., 2019) (**Figure 3A**).

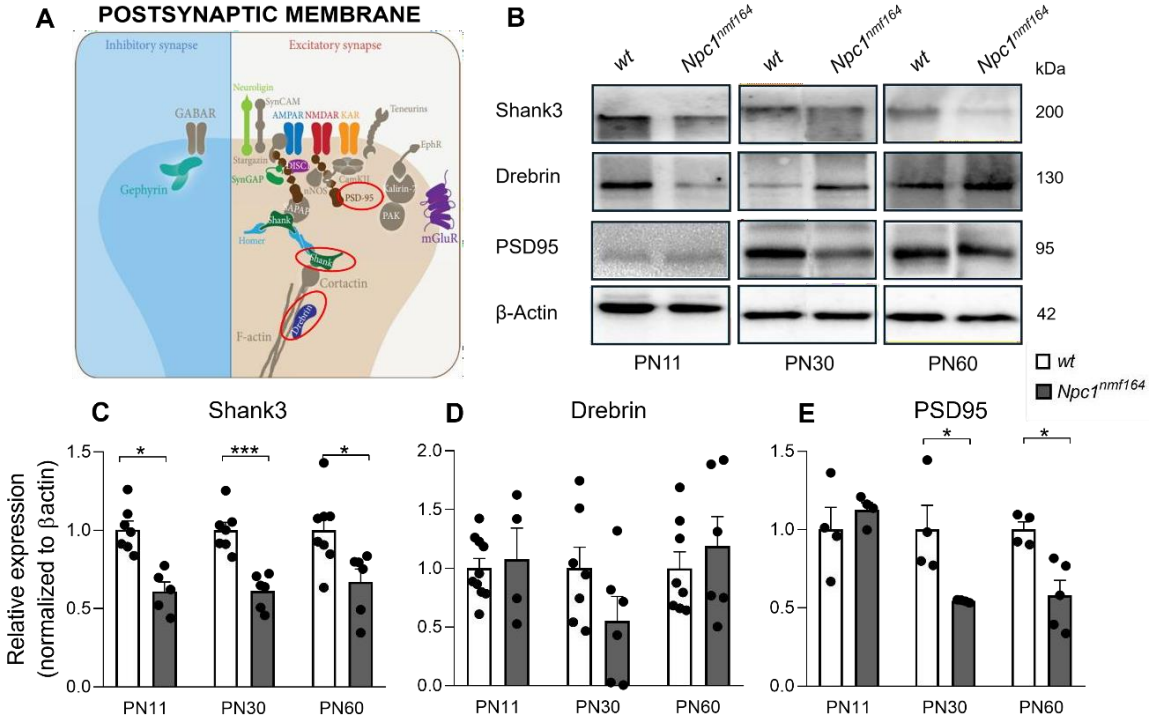

Figure 3. Analysis of postsynaptic proteins expression levels in the postnatal developing cerebellum of *wt* and *Npc1*^{nmf164} mice. (**A**) Schematic representation of scaffolding proteins localization at postsynaptic terminals. (**B**) Representative immunoblots of postsynaptic protein levels in *wt* and *Npc1*^{nmf164} cerebella at increasing timepoints. Densitometric quantification of (**C**) Shank3, (**D**) Drebrin, and (**E**) PSD95 of *wt* (**white bars**) and *Npc1*^{nmf164} (**grey bars**) mice at PN11, PN30, and PN60. Data are presented as fold change relative to *wt* (mean = 1). Each point of the scatter plot represents a biological replicate normalized to β-Actin (target intensity/β-Actin intensity). Error bars indicate SEM (n ≥ 4 per group). Statistical analyses were performed on normalized ratios (target/β-Actin) using two-way ANOVA (genotype × age), followed by Fisher's post hoc test for multiple comparisons. When only a main effect of genotype was detected, *t*-tests were conducted to compare *wt* and *Npc1*^{nmf164} mice at each age. Statistical significance is indicated on the graphs (*p < 0.05; **p < 0.01; ***p < 0.001). * indicates comparisons between genotypes (*wt*, *Npc1*^{nmf164}); **Note:** Age-related comparisons (PN11, PN30, PN60) were analyzed and reported in **Supplementary Tables 7–9.**

Among the analyzed proteins, Shank3 expression resulted in a significant reduction in the cerebellum of *Npc1*^{nmf164} mice compared to *wt* controls at all developmental stages (PN11, PN30, and PN60). In addition, PSD95 levels were significantly decreased in mutants, but only at later stages (PN30 and PN60) relative to *wt*. In contrast, no significant differences were observed in

Drebrin levels between genotypes at all ages examined (**Figures 3C–E**). Furthermore, age-related effects were analyzed and revealed that Shank3 expression progressively decreased with age, regardless of genotype, whereas Drebrin levels showed a significant upregulation between PN30 and PN60 in *Npc1*^{nmf164} mice, and a non-significant increase across development in *wt* mice. Finally, no age-dependent changes were detected for PSD95 (statistical significance reported in supplementary tables 7–9).

To further assess synaptic integrity, we examined the expression of Neuroligin (Nlgn) family members, including Nlgn1, Nlgn2 and Nlgn3, cell-adhesion proteins anchored at the postsynaptic membrane that are differentially distributed across excitatory and inhibitory synapses and play key roles in synapse formation and function (Lisé and El-Husseini, 2006; Ali et al., 2020; Uchigashima et al., 2021) (**Figure 4A**).

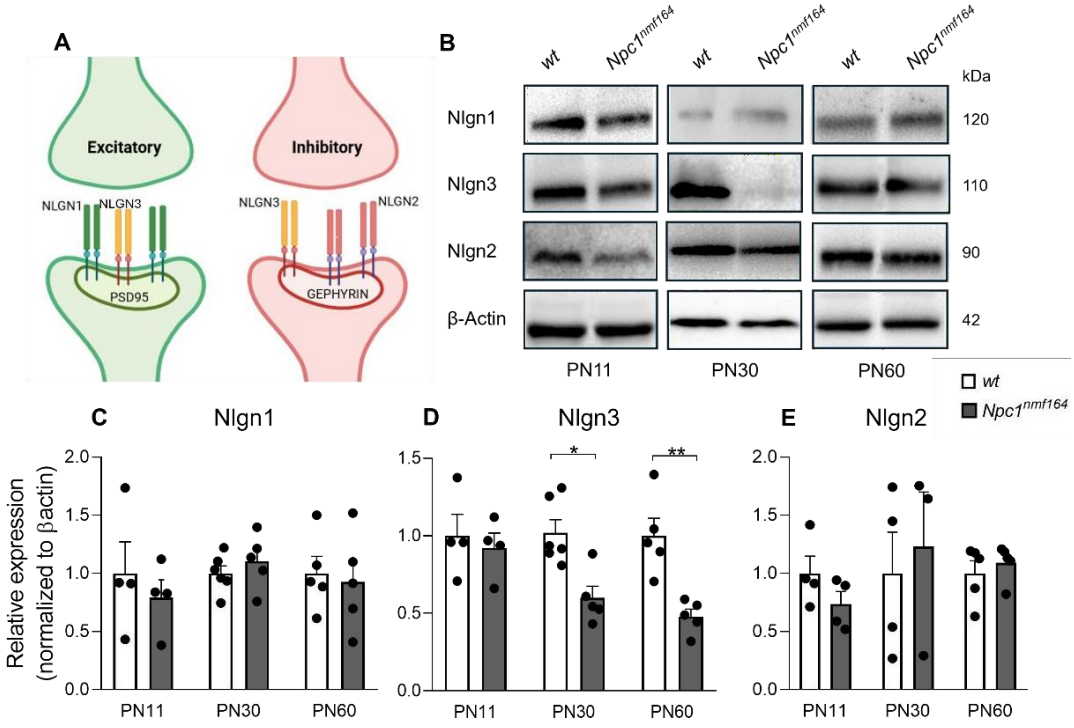

Figure 4. Analysis of synaptic adhesion protein expression levels in the postnatal developing cerebellum of *wt* and *Npc1*^{nmf164} mice. (**A**) Schematic representation of neuroligins differential localization at inhibitory and excitatory postsynaptic terminals. (**B**) Representative immunoblots of neuroligin protein levels in *wt* and *Npc1*^{nmf164} cerebella at increasing timepoints. Densitometric quantification of (**C**) Nlgn1, (**D**) Nlgn3, and (**E**) Nlgn2 of *wt* (**white bars**) and *Npc1*^{nmf164} (**grey bars**) mice at PN11, PN30, and PN60. Data are presented as fold change relative to *wt* (mean = 1). Each point of the scatter plot represents a biological replicate normalized to β-Actin (target intensity/β-Actin intensity). Error bars indicate SEM (n ≥ 4 per group). Statistical analyses were performed on normalized ratios (target/β-Actin) using two-way ANOVA (genotype × age), followed by Fisher's post hoc test for multiple comparisons. When only a main effect of genotype was detected, *t*-tests were conducted to compare *wt* and *Npc1*^{nmf164} mice at each age. Statistical significance is indicated on the graphs (*p < 0.05; **p < 0.01). * indicates comparisons between genotypes (*wt*, *Npc1*^{nmf164}). **Note:** no age-related effect (PN11, PN30, PN60) was detected.

Western blot analysis revealed a marked reduction in Nlgn3 protein levels in *Npc1*^{nmf164} mice compared to *wt* at both PN30 and PN60, whereas Nlgn1 and Nlgn2 expression remained unchanged

between genotypes at all developmental stages (**Figures 4C–E**). Finally, no age-related changes were observed among genotypes.

These results highlight a selective vulnerability of key synaptic components in the *Npc1* mutant cerebellum. Since these proteins are essential for the structural integrity and functional efficacy of synapses, their impairment can contribute to defective synaptic maturation and connectivity.

To investigate potential sex-dependent differences in the expression of those proteins that showed at least a twofold change between *wt* and *Npc1*^{nmf164} mice (i.e. Snap25, Shank3 and Nlgn3), we quantified their cerebellar mRNA levels in male and female *wt* and *Npc1*^{nmf164} mice at PN11, PN30, and PN60 by qRT-PCR. In parallel, we characterized the distribution of these synaptic proteins across cerebellar layers by immunofluorescence in male and female *wt* and *Npc1*^{nmf164} cerebellar sections at PN60 (**Figure 5**).

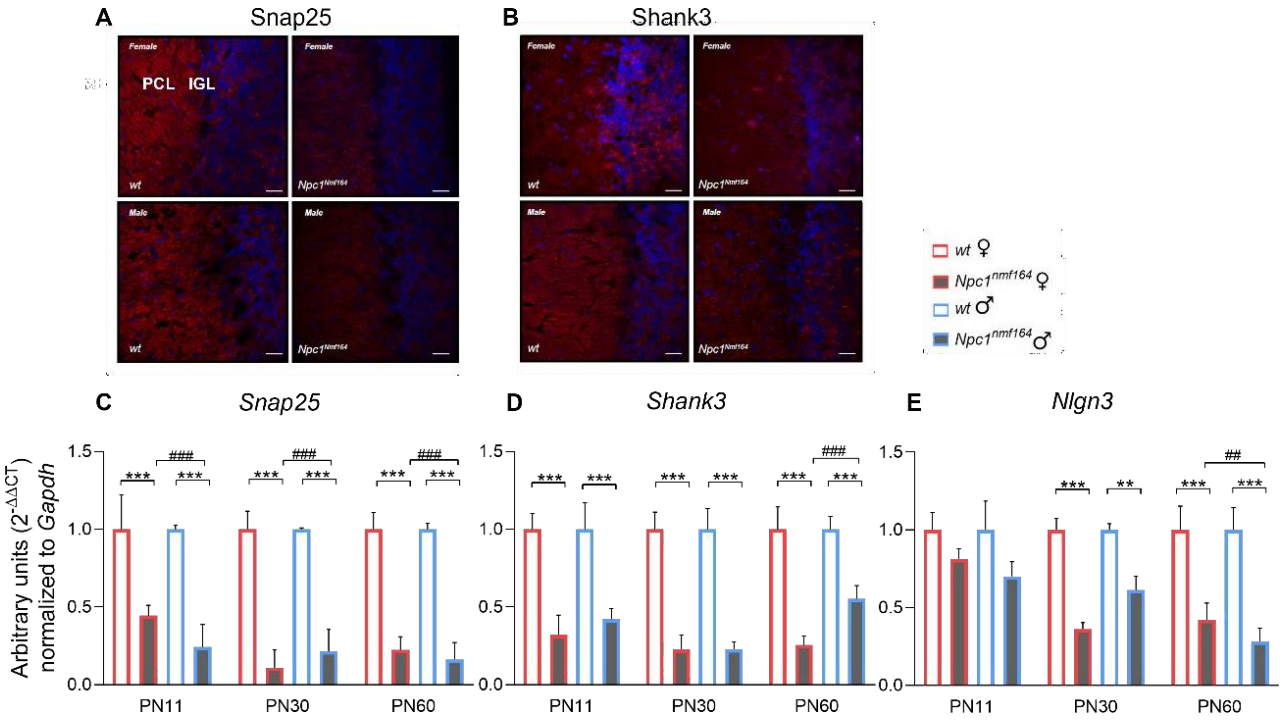

Figure 5. Analysis of sex-related differences in synaptic marker expression profiles in the postnatal developing cerebellum of *wt* and *Npc1*^{nmf164} mice. Representative cerebellar fields of confocal images are shown in the figure. Detection of (**A**) Snap25 (**red**), (**B**) Shank3 (**red**) and nuclei (Hoechst 33258, **blue**) in PN60 cerebellar sections of male (**down**) and female (**up**) *wt* (**left**) and *Npc1*^{nmf164} (**right**) mice. Scale bar: 20 µm. Relative qPCR quantification of (**C**) *Snap25*, (**D**) *Shank3*, and (**E**) *Nlgn3* mRNA levels in the cerebellum of male (♂ **blue contour**) and female (♀ **red contour**) *wt* (**white bars**) and *Npc1*^{nmf164} (**grey bars**) mice at PN11, PN30, and PN60. Data are presented as fold change relative to *wt* (mean = 1). Histograms represent the mean 2^-ΔΔCt of biological replicates normalized to *Gapdh*. Error bars indicate SEM (n = 3 per group). Statistical analyses were performed on ΔCt values (target Ct – *Gapdh* Ct) using three-way ANOVA (genotype × sex × age), followed by Tukey's post hoc test for multiple comparisons. Statistical significance is indicated on the graphs (*p < 0.05; **p < 0.01; ***p < 0.001). * indicates comparisons between genotypes (*wt*, *Npc1*^{nmf164}); # indicates comparisons between sexes (male, female). **Note:** Age-related comparisons (PN11, PN30, PN60) were analyzed and reported in **Supplementary Tables 10-12**.

Consistent with Western blot findings, both male and female *Npc1*^{nmf164} mice showed a significant reduction in *Snap25* and *Shank3* expression at all developmental stages (PN11, PN30, and PN60), whereas *Nlgn3* transcripts were significantly decreased only at PN30 and PN60 compared to *wt* controls. In addition, at all-time points, sex-dependent differences were generally in the same direction across *Npc1*^{nmf164} males and females (both showing either increased or decreased values relative to *wt*) (**Figures 5C–E**). Analysis of age-related effects revealed that *Snap25* and *Shank3* mRNA levels increased from PN11 to PN30 and subsequently declined at PN60, whereas *Nlgn3* expression progressively decreased with age in both *wt* and *Npc1*^{nmf164} mice (statistical significance reported in supplementary tables 10–12).

Immunofluorescence analysis (**Figures 5A–B**) confirmed the localization of these proteins predominantly within the ML and IGL in both genotypes, indicating that despite altered expression levels, their spatial distribution within the cerebellar cortical cytoarchitecture remains preserved. Consistent with molecular data, these analyses revealed genotype-dependent differences with sex-related variations following the same overall trend in *Npc1*^{nmf164} males and females.

3.3.3 Male-biased impairment of dendritic spine maturation and pruning in cerebellar granule neurons of *Npc1*^{nmf164} mice

In several NDDs and neurodegenerative diseases, dysregulation of scaffolding proteins, receptors, and signaling molecules – similar to those observed in *Npc1* mice – is widely documented (Bourgeron, 2015). Given that GCs represent the most abundant neuronal population in the cerebellum and are likely major contributors to the observed cerebellar defects, we next investigated how alterations in synaptic protein expression affect dendritic spine dynamics within the IGL of male and female wt and *Npc1*^{nmf164} mice at different developmental stages (PN11, PN30, and PN60), using Golgi–Cox staining and morphometric analysis performed with Neurolucida software (**Figure 6A**). Previous work has demonstrated that *Npc1*^{nmf164} cerebellar GCs exhibit increased dendritic branching (Lucarelli et al., 2023), however, potential sex-related differences in the development of cerebellar dendritic structures were not explored.

Our results revealed both genotype- and sex-dependent effects on GC dendritic spine density. At PN11, female *Npc1*^{nmf164} mice exhibited a marked increase in GC spine density compared to *wt* females, whereas male mutants showed a significant reduction relative to *wt* males. Interestingly, at PN30, this pattern was reversed, with male mutants displaying higher spine density than their respective *wt* controls. Anyway, the most pronounced difference was detected at PN60, when spine number increased even more in both sexes, suggesting an impairment in physiological dendritic spine pruning during cerebellar maturation in *Npc1*^{nmf164} mice (**Figure 6B**).

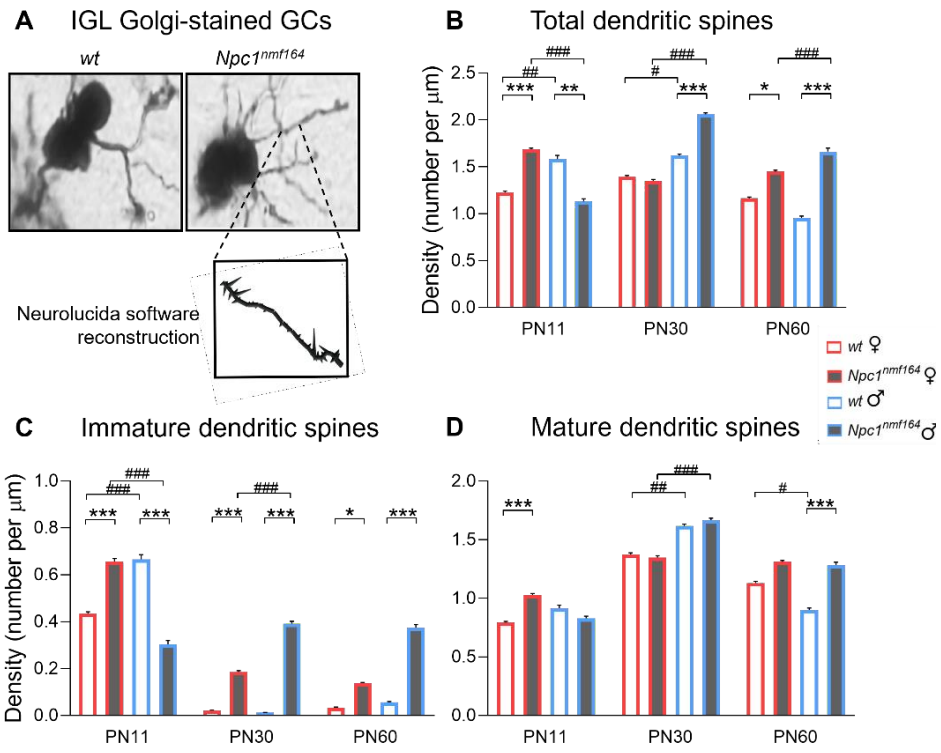

Figure 6. Analysis of GC dendritic spine density in the postnatal developing cerebellum of male and female *wt* and *Npc1*^{nmf164} mice. (**A**) Representative fields of Golgi-impregnated GCs from the IGL of *wt* (**left**) and *Npc1*^{nmf164} (**right**) cerebellar sections, and representative reconstruction of a GC dendrite with relative spines, manually generated in Nerolucida software. Quantification of (**B**) total, (**C**) immature, and (**D**) mature dendritic spine density in cerebellar GCs of male (♂ **blue contour**) and female (♀ **red contour**) *wt* (**white bars**) and *Npc1*^{nmf164} (**grey bars**) mice at PN11, PN30, and PN60. Spine density was calculated as the ratio between the number of total, immature or mature spines and the dendritic segment length. Data are presented as mean ± SEM (n = 10–25 per group). Statistical analyses were performed using three-way ANOVA (genotype × sex × age), followed by Tukey's post hoc test for multiple comparisons. Statistical significance is indicated on the graphs (*p < 0.05; **p < 0.01; ***p < 0.001). * indicates comparisons between genotypes (*wt*, *Npc1*^{nmf164}); # indicates comparisons between sexes (male, female). **Note:** Age-related comparisons (PN11, PN30, PN60) were analyzed and reported in **Supplementary Tables 13–15.**

Synaptic pruning is a critical developmental process that coordinates the stabilization and functional maturation of retained synapses during adolescence (Globus et al., 1973; Feldman and Dowd, 1975). To determine whether the observed alterations in spine density reflect changes in synapse maturation, we performed a detailed morphological classification of dendritic spines into immature (**Figure 6C**) and mature (**Figure 6D**) types, following established criteria (Peters and Kaiserman-Abramof, 1970). Immature spines included filopodia and thin spines – long protrusions without bulbous heads, and small heads connected to the dendrite by narrow necks, respectively. These highly dynamic structures are prevalent during early development, and normally decrease in adulthood (Ziv and Smith, 1996; Tønnesen et al., 2014). In contrast, mature spines comprised stubby and mushroom-shaped spines, which are more stable, functionally integrated, and characterized by larger PSD regions and reduced motility (Grutzendler et al., 2002; Holtmaat et al., 2005; Smitha and Roopa, 2012).

This morphological analysis revealed sex- and age-dependent alterations in GC spine maturation in *Npc1*^{nmf164} mice. At PN11, female mutants exhibited a persistent increase in immature

spine density compared to *wt* females, while male mutants showed a significant reduction relative to *wt* males. By PN30, both male and female *Npc1*^{nmf164} mice displayed a marked increase in immature spine density relative to their sex-matched controls, which persisted until PN60 in both sexes (**Figure 6C**). Regarding GCs mature spines, female mutants displayed an elevated number already at PN11, while males showed no significant difference from *wt*. At PN30, instead, both male and female *Npc1*^{nmf164} revealed mature spine density comparable to *wt* controls, and by PN60 only male mutants exhibited a significant increase in mature spine number, indicating a delay in synapse maturation (**Figure 6D**). Overall, these results indicate that dendritic spine maturation and pruning are disrupted in *Npc1*^{nmf164} mice in a sex- and age-dependent manner.

Under physiological conditions, dendritic spine morphology is highly dynamic and undergoes continuous remodeling throughout development (Tønnesen et al., 2014). To further dissect the nature of synapse alterations, we performed a detailed classification of individual spine subtypes within the immature (**Figure 7**) and mature (**Figure 8**) categories.

At PN11, male *Npc1*^{nmf164} GCs displayed a significant reduction in filopodia, and long thin spines compared to *wt* controls. This pattern was reversed at PN30 and PN60, when a significant increase in all three immature spine subtypes was observed. In contrast, female *Npc1*^{nmf164} GCs showed a significant increase in long thin spines at PN11 and PN30, with no significant changes in filopodia or thin spine density compared to *wt* controls. Accordingly, sex comparisons revealed significant differences in the density of all immature spine subtypes in *Npc1*^{nmf164} mice at both early and adult stages (**Figures 7A–C**).

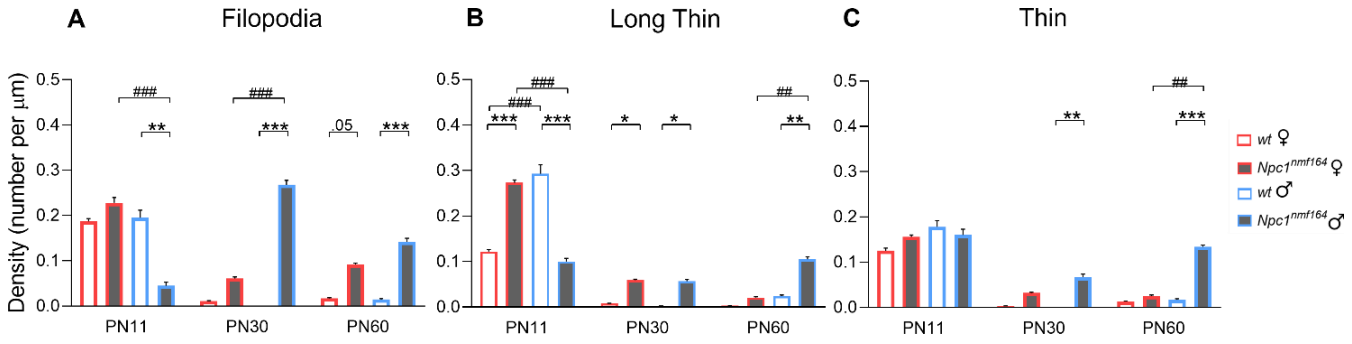

Figure 7. Characterization of key differences across GC immature dendritic spine types in the postnatal developing cerebellum of male and female *wt* and *Npc1*^{nmf16} mice. Quantification of (**A**) filopodia, (**B**) long thin, and (**C**) thin spine density in cerebellar GCs of male (♂ **blue contour**) and female (♀ **red contour**) *wt* (**white bars**) and *Npc1*^{nmf164} (**grey bars**) mice at PN11, PN30, and PN60. Spine density was calculated as the ratio between the number of filopodia, long thin or thin spines and the dendritic segment length. Data are presented as mean ± SEM (n = 10–25 per group). Statistical analyses were performed using a three-way ANOVA (genotype × sex × age), followed by Tukey's post hoc test for multiple comparisons. Statistical significance is indicated on the graphs (*p < 0.05; **p < 0.01; ***p < 0.001). * indicates comparisons between genotypes (*wt*, *Npc1*^{nmf164}); # indicates comparisons between sexes (male, female). **Note:** Age-related comparisons (PN11, PN30, PN60) were analyzed and reported in **Supplementary Tables 16–18.**

Regarding mature spine types, female *Npc1*^{nmf164} GCs exhibited an early increase in stubby spines at PN11, followed by a significant reduction in mushroom spine density at PN30, which

recovered by PN60, when a marked increase was detected relative to *wt*. A similar, though delayed, increase in stubby and mushroom spines was also observed in male mutants at PN60 compared to male *wt* (**Figures 8A–B**). These findings further support the presence of impaired synaptic maturation in *Npc1*^{nmf164} mice, particularly in males, consistent with the alterations previously observed in synaptic protein expression and spine subtype distribution.

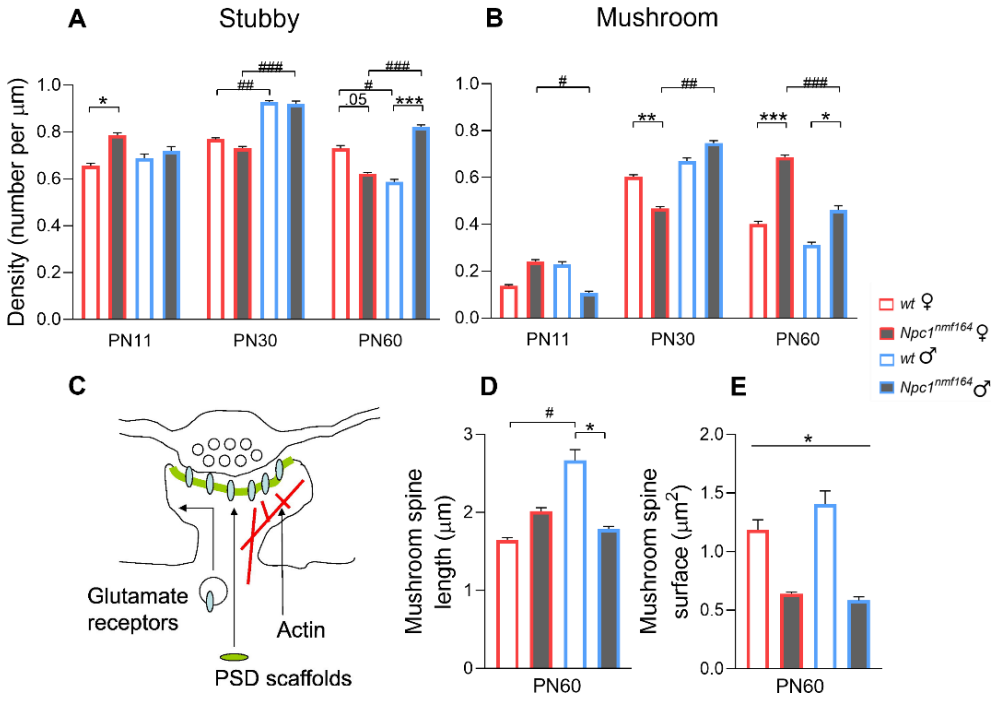

Figure 8. Characterization of key differences across GC mature dendritic spine types in the postnatal developing cerebellum of male and female *wt* and *Npc1*^{nmf16} mice. Quantification of (**A**) stubby and (**B**) mushroom spine density in cerebellar GCs of male (♂ **blue contour**) and female (♀ **red contour**) *wt* (**white bars**) and *Npc1*^{nmf164} (**grey bars**) mice at PN11, PN30, and PN60. Spine density was calculated as the ratio between the number of stubby or mushroom spines and the dendritic segment length. Data are presented as mean ± SEM (n = 10–25 per group). Statistical analyses were performed using a three-way ANOVA (genotype × sex × age), followed by Tukey's post hoc test for multiple comparisons. Statistical significance is indicated on the graphs (*p < 0.05; **p < 0.01; ***p < 0.001). * indicates comparisons between genotypes (*wt*, *Npc1*^{nmf164}); # indicates comparisons between sexes (male, female). **Note:** Age-related comparisons (PN11, PN30, PN60) were analyzed and reported in **Supplementary Tables 19 – 20.** (**C**) Schematic representation of a mature, functional mushroom spine with a wide head and an enriched PSD region. Quantification of (**D**) mushroom spines length and (**E**) surface in male (♂ **blue contour**) and female (♀ **red contour**) *wt* (**white bars**) and *Npc1*^{nmf164} (**grey bars**) GCs at PN60. Data were analyzed by two-way ANOVA (genotype × sex), followed by Tukey's post hoc test for multiple comparisons. Statistical significance is indicated as above.

Given that dendritic spine morphology is closely associated with synaptic strength, stability, and functional maturity, with larger mushroom-shaped spines representing stable and highly active excitatory synapses (Matsuzaki et al., 2004; Bourne and Harris, 2008), we next analyzed morphological parameters of mature spines. Quantitative analysis revealed that mushroom spines in male and female *Npc1*^{nmf164} GCs displayed a significantly reduced surface area compared to *wt* controls, indicating smaller and potentially less stable synaptic contacts, consistent with decreased synaptic scaffold protein levels. Moreover, male *Npc1*^{nmf164} mice also displayed significantly shorter

dendritic spine relative to *wt* males, while no differences were detected between females, suggesting a more pronounced impairment in spine structural maturation in male mutants (**Figures 8C–E**).

Finally, given the extensive synaptic remodeling that occurs during adolescence, largely driven by synapse elimination and refinement (Grutzendler et al., 2002; Zhou et al., 2017), we next quantified the proportion of mature and immature spines relative to the total spine number for each group (**Figure 9**). Consistent with previous analysis, both male and female *Npc1*^{nmf164} mice displayed a persistently higher proportion of immature spines across development compared to controls. Notably, this phenotype was markedly stronger in males, particularly at PN30 and PN60, when adult *wt* animals exhibited almost exclusively mature spines, underscoring a pronounced disruption of synaptic maturation and pruning in the NPC1 cerebellum.

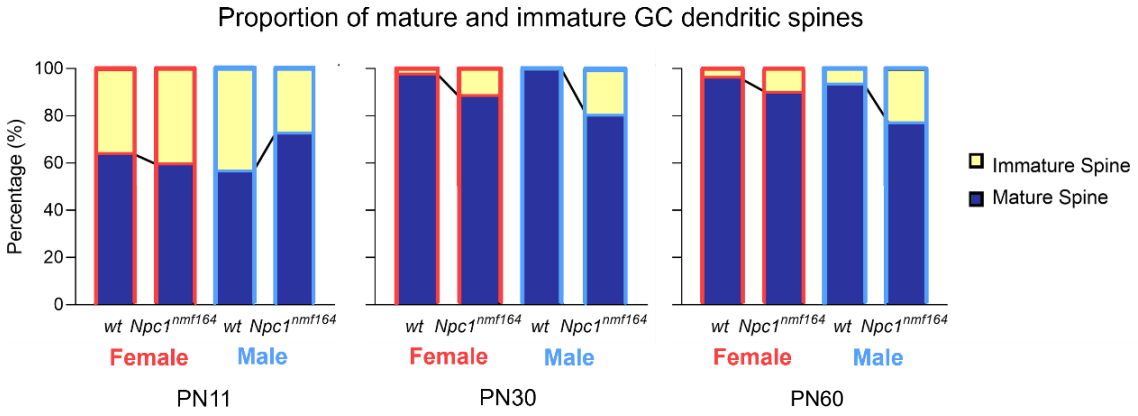

Figure 9. Summary graph of developmental changes in GC dendritic spine composition in *wt* and *Npc1*^{nmf164} cerebella. The proportion (%) of mature and immature dendritic spines in cerebellar GCs from male (♂ **blue contour**) and female (♀ **red contour**) *wt* and *Npc1*^{nmf164} mice at PN11, PN30, and PN60, was calculated over the total number of spines within each experimental group (mean number of mature or immature spines / mean total spine number × 100). The graph visually illustrates the developmental shift from immature to mature spines observed in *wt* mice, contrasted with the persistence of a higher proportion of immature spines in *Npc1*^{nmf164} animals at all ages, indicative of delayed synaptic maturation.

3.3.4 High levels of glutamine underscore potential excitatory–inhibitory imbalance preceding cerebellar neurodegeneration in male and female *Npc1*^{nmf164} mice

In line with previous molecular findings showing a downregulation of key excitatory synaptic scaffolding proteins, such as Shank3 and PSD95, in the *Npc1*^{nmf164} cerebellum, and with morphological evidence of increased dendritic spine density – particularly of immature forms – in GCs of the IGL, potentially contributing to defective synaptic maturation and connectivity we next investigated whether these structural abnormalities at excitatory synapses were associated with neurochemical alterations in the cerebellar excitatory–inhibitory balance (**Figures 10 and 11**).

To this purpose, we initially aimed to quantify the levels of the main inhibitory and excitatory neurotransmitters, GABA and glutamate, in the cerebellum of male and female *wt* and *Npc1*^{nmf164} mice at PN30 – a stage characterized by completed GC differentiation and integration within

cerebellar circuitry, but preceding overt PC degeneration in *Npc1*^{nmf164} (Maue et al., 2012). However, due to the intrinsic instability and rapid degradation of glutamate – a highly reactive excitatory amino acid with neurotoxic potential (Greenamyre and Porter, 1994; Hugon et al., 1996; Al-Nasser et al., 2022) – its direct quantification by HPLC is technically challenging. Therefore, to obtain an indirect yet reliable index of glutamatergic transmission, we measured cerebellar levels of glutamine, which represents both the metabolic precursor and recycling product of glutamate within the glutamate–glutamine cycle (Andersen and Schousboe, 2023; Andersen, 2025).

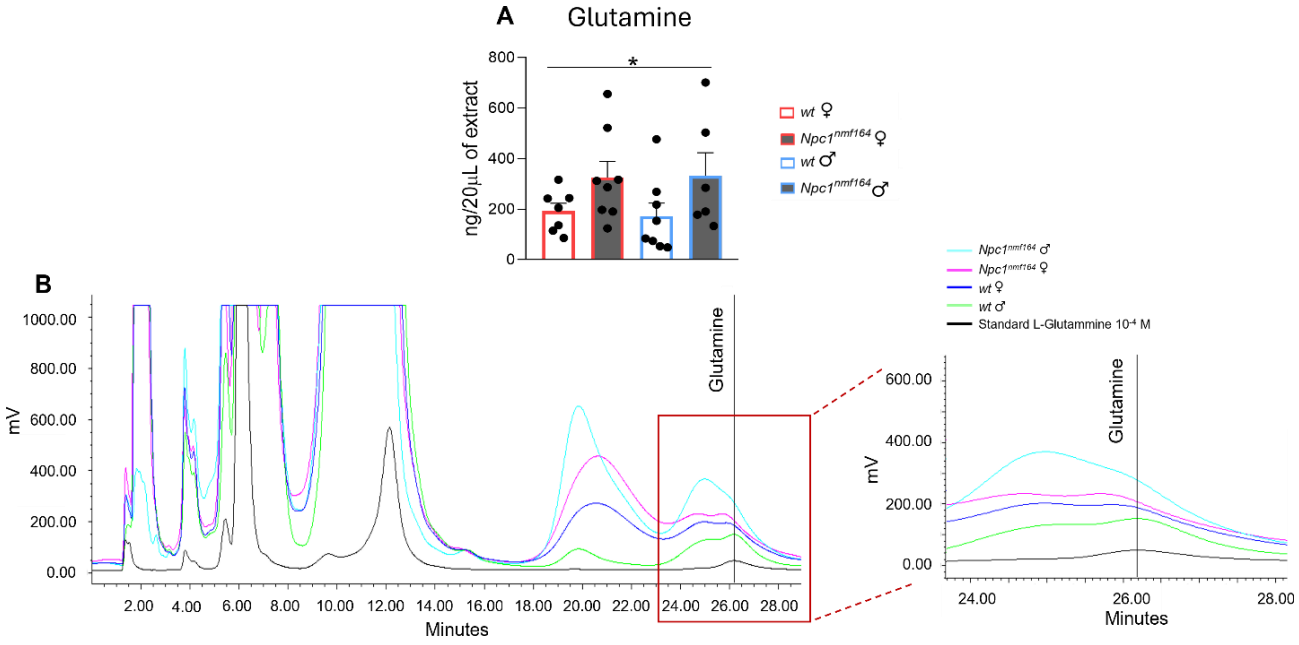

Figure 10. Analysis of glutamine cerebellar levels in male and female *wt* and *Npc1*^{nmf164} mice at PN30. (**A**) Quantification of glutamine levels in the cerebellum of male (♂ **blue contour**) and female (♀ **red contour**) *wt* (**white bars**) and *Npc1*^{nmf164} (**grey bars**) mice. Data are reported as total amount (ng/20 µL of extract) normalized to the respective pellet weight (mean ± SEM). Each point of the scatter plot represents a biological replicate (n ≥ 7 per group). Statistical analyses were performed peak heights normalized to the respective standard (10^{-4} M), using two-way ANOVA (genotype × sex) followed by post hoc *t*-test. Statistical significance is indicated on the graph (*p < 0.05). * indicates a genotype effect (*wt*, *Npc1*^{nmf164}). **Note:** no sex effect (male, female) was detected. (**B**) Representative chromatogram showing the glutamine peaks in male and female *wt* and *Npc1*^{nmf164} mice compared with the respective standard.

HPLC analysis revealed a significant genotype effect on glutamine content, with *Npc1*^{nmf164} mice displaying markedly higher glutamine levels compared to *wt* controls, regardless of sex, at PN30 (**Figure 10A**). Conversely, at the same time point, GABA levels showed a significant sex effect, with female mice exhibiting higher GABA content than males, independently of genotype (**Figure 11A**). This observation is consistent with previous evidence of sex-related differences in cerebellar GABAergic transmission, whereby females generally display an earlier maturation of GABAergic synapses and an earlier shift from depolarizing to hyperpolarizing GABA responses, compared to males (Galanopoulou, 2005; Galanopoulou, 2008; Mercer et al., 2016).

Overall, our results point to an early disruption of glutamate–glutamine metabolism, reflecting increased excitatory drive and a possible shift in the excitatory–inhibitory balance toward excitation, consistent with the higher density of dendritic spines in the *Npc1*^{nmf164} cerebellum.

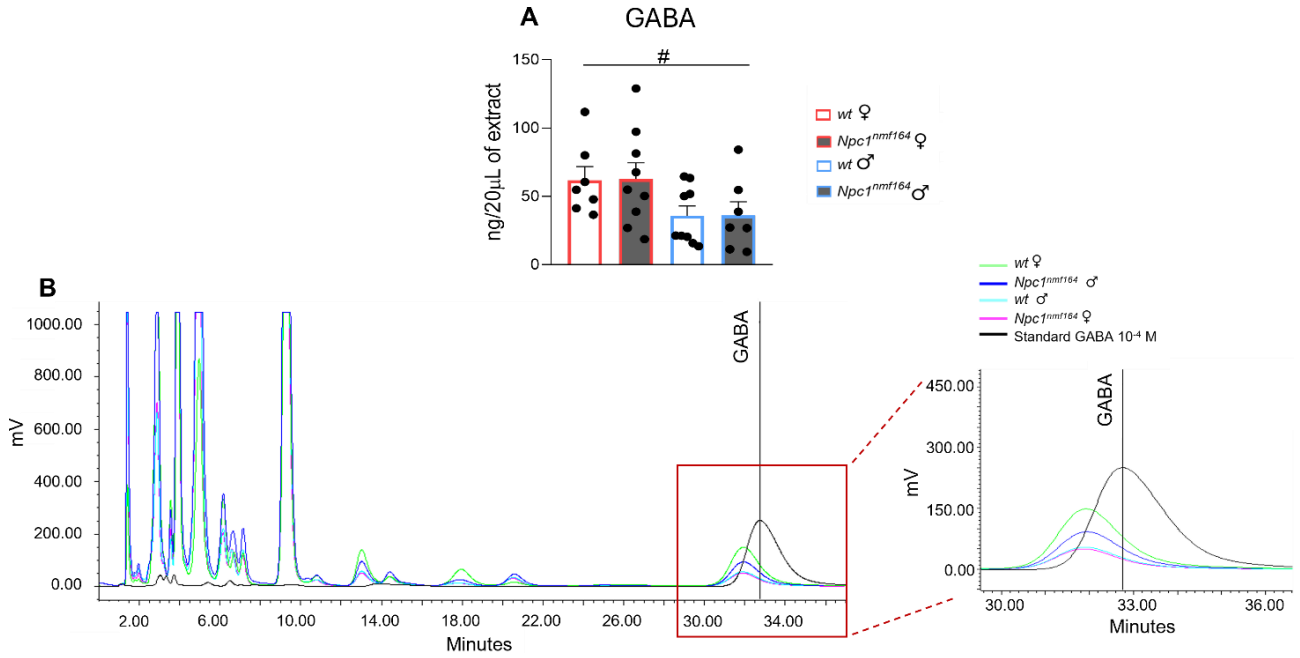

Figure 11. Analysis of GABA cerebellar levels in male and female *wt* and *Npc1*^{nmf164} mice at PN30. (**A**) Quantification of GABA levels in the cerebellum of male (♂ **blue contour**) and female (♀ **red contour**) *wt* (**white bars**) and *Npc1*^{nmf164} (**grey bars**) mice. Data are reported as total amount (ng/20 µL of extract) normalized to the respective pellet weight (mean ± SEM). Each point of the scatter plot represents a biological replicate (n ≥ 7 per group). Statistical analyses were performed on peak heights normalized to the respective standard (10^{-4} M), using two-way ANOVA (genotype × sex) followed by post hoc *t*-test. Statistical significance is indicated on the graph (# $p < 0.05$). # indicates a sex effect (male, female). **Note:** no genotype effect (*wt*, *Npc1*^{nmf164}) was detected. (**B**) Representative chromatogram showing the GABA peaks in male and female *wt* and *Npc1*^{nmf164} mice compared with the respective standard.

3.3.5 iDISCO+ volumetric analysis reveals early internal granule layer impairments in *Npc1*^{nmf164} mice

Previous studies in Npc1$^{-/-}$ mouse models have reported marked cerebellar hypoplasia and a reduction in total cerebellar volume (Nusca et al., 2014; Caporali et al., 2016; Totenhagen et al., 2017; Fiorenza et al., 2022). In the *Npc1*^{nmf164} variant, morphological abnormalities have mainly been described in terms of impaired GC proliferation, PC degeneration, altered glial differentiation, and microglial dysfunction (Maue et al., 2012; Caporali et al., 2016; Kavetsky et al., 2019; Fiorenza et al., 2022). In this study, we specifically focus on the IGL to assess whether the global volumetric reduction is associated with layer-specific and sex-dependent differences across cerebellar regions (vermis and hemispheres). To this aim, we employed an advanced tissue clearing technology, which allows three-dimensional volumetric quantification without the need for sectioning, providing a more accurate and artifact-free analysis of male and female *wt* and *Npc1*^{nmf164} mice at PN15 – a

developmental stage preceding overt PC loss – aiming to detect early structural alterations independent of neurodegeneration.

Using iDISCO-cleared cerebella, we quantified the IGL volume across lobular compartments by segmenting the cerebellar cortex into vermis and hemisphere and grouping individual lobules into functional domains based on established criteria (Ren et al., 2019; Alahmadi, 2023; Kong et al., 2024), enabling us to investigate potential genotype- and sex-dependent differences in IGL development and organization (**Figure12**).

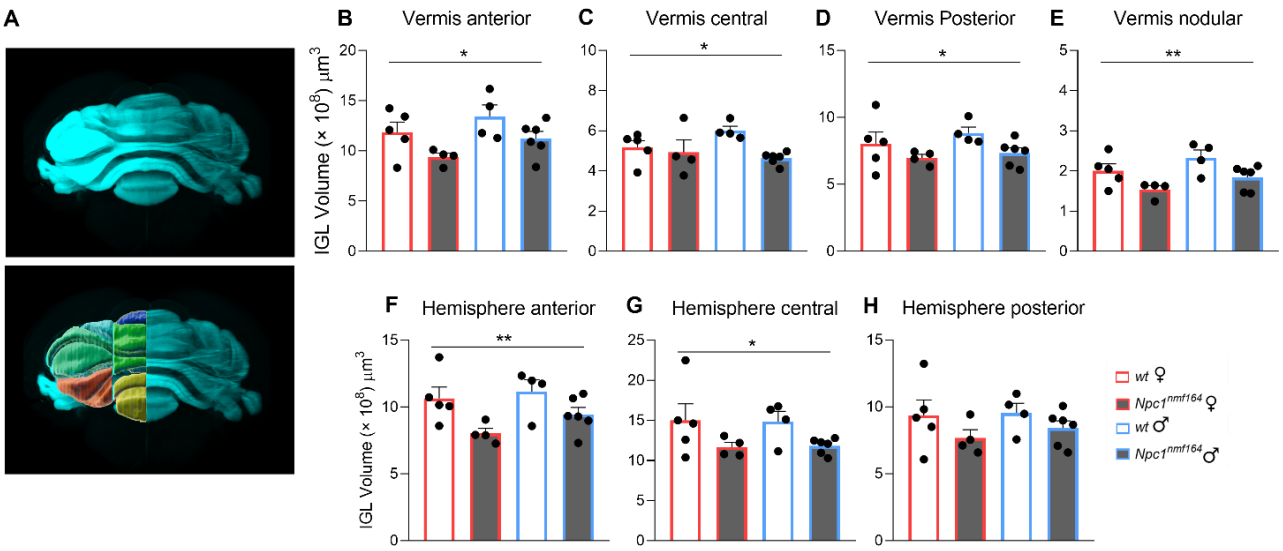

Figure 12. Analysis of IGL volume in male and female *wt* and *Npc1*^{nmf164} mice at PN15. (**A**) Representative 3D reconstructions of cerebellar lobules manually generated in *Imaris* software. Quantification of the absolute IGL volume in the vermis (**B**) anterior (lobules I–V), (**C**) central (lobules VI–VII), (**D**) posterior (lobules VIII–IX), and (**E**) nodular (lobule X); and in the hemisphere (**F**) anterior (lobus simplex), (**G**) central (lobules crus I–II), and (**H**) posterior (lobules paramedian and copula pyramidis) of male (♂ **blue contour**) and female (♀ **red contour**) *wt* (**white bars**) and *Npc1*^{nmf164} (**grey bars**) mice. Data are expressed as mean ± SEM absolute volume (µm³) (n ≥ 4 per group). Statistical analysis was performed using two-way ANOVA (genotype × sex), followed by post hoc *t*-tests. Statistical significance is indicated on the graphs (*p < 0.05; **p < 0.01) * indicates a genotype effect (*wt*, *Npc1*^{nmf164}). **Note:** no sex-related effect (male, female) was detected.

Our analysis detected a significant genotype effect in all vermal lobules, including the anterior (I–V), central (VI–VII), posterior (VIII–IX), and nodular (X) regions, with a consistent reduction in IGL volume in *Npc1*^{nmf164} mice compared to *wt* littermates, independent of sex (**Figures 12B–E**). In parallel, a comparable genotype-dependent reduction was observed in the anterior (lobulus simplex) and central lobules (crus I–II) of the hemispheric cortex, whereas posterior lobules (paramedian and copula pyramidis) did not show significant differences nor between genotypes or sexes (**Figures 12F–H**). These results indicate that Npc1 deficiency leads to an early and regionally selective reduction in IGL volume, particularly affecting the vermis and the anterior–central lobules of the hemispheres at PN15.

To better quantify the extent of these volumetric alterations and evaluate possible sex-related differences in the degree of IGL reduction, we next calculated the relative ΔVolume (expressed as percentage change from *wt* mean) for each functional lobular group, allowing for a direct comparison

of the magnitude of volume loss across cerebellar regions and between male and female *Npc1*^{nmf164} mice, providing a finer resolution of genotype- and sex-dependent patterns (**Figure 13**).

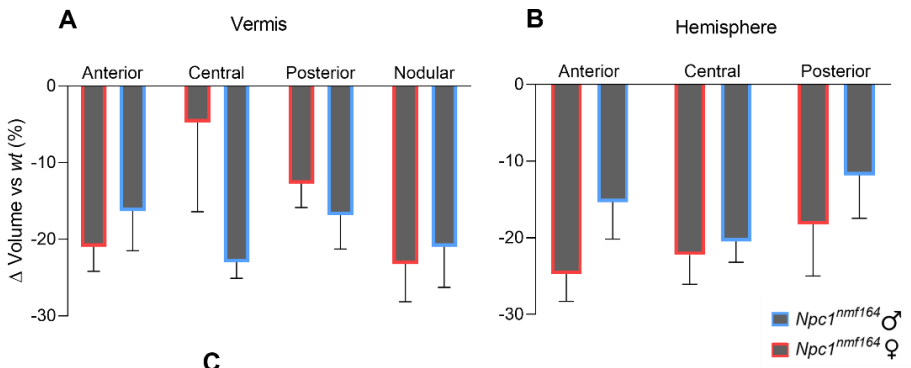

C

Lobule	% Reduction Females	% Reduction Males
Vermis Anterior	20,7	16,2
Vermis Central	4,6	22,9
Vermis Posterior	12,9	16,9
Vermis Nodular	23,3	21,0
Hemisphere Anterior	24,6	15,5
Hemisphere Central	22,2	20,4
Hemisphere Posterior	18,1	11,7

Figure 13. Analysis of sex-related and region-specific differences in IGL Volume of *Npc1*^{nmf164} mice at PN15. (**A–B**) Bars represent the normalized difference in IGL volume, calculated as Δ volume = (V *Npc1*/ V *wt*) − 1, and expressed as percentage change relative to *wt*. Male (♂ **blue contour**) and female (♀ **red contour**) *Npc1*^{nmf164} are shown as **grey bars** across cerebellar lobular groups. Data are expressed as mean ± SEM Δ volume (n ≥ 4 per group). Statistical analysis was performed using repeated-measures ANOVA with between-subjects factor sex (male, female) and within-subjects factor lobule group (anterior, central, posterior, nodular), followed by post hoc *t*-tests. **Note:** no significant effects of sex or lobule group were detected. (**C**) Heatmap summarizing the mean percentage reduction in IGL volume in male and female *Npc1*^{nmf164} mice relative to *wt* for each lobular group. The color scale represents the magnitude of volume loss (% volume reduction vs *wt*): **beige** = very mild reduction (< 10%), **light yellow** = mild reduction (10– 20%), **orange** = moderate (>20%).

Analysis of the ΔVolume confirmed that there were no significant differences between male and female *Npc1*^{nmf164} mice for any of the lobular groups, consistent with previous results on absolute volumes. Furthermore, comparisons across lobuli revealed no significant differences in the percentage of volume reduction, indicating the lack of a spatial gradient of IGL loss.

Overall, these findings confirm the previously reported reductions in cerebellar lobule size in *Npc1* mice, observed using other methodologies (Nusca et al., 2014; Totenhagen et al., 2017), demonstrating that Npc1 deficiency leads to a global reduction of IGL volume in the developing cerebellum. Specifically, through this detailed volumetric analysis that minimizes potential artifacts associated with histological sectioning, we revealed that these volumetric reductions occur homogeneously across the cerebellum in a sex-independent manner, investigating for the first time the absence of a gender-specific effect at this developmental stage.

3.3.6 Only male *Npc1*^{nmf164} mice display social behavior deficits before neurodegeneration and motor symptoms

The convergence of multiple developmental abnormalities observed in the cerebellum of *Npc1*^{nmf164} mice led us to hypothesize that such early alterations may persistently affect cerebellar

output and, consequently, higher-order brain functions. Considering the well-established contribution of the cerebellum to cognitive and socio-affective processes (Stoodley and Schmahmann, 2010; Van Overwalle et al., 2020) and based on our previous volumetric evidence showing a significant reduction of the IGL in anterior and central lobular groups known to sustain these functions, we aimed to determine whether such region-specific structural alterations were accompanied by functional impairments in cerebellar-dependent social behaviors. To this aim, we assessed both early social communication and mature social interaction by performing behavioral tests commonly used to evaluate social functioning, namely USVs and the SIT (**Figures 14–15**).

USVs emitted by pups upon separation from their mother and littermates are widely recognized as an index of early social motivation (Sewell, 1970; Ehret, 2005) and represent a valuable tool for detecting communication deficits in preclinical models (Wöhr and Scattoni, 2013a). USV emission rates typically follow a strain-specific developmental trajectory, peaking during the first postnatal week and progressively declining thereafter (Elwood and Keeling, 1982). Deviations from this trajectory are commonly regarded as indicators of early neurodevelopmental disturbances (Caruso et al., 2020). To assess potential alterations in early social communication, we recorded USVs at PN8, a developmental stage corresponding to the expected peak of emission. Although the total number of emitted calls did not significantly differ between *Npc1*^{nmf164} and *wt* pups (**Figure 14A**), analysis of acoustic parameters revealed a significant genotype-dependent reduction in mean peak amplitude in *Npc1*^{nmf164} mice compared to *wt*, regardless of sex (**Figure 14C**). In addition, our analysis highlighted a significant sex effect, with female pups of both genotypes displaying higher mean peak amplitude than males. Conversely, no significant differences were detected in mean peak frequency across groups (**Figure 14B**).

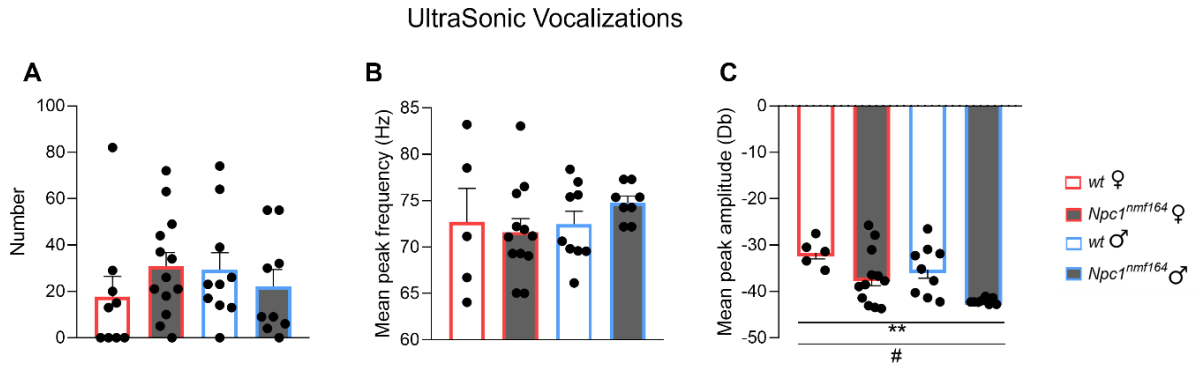

Figure 14. Analysis of early social communication in male and female *wt* and *Npc1*^{nmf164} mice at PN8. Quantification of (**A**) USVs number, (**B**) mean peak frequency, and (**C**) mean peak amplitude in male (♂ **blue contour**) and female (♀ **red contour**) *wt* (**white bars**) and *Npc1*^{nmf164} (**grey bars**) mice. Data are shown as mean ± SEM (n ≥ 9 per group). Statistical analysis was performed using two-way ANOVA (genotype × sex), followed by Tukey's post hoc test for multiple comparisons. Statistical significance is indicated on the graphs (*p < 0.05; **p < 0.01). * indicates a genotype effect (*wt*, *Npc1*^{nmf164}); # indicates a sex effect (male, female).

To evaluate social preference in young adult mice, the SIT was performed in male and female *wt* and *Npc1*^{nmf164} mice at PN30. This behavioral paradigm assesses social motivation based on the

spontaneous preference of the animals to explore the different compartments of a three-chambered apparatus across two trials – habituation and sociability, the latter including the presence of an age- and sex-matched conspecific (Moy et al., 2004; Kaidanovich-Beilin et al., 2011) (**Figure 15**).

Given the well-established cerebellar involvement and consequent motor deficits associated with NPC1 disease, we first assessed whether the *Npc1* mutation could affect motor performance and potentially confound the interpretation of behavioral outcomes. To this end, we analyzed both mean velocity and total distance traveled by tested mice during the habituation trial, as an internal control. Despite the absence of overt PC loss or cerebellar ataxia at this developmental stage (Maue et al., 2012; Caporali et al., 2016), *Npc1*^{nmf164} mice displayed a significant reduction in both parameters compared to *wt* controls, regardless of sex (**Figures 15A–B**). Nevertheless, all groups explored the two empty lateral chambers equally (**Figure 15C**), indicating no intrinsic side preference or motor bias.

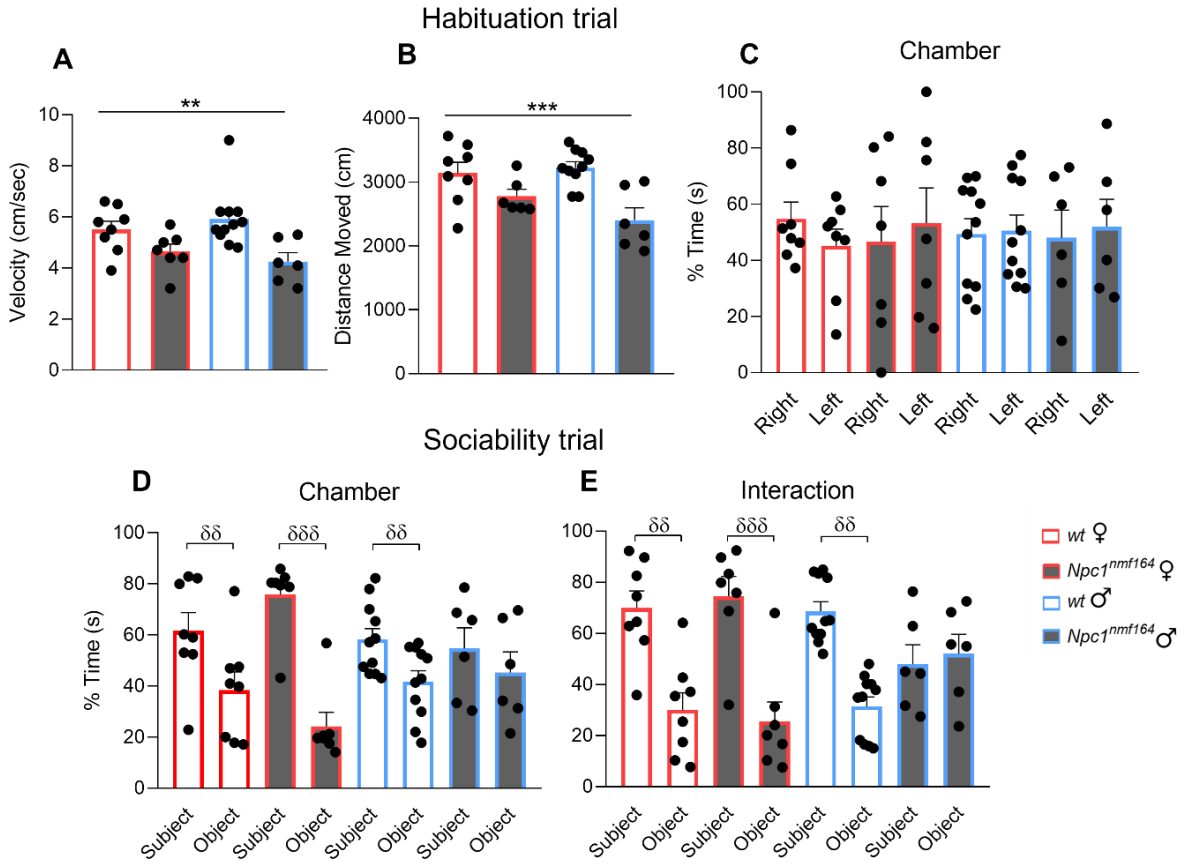

Figure 15. Analysis of social preference behavior in male and female *wt* and *Npc1*^{nmf164} mice at PN30. Quantification of (**A**) mean velocity and (**B**) total distance traveled by male (♂ **blue contour**) and female (♀ **red contour**) *wt* (**white bars**) and *Npc1*^{nmf164} (**grey bars**) mice during the habituation trial. Data are presented as mean ± SEM (n ≥ 6 per group). Statistical analysis was performed using two-way ANOVA (genotype × sex), followed by Tukey's post hoc test for multiple comparisons. Statistical significance is indicated on the graphs (**p < 0.01; ***p < 0.001). * indicates a genotype effect (*wt*, *Npc1*^{nmf164}). **Note:** no sex effect (male, female) was detected. (**C–E**) Quantification of time spent in each lateral chamber of the apparatus and time spent sniffing the age- and sex-matched conspecific by male and female *wt* and *Npc1*^{nmf164} mice (**color-coded as above**) during both habituation and sociability trials. Data are presented as mean ± SEM (n ≥ 6 per group). Statistical analysis was performed using repeated-measures two-way ANOVA with between-subjects factors genotype (*wt*, *Npc1*^{nmf164}) and sex (male, female), and within-subjects factor chamber (subject, object). Statistical significance is indicated as above. δ indicates a within effect (subject, object).

In the subsequent sociability trial, we quantified both the time spent in each lateral chamber and the time spent engaging in direct interaction with the social stimulus (expressed as percentage %). Statistical analysis revealed that both male and female *wt* mice spent more time in the chamber containing the conspecific and showed greater interaction with it compared to the inanimate object contained in the other chamber, indicating a clear preference for social contact (**Figures 15D–E**). Similarly, female *Npc1*^{nmf164} mice displayed a comparable sociability profile, suggesting preserved social motivation. In contrast, male *Npc1*^{nmf164} mice failed to show any significant preference for the social stimulus over the object, pointing to a sex-specific deficit in social motivation or recognition.

3.3.7 Passive coping behavior is not observed in adult *Npc1*^{nmf164} mice

To determine whether the behavioral alterations observed in *Npc1*^{nmf164} males were specifically associated with the social domain or extended to other functional dimensions, we assessed coping strategies by performing the TST at the same developmental stage of the SIT (PN30). The TST relies on the assumption that mice will actively attempt to escape an aversive and stressful situation (Cryan et al., 2005). Therefore, deviations from this behavior – such as prolonged immobility or freezing – are commonly interpreted as indicators of passive coping or depressive-like behavior (Castagné et al., 2011). Interestingly, our analysis revealed no significant differences in total immobility time between groups, highlighting the absence of altered coping strategies in *Npc1*^{nmf164} mice (**Figure 16**).

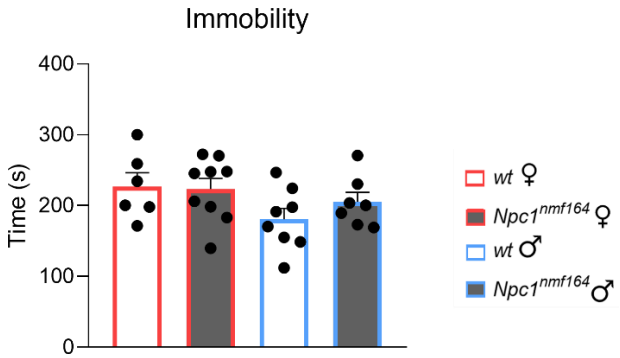

Figure 16. Analysis of coping behavior in male and female *wt* and *Npc1*^{nmf164} mice at PN30. Quantification of total time spent immobile by male (♂ **blue contour**) and female (♀ **red contour**) *wt* (**white bars**) and *Npc1*^{nmf164} (**grey bars**) mice. Data are presented as mean ± SEM (n ≥ 6 per group). Statistical analysis was performed using two-way ANOVA (genotype × sex). **Note:** no significant differences between groups were detected.

Discussion

This study provides compelling evidence that *Npc1* deficiency profoundly affects cerebellar postnatal development by disrupting neurotrophic signaling, impairing synaptic maturation of GCs, and altering global glutamate metabolism, ultimately impacting social behavior in a sex- and age-dependent manner.

Specifically, the results presented here confirm and expand upon our previous findings, which first demonstrated defective BDNF reception and responsiveness, associated with TrkB receptor subcellular mislocalization and altered polarization, leading to impaired GCs migration toward the IGL in *Npc1*^{nmf164} mice during early postnatal life (Lucarelli et al., 2023). The aim of this thesis was to extend the analysis to later stages of cerebellar maturation and to include sex-related differences, which had never been investigated before.

By combining molecular, morphological, and functional approaches, we found:

(i) Persistent disruption of BDNF–TrkB signaling, with downstream mTOR/PTEN dysregulation.

(ii) Downregulation of key synaptic proteins (Snap25, PSD95, Shank3, Nlgn3).

(iii) Impaired GC differentiation and connectivity, with excess immature dendritic spines, particularly in males.

(iv) Increased cerebellar glutamine levels, indicating altered glutamate–glutamine turnover.

(v) Early and uniform reduction of IGL volume, cerebellar hypoplasia.

(vi) Abnormal social behavior, emerging selectively in adult males.

Alteration of BDNF–TrkB signaling in *Npc1*^{nmf164} mice is sexually and developmentally regulated

During prenatal and early postnatal cerebellar development, Shh is expressed by PCs to drive GC precursor proliferation within the EGL through its mitogenic and morphogenetic actions (Wechsler-Reya and Scott, 1999; Lewis et al., 2004). However, our previous studies reported that the generation and reception of the Shh signal at the primary cilium are negatively affected by Npc1 loss of function (Canterini et al., 2017), thereby impairing GC proliferation and cerebellar morphogenesis (Nusca et al., 2014; Caporali et al., 2016; Dragotto et al., 2019; Lucarelli et al., 2023). Beyond its key role in cerebellar foliation and patterning, Shh signaling has been shown to regulate BDNF secretion and activation through post-transcriptional mechanisms (Bond et al., 2013; Delmotte et al., 2020). BDNF, in turn, enhances cerebellar GC precursor maturation, acting as a chemoattractant cue to guide GC migration toward the IGL through a concentration gradient (Borghesani et al., 2002; Camuso et al., 2022).

Therefore, building on previous evidence of altered crosstalk between cholesterol metabolism and BDNF–TrkB signaling in *Npc1*^{nmf164} mice —affecting GC migration and cerebellar maturation (Lucarelli et al., 2023)—we employed qRT-PCR to determine whether the previously observed reductions in BDNF signaling expression were sex-dependent.

Our analysis confirmed an early and persistent (PN11, PN30 and PN60) reduction in BDNF transcripts, in both male and female *Npc1*^{nmf164} mice compared to *wt*. In addition, despite low BDNF levels, mutant mice also displayed a downregulation of TrkB expression at PN11. Interestingly, sex-related differences emerged over development, with female *Npc1*^{nmf164} mice partially recovering TrkB expression by PN30 and PN60, whereas the reduction persisted in males. These results are particularly relevant when compared with our previous characterization of phosphorylated TrkB content in *Npc1* mutants, which revealed reduced receptor levels only during early cerebellar development but not at later stages (Lucarelli et al., 2023). Therefore, it is conceivable that this apparent developmental regulation of TrkB expression previously reported may reflect the averaging of sex-related opposite trends observed here, thereby normalization of TrkB levels is likely driven by female-specific recovery, while male mutants maintain a persistent deficit.

We believe that this sex-dependent pattern may be attributed to estrogen-mediated modulation of neurotrophic signaling (Solum and Handa, 2002; Scharfman and MacLusky, 2005; Sohrabji and Lewis, 2006; de Assis et al., 2025). Indeed, estrogens are known to enhance BDNF and/or TrkB levels in various brain regions (Miranda et al., 1994; Singh et al., 1995; Wang et al., 2016; Gross et al., 2021; Chanana et al., 2024), suggesting hormone-driven compensatory mechanisms contributing to this partial TrkB restoration in female mutants, and providing a further explanation for the overall failure of male *Npc1*^{nmf164} mice to compensate for BDNF reduction via upregulation of its receptor.

Moreover, given the well-established role of the mTOR pathway as a downstream effector of the PI3K–Akt axis (Jozwiak et al., 2005), we also quantified mRNA levels of *mTOR* and its negative regulator *PTEN* across postnatal cerebellar development in *Npc1* mice. Despite the sexually divergent expression of *TrkB*, both male and female *Npc1*^{nmf164} mice exhibited persistent (PN11, PN30 and PN60) downregulation of *PTEN* and, as expected under such conditions, upregulation of *mTOR* compared to *wt* controls.

While reduction of BDNF and TrkB signaling would classically predict decreased activity of downstream mTOR pathway (Takei et al., 2004; Slipczuk et al., 2009; Yoshii and Constantine-Paton, 2010; Sanchez-Bezanilla et al., 2022), concomitant decreased PTEN levels lead to mTOR upregulation by removing its inhibitory brake (Shi et al., 2011; Guan et al., 2021; Dhaliwal et al., 2024). This pattern is present in both sexes, but with important differences: while males exhibit a persistent reduction of TrkB, females show a partial recovery at later stages (PN30–PN60).

Collectively, these findings indicate that the early neurotrophic deficit in the *Npc1*^{nmf164} cerebellum follows a sex- and age-dependent trajectory and is associated with a compensatory upregulation of the mTOR pathway, which over time may become maladaptive, promoting dysregulated synaptogenesis, dendritic spine overgrowth, and excitatory–inhibitory imbalance (Bowling and Klann, 2014; LaSarge and Danzer, 2014; Winden et al., 2018; Thomas et al., 2023; Cullen et al., 2024), widely implicated in the pathogenesis of several NDDS.

Nonetheless, it should be noted that our results are based on mRNA expression analyses, and future studies assessing protein phosphorylation and activation states will be necessary to confirm whether these transcriptional changes translate into functional alterations of the BDNF–TrkB–mTOR pathway, driving synaptic and connectivity abnormalities.

Synaptic alterations in *Npc1^{nmf164}* mice encompass molecular, structural, and functional levels

mTOR plays a key role in synaptic protein synthesis and dendritic remodeling (Kelleher et al., 2004; Jaworski and Sheng, 2006; Richter and Klann, 2009; Hoeffer and Klann, 2010), and we found it to be dysregulated in the developing cerebellum of *Npc1^{nmf164}*, together with the known reduction of membrane cholesterol content in Npc1-deficient neurons (Peake and Vance, 2010; Cariati et al., 2021). This prompted us to investigate whether synaptic compartments were affected.

Since cholesterol is essential for SNARE complex assembly and vesicle fusion (Schoch et al., 2001; Zhang et al., 2013) and altered exo/endocytosis has already been reported in *Npc1*$^{-/-}$ models (Xu et al., 2010), we examined SNARE presynaptic proteins. Consistent with this hypothesis, our Western blot analysis revealed a persistent reduction of Snap25 levels in the cerebellum of *Npc1^{nmf164}* mice, from early postnatal life to adulthood.

Although Snap25 is classically recognized as a regulator of synaptic vesicle exocytosis (Schoch et al., 2001; Zhang et al., 2013), it also contributes to postsynaptic receptor trafficking, short-term plasticity, and dendritic spine morphogenesis (Selak et al., 2009; Jurado et al., 2013; Tomasoni et al., 2013; Antonucci et al., 2016). Reduced Snap25 has been linked to mislocalized PSD proteins, immature spine morphology, and consequent cognitive deficits (Gosso et al., 2006; Tomasoni et al., 2013; Fossati et al., 2015). Thus, the Snap25 downregulation observed in *Npc1^{nmf164}* mice likely contributes to impaired synaptic refinement, consistent with its involvement in various neurodegenerative and psychiatric disorders (Barr et al., 2000; Etain et al., 2010).

The clustering and function of postsynaptic scaffolding and adhesion proteins are also cholesterol-sensitive (Hering et al., 2003; Tulodziecka et al., 2016). Accordingly, we found a marked reduction in Shank3 in the developing cerebellum of *Npc1^{nmf164}* mice, followed by selective downregulation of PSD95 and Nlgn3 at PN30 and PN60. These proteins are central to spine maturation and receptor stabilization at excitatory synapses (Sheng and Kim, 2000; Durand et al., 2007; Coley and Gao, 2018; Xie et al., 2019). Several studies on knockout models for either Shank3 and PSD95 reported immature or poorly organized dendritic spines, lacking the mushroom-shaped morphology typical of stable and functional excitatory synapses (Steiner et al., 2008; Sweet et al., 2011; Durand et al., 2012; Bustos et al., 2014; Jacot-Descombes et al., 2020). Nlgn3 loss may further compromise the precise alignment of pre- and postsynaptic elements, impairing synaptic connectivity, as seen in several NDD models (Baig et al., 2017; Quartier et al., 2019; Muellerleile et al., 2022).

Despite preserved spatial distribution of these proteins across cerebellar cortex layers, as revealed by immunofluorescence detection, qRT-PCR revealed synaptic dysregulation in both male and female *Npc1*^{nmf164} mice, in line with mTOR pathway defects. Thus, while mTOR expression was increased, the downregulation of these key pre- and postsynaptic proteins likely reflects its ineffective compensatory activation for synaptic refinement and maintenance.

Collectively, these findings point to converging mechanisms underlying synaptic alterations in *Npc1*^{nmf164} mice: neurotrophic signaling deficits (BDNF–TrkB–mTOR) and lipid-related dysfunctions compromising membrane composition and synaptic organization, resulting in a broader synaptopathy consistent with the alterations commonly reported in several ASD models (Carroll et al., 2012; Ebrahimi-Fakhari and Sahin, 2015; Brown et al., 2018).

In line with this molecular scenario, we next assessed structural abnormalities in GC dendritic spine dynamics, since GCs—being the most abundant cerebellar neurons (Herculano-Houzel et al., 2006)—likely drive the observed synaptic alterations in *Npc1* mutant cerebellum. Golgi-Cox staining of cerebellar sections revealed persistently increased spine density in *Npc1*^{nmf164} mice of both sexes, consistent with enhanced dendritic arborization previously reported in mutant GCs (Lucarelli et al., 2023). This phenotype may reflect a compensatory attempt by the reduced number of GCs reaching the IGL —following impaired proliferation and defective migration—to establish a higher number of synaptic contacts to maintain functional connectivity within the cerebellar circuitry.

In the developing mouse brain, dendritic spines—hosting most glutamatergic excitatory synapses (Runge et al., 2020)—typically form in the first 21–28 postnatal days through spinogenesis (Chen et al., 2014; Elston and Fujita, 2014), followed by activity-dependent pruning which removes excessive connections (Elston et al., 2009). Through these processes, dendritic spines undergo morphological transitions reflecting their maturation, ranging from thin filopodia to mushroom-shaped spines (Zuo et al., 2005; Runge et al., 2020; Khanal and Hotulainen, 2021). In *Npc1* GCs, we found a marked retention of immature spines beyond the spinogenesis window, particularly pronounced in male mutants at PN30 and PN60, when *wt* animals displayed almost exclusively mature spines, as expected following normal development (Elston et al., 2009; Chen et al., 2014). Even morphologically mature spines were smaller and shorter, especially in male *Npc1,* consistent with Shank3, PSD95, and Nlgn3 downregulation.

Altogether, our results indicate a delayed and structurally compromised synaptic maturation in *Npc1*^{nmf164} mice, likely reflecting the combined effects of disrupted neurotrophic signaling and synaptic protein loss. This is further supported by evidence showing that BDNF–TrkB inhibition impairs both growth and maturation of dendritic spines, whereas BDNF infusion promotes spine enlargement and stabilization (Tyler and Pozzo-Miller, 2001; Ji et al., 2005; Ji et al., 2010; Kellner et al., 2014). Moreover, previous studies revealed activated, phagocytic microglia in *Npc1*^{nmf164} cerebellum (Rava et al., 2022). Since microglia normally refine synaptic circuits via activity-dependent spine engulfment (Paolicelli et al., 2011; Guedes et al., 2022), their dysfunction could

exacerbate defective pruning leading to immature synapse persistence and impaired circuit refinement.

It is also conceivable that these cellular abnormalities translate into macroscopic structural alterations, as revealed by our iDISCO-based 3D volumetric analysis of the IGL. Consistent with previous reports describing cerebellar hypoplasia in *Npc1*-deficient mice (Nusca et al., 2014; Caporali et al., 2016; Totenhagen et al., 2017; Fiorenza et al., 2022), we found a significant and regionally uniform reduction of the IGL volume—ranging between 10% and 20%—across all vermal and hemispheric lobules in *Npc1*^{nmf164} mice at PN15. Importantly, this study was conceived to first explore potential sex-related differences in cerebellar morphology, never investigated in this model, yet no significant changes between male and female mutants were detected.

We believe that the observed reduction likely reflects the cumulative consequence of reduced neuronal recruitment to the IGL previously reported in *Npc1*^{nmf164} mice (Lucarelli et al., 2023). Such layer-specific thinning may thus represent the macroscopic correlate of the cellular alterations described above, ultimately contributing to the overall cerebellar hypoplasia characteristic of NPC1 pathology.

Finally, consistent with the excess of immature excitatory synapses, metabolic profiling by HPLC analysis of excitatory and inhibitory amino acid neurotransmitters revealed increased cerebellar glutamine levels in male and female *Npc1*^{nmf164} mice at PN30, suggesting altered glutamate–glutamine turnover and a potential excitatory imbalance within cerebellar networks. Similar alterations in glutamate and GABA metabolism have also been described in other brain regions (i.e the hippocampus) of *Npc1*-deficient mice and in *in vitro* studies, supporting the notion of a widespread neurotransmitter imbalance in NPC1 (Byun et al., 2006; D'Arcangelo et al., 2011; Kennedy et al., 2016; Cougnoux et al., 2021).

Previous studies specifically in the *Npc1*^{nmf164} cerebellum reported a reduction of vesicular glutamate transporter subtype 2 (VGluT2) and glutamine synthetase already at P15 (Caporali et al., 2016), indicating an early impairment of the neuron–astrocyte glutamate–glutamine cycle (Bak et al., 2006). We hypothesize that elevated glutamine levels in *Npc1* mutants may reflect a homeostatic feedback response, in which reduced neuronal VGluT2 limits glutamate synaptic release, decreasing its availability for astrocytic uptake. In turn, astrocytes may release more glutamine as a compensatory mechanism to restore neuronal glutamate levels (Yu and Hertz, 1982; Bak et al., 2006; Hertz and Rothman, 2017; Andersen, 2025). Accordingly, the concurrent downregulation of glutamine synthetase could represent an adaptive attempt to prevent excessive glutamine accumulation (Rose et al., 2013).

Functionally, this imbalance may generate hyperactive but structurally immature synapses, where excitatory activity is not effectively stabilized due to reduced postsynaptic scaffolding (PSD95, Shank3). Consequently, although spine density is increased and glutamate-glutamine turnover is enhanced, synapses fail to effectively channel this activity into mature, functional connections,

providing a mechanistic link between early synaptic defects and later cerebellar dysfunction in *Npc1*^{nmf164} mice.

Male-specific emergence of social behavior deficits in adult *Npc1*^{nmf164} mice

Although traditionally viewed primarily as a coordinator of motor control, the cerebellum also plays a key role in higher-order cognitive and socio-emotional functions (D'Angelo, 2019; Clausi et al., 2021). Alterations in cerebellar development—particularly those affecting neurotrophic signaling—have been implicated as risk factors for various NDDs, including ASD (Kloth et al., 2015; Rylaarsdam and Guemez-Gamboa, 2019; van der Heijden et al., 2021). Reduced cerebellar BDNF in ASD models is linked to cognitive and behavioral deficits (Branchi et al., 2006; Gould et al., 2011; Halepoto et al., 2014). Accordingly, the cerebellum is now thought to represent a key structure in the pathogenesis of ASD (Kloth et al., 2015). Postmortem and imaging studies have reported reductions in cerebellar volume—particularly in the vermis and cerebellar gray matter—of ASD patients (Courchesne et al., 2001; Scott et al., 2009; D'Mello et al., 2015). Similarly, cerebellar structural abnormalities, including PC loss and altered social behavior, have been described in several mouse models of ASD (Reith et al., 2013; Kloth et al., 2015; Yamashiro et al., 2020). Moreover, emerging evidence suggests that cholesterol dysregulation, including altered synthesis and trafficking, may contribute to synaptic dysfunction and cerebellar pathology in ASD, highlighting a potential link between lipid homeostasis and neurodevelopmental alterations (Wang, 2014; Vallés and Barrantes, 2021).

Building on the results of this study, which highlighted sex-related differences in molecular deficits and aberrant spine morphology, along with a potential excitatory imbalance in *Npc1*^{nmf164} mice during cerebellar postnatal development—signatures frequently reported in both human patients and preclinical models of synaptopathies, neurodevelopmental and psychiatric disorders (Peça et al., 2011; Washbourne, 2015; Batool et al., 2019)—we next examined whether these alterations translated into measurable deficits in early communicative and social behaviors.

We first assessed UltraSonic Vocalizations, which represent an early form of social communication in mouse pups and are highly sensitive to neurodevelopmental alterations (Scattoni et al., 2009; Caruso et al., 2020). Although the total number of emitted calls did not significantly differ between *Npc1*^{nmf164} and *wt* pups, our analysis revealed a sex-independent reduction in mean peak amplitude in *Npc1*^{nmf164} mice. Given that call amplitude reflects the intensity of social arousal and the pup's ability to elicit maternal care (Portfors, 2007; Caruso et al., 2022), this subtle alteration may indicate early deficits in the affective or motivational components of social communication. We propose that such early disruptions could set the stage for later-emerging socio-behavioral impairments, particularly in males, as suggested by the adult behavioral phenotype observed in this model.

Under physiological conditions, rodents naturally exhibit social motivation to seek the

company of a conspecific (Kaidanovich-Beilin et al., 2011), as observed in both male and female *wt* mice during the Social Interaction Test. Interestingly, *Npc1* females displayed a comparable *wt*-like behavior at PN30. Conversely, male *Npc1*^{nmf164} mice failed to show a preference for the social stimulus (the age- and sex-matched conspecific) over the neutral object, indicating reduced sociability consistent with the emergence of an autistic-like phenotype.

Importantly, although mutant mice displayed reduced locomotor activity (velocity and distance moved), both genotypes explored the testing apparatus similarly during habituation, ruling out general hypoactivity as a confounding factor. These observations suggest that the social deficits in male *Npc1*^{nmf164} mice are not secondary to impaired motor function, which has been observed only at later stages of disease progression in Npc1 models (Caporali et al., 2016).

In addition, to determine whether these social deficits reflected broader affective disturbances, we evaluated depressive-like behaviors using the Tail Suspension Test, in which increased immobility time is indicative of a depressive phenotype (Castagné et al., 2011; Cooper et al., 2018). No significant differences were observed between Npc1nmf164 and wt mice, confirming that the behavioral alterations are specifically confined to the social domain.

Conclusion

Collectively, these findings (**Table 4**) suggest that loss of Npc1 function disrupts GC synaptic maturation and cerebellar circuitry formation, leading to sex-dependent differences in the emergence of autistic-like behavioral phenotypes. This integrative view supports the hypothesis that early postnatal cerebellar abnormalities—through impaired neurotrophic signaling and altered synaptic development—impact socio-emotional processing in male mutants, linking early communicative and synaptic defects to measurable autistic-like phenotypes in adulthood, and paralleling mechanisms described in other NDDs such as ASD.

Postnatal Stage	Main findings in *Npc1*^{nmf164} mice
PN8	Early alterations in social communication, reflected by a significant reduction in USVs mean peak amplitude in *Npc1* mice, irrespective of sex.
PN11	Early disruption of BDNF–TrkB signaling, associated with dysregulation of downstream mTOR/PTEN pathways in both sexes. Downregulation of key synaptic proteins (Snap25 and Shank3) in male and female *Npc1* mice. Impaired GC differentiation and connectivity, with sex-dependent dendritic spine abnormalities (reduced spine density in males and increased spine density in females).
PN15	Early and sexually uniform reduction of IGL volume, consistent with the onset of cerebellar hypoplasia.
PN30	Sex-dependent modulation of BDNF–TrkB signaling disruption, with persistent downstream mTOR/PTEN dysregulation in the *Npc1* cerebellum. Broad downregulation of synaptic proteins (Snap25, Shank3, PSD95, Nlgn3) in both sexes. Marked impairment of GC differentiation and connectivity, characterized by an excess of immature

	dendritic spines, particularly pronounced in male *Npc1* mice, while females display partial structural recovery. Increased cerebellar glutamine levels, indicating altered glutamate–glutamine turnover and a potential excitatory–inhibitory imbalance. Emergence of abnormal social behavior, selectively observed in adult male *Npc1* mice.
PN60	Persistent impairment of BDNF–TrkB signaling with sustained mTOR/PTEN dysregulation in both sexes. Continued downregulation of key pre- and postsynaptic proteins (Snap25, Shank3, PSD95, Nlgn3). Long-lasting defects in GC connectivity, with both male and female *Npc1* mice exhibiting excess immature spines and reduced mature spine length.

Table 4. Main developmental features of the *Npc1^{nmf164}* animal model.

Supplementary materials

Supplementary Table 1. Post hoc multiple comparisons for *BDNF* mRNA expression

ANOVA table of BDNF			
Source of Variation	**% of total variation**	**P value**	**P value summary**
Age	52,81	<0,0001	****
Genotype	16,21	<0,0001	****
Sex	9,64	<0,0001	****
Age x Genotype	0,6519	0,0257	*
Age x Sex	16,8	<0,0001	****
Genotype x Sex	1,511	0,0002	***
Age x Genotype x Sex	0,552	0,0421	*

Tukey's multiple comparisons test	Mean Diff.	95,00% CI of diff	Adjusted P Value	Summary
PN11:wt Female vs. PN11:Npc1nmf164 Female	-0,697	-1,246 to -0,1479	0,0054	**
PN11:wt Female vs. PN30:wt Female	0,018	-0,5311 to 0,5671	>0,9999	ns
PN11:wt Female vs. PN60:wt Female	-0,592	-1,141 to -0,04288	0,0269	@
PN11:wt Male vs. PN11:Npc1nmf164 Male	-0,614	-1,163 to -0,06488	0,0194	*
PN11:wt Male vs. PN30:wt Male	-2,264	-2,813 to -1,715	<0,0001	@@@
PN11:wt Male vs. PN60:wt Male	-2,935	-3,484 to -2,386	<0,0001	@@@
PN11:Npc1nmf164 Female vs. PN11:Npc1nmf164 Male	0,648	0,09888 to 1,197	0,0116	#
PN11:Npc1nmf164 Female vs. PN30:Npc1nmf164 Female	-0,646	-1,195 to -0,09688	0,0119	@
PN11:Npc1nmf164 Female vs. PN60:Npc1nmf164 Female	-1,39	-1,939 to -0,8409	<0,0001	@@@
PN11:Npc1nmf164 Male vs. PN30:Npc1nmf164 Male	-2,264	-2,813 to -1,715	<0,0001	@@@
PN11:Npc1nmf164 Male vs. PN60:Npc1nmf164 Male	-2,984	-3,533 to -2,435	<0,0001	@@@
PN30:wt Female vs. PN30:Npc1nmf164 Female	-1,361	-1,910 to -0,8119	<0,0001	****
PN30:wt Female vs. PN60:wt Female	-0,61	-1,159 to -0,06088	0,0206	@
PN30:wt Male vs. PN30:Npc1nmf164 Male	-0,614	-1,163 to -0,06488	0,0194	*
PN30:wt Male vs. PN60:wt Male	-0,671	-1,220 to -0,1219	0,0081	@@@
PN30:Npc1nmf164 Female vs. PN30:Npc1nmf164 Male	-0,97	-1,519 to -0,4209	<0,0001	###
PN30:Npc1nmf164 Female vs. PN60:Npc1nmf164 Female	-0,744	-1,293 to -0,1949	0,0026	@@
PN30:Npc1nmf164 Male vs. PN60:Npc1nmf164 Male	-0,72	-1,269 to -0,1709	0,0038	@@
PN60:wt Female vs. PN60:Npc1nmf164 Female	-1,495	-2,044 to -0,9459	<0,0001	****
PN60:wt Male vs. PN60:Npc1nmf164 Male	-0,663	-1,212 to -0,1139	0,0092	**
PN60:Npc1nmf164 Female vs. PN60:Npc1nmf164 Male	-0,946	-1,495 to -0,3969	0,0001	###

Table 1S. The table reports p-values from the three-way ANOVA (genotype × sex × age) followed by Tukey's post hoc test for *BDNF* mRNA expression in the cerebellum of male and female *wt* and *Npc1*^{nmf164} mice at PN11, PN30, and PN60. * indicates comparisons between genotypes (*wt*, *Npc1*^{nmf164}); # indicates comparisons between sexes (male, female); @ indicates comparisons between ages (PN11, PN30, PN60). Statistical significance is reported in the tables above.

Supplementary Table 2. Post hoc multiple comparisons for *TrkB* mRNA expression

ANOVA table of TrkB			
Source of Variation	**% of total variation**	**P value**	**P value summary**
Age	72,92	<0,0001	****
Genotype	10,58	<0,0001	****
Sex	3,675	<0,0001	****
Age x Genotype	3,997	<0,0001	****
Age x Sex	4,73	<0,0001	****
Genotype x Sex	2,077	<0,0001	****
Age x Genotype x Sex	0,2654	0,1859	ns

Tukey's multiple comparisons test	Mean Diff.	95,00% CI of diff	Adjusted P Value	Summary
PN11:wt Female vs. PN11:Npc1nmf164 Female	-1,606	-2,508 to -0,7040	<0,0001	****
PN11:wt Female vs. PN30:wt Female	2,923	2,021 to 3,825	<0,0001	@@@
PN11:wt Female vs. PN60:wt Female	0,052	-0,8500 to 0,9540	>0,9999	ns
PN11:wt Male vs. PN11:Npc1nmf164 Male	-2,753	-3,655 to -1,851	<0,0001	****
PN11:wt Male vs. PN30:wt Male	1,505	0,6030 to 2,407	0,0002	@@@
PN11:wt Male vs. PN60:wt Male	-2,074	-2,976 to -1,172	<0,0001	@@@
PN11:Npc1nmf164 Female vs. PN11:Npc1nmf164 Male	-0,145	-1,047 to 0,7570	>0,9999	ns
PN11:Npc1nmf164 Female vs. PN30:Npc1nmf164 Female	4,955	4,053 to 5,857	<0,0001	@@@
PN11:Npc1nmf164 Female vs. PN60:Npc1nmf164 Female	0,791	-0,1110 to 1,693	0,1244	ns
PN11:Npc1nmf164 Male vs. PN30:Npc1nmf164 Male	3,156	2,254 to 4,058	<0,0001	@@@
PN11:Npc1nmf164 Male vs. PN60:Npc1nmf164 Male	-0,771	-1,673 to 0,1310	0,145	ns
PN30:wt Female vs. PN30:Npc1nmf164 Female	0,426	-0,4760 to 1,328	0,8502	ns
PN30:wt Female vs. PN60:wt Female	-2,871	-3,773 to -1,969	<0,0001	@@@
PN30:wt Male vs. PN30:Npc1nmf164 Male	-1,102	-2,004 to -0,2000	0,0081	**
PN30:wt Male vs. PN60:wt Male	-3,579	-4,481 to -2,677	<0,0001	@@@
PN30:Npc1nmf164 Female vs. PN30:Npc1nmf164 Male	-1,944	-2,846 to -1,042	<0,0001	###
PN30:Npc1nmf164 Female vs. PN60:Npc1nmf164 Female	-4,164	-5,066 to -3,262	<0,0001	@@@
PN30:Npc1nmf164 Male vs. PN60:Npc1nmf164 Male	-3,927	-4,829 to -3,025	<0,0001	@@@
PN60:wt Female vs. PN60:Npc1nmf164 Female	-0,867	-1,769 to 0,03501	0,0673	ns
PN60:wt Male vs. PN60:Npc1nmf164 Male	-1,45	-2,352 to -0,5480	0,0003	***
PN60:Npc1nmf164 Female vs. PN60:Npc1nmf164 Male	-1,707	-2,609 to -0,8050	<0,0001	###

Table 2S. The table reports p-values from the three-way ANOVA (genotype × sex × age) followed by Tukey's post hoc test for *TrkB* mRNA expression in the cerebellum of male and female *wt* and *Npc1^{nmf164}* mice at PN11, PN30, and PN60. * indicates comparisons between genotypes (*wt*, *Npc1^{nmf164}*); # indicates comparisons between sexes (male, female); @ indicates comparisons between ages (PN11, PN30, PN60). Statistical significance is reported in the tables above.

Supplementary Table 3. Post hoc multiple comparisons for *PTEN* mRNA expression

ANOVA table of PTEN			
Source of Variation	**% of total variation**	**P value**	**P value summary**
Age	71,84	<0,0001	****
Genotype	19,19	<0,0001	****
Sex	0,3717	0,0289	*
Age x Genotype	2,359	<0,0001	****
Age x Sex	4,418	<0,0001	****
Genotype x Sex	0,04854	0,4094	ns
Age x Genotype x Sex	0,1296	0,4042	ns

Tukey's multiple comparisons test	Mean Diff.	95,00% CI of diff	Adjusted P Value	Summary
PN11:wt Female vs. PN11:Npc1nmf164 Female	-0,802	-1,499 to -0,1048	0,0148	*
PN11:wt Female vs. PN30:wt Female	-1,632	-2,329 to -0,9348	<0,0001	@@@
PN11:wt Female vs. PN60:wt Female	0,02734	-0,6698 to 0,7245	>0,9999	ns
PN11:wt Male vs. PN11:Npc1nmf164 Male	-1,143	-1,840 to -0,4458	0,0002	***
PN11:wt Male vs. PN30:wt Male	-2,523	-3,221 to -1,826	<0,0001	@@@
PN11:wt Male vs. PN60:wt Male	0,489	-0,2082 to 1,186	0,3693	ns
PN11:Npc1nmf164 Female vs. PN11:Npc1nmf164 Male	0,052	-0,6452 to 0,7492	>0,9999	ns
PN11:Npc1nmf164 Female vs. PN30:Npc1nmf164 Female	-2,69	-3,387 to -1,992	<0,0001	@@@
PN11:Npc1nmf164 Female vs. PN60:Npc1nmf164 Female	-0,2636	-0,9607 to 0,4336	0,9601	ns
PN11:Npc1nmf164 Male vs. PN30:Npc1nmf164 Male	-3,463	-4,160 to -2,766	<0,0001	@@@
PN11:Npc1nmf164 Male vs. PN60:Npc1nmf164 Male	0,7051	0,007893 to 1,402	0,0458	@
PN30:wt Female vs. PN30:Npc1nmf164 Female	-1,86	-2,557 to -1,162	<0,0001	****
PN30:wt Female vs. PN60:wt Female	1,659	0,9622 to 2,357	<0,0001	@@@
PN30:wt Male vs. PN30:Npc1nmf164 Male	-2,082	-2,780 to -1,385	<0,0001	****
PN30:wt Male vs. PN60:wt Male	3,012	2,315 to 3,710	<0,0001	@@@
PN30:Npc1nmf164 Female vs. PN30:Npc1nmf164 Male	-0,7212	-1,418 to -0,02401	0,0382	#
PN30:Npc1nmf164 Female vs. PN60:Npc1nmf164 Female	2,426	1,729 to 3,123	<0,0001	@@@
PN30:Npc1nmf164 Male vs. PN60:Npc1nmf164 Male	4,168	3,471 to 4,865	<0,0001	@@@
PN60:wt Female vs. PN60:Npc1nmf164 Female	-1,093	-1,790 to -0,3957	0,0004	***
PN60:wt Male vs. PN60:Npc1nmf164 Male	-0,9269	-1,624 to -0,2297	0,0032	**
PN60:Npc1nmf164 Female vs. PN60:Npc1nmf164 Male	1,021	0,3234 to 1,718	0,001	##

Table 3S. The table reports p-values from the three-way ANOVA (genotype × sex × age) followed by Tukey's post hoc test for *PTEN* mRNA expression in the cerebellum of male and female *wt* and *Npc1*^{nmf164} mice at PN11, PN30, and PN60. * indicates comparisons between genotypes (*wt*, *Npc1*^{nmf164}); # indicates comparisons between sexes (male, female); @ indicates comparisons between ages (PN11, PN30, PN60). Statistical significance is reported in the tables above.

Supplementary Table 4. Post hoc multiple comparisons for *mTOR* mRNA expression

ANOVA table of mTOR			
Source of Variation	**% of total variation**	**P value**	**P value summary**
Age	56,13	<0,0001	****
Genotype	20,53	<0,0001	****
Sex	2,008	0,0014	**
Age x Genotype	0,1257	0,6716	ns
Age x Sex	17,03	<0,0001	****
Genotype x Sex	0,1689	0,3073	ns
Age x Genotype x Sex	0,2763	0,4238	ns

Tukey's multiple comparisons test	Mean Diff.	95,00% CI of diff.	Adjusted P Value	Summary
PN11:wt Female vs. PN11:Npc1nmf164 Female	1,093	0,3705 to 1,816	0,0007	***
PN11:wt Female vs. PN30:wt Female	0,1174	-0,6052 to 0,8399	>0,9999	ns
PN11:wt Female vs. PN60:wt Female	1,42	0,6972 to 2,142	<0,0001	@@@
PN11:wt Male vs. PN11:Npc1nmf164 Male	0,908	0,1855 to 1,631	0,006	**
PN11:wt Male vs. PN30:wt Male	-1,733	-2,455 to -1,010	<0,0001	@@@
PN11:wt Male vs. PN60:wt Male	0,9104	0,1879 to 1,633	0,0059	@@
PN11:Npc1nmf164 Female vs. PN11:Npc1nmf164 Male	0,981	0,2585 to 1,704	0,0025	##
PN11:Npc1nmf164 Female vs. PN30:Npc1nmf164 Female	0,2246	-0,4980 to 0,9471	0,9904	ns
PN11:Npc1nmf164 Female vs. PN60:Npc1nmf164 Female	1,112	0,3896 to 1,835	0,0005	@@@
PN11:Npc1nmf164 Male vs. PN30:Npc1nmf164 Male	-1,871	-2,593 to -1,148	<0,0001	@@@
PN11:Npc1nmf164 Male vs. PN60:Npc1nmf164 Male	0,8914	0,1688 to 1,614	0,0073	@@
PN30:wt Female vs. PN30:Npc1nmf164 Female	1,2	0,4777 to 1,923	0,0002	***
PN30:wt Female vs. PN60:wt Female	1,302	0,5799 to 2,025	<0,0001	@@@
PN30:wt Male vs. PN30:Npc1nmf164 Male	0,7697	0,04713 to 1,492	0,0298	*
PN30:wt Male vs. PN60:wt Male	2,643	1,920 to 3,366	<0,0001	@@@
PN30:Npc1nmf164 Female vs. PN30:Npc1nmf164 Male	-1,114	-1,837 to -0,3919	0,0005	###
PN30:Npc1nmf164 Female vs. PN60:Npc1nmf164 Female	0,8876	0,1650 to 1,610	0,0077	@@
PN30:Npc1nmf164 Male vs. PN60:Npc1nmf164 Male	2,762	2,040 to 3,485	<0,0001	@@@
PN60:wt Female vs. PN60:Npc1nmf164 Female	0,7854	0,06285 to 1,508	0,025	*
PN60:wt Male vs. PN60:Npc1nmf164 Male	0,8889	0,1664 to 1,611	0,0076	**
PN60:Npc1nmf164 Female vs. PN60:Npc1nmf164 Male	0,7602	0,03768 to 1,483	0,0331	#

Table 4S. The table reports p-values from the three-way ANOVA (genotype × sex × age) followed by Tukey's post hoc test for *mTOR* mRNA expression in the cerebellum of male and female *wt* and *Npc1*^{nmf164} mice at PN11, PN30, and PN60. * indicates comparisons between genotypes (*wt*, *Npc1*^{nmf164}); # indicates comparisons between sexes (male, female); @ indicates comparisons between ages (PN11, PN30, PN60). Statistical significance is reported in the tables above.

Supplementary Table 5. Post hoc multiple comparisons for Snap25 protein expression

Two-way ANOVA	SNAP25		
Source of Variation	**% of total variation**	**P value**	**P value summary**
Interaction	0,6911	0,7027	ns
Age	42,89	<0,0001	****
Genotype	24,67	<0,0001	****

Uncorrected Fisher's LSD	Predicted (LS) mean diff	95,00% CI of diff	Individual P Value	Summary
PN11 vs. PN30	-0,3803	-0,4974 to -0,2631	<0,0001	****
PN11 vs. PN60	-0,2639	-0,4109 to -0,1169	0,0008	***
PN30 vs. PN60	0,1164	-0,02776 to 0,2606	0,1102	ns

Unpaired t test SNAP25	Difference between means ± SEM	95,00% CI of diff	P value	Summary
PN11 Npc1^{nmf164} vs. wt	-0,2211 ± 0,08930	-0,4126 to -0,02961	0,0267	*
PN30 Npc1^{nmf164} vs. wt	-0,3164 ± 0,08276	-0,4918 to -0,1409	0,0003	***
PN60 Npc1^{nmf164} vs. wt	-0,2956 ± 0,08006	-0,4915 to -0,09970	0,0102	*

Table 5S. The table reports p-values from the two-way ANOVA (genotype × age) followed by Student's t-test and Fisher post hoc test for Snap25 protein expression in the cerebellum of *wt* and *Npc1^{nmf164}* mice at PN11, PN30, and PN60. * indicates comparisons between genotypes (*wt*, *Npc1^{nmf164}*); @ indicates comparisons between ages (PN11, PN30, PN60). Statistical significance is reported in the tables above.

Supplementary Table 6. Post hoc multiple comparisons for Vamp2 protein expression

Two-way ANOVA	VAMP2		
Source of Variation	**% of total variation**	**P value**	**P value summary**
Interaction	1,841	0,496	ns
Age	51,89	<0,0001	****
Genotype	0,4441	0,5607	ns

Uncorrected Fisher's LSD	Predicted (LS) mean diff	95,00% CI of diff	Individual P Value	Summary
PN11 vs. PN30	-0,2072	-0,4633 to 0,04890	0,1095	ns
PN11 vs. PN60	-0,9904	-1,312 to -0,6691	<0,0001	@@@
PN30 vs. PN60	-0,7832	-1,098 to -0,4681	<0,0001	@@@

Table 6S. The table reports p-values from the two-way ANOVA (genotype × age) followed by Fisher post hoc test for Vamp2 protein expression in the cerebellum of *wt* and *Npc1*^{nmf164} mice at PN11, PN30, and PN60. @ indicates comparisons between ages (PN11, PN30, PN60). Statistical significance is reported in the tables above.

Supplementary Table 7. Post hoc multiple comparisons for Shank3 protein expression

Two-way ANOVA	SHANK3		
Source of Variation	**% of total variation**	**P value**	**P value summary**
Interaction	1,866	0,5774	ns
Age	24,58	0,0023	**
Genotype	15,43	0,0046	**

Uncorrected Fisher's LSD	Predicted (LS) mean diff	95,00% CI of diff	Individual P Value	Summary
PN11 vs. PN30	0,6386	0,1982 to 1,079	0,0058	@@
PN11 vs. PN60	0,7783	0,3440 to 1,213	0,0009	@@@
PN30 vs. PN60	0,1397	-0,2831 to 0,5625	0,5061	ns

Unpaired t test SHANK3	Difference between means ± SEM	95,00% CI of diff	P value	Summary
PN11 Npc1^{nmf164} vs. wt	-1,554 ± 0,5987	-2,888 to -0,2202	0,0267	*
PN30 Npc1^{nmf164} vs. wt	-0,4938 ± 0,09798	-0,7095 to -0,2781	0,0004	***
PN60 Npc1^{nmf164} vs. wt	-0,3028 ± 0,1168	-0,5574 to -0,04830	0,0236	*

Table 7S. The table reports p-values from the two-way ANOVA (genotype × age) followed by Student's t-test and Fisher post hoc test for Shank3 protein expression in the cerebellum of *wt* and *Npc1^{nmf164}* mice at PN11, PN30, and PN60. * indicates comparisons between genotypes (*wt*, *Npc1^{nmf164}*); @ indicates comparisons between ages (PN11, PN30, PN60). Statistical significance is reported in the tables above.

Supplementary Table 8. Post hoc multiple comparisons for Drebrin protein expression

Two-way ANOVA	DREBRIN		
Source of Variation	**% of total variation**	**P value**	**P value summary**
Interaction	4,035	0,2951	ns
Age	40,79	<0,0001	****
Genotype	0,02153	0,9082	ns

Uncorrected Fisher's LSD	Predicted (LS) mean diff	95,00% CI of diff	Individual P Value	Summary
PN11 vs. PN30	0,15	-0,1993 to 0,4992	0,3894	ns
PN11 vs. PN60	-0,6327	-0,9772 to -0,2882	0,0007	@@@
PN30 vs. PN60	-0,7827	-1,116 to -0,4492	<0,0001	@@@

Table 8S. The table reports p-values from the two-way ANOVA (genotype × age) followed by Fisher post hoc test for Drebrin protein expression in the cerebellum of *wt* and *Npc1*^{nmf164} mice at PN11, PN30, and PN60. @ indicates comparisons between ages (PN11, PN30, PN60). Statistical significance is reported in the tables above.

Supplementary Table 9. Post hoc multiple comparisons for PSD95 protein expression

Two-way ANOVA	PSD95		
Source of Variation	**% of total variation**	**P value**	**P value summary**
Interaction	17,8	0,0814	ns
Age	0,3339	0,9481	ns
Genotype	18,18	0,0255	*

Unpaired t test PSD95	Difference between means ± SEM	95,00% CI of diff	P value	Summary
PN11 Npc1 ^{nmf164} vs. wt	0,1228 ± 0,1452	-0,2324 to 0,4781	0,43	ns
PN30 Npc1 ^{nmf164} vs. wt	-0,6381 ± 0,2178	-1,171 to -0,1052	0,0263	*
PN60 Npc1 ^{nmf164} vs. wt	-0,6281 ± 0,1938	-1,086 to -0,1697	0,0142	*

Table 9S. The table reports p-values from the two-way ANOVA (genotype × age) followed by Student's t-test for PSD95 protein expression in the cerebellum of *wt* and *Npc1^{nmf164}* mice at PN11, PN30, and PN60. * indicates comparisons between genotypes (*wt*, *Npc1^{nmf164}*). Statistical significance is reported in the tables above.

Supplementary Table 10. Post hoc multiple comparisons for *Snap25* mRNA expression

Three-way ANOVA	SNAP25		
Source of Variation	**% of total variation**	**P value**	**P value summary**
Age	21,26	<0,0001	****
Genotype	29,84	<0,0001	****
Sex	29,51	<0,0001	****
Age x Genotype	1,246	<0,0001	****
Age x Sex	16,56	<0,0001	****
Genotype x Sex	0,02243	0,3599	ns
Age x Genotype x Sex	0,9389	<0,0001	****

Tukey's multiple comparisons test	Mean Diff	95,00% CI of diff	Adjusted P Value	Summary
PN11:wt Female vs. PN11:Npc1nmf164 Female	-1,168	-1,745 to -0,5909	<0,0001	****
PN11:wt Female vs. PN30:wt Female	1,408	0,8309 to 1,985	<0,0001	@@@
PN11:wt Female vs. PN60:wt Female	1,524	0,9469 to 2,101	<0,0001	@@@
PN11:wt Male vs. PN11:Npc1nmf164 Male	-2,044	-2,621 to -1,467	<0,0001	****
PN11:wt Male vs. PN30:wt Male	-3,212	-3,789 to -2,635	<0,0001	@@@
PN11:wt Male vs. PN60:wt Male	0,918	0,3409 to 1,495	0,0003	@@@
PN11:Npc1nmf164 Female vs. PN11:Npc1nmf164 Male	-1,286	-1,863 to -0,7089	<0,0001	###
PN11:Npc1nmf164 Female vs. PN30:Npc1nmf164 Female	-0,593	-1,170 to -0,01586	0,0403	@
PN11:Npc1nmf164 Female vs. PN60:Npc1nmf164 Female	0,536	-0,04114 to 1,113	0,0858	ns
PN11:Npc1nmf164 Male vs. PN30:Npc1nmf164 Male	-3,369	-3,946 to -2,792	<0,0001	@@@
PN11:Npc1nmf164 Male vs. PN60:Npc1nmf164 Male	0,348	-0,2291 to 0,9251	0,5808	ns
PN30:wt Female vs. PN30:Npc1nmf164 Female	-3,169	-3,746 to -2,592	<0,0001	****
PN30:wt Female vs. PN60:wt Female	0,116	-0,4611 to 0,6931	0,9998	ns
PN30:wt Male vs. PN30:Npc1nmf164 Male	-2,201	-2,778 to -1,624	<0,0001	****
PN30:wt Male vs. PN60:wt Male	4,13	3,553 to 4,707	<0,0001	@@@
PN30:Npc1nmf164 Female vs. PN30:Npc1nmf164 Male	-4,062	-4,639 to -3,485	<0,0001	###
PN30:Npc1nmf164 Female vs. PN60:Npc1nmf164 Female	1,129	0,5519 to 1,706	<0,0001	@@@
PN30:Npc1nmf164 Male vs. PN60:Npc1nmf164 Male	3,717	3,140 to 4,294	<0,0001	@@@
PN60:wt Female vs. PN60:Npc1nmf164 Female	-2,156	-2,733 to -1,579	<0,0001	****
PN60:wt Male vs. PN60:Npc1nmf164 Male	-2,614	-3,191 to -2,037	<0,0001	****
PN60:Npc1nmf164 Female vs. PN60:Npc1nmf164 Male	-1,474	-2,051 to -0,8969	<0,0001	###

Table 10S. The table reports p-values from the three-way ANOVA (genotype × sex × age) followed by Tukey's post hoc test for *Snap25* mRNA expression in the cerebellum of male and female *wt* and *Npc1*^{nmf164} mice at PN11, PN30, and PN60. * indicates comparisons between genotypes (*wt*, *Npc1*^{nmf164}); # indicates comparisons between sexes (male, female); @ indicates comparisons between ages (PN11, PN30, PN60). Statistical significance is reported in the tables above.

Supplementary Table 11. Post hoc multiple comparisons for *Shank3* mRNA expression

Three-way ANOVA	SHANK3		
Source of Variation	**% of total variation**	**P value**	**P value summary**
Age	60,62	<0,0001	****
Genotype	25,4	<0,0001	****
Sex	6,71	<0,0001	****
Age x Genotype	1,005	<0,0001	****
Age x Sex	4,33	<0,0001	****
Genotype x Sex	0,6005	0,0004	***
Age x Genotype x Sex	0,4775	0,0049	**

Tukey's multiple comparisons test	Mean Diff	95,00% CI of diff	Adjusted P Value	Summary
PN11:wt Female vs. PN11:Npc1nmf164 Female	-1,647	-2,197 to -1,097	<0,0001	****
PN11:wt Female vs. PN30:wt Female	3,369	2,819 to 3,919	<0,0001	@@@
PN11:wt Female vs. PN60:wt Female	1,826	1,276 to 2,376	<0,0001	@@@
PN11:wt Male vs. PN11:Npc1nmf164 Male	-1,244	-1,794 to -0,6939	<0,0001	****
PN11:wt Male vs. PN30:wt Male	3,441	2,891 to 3,991	<0,0001	@@@
PN11:wt Male vs. PN60:wt Male	-0,044	-0,5941 to 0,5061	>0,9999	ns
PN11:Npc1nmf164 Female vs. PN11:Npc1nmf164 Male	-0,108	-0,6581 to 0,4421	0,9998	ns
PN11:Npc1nmf164 Female vs. PN30:Npc1nmf164 Female	2,878	2,328 to 3,428	<0,0001	@@@
PN11:Npc1nmf164 Female vs. PN60:Npc1nmf164 Female	1,502	0,9519 to 2,052	<0,0001	@@@
PN11:Npc1nmf164 Male vs. PN30:Npc1nmf164 Male	2,562	2,012 to 3,112	<0,0001	@@@
PN11:Npc1nmf164 Male vs. PN60:Npc1nmf164 Male	0,345	-0,2051 to 0,8951	0,5261	ns
PN30:wt Female vs. PN30:Npc1nmf164 Female	-2,138	-2,688 to -1,588	<0,0001	****
PN30:wt Female vs. PN60:wt Female	-1,543	-2,093 to -0,9929	<0,0001	@@@
PN30:wt Male vs. PN30:Npc1nmf164 Male	-2,123	-2,673 to -1,573	<0,0001	****
PN30:wt Male vs. PN60:wt Male	-3,485	-4,035 to -2,935	<0,0001	@@@
PN30:Npc1nmf164 Female vs. PN30:Npc1nmf164 Male	-0,424	-0,9741 to 0,1261	0,2493	ns
PN30:Npc1nmf164 Female vs. PN60:Npc1nmf164 Female	-1,376	-1,926 to -0,8259	<0,0001	@@@
PN30:Npc1nmf164 Male vs. PN60:Npc1nmf164 Male	-2,217	-2,767 to -1,667	<0,0001	@@@
PN60:wt Female vs. PN60:Npc1nmf164 Female	-1,971	-2,521 to -1,421	<0,0001	****
PN60:wt Male vs. PN60:Npc1nmf164 Male	-0,855	-1,405 to -0,3049	0,0005	***
PN60:Npc1nmf164 Female vs. PN60:Npc1nmf164 Male	-1,265	-1,815 to -0,7149	<0,0001	###

Table 11S. The table reports p-values from the three-way ANOVA (genotype × sex × age) followed by Tukey's post hoc test for *Shank3* mRNA expression in the cerebellum of male and female *wt* and *Npc1*^{nmf164} mice at PN11, PN30, and PN60. * indicates comparisons between genotypes (*wt*, *Npc1*^{nmf164}); # indicates comparisons between sexes (male, female); @ indicates comparisons between ages (PN11, PN30, PN60). Statistical significance is reported in the tables above.

Supplementary Table 12. Post hoc multiple comparisons for *Nlgn3* mRNA expression

Three-way ANOVA	NLGN3		
Source of Variation	**% of total variation**	**P value**	**P value summary**
Age	51,69	<0,0001	****
Genotype	27,57	<0,0001	****
Sex	3,406	<0,0001	****
Age x Genotype	5,827	<0,0001	****
Age x Sex	6,8	<0,0001	****
Genotype x Sex	0,0007438	0,9339	ns
Age x Genotype x Sex	2,172	0,0006	***

Tukey's multiple comparisons test	Mean Diff	95,00% CI of diff	Adjusted P Value	Summary
PN11:wt Female vs. PN11:Npc1nmf164 Female	-0,298	-0,8485 to 0,2525	0,7183	ns
PN11:wt Female vs. PN30:wt Female	0,982	0,4315 to 1,533	<0,0001	@@@
PN11:wt Female vs. PN60:wt Female	1,573	1,022 to 2,124	<0,0001	@@@
PN11:wt Male vs. PN11:Npc1nmf164 Male	-0,511	-1,062 to 0,03952	0,0861	ns
PN11:wt Male vs. PN30:wt Male	0,3843	-0,1662 to 0,9349	0,3755	ns
PN11:wt Male vs. PN60:wt Male	2,755	2,204 to 3,305	<0,0001	@@@
PN11:Npc1nmf164 Female vs. PN11:Npc1nmf164 Male	-0,049	-0,5995 to 0,5015	>0,9999	ns
PN11:Npc1nmf164 Female vs. PN30:Npc1nmf164 Female	-0,183	-0,7335 to 0,3675	0,984	ns
PN11:Npc1nmf164 Female vs. PN60:Npc1nmf164 Female	0,631	0,08048 to 1,182	0,0154	@
PN11:Npc1nmf164 Male vs. PN30:Npc1nmf164 Male	0,1919	-0,3587 to 0,7424	0,9773	ns
PN11:Npc1nmf164 Male vs. PN60:Npc1nmf164 Male	1,448	0,8974 to 1,998	<0,0001	@@@
PN30:wt Female vs. PN30:Npc1nmf164 Female	-1,463	-2,014 to -0,9125	<0,0001	****
PN30:wt Female vs. PN60:wt Female	0,591	0,04048 to 1,142	0,0279	@
PN30:wt Male vs. PN30:Npc1nmf164 Male	-0,7035	-1,254 to -0,1529	0,005	@@
PN30:wt Male vs. PN60:wt Male	2,37	1,820 to 2,921	<0,0001	@@@
PN30:Npc1nmf164 Female vs. PN30:Npc1nmf164 Male	0,3259	-0,2247 to 0,8764	0,6059	ns
PN30:Npc1nmf164 Female vs. PN60:Npc1nmf164 Female	0,814	0,2635 to 1,365	0,0009	@@@
PN30:Npc1nmf164 Male vs. PN60:Npc1nmf164 Male	1,256	0,7055 to 1,807	<0,0001	@@@
PN60:wt Female vs. PN60:Npc1nmf164 Female	-1,24	-1,791 to -0,6895	<0,0001	****
PN60:wt Male vs. PN60:Npc1nmf164 Male	-1,818	-2,368 to -1,267	<0,0001	****
PN60:Npc1nmf164 Female vs. PN60:Npc1nmf164 Male	0,7679	0,2174 to 1,318	0,0018	##

Table 12S. The table reports p-values from the three-way ANOVA (genotype × sex × age) followed by Tukey's post hoc test for *Nlgn3* mRNA expression in the cerebellum of male and female *wt* and *Npc1*^{nmf164} mice at PN11, PN30, and PN60. * indicates comparisons between genotypes (*wt*, *Npc1*^{nmf164}); # indicates comparisons between sexes (male, female); @ indicates comparisons between ages (PN11, PN30, PN60). Statistical significance is reported in the tables above.

Supplementary Table 13. Post hoc multiple comparisons for total spine density

Type III Sums of Squares

Source	df	Sum of Squares	Mean Square	F-Value	P-Value
GENOTYPE	1	2,538	2,538	24,530	,0001
SEX	1	,719	,719	6,949	,0091
TIMEPOINT	2	3,220	1,610	15,559	,0001
GENOTYPE * SEX	1	7,475E-5	7,475E-5	,001	,9786
GENOTYPE * TI...	2	1,808	,904	8,738	,0002
SEX * TIMEPOINT	2	3,050	1,525	14,739	,0001
GENOTYPE * SE...	2	4,511	2,256	21,798	,0001
Residual	193	19,971	,103		

Dependent: DENS TOT

Least Squares Means Table	**DENSINTY TOTAL SPINES**					
	Vs.	**Diff.**	**Std. Error**	**t-Test**	**P-Value**	**Summary**
PN11 Npc1nm164 Female	PN11 wt Female	0,461	0,102	4,53	0,0001	***
	PN11 Npc1nm164 male	0,556	0,125	4,459	0,0001	###
	PN30 Npc1nm164 Female	0,336	0,097	3,477	0,0006	@@@
	PN60 Npc1nm164 Female	0,238	0,102	2,337	0,0204	@
PN11 Npc1nm164 Male	PN11 wt Male	-0,452	0,144	-3,139	0,002	**
	PN30 Npc1nm164 Male	-0,928	0,131	-7,068	0,0001	@@@
	PN60 Npc1nm164 Male	-0,532	0,131	-4,05	0,0001	@@@
PN30 Npc1nm164 Female	PN30 wt Female	-0,045	0,091	-0,492	0,6233	ns
	PN30 Npc1nm164 Male	-0,708	0,105	-6,741	0,0001	###
	PN60 Npc1nm164 Female	-0,098	0,097	-1,013	0,3122	ns
PN30 Npc1nm164 Male	PN30 wt Male	0,439	0,117	3,734	0,0002	***
	PN60 Npc1nm164 Male	0,396	0,117	3,374	0,0009	@@@
PN60 Npc1nm164 Female	PN60 wt Female	0,284	0,11	2,582	0,0106	*
	PN60 Npc1nm164 Male	-0,214	0,11	-1,948	0,0529	ns
PN60 Npc1nm164 Male	PN60 wt Male	0,705	0,117	6,003	0,0001	***

Table 13S. The table reports p-values from the three-way ANOVA (genotype × sex × age) followed by Tukey's post hoc test for total spine density in the IGL of male and female *wt* and *Npc1*^{nmf164} mice at PN11, PN30, and PN60. * indicates comparisons between genotypes (*wt*, *Npc1*^{nmf164}); # indicates comparisons between sexes (male, female); @ indicates comparisons between ages (PN11, PN30, PN60). Statistical significance is reported in the tables above.

Supplementary Table 14. Post hoc multiple comparisons for immature spine density

Type III Sums of Squares

Source	df	Sum of Squares	Mean Square	F-Value	P-Value
TIMEPOINT	2	5,123	2,562	130,390	,0001
SEX	1	,136	,136	6,940	,0091
GENOTYPE	1	,922	,922	46,912	,0001
TIMEPOINT * SEX	2	,290	,145	7,369	,0008
TIMEPOINT * GE...	2	1,000	,500	25,452	,0001
SEX * GENOTYPE	1	,028	,028	1,424	,2342
TIMEPOINT * SE...	2	1,562	,781	39,758	,0001
Residual	193	3,792	,020		

Dependent: DENS IMMATURE

Least Squares Means Table	DENSINTY IMMATURE SPINES					
	Vs.	Diff.	Std. Error	t-Test	P-Value	Summary
PN11 Npc1nm164 Female	PN11 wt Female	0,223	0,044	5,04	0,0001	***
	PN11 Npc1nm164 male	0,353	0,054	6,503	0,0001	###
	PN30 Npc1nm164 Female	0,471	0,042	11,193	0,0001	@@@
	PN60 Npc1nm164 Female	0,519	0,044	11,7	0,0001	@@@
PN11 Npc1nm164 Male	PN11 wt Male	-0,362	0,063	-5,773	0,0001	***
	PN30 Npc1nm164 Male	-0,087	0,057	-1,523	0,1295	ns
	PN60 Npc1nm164 Male	-0,071	0,057	-1,241	0,2162	ns
PN30 Npc1nm164 Female	PN30 wt Female	0,165	0,04	4,156	0,0001	***
	PN30 Npc1nm164 Male	-0,205	0,046	-4,472	0,0001	###
	PN60 Npc1nm164 Female	0,048	0,042	1,14	0,2556	ns
PN30 Npc1nm164 Male	PN30 wt Male	0,389	0,051	7,606	0,0001	***
	PN60 Npc1nm164 Male	0,016	0,051	0,315	0,7531	ns
PN60 Npc1nm164 Female	PN60 wt Female	0,104	0,048	2,179	0,0305	*
	PN60 Npc1nm164 Male	-0,237	0,048	-4,941	0,0001	###
PN60 Npc1nm164 Male	PN60 wt Male	0,319	0,051	6,231	0,0001	***

Table 14S. The table reports p-values from the three-way ANOVA (genotype × sex × age) followed by Tukey's post hoc test for immature spine density in the IGL of male and female *wt* and *Npc1*^{nmf164} mice at PN11, PN30, and PN60. * indicates comparisons between genotypes (*wt*, *Npc1*^{nmf164}); # indicates comparisons between sexes (male, female); @ indicates comparisons between ages (PN11, PN30, PN60). Statistical significance is reported in the tables above.

Supplementary Table 15. Post hoc multiple comparisons for mature spine density

Type III Sums of Squares

Source	df	Sum of Squares	Mean Square	F-Value	P-Value
TIMEPOINT	2	11,968	5,984	75,623	,0001
SEX	1	,071	,071	,896	,3451
GENOTYPE	1	,704	,704	8,902	,0032
TIMEPOINT * SEX	2	1,625	,812	10,265	,0001
TIMEPOINT * GE...	2	,659	,329	4,163	,0170
SEX * GENOTYPE	1	,003	,003	,037	,8484
TIMEPOINT * SE...	2	,541	,270	3,417	,0348
Residual	193	15,272	,079		

Dependent: DENS MATURE

Least Squares Means Table	DENSINTY MATURE SPINES					
	Vs.	Diff.	Std. Error	t-Test	P-Value	Summary
PN11 Npc1nm164 Female	PN30 Npc1nm164 Female	-0,45	0,062	-7,252	0,0001	@@@
	PN60 Npc1nm164 Female	-0,31	0,068	-4,552	0,0001	@@@
PN11 Npc1nm164 Male	PN11 wt Male	-0,087	0,117	-0,744	0,4592	ns
	PN30 Npc1nm164 Male	-0,839	0,107	-7,833	0,0001	@@@
	PN60 Npc1nm164 Male	-0,453	0,107	-4,234	0,0001	@@@
PN30 Npc1nm164 Female	PN60 Npc1nm164 Female	0,14	0,065	2,161	0,0327	ns
PN30 Npc1nm164 Male	PN30 wt Male	0,049	0,096	0,515	0,608	ns
	PN60 Npc1nm164 Male	0,385	0,096	4,024	0,0001	@@@
PN60 Npc1nm164 Male	PN60 wt Male	0,381	0,096	3,979	0,0002	***
Npc1nm164 Female	wt Female	0,13	0,053	2,449	0,0158	* Genotype effct

Table 15S. The table reports p-values from the three-way ANOVA (genotype × sex × age) followed by Tukey's post hoc test for mature spine density in the IGL of male and female *wt* and *Npc1*^{nmf164} mice at PN11, PN30, and PN60. * indicates comparisons between genotypes (*wt*, *Npc1*^{nmf164}); # indicates comparisons between sexes (male, female); @ indicates comparisons between ages (PN11, PN30, PN60). Statistical significance is reported in the tables above.

Supplementary Table 16. Post hoc multiple comparisons for filopodia spine density

Type III Sums of Squares

Source	df	Sum of Squares	Mean Square	F-Value	P-Value
TIMEPOINT	2	,304	,152	12,352	,0001
SEX	1	,006	,006	,499	,4809
GENOTYPE	1	,220	,220	17,817	,0001
TIMEPOINT * SEX	2	,268	,134	10,885	,0001
TIMEPOINT * GE...	2	,366	,183	14,836	,0001
SEX * GENOTYPE	1	,008	,008	,665	,4157
TIMEPOINT * SE...	2	,327	,164	13,276	,0001
Residual	193	2,378	,012		

Dependent: DENS FILOPODIA

Least Squares Means Table	**DENSINTY FILOPODIA**					
	Vs.	**Diff.**	**Std. Error**	**t-Test**	**P-Value**	**Summary**
PN11 Npc1nm164 Female	PN11 wt Female	0,041	0,035	1,165	0,2454	ns
	PN11 Npc1nm164 male	0,183	0,043	4,263	0,0001	###
	PN30 Npc1nm164 Female	0,167	0,033	5,019	0,0001	@@@
	PN60 Npc1nm164 Female	0,136	0,035	3,87	0,0001	@@@
PN11 Npc1nm164 Male	PN11 wt Male	-0,151	0,05	-3,033	0,0028	**
	PN30 Npc1nm164 Male	-0,223	0,045	-4,926	0,0001	@@@
	PN60 Npc1nm164 Male	-0,097	0,045	-2,149	0,0329	@
PN30 Npc1nm164 Female	PN30 wt Female	0,05	0,031	1,58	0,1157	ns
	PN30 Npc1nm164 Male	-0,207	0,036	-5,713	0,0001	###
	PN60 Npc1nm164 Female	-0,031	0,033	-0,94	0,3484	ns
PN30 Npc1nm164 Male	PN30 wt Male	0,268	0,041	6,61	0,0001	***
	PN60 Npc1nm164 Male	0,126	0,041	3,106	0,0022	@@
PN60 Npc1nm164 Female	PN60 wt Female	0,075	0,038	1,968	0,0505	-
	PN60 Npc1nm164 Male	-0,05	0,038	-1,317	0,1893	ns
PN60 Npc1nm164 Male	PN60 wt Male	0,127	0,041	3,13	0,002	**

Table 16S. The table reports p-values from the three-way ANOVA (genotype × sex × age) followed by Tukey's post hoc test for filopodia spine density in the IGL of male and female *wt* and *Npc1*^{nmf164} mice at PN11, PN30, and PN60. * indicates comparisons between genotypes (*wt*, *Npc1*^{nmf164}); # indicates comparisons between sexes (male, female); @ indicates comparisons between ages (PN11, PN30, PN60). Statistical significance is reported in the tables above.

Supplementary Table 17. Post hoc multiple comparisons for long thin spine density

Type III Sums of Squares

Source	df	Sum of Squares	Mean Square	F-Value	P-Value
TIMEPOINT	2	1,019	,509	92,507	,0001
SEX	1	,011	,011	2,055	,1534
GENOTYPE	1	,035	,035	6,304	,0129
TIMEPOINT * SEX	2	,032	,016	2,895	,0577
TIMEPOINT * GE...	2	,051	,025	4,605	,0111
SEX * GENOTYPE	1	,101	,101	18,407	,0001
TIMEPOINT * SE...	2	,346	,173	31,468	,0001
Residual	193	1,063	,006		

Dependent: DENS LONG THIN

Least Squares Means Table	DENSINTY LONG THIN					
	Vs.	Diff.	Std. Error	t-Test	P-Value	Summary
PN11 Npc1nm164 Female	PN11 wt Female	0,151	0,023	6,438	0,0001	***
	PN11 Npc1nm164 male	0,173	0,029	6,028	0,0001	###
	PN30 Npc1nm164 Female	0,214	0,022	9,61	0,0001	@@@
	PN60 Npc1nm164 Female	0,252	0,023	10,724	0,0001	@@@
PN11 Npc1nm164 Male	PN11 wt Male	-0,193	0,033	-5,823	0,0001	***
	PN30 Npc1nm164 Male	0,043	0,03	1,426	0,1554	ns
	PN60 Npc1nm164 Male	-0,005	0,03	-0,157	0,8754	ns
PN30 Npc1nm164 Female	PN30 wt Female	0,051	0,021	2,451	0,0151	*
	PN30 Npc1nm164 Male	0,003	0,024	0,104	0,9173	ns
	PN60 Npc1nm164 Female	0,038	0,022	1,694	0,0919	ns
PN30 Npc1nm164 Male	PN30 wt Male	0,055	0,027	2,02	0,0448	*
	PN60 Npc1nm164 Male	-0,048	0,027	-1,77	0,0783	ns
PN60 Npc1nm164 Female	PN60 wt Female	0,018	0,025	0,708	0,4799	ns
	PN60 Npc1nm164 Male	-0,083	0,025	-3,281	0,0012	##
PN60 Npc1nm164 Male	PN60 wt Male	0,081	0,027	2,983	0,0032	**

Table 17S. The table reports p-values from the three-way ANOVA (genotype × sex × age) followed by Tukey's post hoc test for long thin spine density in the IGL of male and female *wt* and *Npc1*^{nmf164} mice at PN11, PN30, and PN60. * indicates comparisons between genotypes (*wt*, *Npc1*^{nmf164}); # indicates comparisons between sexes (male, female); @ indicates comparisons between ages (PN11, PN30, PN60). Statistical significance is reported in the tables above.

Supplementary Table 18. Post hoc multiple comparisons for thin spine density

Type III Sums of Squares

Source	df	Sum of Squares	Mean Square	F-Value	P-Value
TIMEPOINT	2	,563	,282	53,163	,0001
SEX	1	,053	,053	9,997	,0018
GENOTYPE	1	,074	,074	13,897	,0003
TIMEPOINT * SEX	2	,014	,007	1,358	,2596
TIMEPOINT * GE...	2	,025	,013	2,366	,0966
SEX * GENOTYPE	1	,011	,011	2,126	,1464
TIMEPOINT * SE...	2	,043	,022	4,079	,0184
Residual	193	1,022	,005		

Dependent: DENS THIN

Least Squares Means Table	**DENSINTY THIN**					
	Vs.	**Diff.**	**Std. Error**	**t-Test**	**P-Value**	**Summary**
PN11 Npc1nm164 Female	PN11 wt Female	0,031	0,023	1,365	0,1738	ns
	PN11 Npc1nm164 male	-0,003	0,028	-0,123	0,9026	ns
	PN30 Npc1nm164 Female	0,124	0,022	5,693	0,0001	@@@
	PN60 Npc1nm164 Female	0,131	0,023	5,697	0,0001	@@@
PN11 Npc1nm164 Male	PN11 wt Male	-0,018	0,033	-0,556	0,5788	ns
	PN30 Npc1nm164 Male	0,093	0,03	3,127	0,002	@@
	PN60 Npc1nm164 Male	0,026	0,03	0,875	0,3828	ns
PN30 Npc1nm164 Female	PN30 wt Female	0,029	0,021	1,408	0,1607	ns
	PN30 Npc1nm164 Male	-0,035	0,024	-1,466	0,1443	ns
	PN60 Npc1nm164 Female	0,007	0,022	0,312	0,7552	ns
PN30 Npc1nm164 Male	PN30 wt Male	0,067	0,027	2,507	0,013	**
	PN60 Npc1nm164 Male	-0,067	0,027	-2,518	0,0126	@
PN60 Npc1nm164 Female	PN60 wt Female	0,012	0,025	0,473	0,6367	ns
	PN60 Npc1nm164 Male	-0,109	0,025	-4,368	0,0001	###
PN60 Npc1nm164 Male	PN60 wt Male	0,116	0,027	4,378	0,0001	***

Table 18S. The table reports p-values from the three-way ANOVA (genotype × sex × age) followed by Tukey's post hoc test for thin spine density in the IGL of male and female *wt* and *Npc1*^{nmf164} mice at PN11, PN30, and PN60. * indicates comparisons between genotypes (*wt*, *Npc1*^{nmf164}); # indicates comparisons between sexes (male, female); @ indicates comparisons between ages (PN11, PN30, PN60). Statistical significance is reported in the tables above.

Supplementary Table 19. Post hoc multiple comparisons for stubby spine density

Type III Sums of Squares

Source	df	Sum of Squares	Mean Square	F-Value	P-Value
TIMEPOINT	2	,855	,427	14,741	,0001
SEX	1	,177	,177	6,110	,0143
GENOTYPE	1	,078	,078	2,705	,1017
TIMEPOINT * SEX	2	,324	,162	5,583	,0044
TIMEPOINT * GE...	2	,102	,051	1,751	,1764
SEX * GENOTYPE	1	,096	,096	3,315	,0702
TIMEPOINT * SE...	2	,387	,193	6,673	,0016
Residual	192	5,567	,029		

Dependent: DENS STUBBY

Least Squares Means Table	**DENSINTY STUBBY**					
	Vs.	**Diff.**	**Std. Error**	**t-Test**	**P-Value**	**Summary**
PN11 Npc1nm164 Female	PN11 wt Female	0,132	0,054	2,446	0,0154	*
	PN11 Npc1nm164 male	0,067	0,066	1,012	0,313	ns
	PN30 Npc1nm164 Female	0,055	0,051	1,085	0,2791	ns
	PN60 Npc1nm164 Female	0,164	0,054	3,051	0,0026	@@
PN11 Npc1nm164 Male	PN11 wt Male	0,032	0,076	0,416	0,678	ns
	PN30 Npc1nm164 Male	-0,2	0,07	-2,877	0,0045	@@
	PN60 Npc1nm164 Male	-0,101	0,07	-1,449	0,1489	ns
PN30 Npc1nm164 Female	PN30 wt Female	-0,038	0,048	-0,781	0,436	ns
	PN30 Npc1nm164 Male	-0,189	0,056	-3,393	0,0008	###
	PN60 Npc1nm164 Female	0,109	0,051	2,131	0,0344	@
PN30 Npc1nm164 Male	PN30 wt Male	-0,007	0,063	-0,104	0,9169	ns
	PN60 Npc1nm164 Male	0,099	0,062	1,596	0,1122	ns
PN60 Npc1nm164 Female	PN60 wt Female	-0,107	0,058	-1,843	0,0668	ns
	PN60 Npc1nm164 Male	-0,198	0,058	-3,41	0,0008	###
PN60 Npc1nm164 Male	PN60 wt Male	0,234	0,062	3,756	0,0002	***

Table 19S. The table reports p-values from the three-way ANOVA (genotype × sex × age) followed by Tukey's post hoc test for stubby spine density in the IGL of male and female *wt* and *Npc1*^{nmf164} mice at PN11, PN30, and PN60. * indicates comparisons between genotypes (*wt*, *Npc1*^{nmf164}); # indicates comparisons between sexes (male, female); @ indicates comparisons between ages (PN11, PN30, PN60). Statistical significance is reported in the tables above.

Supplementary Table 20. Post hoc multiple comparisons for mushroom spine density

Type III Sums of Squares

Source	df	Sum of Squares	Mean Square	F-Value	P-Value
TIMEPOINT	2	6,133	3,066	97,474	,0001
SEX	1	1,299E-4	1,299E-4	,004	,9488
GENOTYPE	1	,168	,168	5,332	,0220
TIMEPOINT * SEX	2	,949	,474	15,075	,0001
TIMEPOINT * GE...	2	,604	,302	9,598	,0001
SEX * GENOTYPE	1	,031	,031	,974	,3249
TIMEPOINT * SE...	2	,447	,223	7,103	,0011
Residual	192	6,040	,031		

Dependent: DENS MUSHROOM

Least Squares Means Table	**DENSINTY MUSHROOM**					
	Vs.	**Diff.**	**Std. Error**	**t-Test**	**P-Value**	**Summary**
PN11 Npc1nm164 Female	PN11 wt Female	0,106	0,056	1,885	0,0609	ns
	PN11 Npc1nm164 male	0,136	0,069	1,977	0,0495	#
	PN30 Npc1nm164 Female	-0,225	0,053	-4,233	0,0001	@@@
	PN60 Npc1nm164 Female	-0,445	0,056	-7,936	0,0001	@@@
PN11 Npc1nm164 Male	PN11 wt Male	-0,121	0,079	-1,529	0,1279	ns
	PN30 Npc1nm164 Male	-0,641	0,072	-8,854	0,0001	@@@
	PN60 Npc1nm164 Male	-0,355	0,072	-4,902	0,0001	@@@
PN30 Npc1nm164 Female	PN30 wt Female	-0,136	0,05	-2,714	0,0073	**
	PN30 Npc1nm164 Male	-0,28	0,058	-4,834	0,0001	###
	PN60 Npc1nm164 Female	-0,22	0,053	-4,131	0,0001	@@@
PN30 Npc1nm164 Male	PN30 wt Male	0,077	0,066	1,161	0,2472	ns
	PN60 Npc1nm164 Male	0,347	0,065	5,355	0,0001	@@@
PN60 Npc1nm164 Female	PN60 wt Female	0,287	0,061	4,73	0,0001	***
	PN60 Npc1nm164 Male	0,226	0,061	3,73	0,0003	###
PN60 Npc1nm164 Male	PN60 wt Male	0,148	0,065	2,278	0,0238	*

Table 20S. The table reports p-values from the three-way ANOVA (genotype × sex × age) followed by Tukey's post hoc test for mushroom spine density in the IGL of male and female *wt* and *Npc1*^{nmf164} mice at PN11, PN30, and PN60. * indicates comparisons between genotypes (*wt*, *Npc1*^{nmf164}); # indicates comparisons between sexes (male, female); @ indicates comparisons between ages (PN11, PN30, PN60). Statistical significance is reported in the tables above.

References

Adeosun SO, Hou X, Jiao Y, Zheng B, Henry S, Hill R, He Z, Pani A, Kyle P et al (2012) Allopregnanolone reinstates tyrosine hydroxylase immunoreactive neurons and motor performance in an MPTP-lesioned mouse model of Parkinson's disease. *PLos One.*7:e50040.

Ahmad I, Lope-Piedrafita S, Bi X, Hicks C, Yao Y, Yu C, Chaitkin E, Howison CM, Weberg L et al (2005) Allopregnanolone treatment, both as a single injection or repetitively, delays demyelination and enhances survival of Niemann-Pick C mice. *J Neurosci Res.*82:811-821.

Alahmadi AAS (2023) The Cerebellum's Orchestra: Understanding the Functional Connectivity of Its Lobes and Deep Nuclei in Coordination and Integration of Brain Networks. *Tomography.*9(2):883-893.

Ali H, Marth L, Krueger-Burg D (2020) Neuroligin-2 as a central organizer of inhibitory synapses in health and disease. *Sci Signal.*13(663):eabd8379.

Allen GI, Tsukahara N (1974) Cerebrocerebellar communication systems (1974) Cerebrocerebellar communication systems. *Physiol Rev.*54:957-1006.

Al-Nasser MN, Mellor IR, Carter WG (2022) Is L-Glutamate Toxic to Neurons and Thereby Contributes to Neuronal Loss and Neurodegeneration? A Systematic Review. *Brain Sci*12(5):577.

Amaral DG, Schumann CM, Nordahl CW (2008) Neuroanatomy of autism. *Trends Neurosci.*31(3):137-145.

Ambrosi G, Flace P, Lorusso L, Girolamo F, Rizzi A, Bosco L, Errede M, Virgintino D, Roncali L (2007) Non-traditional large neurons in the granular layer of the cerebellar cortex. *Eur J Histochem.*1:59-64.

Ammann A, Gottlieb D (1955) Paper chromatography of antifungal antibiotics. *Appl Microbiol* 3:181-186.

Amore G, Spoto G, Ieni A, Vetri L, Quatrosi G, Di Rosa G, Nicotera AG (2021) A Focus on the Cerebellum: From Embryogenesis to an Age-Related Clinical Perspective. *Front Syst Neurosci.*15:646052.

Andersen JV (2025) The Glutamate/GABA-Glutamine Cycle: Insights, Updates, and Advances. *J Neurochem.*169(3):e70029.

Andersen JV, Schousboe A (2023) Milestone Review: Metabolic dynamics of glutamate and GABA mediated neurotransmission - The essential roles of astrocytes. *J Neurochem.*166(2):109-137.

Andolina D, Conversi D, Cabib S, et al (2011) 5-Hydroxytryptophan during critical postnatal period improves cognitive performances and promotes dendritic spine maturation in genetic mouse model of phenylketonuria. *Int J Neuropsychopharmacol.*14(4):479-489.

Angelaki DE, Cullen KE (2008) Vestibular system: the many facets of a multimodal sense. *Annu Rev Neurosci.*31:125-150.

Antonucci F, Corradini I, Fossati G, Tomasoni R, Menna E, Matteoli M (2016) SNAP-25, a known presynaptic protein with emerging postsynaptic functions. *Front Synaptic Neurosci.*8:7.

Aoki C, Sekino Y, Hanamura K, Fujisawa S, Mahadomrongkul V, Ren Y, Shirao T (2005) Drebrin A is a postsynaptic protein that localizes in vivo to the submembranous surface of dendritic sites forming excitatory synapses. *J Comp Neurol.*483:383-402.

Apps R, Garwicz M (2005) Anatomical and physiological foundations of cerebellar information processing. *Nat Rev Neurosci.*6(4):297-311.

Apps R, Hawkes R (2009) Cerebellar cortical organization: a one-map hypothesis. *Nat Rev Neurosci.*10(9):670-681.

Apps R, Hawkes R, Aoki S, Bengtsoon F, Brown AM, Chen G, Ebner TJ, Isope P, Jörntell H et al (2018) Cerebellar modules and their role as operational cerebellar processing units. *Cerebellum.*17:654-682.

Badura A, Verpeut JL, Metzger JW, et al (2018) Normal cognitive and social development require posterior cerebellar activity. *Elife.*7:e36401.

Baig DN, Yanagawa T, Tabuchi K (2017) Distortion of the normal function of synaptic cell adhesion molecules by genetic variants as a risk for autism spectrum disorders. *Brain Res Bull.*129:82-90.

Bak LK, Schousboe A, Waagepetersen HS (2006) The glutamate/GABA-glutamine cycle: aspects of transport, neurotransmitter homeostasis and ammonia transfer. *J Neurochem.*98(3):641-653.

Balch WE, Morimoto RI, Dillin A, Kelly JW (2008) Adapting proteostasis for disease intervention. *Science*. 319:916-919.

Balsters JH, Laird AR, Fox PT, Eickhoff SB (2014) Bridging the gap between functional and anatomical features of cortico-cerebellar circuits using meta-analytic connectivity modeling. *Hum Brain Mapp*.35(7):3152-3169.

Barr CL, Feng Y, Wigg K, Bloom S, Roberts W, Malone M, Schachar R, Tannock R, Kennedy JL (2000) Identification of DNA variants in the SNAP-25 gene and linkage study of these polymorphisms and attention-deficit hyperactivity disorder. *Mol Psychiatry.*5:405-409.

Batool S, Raza H, Zaidi J, Riaz S, Hasan S, Syed NI (2019) Synapse formation: from cellular and molecular mechanisms to neurodevelopmental and neurodegenerative disorders. *J Neurophysiol*.121(4):1381-1397.

Baudry M, Yao Y, Simmons D, Liu J, Bi X (2003) Postnatal development of inflammation in a murine model of Niemann-Pick type C disease: immunohistochemical observations of microglia and astroglia. *Exp Neurol.*184(2):887-903.

Bauer P, Knoblich R, Bauer C, Finckh U, Hufen A, Kropp J, Braun S, Kustermann-Kuhn B, Schmidt D et al (2002) NPC1: complete genomic sequence, mutation analysis, and characterization of haplotypes. *Hum Mutat.*19:30-38.

Belle M, Godefroy D, Couly G, et al (2017) Tridimensional Visualization and Analysis of Early Human Development. *Cell*.169(1):161-173.e12.

Benarroch EE (2008) Brain cholesterol metabolism and neurologic disease. *Neurology.*71:1368-1373.

Berg TO, Fengsrud M, Strømhaug PE, Berg T, Seglen PO (1998) Isolation and characterization of rat liver amphisomes. Evidence for fusion of autophagosomes with both early and late endosomes. *J Biol Chem.*273:21883-21892.

Berghoff SA, Spieth L, Sun T, Hosang L, Depp C, Sasmita AO, Vasileva MH, Scholz P, Zhao Y et al (2021) Neuronal cholesterol synthesis is essential for repair of chronically demyelinated lesions in mice. *Cell Rep.*37:109889.

Bernardo A, De Nuccio C, Visentin S, Martire A, Minghetti L, Popoli P, Ferrante A (2021) Myelin defects in Niemann-Pick type C disease: mechanism and possible therapeutic perspectives. *Int J Mol Sci.*22:8858.

Berry-Kravis E (2021) Niemann-Pick disease, type C: diagnosis, management and disease-targeted therapies in development. *Semin Pediatr Neurol.*37:100879.

Beuriat PA, Cohen-Zimerman S, Smith GNL, Krueger F, Gordon B, Grafman J (2022) Evidence of the role of the cerebellum in cognitive theory of mind using voxel-based lesion mapping. *Sci Rep*.12(1):4999.

Björkhem I, Meaney S (2004) Brain cholesterol: long secret life behind a barrier. *Arterioscler Thromb Vasc Biol.*24:806-815.

Bond CW, Angeloni N, Harrington D, Stupp S, Podlasek CA (2013) Sonic Hedgehog regulates brain-derived neurotrophic factor in normal and regenerating cavernous nerves. *J Sex Med.*10:730-737.

Bootman MD, Chehab T, Bultynck G, Parys JB, Rietdorf K (2018) The regulation of autophagy by calcium signals: Do we have a consensus? *Cell Calcium.*70:32-46.

Borbon I, Totenhagen J, Fiorenza MT, et al (2012) Niemann-Pick C1 mice, a model of "juvenile Alzheimer's disease", with normal gene expression in neurons and fibrillary astrocytes show long term survival and delayed neurodegeneration. *J Alzheimers Dis*.30(4):875-887.

Borghesani PR, Peyrin JM, Klein R, Rubin J, Carter AR, Schwartz PM, Luster A, Corfas G, Segal RA (2002) BDNF stimulates migration of cerebellar granule cells. *Development.*129:1435-1442.

Bosco G, Poppele RE (2001) Proprioception from a spinocerebellar perspective. *Physiol Rev*.81(2):539-568.

Bostan AC, Strick PL (2018) The basal ganglia and the cerebellum: nodes in an integrated network. *Nat Rev Neurosci*.19(6):338-350.

Bountouvi E, Papadopoulou A, Vanier MT, Nyktari G, Kanellakis S, Michelakakis H, Dinopoulos A (2017) Novel NPC1 mutations with different segregation in two related Greek patients with Niemann-Pick type C disease: molecular study in the extended pedigree and clinical correlations. *BMC Med Genet.*18:51.

Bourne JN, Harris KM (2008) Balancing structure and function at hippocampal dendritic spines. *Annu Rev Neurosci*.31:47-67.

Bourque M, Dluzen DE, Di Paolo T (2009) Neuroprotective actions of sex steroids in Parkinson's disease. *Front Neuroendocrinol.*30:142-157.

Bowling H, Klann E (2014) Shaping dendritic spines in autism spectrum disorder: mTORC1-dependent macroautophagy. *Neuron*.83(5):994-996.

Boyles JK, Zoellner CD, Anderson LJ, Kosik LM, Pitas RE, Weisgraber KH, Hui DY, Mahley RW, Gebicke-Haerter PJ et al (1989) A role for apolipoprotein E, apolipoprotein A-I, and low density lipoprotein receptors in cholesterol transport during regeneration and remyelination of the rat sciatic nerve. *J Clin Invest.*83:1015-1031.

Bramham CR, Messaoudi E (2005) BDNF function in adult synaptic plasticity: the synaptic consolidation hypothesis. *Prog Neurobiol*.76(2):99-125.

Branchi I, D'Andrea I, Fiore M, Di Fausto V, Aloe L, Alleva E (2006) Early social enrichment shapes social behavior and nerve growth factor and brain-derived neurotrophic factor levels in the adult mouse brain. *Biol Psychiatry.*60:690-696.

Broussard DM, Titley HK, Antflick J, Hampson DR (2011) Motor learning in the VOR: the cerebellar component. *Exp Brain Res*.210(3-4):451-463.

Brown AM, Arancillo M, Lin T, Catt DR, Zhou J, Lackey EP, Stay TL, Zuo Zm White JJ et al (2019) Molecular layer interneurons shape the spike activity of cerebellar Purkinje cells. *Sci Rep*.9:1742.

Brown EA, Lautz JD, Davis TR, et al (2018) Clustering the autisms using glutamate synapse protein interaction networks from cortical and hippocampal tissue of seven mouse models. *Mol Autism*.9:48.

Brown MS, Goldstein JL (1986) A receptor-mediated pathway for cholesterol homeostasis. *Science.*232:34-47.

Bruno F, Camuso S, Capuozzo E, Canterini S (2023) The Antifungal Antibiotic Filipin as a Diagnostic Tool of Cholesterol Alterations in Lysosomal Storage Diseases and Neurodegenerative Disorders. *Antibiotics*.*12*(1), 122.

Buccarello L, Musi CA, Turati A, Borsello T (2018) The stress c-Jun N-terminal Kinase signaling pathway activation correlates with synaptic pathology and presents a sex bias in P301L mouse model of tauopathy. *Neuroscience*.393:196-205.

Bustos FJ, Varela-Nallar L, Campos M, et al (2014) PSD95 suppresses dendritic arbor development in mature hippocampal neurons by occluding the clustering of NR2B-NMDA receptors. *PLoS One*.9(4):e94037.

Byun K, Kim J, Cho SY, et al (2006) Alteration of the glutamate and GABA transporters in the hippocampus of the Niemann-Pick disease, type C mouse using proteomic analysis. *Proteomics*.6(4):1230-1236.

Cajal SRY (1995) Histology of the nervous system of man and vertebrates. *Oxford NY Oxford University Press.*

Camuso S, La Rosa P, Fiorenza MT, Canterini S (2022) Pleiotropic effects of BDNF on the cerebellum and hippocampus: Implication for neurodevelopmental disorders. *Neurobiol Dis.*163:105606.

Can A, Dao DT, Terrillion CE, Piantadosi SC, Bhat S, Gould TD (2012) The tail suspension test. *J Vis Exp*.(59):e3769.

Canterini S, Carletti V, Nusca S, Mangia F, Fiorenza MT (2013) Multiple TSC22D4 iso-/phospho-glycoforms display idiosyncratic subcellular localizations and interacting protein partners. *FEBS J*.280(5):1320-1329.

Canterini S, Dragotto J, Dardis A, Zampieri S, De Stefano ME, Mangia F, Erickson RP, Fiorenza MT (2017) Shortened primary cilium lenght and dysregulated Sonic hedgehog signaling in Niemann-Pick C1 disease. *Hum Mol Genet.*6:2277-2289.

Caporali P, Bruno F, Palladino G, Dragotto J, Petrosini L, Mangia F, Erickson RP, Canterini S, Fiorenza MT (2016) Developmental delay in motor skill acquisition in Niemann-Pick C1 mice reveals abnormal cerebellar morphogenesis. *Acta Neuropathol Commun.*4:94.

Carballo GB, Honorato JR, de Lopes GPF, Spohr TCLSE (2018) A highlight on Sonic hedgehog pathway. *Cell Commun Signal*.16(1):11.

Cariati I, Masuelli L, Bei R, Tancredi V, Frank C, D'Arcangelo G (2021) Neurodegeneration in Niemann-Pick type C disease: an update review on pharmacological and non-pharmacological approaches to counteract brain and cognitive impairment. *Int J Mol Sci.*22:6600.

Carroll L, Braeutigam S, Dawes JM, et al (2021) Autism Spectrum Disorders: Multiple Routes to, and Multiple Consequences of, Abnormal Synaptic Function and Connectivity. *Neuroscientist*.27(1):10-29.

Carstea ED, Morris JA, Coleman KG, Loftus SK, Zhang D, Cummings C, Gu J, Rosenfeld MA, Pavan WJ et al (1997) Niemann-Pick C1 disease gene: homology to mediators of cholesterol homeostasis. *Science.*277:228-231.

Carter AR, Chen C, Schwartz PM, Segal RA (2022) Brain-derived neurotrophic factor modulates cerebellar plasticity and synaptic ultrastructure. *J Neurosci*.22(4):1316-1327.

Caruso A, Marconi MA, Scattoni ML, Ricceri L (2022) Ultrasonic vocalizations in laboratory mice: strain, age, and sex differences. *Genes Brain Behav*.21(5):e12815.

Caruso A, Ricceri L, Scattoni ML (2020) Ultrasonic vocalizations as a fundamental tool for early and adult behavioral phenotyping of Autism Spectrum Disorder rodent models. *Neurosci Biobehav Rev*.116:31-43.

Castagné V, Moser P, Roux S, Porsolt RD (2011) Rodent models of depression: forced swim and tail suspension behavioral despair tests in rats and mice. *Curr Protoc Neurosci.*8:8-10.

Cerilli E, Dall'O GM, Chelini G, et al (2024) Immune system dysfunction and inflammation in aging *Shank3b* mutant mice, a model of autism spectrum disorder. *Front Immunol*.15:1447385.

Cerminara NL, Lang EJ, Sillitoe RV, Apps R (2015) Redefining the cerebellar cortex as an assembly of non-uniform Purkinje cell microcircuits. *Nat Rev Neurosci.*16:79-93.

Chanana V, Zafer D, Kintner DB, et al (2024) TrkB-mediated neuroprotection in female hippocampal neurons is autonomous, estrogen receptor alpha-dependent, and eliminated by testosterone: a proposed model for sex differences in neonatal hippocampal neuronal injury. *Biol Sex Differ.*15(1):30.

Chen AI, Zang K, Masliah E, Reichardt LF (2016) Glutamatergic axon- derived BDNF controls GABAergic synaptic differentiation in the cerebellum. *Sci Rep*.6:20201.

Chen CC, Lu J, Zuo Y (2014) Spatiotemporal dynamics of dendritic spines in the living brain. *Front Neuroanat*.8:28.

Chen H, Yang J, Low PS, Cheng JX (2008) Cholesterol level regulates endosome motility via Rab proteins. *Biophys J.*94:1508-1520.

Chen L, Li Y, Song Z, Xue S, Liu F, Chang X, Wu Y, Duan X, Wu H (2022) O-GlcNAcylation promotes cerebellum development and medulloblastoma oncogenesis via SHH signaling. *Proc. Natl. Acad. Sci. U.S.A*.119(34):e2202821119.

Chen S, Wang JM, Irwin RW, Yao J, Liu L, Brinton RD (2011) Allopregnanolone promotes regeneration and reduces β-amyloid burden in a preclinical model of Alzheimer's disease. *PLos One.*6:e24293.

Choudhury A, Sharma DK, Marks DL, Pagano RE (2004) Elevated endosomal cholesterol levels in Niemann-Pick cells inhibit rab4 and perturb membrane recycling. *Mol Biol Cell.*15:4500-4511.

Cinque C, Pondiki S, Oddi D, et al (2012) Modeling socially anhedonic syndromes: genetic and pharmacological manipulation of opioid neurotransmission in mice. *Transl Psychiatry*.2(8):e155.

Cirulli F, Berry A, Chiarotti F, Alleva E (2004) Intrahippocampal administration of BDNF in adult rats affects short-term behavioral plasticity in the Morris water maze and performance in the elevated plus-maze. *Hippocampus.*14(7):802-807.

Clausi S, Olivito G, Siciliano L, Lupo M, Laghi F, Baiocco R, Leggio M (2021) The cerebellum is linked to theory of mind alterations in autism. A direct clinical and MRI comparison between individuals with autism and cerebellar neurodegenerative pathologies. *Autism Res.*14:2300-2313.

Coley AA, Gao WJ (2018) PSD95: A synaptic protein implicated in schizophrenia or autism?. *Prog Neuropsychopharmacol Biol Psychiatry*.82:187-194.

Consalez GG, Goldowitz D, Casoni F, Hawkes R (2021) Origins, development, and compartmentation of the granule cells of the cerebellum. *Front Neural Circuits.*14:611841.

Cooper JA, Arulpragasam AR, Treadway MT (2018) Anhedonia in depression: biological mechanism and computational models. *Curr Opin Behav Sci.*22:128-135.

Corrales JD, Blaess S, Mahoney EM, Joyner AL (2006) The level of sonic hedgehog signaling regulates the complexity of cerebellar foliation. *Development*.133(9):1811-1821.

Corrales JD, Rocco GL, Blaess S, Guo Q, Joyner AL (2004) Spatial pattern of sonic hedgehog signaling through Gli genes during cerebellum development. *Development*.131(22):5581-5590.

Cougnoux A, Drummond RA, Collar AL, Iben JR, Salman A, Westgarth H, Wassif CA, Cawley NX, Farhat NY et al (2018) Microglia activation in Niemann-Pick disease, type C1 is amendable to therapeutic intervention. *Hum Mol Genet.*27:2076-2089.

Cougnoux A, Yerger JC, Fellmeth M, et al (2021) Reduction of glutamate neurotoxicity: A novel therapeutic approach for Niemann-Pick disease, type C1. *Mol Genet Metab*.134(4):330-336.

Courchesne E, Karns CM, Davis HR, Ziccardi R, Carper RA, Tigue ZD, Chisum HJ, Moses P, Pierce K et al (2001) Unusual brain growth patterns in early life in patients with autistic disorder: an MRI study. *Neurology.*57:245-254.

Crocker AC (1961) The cerebral defect in Tay-Sachs disease and Niemann-Pick disease. *J Neurochem.*7:69-80.

Crocker AC, Farber S (1958) Niemann-Pick disease: a review of eighteen patients. *Medicine (Baltimore).*37:1-95.

Cruz JC, Sugii S, Yu C, Chang TY (2000) Role of Niemann-Pick type C1 protein in intracellular trafficking of low density lipoprotein-derived cholesterol. *J Biol Chem.*275:4013-4021.

Cryan JF, Mombereau C, Vassout A (2005) The tail suspension test as a model for assessing antidepressant activity: review of pharmacological and genetic studies in mice. *Neurosci Biobehav.*29:571-625.

Cullen ER, Safari M, Mittelstadt I, Weston MC (2024) Hyperactivity of mTORC1- and mTORC2-dependent signaling mediates epilepsy downstream of somatic PTEN loss. *Elife*.12:RP91323.

D'Angelo E (2018) Physiology of the cerebellum. *Handb Clin Neurol.*154:85-108.

D'Angelo E (2019) The cerebellum gets social. *Science.*363:229.

D'Mello AM, Crocetti D, Mostofsky SH, Stoodley CJ (2015) Cerebellar gray matter and lobular volumes correlate with core autism symptoms. *Neuroimage Clin.*7:631-639.

D'Amato FR, Zanettini C, Lampis V, et al (2011) Unstable maternal environment, separation anxiety, and heightened CO2 sensitivity induced by gene-by-environment interplay. *PLoS One*.6(4):e18637.

D'Angelo E, Casali S (2013) Seeking a unified framework for cerebellar function and dysfunction: from circuit operations to cognition. *Front Neural Circuits*.6:116.

D'Arcangelo G, Grossi D, De Chiara G, et al (2011) Glutamatergic neurotransmission in a mouse model of Niemann-Pick type C disease. *Brain Res*.1396:11-19.

Dardis A, Zampieri S, Gellera C, Carrozzo R, Cattarossi S, Peruzzo P, Dariol R, Sechi A, Deodato F et al (2020) Molecular genetics of Niemann-Pick type C disease in Italy: an update on 15 patients and description of 18 NPC1 novel variants. *J Clin Med.*9:679.

Davidson CD, Walkley SU (2010) Niemann-Pick type C disease-pathophysiology and future perspectives for treatment. *US Neurol Touch Brief.*6:88-94.

Davies JP, Ioannou YA (2000) Topological analysis of Niemann-Pick C1 protein reveals that the membrane orientation of the putative sterol-sensing domain is identical to those of 3-hydroxy-3-methylglutaryl-CoA reductase and sterol regulatory element binding protein cleavage-activating protein. *J Biol Chem.*275:24367-24374.

de Assis GG, de Sousa MBC, Murawska-Ciałowicz E (2025) Sex Steroids and Brain-Derived Neurotrophic Factor Interactions in the Nervous System: A Comprehensive Review of Scientific Data. *Int J Mol Sci*.26(6):2532.

de Bartolomeis A, Latte G, Tomasetti C, Iasevoli F (2014) Glutamatergic postsynaptic density protein dysfunctions in synaptic plasticity and dendritic spines morphology: relevance to schizophrenia and other behavioral disorders pathophysiology, and implications for novel therapeutic approaches. *Mol Neurobiol*.49(1):484-511.

De Luca A, Cerrato V, Fucà E, Parmigiani E, Buffo A, Leto K (2016) Sonic hedgehog patterning during cerebellar development. *Cell Mol Life Sci.*73(2):291-303.

De Schutter E (2002) Cerebellar cortex: computation by extrasynaptic inhibition? *Curr Biol.*12:363-365.

De Smet HJ, Paquier P, Verhoeven J, Mariën P (2013) The cerebellum: its role in language and related cognitive and affective functions. *Brain Lang.*127(3):334-342.

Deffieu MS, Pfeffer SR (2011) Niemann-Pick type C1 function requires luminal domain residues that mediate cholesterol-dependent NPC2 binding. *Proc Natl Acad Sci USA.*108:18932-18936.

Delmotte Q, Diabira D, Belaidouni Y, Hamze M, Kochmann M, Montheil A, Gaiarsa JL, Porcher C, Belgacem YH (2020) Sonic Hedgehog signaling agonist (SAG) triggers BDNF secretion and promotes the maturation of GABAergic networks in the postnatal rat hippocampus. *Front Cell Neurosci.*14:98.

Dhaliwal NK, Weng OY, Dong X, et al (2024) Synergistic hyperactivation of both mTORC1 and mTORC2 underlies the neural abnormalities of PTEN-deficient human neurons and cortical organoids. *Cell Rep*.43(5):114173.

Di Segni M, Andolina D, Coassin A, et al (2017) Sensitivity to cocaine in adult mice is due to interplay between genetic makeup, early environment and later experience. *Neuropharmacol*.125:87-98.

Diedrichsen J, King M, Hernandez-Castillo C, Sereno M, Ivry RB (2019) Universal Transform or Multiple Functionality? Understanding the Contribution of the Human Cerebellum across Task Domains. *Neuron*.102(5):918-928.

Dierks T, Schlotawa L, Frese MA, Radhakrishnan K, von Figura K, Schmidt B (2009) Molecular basis of multiple sulfatase deficiency, mucolipidosis II/III and Niemann-Pick C1 disease-Lysosomal storage disorders caused by defects of non-lysosomal proteins. *Biochim Biophys Acta*.793:710-725.

Dietschy JM, Turley SD (2004) Thematic review series: brain Lipids. Cholesterol metabolism in the central nervous system during early development and in the mature animal. *J Lipid Res*.45:1375-1397.

Diviccaro S, Cioffi L, Falvo E, Giatti S, Melcangi RC (2022) Allopregnanolone: An overview on its synthesis and effects. *J Neuroendocrinol*.34:e12996.

Dixit SS, Jadot M, Sohar I, Sleat DE, Stock AM, Lobel P (2011) Loss of Niemann-Pick C1 or C2 protein results in similar biochemical changes suggesting that these proteins function in a common lysosomal pathway. *PLos One*.6:e23677.

Djebaili M, Hoffman SW, Stein DG (2004) Allopregnanolone and progesterone decrease cell death and cognitive deficits after a contusion of the rat pre-frontal cortex. *Neuroscience*.123:349-359.

Dragotto J, Canterini S, Del Porto P, Bevilacqua A, Fiorenza MT (2019) The interplay between TGF-β-stimulated TSC22 domain family proteins regulates cell-cycle dynamics in medulloblastoma cells. *J Cell Physiol*.234(10):18349-18360.

Dragotto J, Palladino G, Canterini S, et al (2019) Decreased neural stem cell proliferation and olfaction in mouse models of Niemann-Pick C1 disease and the response to hydroxypropyl-β-cyclodextrin. *J Appl Genet*.60(3-4):357-365.

Du X, Kumar J, Ferguson C, Schulz TA, Ong YS, Hong W, Prinz WA, Parton RG, Brown AJ et al (2011) A role for oxysterol-binding protein-related protein 5 in endosomal cholesterol trafficking. *J Cell Biol*.192:121-135.

Durand CM, Betancur C, Boeckers TM, Bockmann J, Chaste P, Fauchereau F, Nygren G, Rastam M, Gillberg IC et al (2007) Mutations in the gene encoding the synaptic scaffolding protein SHANK3 are associated with autism spectrum disorders. *Nat Genet*.39:25-27.

Durand CM, Perroy J, Loll F, et al (2012) SHANK3 mutations identified in autism lead to modification of dendritic spine morphology via an actin-dependent mechanism. *Mol Psychiatry*.17(1):71-84.

Ebrahimi-Fakhari D, Sahin M (2015) Autism and the synapse: emerging mechanisms and mechanism-based therapies. *Curr Opin Neurol*.28(2):91-102.

Edelmann E, Lessmann V, Brigadski T (2014) Pre- and postsynaptic twists in BDNF secretion and action in synaptic plasticity. *Neuropharmacol*.76 Pt C:610-627.

Ehret G (2005) Infant rodent ultrasounds -- a gate to the understanding of sound communication. *Behav Genet*.35(1):19-29.

Elandaloussi Y, Floris DL, Coupé P, et al (2023) Understanding the relationship between cerebellar structure and social abilities. *Mol Autism*.14(1):18.

Elrick MJ, Lieberman AP (2013) Autophagic dysfunction in a lysosomal storage disorder due to impaired proteolysis. *Autophagy*.9:234-235.

Elrick MJ, Pacheco CD, Yu T, Dadgar N, Shakkottai VG, Ware C, Paulson HL, Lieberman AP (2010) Conditional Niemann-Pick C mice demonstrate cell autonomous Purkinje cell neurodegeneration. *Hum Mol Genet*.19:837-847.

Elrick MJ, Yu T, Chung C, Lieberman AP (2012) Impaired proteolysis underlies autophagic dysfunction in Niemann-Pick type C disease. *Hum Mol Genet*.21:4876-4887.

Elston GN, Fujita I (2014) Pyramidal cell development: postnatal spinogenesis, dendritic growth, axon growth, and electrophysiology. *Front Neuroanat*.8:78.

Elston GN, Oga T, Fujita I (2009) Spinogenesis and pruning scales across functional hierarchies. *J Neurosci*.29(10):3271-3275.

Elwood RW, Keeling F (1982) Temporal organization of ultrasonic vocalizations in infant mice. *Dev Psychobiol*.15(3):221-227.

Erickson KI, Prakash RS, Voss MW, et al (2010) Brain-derived neurotrophic factor is associated with age-related decline in hippocampal volume. *J Neurosci*.30(15):5368-5375.

Esposito M, Dubbioso R, Tozza S, Iodice R, Aiello M, Nicolai E, Cavaliere C, Salvatore M, Santoro L et al (2019) In vivo evidence of cortical amyloid deposition in the adult form of Niemann Pick type C. *Heliyon.*5:e02776.

Etain B, Dumaine A, Mathieu F, Chevalier F, Henry C, Kahn JP, Deshommes J, Bellivier F, Leboyer M et al (2010) A SNAP25 promoter variant is associated with early-onset bipolar disorder and a high expression level in brain. *Mol Psychiatry.*15:748-755.

Evans WR, Hendriksz CJ (2017) Niemann-Pick type C disease-the tip of the iceberg? A review of neuropsychiatric presentation, diagnosis and treatment. *BJPsych Bull.*41:109-114.

Farini D, Marazziti D, Geloso MC, Sette C (2021) Transcriptome programs involved in the development and structure of the cerebellum. *Cell Mol Life Sci.*78:6431-6451.

Fechner PY (1996) The role of SRY in mammalian sex determination. *Acta Paediatr Jpn*.38(4):380-389.

Fetit R, Hillary RF, Price DJ, Lawrie SM (2021) The neuropathology of autism: A systematic review of post-mortem studies of autism and related disorders. *Neurosci Biobehav Rev*.129:35-62.

Fink AJ, Englud C, Daza RA, Pham D, Lau C, Nivison M, Kowalczyk T, Hevner RF (2006) Development of the deep cerebellar nuclei: transcription factors and cell migration from the rhombic lip. *J Neurosci.*26:3066-3076.

Fiorenza MT, La Rosa P, Canterini S, Erickson RP (2022) The cerebellum in Niemann-Pick C1 Disease: Mouse Versus Man. *Cerebellum.* Online ahead of print.

Fiorenza MT, Moro E, Erickson RP (2018) The pathogenesis of lysosomal storage disorders: beyond the engorgement of lysosomes to abnormal development and neuroinflammation. *Hum Mol Genet.*27:119-129.

Fiori E, Babicola L, Andolina D, et al (2015) Neurobehavioral Alterations in a Genetic Murine Model of Feingold Syndrome 2. *Behav Genet*.45(5):547-559.

Fischer A, Sananbenesi F, Mungenast A, Tsai LH (2010) Targeting the correct HDAC(s) to treat cognitive disorders. *Trends Pharmacol Sci.*31:605-617.

Fog CK, Kirkegaard T (2019) Animal models for Niemann-Pick type C: implications for drug discovery & development. *Expert Opin Drug Discov.*14:499-509.

Fossati G, Morini R, Corradini I, Antonucci F, Trepte P, Edry E, Sharma V, Papale A, Pozzi D et al (2015) Reduced SNAP-25 increases PSD-95 mobility and impairs spine morphogenesis. *Cell Death Differ.*22:1425-1436.

Fox CA, Barnard JW (1957) A quantitative study of the Purkinje cell dendritic branchlets and their relationship to afferent fibres. *J Anat*.91:299-313.

Friendland N, Liou HL, Lobel P, Stock AM (2003) Structure of a cholesterol-binding protein deficient in Niemann-Pick type C2 disease. *Proc Natl Acad Sci USA.*100:2512-2517.

Frith TJR, Briscoe J, Boezio GLM (2024) From signalling to form: the coordination of neural tube patterning. *Curr Top Dev Biol.*159:168-231.

Frolov A, Zielinski SE, Crowley JR, Dudley-Rucker N, Schaffer JE, Ory DS (2003) NPC1 and NPC2 regulate cellular cholesterol homeostasis through generation of low density lipoprotein cholesterol-derived oxysterols. *J Biol Chem.*278:25517-25525.

Fu R, Yanjanin NM, Bianconi S, Pavan WJ, Porter FD (2010) Oxidative stress in Niemann-Pick disease, type C. *Mol Genet Metab.*101:214-218.

Fukuda H, Karaki F, Dodo K, Noguchi-Yachide T, Ishikawa M, Hashimoto Y, Ohgane K (2017) Phenanthridin-6-one derivatives as the first class of non-steroidal pharmacological chaperones for Niemann-Pick disease type C1 protein. *Bioorg Med Chem Lett.*27:2781-2787.

Fukuda M, Viitala J, Matteson J, Carlsson SR (1988) Cloning of cDNAs encoding human lysosomal membrane glycoproteins, h-lamp-1 and h-lamp-2. Comparison of their deduced amino acid sequences. *J Biol Chem.*263:18920-18928.

Fünfschilling U, Jockusch WJ, Sivakumar N, Möbius W, Corthals K, Li S, Quintes S, Kim Y, Schaap IA et al (2012) Critical time window of neuronal cholesterol synthesis during neurite outgrowth. *J Neurosci.*32:7632-7645.

Galanopoulou AS (2005) GABA receptors as broadcasters of sexually differentiating signals in the brain. *Epilepsia*.46 Suppl 5(Suppl 5):107-112.

Galanopoulou AS (2008) Sexually dimorphic expression of KCC2 and GABA function. *Epilepsy Res*.80(2-3):99-113.

Gao Z, Davis C, Thomas AM, et al (2018) A cortico-cerebellar loop for motor planning. *Nature*.563(7729):113-116.

Garay L, Gonzalez Deniselle MC, Lima A, Roig P, De Nicola AF (2007) Effects of progesterone in the spinal cord of a mouse model of multiple sclerosis. *J Steroid Biochem Mol Biol.*107:228-237.

Geberhiwot T, Moro A, Dardis A, Ramaswami U, Sirrs S, Marfa MP, Vanier MT, Walterfang M, Bolton S et al (2018) Consensus clinical management guidelines for Niemann-Pick disease type C. *Orphanet J Rare Dis.*13:50.

Gilmore CP, Donaldson I, Bö L, Owens T, Lowe J, Evangelou N (2009) Regional variations in the extent and pattern of grey matter demyelination in multiple sclerosis: a comparison between the cerebral cortex, cerebellar cortex, deep grey matter nuclei and the spinal cord. *J Neurol Neurosurg Psychiatry.*80:182-187.

Ginzburg L, Kacher Y, Futerman AH (2004) The pathogenesis of glycosphingolipid storage disorders. *Semin Cell Dev Biol.*15:417-431.

Glick D, Barth S, Macleod KF (2010) Autophagy: cellular and molecular mechanism. *J Pathol*.221:3-12.

Glickstein M, Strata P, Voogd J (2009) Cerebellum: history. *Neuroscience.*162:549-559.

Goetz SC, Ocbina PJ, Anderson KV (2009) The primary cilium as a Hedgehog signal transduction machine. *Methods Cell Biol*.94:199-222.

Gong X, Qian H, Cao P, et al (2018) Structural basis for the recognition of Sonic Hedgehog by human Patched1. *Science*.361(6402):eaas8935.

Gonzales ML, LaSalle JM (2010) The role of MeCP2 in brain development and neurodevelopmental disorders. *Curr Psychiatry Rep*.12(2):127-134.

Goritz C, Mauch DH, Pfrieger FW (2005) Multiple mechanisms mediate cholesterol-induced synaptogenesis in a CNS neuron. *Mol Cell Neurosci*.29(2):190-201.

Gosso MF, de Geus EJ, van Belzen MJ, Polderman TJ, Heuntink P, Boomsma DI, Posthuma D (2006) The SNAP-25 gene is associated with cognitive ability: evidence from a family-based study in two independent Dutch cohorts. *Mol Psychiatry.*11:878-886.

Gould GG, Hensler JG, Burke TF, Benno RH, Onaivi ES, Daws LC (2011) Density and functional of central serotonin (5-HT) transporters, 5-HT1A and 5-HT2A receptors, and effects of their targeting on BTBR T+ tf/J mouse social behavior. *J Neurochem.*116:291-303.

Gould S, Scott RC (2005) 2-Hydroxypropyl-beta-cyclodextrin (HP-beta-CD): a toxicologic review. *Food Chem Toxicol.*43:1451-1459.

Granger E, McNee G, Allan V, Woodman P (2014) The role of the cytoskeleton and molecular motors in endosomal dynamics. *Semin Cell Dev Biol.*31:20-29.

Green MJ, Wingate RJ (2014) Developmental origins of diversity in the cerebellar output nuclei. *Neural Dev.*9:1.

Greenamyre JT, Porter RH (1994) Anatomy and physiology of glutamate in the CNS. *Neurology*.44(11 Suppl 8):S7-S13.

Greer WL, Dobson MJ, Girouard GS, Byers DM, Riddell DC, Neumann PE (1999) Mutations in NPC1 highlight a conserved NPC1-specific cysteine-rich domain. *Am J Hum Genet.*65:1252-1260.

Greer WL, Riddell DC, Gillan TL, Girouard GS, Sparrow SM, Byers DM, Dobson MJ, Neumann PE (1998) The Nova Scotia (type D) form of Niemann-Pick disease is caused by a G3097-->T transversion in NPC1. *Am J Hum Genet.*63:52-54.

Griffin LD, Gong W, Verot L, Mellon SH (2004) Niemann-Pick type C disease involves disrupted neurosteroidogenesis and responds to allopregnanolone. *Nat Med.*10:704-711.

Griffin LD, Mellon SH (1999) Selective serotonin in reuptake inhibitors directly alter activity of neurosteroidogenic enzymes. *Proc Natl Acad Sci USA*.96:13512-13517.

Gross KS, Alf RL, Polzin TR, Frick KM (2021) 17β-estradiol activation of dorsal hippocampal TrkB is independent of increased mature BDNF expression and is required for enhanced memory consolidation in female mice. *Psychoneuroendocrinol*.125:105110.

Guan C, Luan L, Li J, Yang L (2021) MiR-212-3p improves rat functional recovery and inhibits neurocyte apoptosis in spinal cord injury models via PTEN downregulation-mediated activation of AKT/mTOR pathway. *Brain Res*.1768:147576.

Guedes JR, Ferreira PA, Costa JM, Cardoso AL, Peça J (2022) Microglia-dependent remodeling of neuronal circuits. *J Neurochem.*163(2):74-93.

Guillemot N, Troadec C, de Villemeur TB, Clèment A, Fauroux B (2007) Lung disease in Niemann-Pick disease. *Pediatr Pulmonol.*42:1207-1214.

Gumus E, Haliloglu G, Karhan AN, Demir H, Gurakan F, Topcu M, Yuce A (2017) Niemann-Pick disease type C in the newborn period: a single-center experience. *Eur J Pediatr.*176:1669-1676.

Habart M, Lio G, Soumier A, Demily C, Sirigu A (2023) An optimized iDISCO+ protocol for tissue clearing and 3D analysis of oxytocin and vasopressin cell network in the developing mouse brain. *STAR Protoc.*4(1):101968.

Haihambo N, Baetens K, Deroost N, Baeken C, Van Overwalle F (2025) Crus control: effective cerebello-cerebral connectivity during social action prediction using dynamic causal modelling. *Soc Cogn Affect Neurosci.*20(1):nsaf019.

Halepoto DM, Bashir S, A L-Ayadhi L (2014) Possible role of brain-derived neurotrophic factor (BDNF) in autism spectrum disorder: current status. *J Coll Physicians Surg Pak*.24:274-278.

Harzer K, Kustermann-Kuhn B (2001) Quantified increases of cholesterol, total lipid and globotriaosylceramide in filipin-positive Niemann-Pick type C fibroblasts. *Clin Chim Acta.*305:65-73.

Hashimoto K, Iwata Y, Nakamura K, et al (2006) Reduced serum levels of brain-derived neurotrophic factor in adult male patients with autism. *Prog Neuropsychopharmacol Biol Psychiatry*.30(8):1529-1531.

Hashimoto K, Kano M (2013) Synapse elimination in the developing cerebellum. *Cell Mol Life Sci.*70:4667-4680.

Hatten ME (1999) Central nervous system neuronal migration. *Annu Rev Neurosci*.22:511-539.

Haubensak W, Attardo A, Denk W, Huttner WB (2004) Neurons arise in the basal neuroepithelium of the early mammalian telencephalon: a major site of neurogenesis. *Proc Natl Acad Sci USA.*101(9):3196-3201.

Hawes CM, Wiemer H, Krueger SR, Karten B (2010) Pre-synaptic defects of NPC1-deficient hippocampal neurons are not directly related to plasma membrane cholesterol. *J Neurochem.*114:311-322.

He J, Evans CO, Hoffman SW, Oyesiku NM, Stein DG (2004) Progesterone and allopregnanolone reduce inflammatory cytokines after traumatic brain injury. *Exp Neurol.*189:404-412.

Heck D, Sultan F (2002) Cerebellar structure and function: making sense of parallel fibers. *Hum Mov Sci* 21:411-421.

Heckmann BL, Tummers B, Green DR (2019) Crashing the computer: apoptosis vs. necroptosis in neuroinflammation. *Cell Death Differ.*26:41-52.

Heitz C, Epelbaum S, Nadjar Y (2017) Cognitive impairment profile in adult patients with Niemann pick type C disease. *Orphanet J Rare Dis.*12:166.

Heleven E, van Dun K, Van Overwalle F (2019) The posterior Cerebellum is involved in constructing Social Action Sequences: An fMRI Study. *Sci Rep*.9(1):11110.

Helquist P, Maxfield FR, Wiech NL, Wiest O (2013) Treatment of Niemann-Pick type C disease by histone deacetylase inhibitors. *Neurotherapeutics.*10:688-697.

Herbst SM, Schirmer S, Posovszky C, Jochum F, Rödl T, Schroeder JA, Barth TF, Hehr U, Melter M, et al (2015) Taking the next step forward-diagnosing inherited infantile cholestatic disorders with next generation sequencing. *Mol Cell Probes.*29:291-298.

Herculano-Houzel S (2010) Coordinated scaling of cortical and cerebellar numbers of neurons. *Front Neuroanat.*4:12.

Herculano-Houzel S, Mota B, Lent R (2006) Cellular scaling rules for rodent brains. *Proc Natl Acad Sci USA* 103:12138-12143.

Hering H, Lin CC, Sheng M (2003) Lipid rafts in the maintenance of synapses, dendritic spines, and surface AMPA receptor stability. *J Neurosci.*23(8):3262-3271.

Hertz L, Rothman DL (2017) Glutamine-Glutamate Cycle Flux Is Similar in Cultured Astrocytes and Brain and Both Glutamate Production and Oxidation Are Mainly Catalyzed by Aspartate Aminotransferase. *Biology (Basel).*6(1):17.

Herz J (2009) Apolipoprotein E receptors in the nervous system. *Curr Opin Lipidol* 20:190-196.

Herz J, Bock HH (2002) Lipoprotein receptors in the nervous system. *Annu Rev Biochem* 71:405-434.

Hibi M, Shimizu T (2012) Development of the cerebellum and cerebellar neural circuits. *Dev Neurobiol* 72:282-301.

Higashi Y, Murayama S, Pentchev PG, Suzuki K (1993) Cerebellar degeneration in the Niemann-Pick type C mouse. *Acta Neuropathol* 85:175-184.

Higgins ME, Davies JP, Chen FW, Ioannou YA (1999) Niemann-Pick C1 is a late endosome-resident protein that transiently associates with lysosomes and the trans-Golgi network. *Mol Genet Metab* 68:1-13.

Hoeffer CA, Klann E (2010) mTOR signaling: at the crossroads of plasticity, memory and disease. *Trends Neurosci*.33(2):67-75.

Hollyday M (2001) Neurogenesis in the vertebrate neural tube. *Int J Dev Neurosci* 19(2):161-173.

Hovakimyan M, Maass F, Petersen J, Holzmann C, Witt M, Lukas J, Frech MJ, Hübner R, Rolfs A et al (2013) Combined therapy with cyclodextrin/allopregnanolone and miglustat improves motor but not cognitive functions in Niemann-Pick Type C1 mice. *Neuroscience* 252:201-211.

Huang X, Litingtung Y, Chiang C (2007) Region-specific requirement for cholesterol modification of sonic hedgehog in patterning the telencephalon and spinal cord. *Development*.134(11):2095-2105.

Huang X, Liu J, Ketova T, Fleming JT, Grover VK, Cooper MK, Litingtung Y, Chiang C (2010) Transventricular delivery of Sonic hedgehog is essential to cerebellar ventricular zone development. *Proc. Natl. Acad. Sci. U.S.A.* 107(18):8422-8427.

Hugon J, Vallat JM, Dumas M (1996) Rôle du glutamate et de l'excitotoxicité dans les maladies neurologiques [Role of glutamate and excitotoxicity in neurologic diseases]. *Rev Neurol (Paris)*.152(4):239-248.

Humke EW, Dorn KV, Milenkovic L, Scott MP, Rohatgi R (2010) The output of Hedgehog signaling is controlled by the dynamic association between Suppressor of Fused and the Gli proteins. *Genes Dev*.24(7):670-682.

Hussain G, Wang J, Rasul A, Anwar H, Imran A, Qasim M, Zafar S, Kamran SKS, Razzaq A et al (2019) Role of cholesterol and sphingolipids in brain development and neurological diseases. *Lipids Health Dis* 18:26.

Imamizu H, Kawato M (2012) Cerebellar internal models: implications for the dexterous use of tools. *Cerebellum*.11(2):325-335.

Imrie J, Dasgupta S, Besley GT, Harris C, Heptinstall L, Knight S, Vanier MT, Fensom AH, Ward C et al (2007) The natural history of Niemann-Pick disease type C in the UK. *J Inherit Metab Dis* 30:51-59.

Infante RE, Wang ML, Radhakrishnan A, Kwon HJ, Brown MS, Goldstein JL (2008) NPC2 facilitates bidirectional transfer of cholesterol between NPC1 and lipid bilayers, a step in cholesterol egress from lysosomes. *Proc Natl Acad Sci USA* 105:15287-15292.

Ioannou YA (2000) The structure and function of the Niemann-Pick C1 protein. *Mol Genet Metab* 71:175-181.

Ioannou YA (2005) Guilty until proven innocent: the case of NPC1 and cholesterol. *Trends Biochem Sci* 30:498-505.

Irwin RW, Brinton RD (2014) Allopregnanolone as regenerative therapeutic for Alzheimer's disease: translational development and clinical promise. *Prog Neurobiol* 113:40-55.

Ishibashi S, Yamazaki T, Okamoto K (2009) Association of autophagy with cholesterol-accumulated compartments in Niemann-Pick disease type C cells. *J Clin Neurosci* 16:954-959.

Ito M (1984) The modifiable neuronal network of the cerebellum. *Jpn J Physiol* 34:781-792.

Ito M (1991) Structural-functional relationships in cerebellar and vestibular systems. *Arch Ital Biol*.129(1):53-61.

Ito M (1993) Movement and thought: identical control mechanisms by the cerebellum. *Trends Neurosci*.16(11):448-454.

Ito M (1993) Neurophysiology of the nodulofloccular system. *Rev Neurol (Paris)*.149(11):692-697.

Ito M (1998) Cerebellar learning in the vestibulo-ocular reflex. *Trends Cogn Sci*. 2(9):313-321.

Ito M (2005) Bases and implications of learning in the cerebellum--adaptive control and internal model mechanism. *Prog Brain Res*.148:95-109.

Ito M (2006) Cerebellar circuitry as a neuronal machine. *Prog Neurobiol*.78(3-5):272-303.

Iulianella A, Wingate RJ, Moens CB, Capaldo E (2019) The generation of granule cells during the development and evolution of the cerebellum. *Dev Dyn* 248:506-513.

Jacot-Descombes S, Keshav NU, Dickstein DL, et al (2020) Altered synaptic ultrastructure in the prefrontal cortex of Shank3-deficient rats. *Mol Autism*.11(1):89.

Jahnova H, Dvorakova L, Vlaskova H, Hulkova H, Poupetova H, Hrebicek M, Jesina P (2014) Observational, retrospective study of a large cohort of patients with Niemann-Pick disease type C in the Czech Republic: a surprisingly stable diagnostic rate spanning almost 40 years. *Orphanet J Rare Dis* 9:140.

Jaworski J, Sheng M (2006) The growing role of mTOR in neuronal development and plasticity. *Mol Neurobiol*.34(3):205-219.

Jaworski J, Spangler S, Seeburg DP, Hoogenraad CC, Sheng M (2005) Control of dendritic arborization by the phosphoinositide-3'-kinase-Akt-mammalian target of rapamycin pathway. *J Neurosci*.25(49):11300-11312.

Jeyakumar M, Dwek RA, Butters TD, Platt FM (2005) Storage solutions: treating lysosomal disorders of the brain. *Nat Rev Neurosci* 6:713-725.

Ji Y, Lu Y, Yang F, Shen W, Tang TT, Feng L, Duan S, Lu B (2010) Acute and gradual increases in BDNF concentration elicit distinct signaling and functions in neurons. *Nat Neurosci* 13:302-309.

Ji Y, Pang PT, Feng L, Lu B (2005) Cyclic AMP controls BDNF-induced TrkB phosphorylation and dendritic spine formation in mature hippocampal neurons. *Nat Neurosci* 8:164-172.

Jiang X, Ory DS (2021) Advancing diagnosis and treatment of Niemann-Pick C disease through biomarker discovery. *Explor Neuroprotective Ther* 30:146-158.

Jozwiak J, Jozwiak S, Grzela T, Lazarczyk M (2005) Positive and negative regulation of TSC2 activity and its effects on downstream effectors of the mTOR pathway. *Neuromolecular Med*.7(4):287-296.

Jung SJ, Vlasov K, D'Ambra AF, et al (2022) Novel Cerebello-Amygdala Connections Provide Missing Link Between Cerebellum and Limbic System. *Front Syst Neurosci*.16:879634.

Jurado S, Goswami D, Zhang Y, Molina AJ, Südhof TC, Malenka RC (2013) LTP requires a unique postsynaptic SNARE fusion machinery. *Neuron* 77:542-558.

Jurevics H, Morell P (1995) Cholesterol for synthesis of myelin is made locally, not imported into brain. *J Neurochem* 64:895-901.

Kaidanovich-Beilin O, Lipina T, Vukobradovic I, Roder J, Woodgett JR (2011) Assessment of social interaction behaviors. *J Vis Exp*.(48):2473.

Kaminski WE, Klünemann HH, Ibach B, Aslanidis C, Klein HE, Schmitz G (2002) Identification of novel mutations in the NPC1 gene in German patients with Niemann-Pick C disease. *J Inherit Metab Dis* 25:385-389.

Kandel E, Schwartz J (2013) Principles of neural science (5th Edition). *McGraw-Hill Education*

Kavetsky L, Green KK, Boyle BR, Yousufzai FAK, Padron ZM, Melli SE, Kuhnel VL, Jackson HM, Blanco RE et al (2019) Increased interactions and engulfment of dendrites by microglia precede Purkinje cell degeneration in a mouse model of Niemann Pick Type- C. *Sci Rep* 9:14722.

Kawazoe T, Yamamoto T, Narita A, Ohno K, Adachi K, Nanba E, Noguchi A, Takahashi T, Maekawa M et al (2018) Phenotypic variability of Niemann-Pick disease type C including a case with clinically pure schizophrenia: a case report. *BMC Neurol* 18:117.

Kelleher RJ 3rd, Govindarajan A, Tonegawa S (2004) Translational regulatory mechanisms in persistent forms of synaptic plasticity. *Neuron*.44(1):59-73.

Kellner Y, Gödecke N, Dierkes T, Thieme N, Zagrebelsky M, Korte M (2014) The BDNF effects on dendritic spines of mature hippocampal neurons depend on neuronal activity. *Front Synaptic Neurosci* 6:5.

Kelly RM, Strick PL (2003) Cerebellar loops with motor cortex and prefrontal cortex of a nonhuman primate. *J Neurosci*.23(23):8432-8444.

Kennedy BE, Hundert AS, Goguen D, Weaver IC, Karten B (2016) Presymptomatic Alterations in Amino Acid Metabolism and DNA Methylation in the Cerebellum of a Murine Model of Niemann-Pick Type C Disease. *Am J Pathol*.186(6):1582-1597.

Kennedy BE, Madreiter CT, Vishnu N, Malli R, Graier WF, Karten B (2014) Adaptations of energy metabolism associated with increased levels of mitochondrial cholesterol in Niemann-Pick type C1-deficient cells. *J Biol Chem* 289:16278-16289.

Kern JK (2003) Purkinje cell vulnerability and autism: a possible etiological connection. *Brain Dev*.25(6):377-382.

Khamsing D, Lebrun S, Fanget I, et al (2021) A role for BDNF- and NMDAR-induced lysosomal recruitment of mTORC1 in the regulation of neuronal mTORC1 activity. *Mol Brain*.14(1):112.

Khanal P, Hotulainen P (2021) Dendritic Spine Initiation in Brain Development, Learning and Diseases and Impact of BAR-Domain Proteins. *Cells*.10(9):2392.

Kheder A, Scott C, Olpin S, Hadjivassiliou M (2013) Niemann-Pick type C: a potentially treatable disorder?. *Pract Neurol* 13:382-385.

Kim J, Augustine GJ (2021) Molecular Layer Interneurons: Key Elements of Cerebellar Network Computation and Behavior. *Neuroscience* 462:22-35.

Kipping JA, Grodd W, Kumar V, Taubert M, Villringer A, Margulies DS (2013) Overlapping and parallel cerebello-cerebral networks contributing to sensorimotor control: an intrinsic functional connectivity study. *Neuroimage*.83:837-848.

Kipping JA, Tuan TA, Fortier MV, Qiu A (2017) Asynchronous Development of Cerebellar, Cerebello-Cortical, and Cortico-Cortical Functional Networks in Infancy, Childhood, and Adulthood. *Cereb Cortex*.27(11):5170-5184.

Kirkegaard T, Gray J, Priestman DA, Wallom KL, Atkins J, Olsen OD, Klein A, Drndarski S, Petersen NH et al (2016) Heat shock protein-based therapy as a potential candidate for treating the sphingolipidoses. *Sci Transl Med* 8:355ra118.

Klein A, Maldonado C, Vargas LM, Gonzalez M, Robledo F, Perez de Arce K, Muñoz FJ, Hetz C, Alvarez AR et al (2011) Oxidative stress activates the c-Abl/p73 proapoptotic pathway in Niemann-Pick type C neurons. *Neurobiol Dis* 41:209-218.

Kloth AD, Badura A, Li A, et al (2015) Cerebellar associative sensory learning defects in five mouse autism models. *Elife*.4:e06085.

Klünemann HH, Elleder M, Kaminski WE, Snow K, Peyser JM, O'Brien JF, Munoz D, Schmitz G, Klein HE et al (2002) Frontal lobe atrophy due to a mutation in the cholesterol binding protein HE1/NPC2. *Ann Neurol* 52:743-749.

Ko DC, Binkley J, Sidow A, Scott MP (2003) The integrity of a cholesterol-binding pocket in Niemann-Pick C2 protein is necessary to control lysosome cholesterol levels. *Proc Natl Acad Sci USA* 100:2518-2525.

Ko DC, Milenkovic L, Beier SM, Manuel H, Buchanan J, Scott MP (2005) Cell-autonomous death of cerebellar purkinje neurons with autophagy in Niemann-Pick type C disease. *PLos Genet* 1:81-95.

Koh CH, Whiteman M, Li QX, Halliwell B, Jenner AM, Wong BS, Laughton KM, Wenk M, Maters CL et al (2006) Chronic exposure to U18666A is associated with oxidative stress in cultured murine cortical neurons. *J Neurochem* 98:1278-1289.

Kong Y, Roser M, Bègue I, et al (2024) Cerebellum and social abilities: A structural and functional connectivity study in a transdiagnostic sample. *Hum Brain Mapp*.45(10):e26749.

Koudinov AR, Koudinova NV (2001) Essential role for cholesterol in synaptic plasticity and neuronal degeneration. *FASEB J* 15:1858-1860.

Koziol LF, Budding D, Andreasen N, et al (2014) Consensus paper: the cerebellum's role in movement and cognition. *Cerebellum*.13(1):151-177.

Kulkarni A, Caporali P, Dolas A, Johny S, Goyal S, Dragotto J, Macone A, Jayaraman R, Fiorenza MT (2018) Linear cyclodextrin polymer prodrugs as novel therapeutics for Niemann-Pick type C1 disorder. *Sci Rep* 8:9547.

Kumar V, Zhang MX, Swank MW, Kunz J, Wu GY (2005) Regulation of dendritic morphogenesis by Ras-PI3K-Akt-mTOR and Ras-MAPK signaling pathways. *J Neurosci*.25(49):11288-11299.

Kuter DJ, Mehta A, Hollak CE, Giraldo P, Hughes D, Belmatoug N, Brand M, Muller A, Schaaf B, et al (2013) Miglustat therapy in type 1 Gaucher disease: clinical and safety outcomes in a multicenter retrospective cohort study. *Blood Cells Mol Dis* 51:116-124.

Kwon HJ, Abi-Mosleh L, Wang ML, Deisenhofer J, Goldstein JL, Brown MS, Infante RE (2009) Structure of N-terminal domain of NPC1 reveals distinct subdomains for binding and transfer cholesterol. *Cell* 137:1213-1224.

Lachmann RH, te Vruchte D, Lloyd-Evans E, Reinkensmeier G, Sillence DJ, Fernandez-Guillen L, Dwek RA, Butters TD, Cox TM et al (2004) Treatment with miglustat reverses the lipid-trafficking defect in Niemann-Pick disease type C. *Neurobiol Dis* 16:654-658.

Lad M, Thomas RH, Anderson K, Griffiths TD (2019) Niemann-Pick type C: contemporary diagnosis and treatment of a classical disorder. *Pract Neurol* 19:420-423.

Laine J, Axelrad H (1994) The candelabrum cell: A new interneuron in the cerebellar cortex. *J Comp Neurol* 339:159-173.

Lanier JC, Abrams AN (2017) Posterior fossa syndrome: Review of the behavioral and emotional aspects in pediatric cancer patients. *Cancer*.123(4):551-559.

Larsell, O (1970) The comparative Anatomy and Histology of the Cerebellum from Monotremes through Apes. Minneapolis: University of Minnesota Press.

Lasarge CL, Danzer SC (2014) Mechanisms regulating neuronal excitability and seizure development following mTOR pathway hyperactivation. *Frontiers in molecular neuroscience*.7,18.

Lebrand C, Corti M, Goodson H, Cosson P, Cavalli V, Mayran N, Faurè J, Gruenberg J (2002) Late endosome motility depends on lipids via the small GTPase Rab7. *EMBO J* 21:1289-1300.

Leto K, Rossi F (2012) Specification and differentiation of cerebellar GABAergic neurons. *Cerebellum* 11:434-435.

Lewis PM, Gritli-Linde A, Smeyne R, Kottmann A, McMahon AP (2004) Sonic hedgehog signaling is required for expansion of granule neuron precursors and patterning of the mouse cerebellum. *Dev Biol*.270(2):393-410.

Li X, Wang J, Coutavas E, Shi H, Hao Q, Blobel G (2016) Structure of human Niemann-Pick C1 protein. *Proc Natl Acad Sci USA* 113:8212-8217.

Liao G, Cheung S, Galeano J, Ji AX, Qin Q, Bi X (2009) Allopregnanolone treatment delays cholesterol accumulation and reduces autophagic/lysosomal dysfunction and inflammation in Npc1-/- mouse brain. Brain Res 1270:140-151.

Lieberman AP, Puertollano R, Raben N, Slaugenhaupt S, Walkley SU, Ballabio A (2012) Autophagy in lysosomal storage disorders. *Autophagy* 8:719-730.

Liedtke M, Völkner C, Hermann A, French MJ (2022) Impact of Organelle Transport Deficits on Mitophagy and Autophagy in Niemann-Pick Disease type C. *Cells* 11:507.

Lin PY, Kavalali ET, Monteggia LM (2018) Genetic Dissection of Presynaptic and Postsynaptic BDNF-TrkB Signaling in Synaptic Efficacy of CA3-CA1 Synapses. *Cell Rep*. 24(6):1550-1561.

Lin YC, Hsu CH, Wang PN, Lin CP, Chang LH (2020) The Relationship Between Zebrin Expression and Cerebellar Functions: Insights From Neuroimaging Studies. *Front Neurol* 11:315.

Lin Z, Sheng H, You C, et al (2017) Inhibition of the CyclinD1 promoter in response to sonic hedgehog signaling pathway transduction is mediated by Gli1. *Exp Ther Med*.13(1):307-314.

Lindholm D, Hamnèr S, Zirrgiebel U (1997) Neurotrophins and cerebellar development. *Perspect Dev Neurobiol*.5:83–94.

Lindroth P, Mopper K (1979) High Performance Liquid Chromatographic determination of subpicomole amounts of amino acids by precolumn fluorescence derivitization with opthalaldehyde. *Anal.Chem*.51, 1667–1674.

Lisberger SG (2021) The Rules of Cerebellar Learning: Around the Ito Hypothesis. *Neuroscience*.462:175-190.

Lisé MF, El-Husseini A (2006) The neuroligin and neurexin families: from structure to function at the synapse. *Cell Mol Life Sci*.63(16):1833-1849.

Livak KJ, Schmittgen TD (2001) Analysis of relative gene expression data using real-time quantitative PCR and the 2(-Delta Delta C(T)) Method. *Methods*.25(4):402-408.

Lloyd-Evans E, Morgan AJ, He X, Smith DA, Elliot-Smith E, Sillence DJ, Churchill GC, Schuchman EH, Galione A et al (2008) Niemann-Pick disease type C1 is a sphingosine storage disease that causes deregulation of lysosomal calcium. *Nat Med* 14:1247-1255.

Lo Iacono L, Mancini C, Babicola L, Pietrosanto M, Di Segni M, D'Addario SL, Municchi D, Ielpo D, Pascucci T et al (2021) Early life adversity affecting the attachment bond alters ventral tegmental area transcriptomic patterning and behavior almost exclusively in female mice. *Neurobiol Stress* 15:100406.

Loftus SK, Morris JA, Carstea ED, Gu JZ, Cummings C, Brown A, Ellison J, Ohno K, Rosenfeld MA et al (1997) Murine model of Niemann-Pick C disease: mutation in a cholesterol homeostasis gene. *Science* 277:232-235.

Long T, Qi X, Hassan A, Liang Q, De Brabander JK, Li, X (2020) Structural basis for itraconazole-mediated NPC1 inibition. *Nat Commun* 11:152.

Lopez ME, Scott MP (2013) Genetic dissection of a cell-autonomous neurodegenerative disorder: lessons learned from mouse models of Niemann-Pick disease type C. *Dis Model Mech* 6:1089-1100.

Love S, Bridges LR, Case CP (1995) Neurofibrillary tangles in Niemann-Pick disease type C. *Brain* 118:119-129.

Lu F, Liang Q, Abi-Mosleh L, Das A, De Brabander JK, Goldstein JL, Brown MS (2015) Identification of NPC1 as the target of U18666A, an inhibitor of lysosomal cholesterol export and Ebola infection. *Elife* 4:e12177.

Lucarelli M, Camuso S, Di Pietro C, et al (2023) Reduced Cerebellar BDNF Availability Affects Postnatal Differentiation and Maturation of Granule Cells in a Mouse Model of Cholesterol Dyshomeostasis. *Mol Neurobiol*.60(9):5395-5410.

Luna EJ, Pestonjamasp KN, Cheney RE, et al (1997) Actin-binding membrane proteins identified by F-actin blot overlays. *Soc Gen Physiol Ser*.52:3-18.

Lyseng-Williamson (2014) Miglustat: a review of its use in Niemann-Pick disease type C. *Drugs* 74:61-74.

Ma Q, Pu M, Haihambo N, et al (2023) Effective cerebello-cerebral connectivity during implicit and explicit social belief sequence learning using dynamic causal modeling. *Soc Cogn Affect Neurosci*.18(1):nsac044.

Maceyka M, Milstien S, Spiegel S (2013) The potential of histone deacetylase inhibitors in Niemann-Pick type C disease. *FEBS J* 280:6367-6372.

Madra M, Sturley SL (2010) Niemann-Pick type C pathogenesis and treatment: from statins to sugars. *Clin Lipidol* 5:387-395.

Maetzel D, Sarkar S, Wang H, Abi-Mosleh L, Xu P, Cheng AW, Gao Q, Mitalipova M, Jaenisch R (2014) Genetic and chemical correction of cholesterol accumulation and impaired autophagy in hepatic and neural cells derived from Niemann-Pick Type C patient-specific iPS cells. *Stem Cell Reports* 2:866-880.

Maisonpierre PC, Belluscio L, Friedman B, Alderson RF, Wiegand SJ, Furth ME, Lindsay RM, Yancopoulos GD (1990) NT-3, BDNF, and NGF in the developing rat nervous system: parallel as well as reciprocal patterns of expression. *Neuron*.5:501–509.

Manni E, Petrosini L (2004) A century of cerebellar somatotopy: a debated representation. *Nat Rev Neurosci*.5(3):241-249.

Manto M, Mariën P (2015) Schmahmann's syndrome - identification of the third cornerstone of clinical ataxiology. *Cerebellum Ataxias*.2:2. Published 2015 Feb 27.

Manto M, Oulad Ben Taib N (2010) Cerebellar nuclei: key roles for strategically located structures. *Cerebellum* 9:17-21.

Mapelli L, Solinas S, D'Angelo E (2014) Integration and regulation of glomerular inhibition in the cerebellar granular layer circuit. *Front Cell Neurosci* 8:55.

Marks PA, Miller T, Richon VM (2003) Histone deacetylases. *Curr Opin Pharmacol* 3:344-351.

Martin KB, Williams IM, Cluzeau CV, Cougnoux A, Dale RK, Iben JR, Cawley NX, Wassif CA, Porter FD (2019) Identification of novel pathways associated with patterned cerebellar Purkinje neuron degeneration in Niemann-Pick disease, type C1. *Int J Mol Sci* 21:292.

Matencio A, Rubin Pedrazzo A, Difalco A, Navarro-Orcajada A, Khazeai Monfared Y, Conesa I, Rezayat A, López-Nicolás JM, Trotta F (2021) Advances and classification of cyclodextrin-based polymers for food-related issues. *Polymers (Basel)* 13:4226.

Mathews ES, Appel B (2016) Cholesterol Biosynthesis Supports Myelin Gene Expression and Axon Ensheathment through Modulation of P13K/Akt/mTor Signaling. *J Neurosci*.36(29):7628-7639.

Matsuzaki M, Honkura N, Ellis-Davies GC, Kasai H (2004) Structural basis of long-term potentiation in single dendritic spines. *Nature*.429(6993):761-766.

Maue RA, Burgess RW, Wang B, Wooley CM, Seburn KL, Vanier MT, Rogers MA, Chang CC, Chang TY et al (2012) A novel mouse model of Niemann-Pick type C disease carrying a D1005G-Npc1 mutation comparable to commonly observed human mutations. *Hum Mol Genet* 21:730-750.

Maxfield FR, Menon AK (2006) Intracellular sterol transport distribution. *Curr Opin Cell Biol* 18:379-385.

Maxfield FR, Wüstner D (2012) Analysis of cholesterol trafficking with fluorescent probes. *Methods Cell Biol* 108:367-393.

Mazzacuva F, Mills P, Mills K, Camuzeaux S, Gissen P, Nicoli ER, Wassif C, Te Vruchte D, Porter FD et al (2016) Identification of novel bile acids as biomarker for the early diagnosis of Niemann-Pick C disease. *FEBS Lett* 590:1651-1662.

McCarthy MM, Wright CL (2017) Convergence of Sex Differences and the Neuroimmune System in Autism Spectrum Disorder. *Biol Psychiatry*.81(5):402-410.

McKay Bounford K, Gissen P (2014) Genetic and laboratory diagnostic approach in Niemann Pick disease type C. *J Neurol* 2:569-575.

Men Y, Zhang A, Li H, et al (2015) LKB1 Regulates Cerebellar Development by Controlling Sonic Hedgehog-mediated Granule Cell Precursor Proliferation and Granule Cell Migration. *Sci Rep*.5:16232.

Mengel E, Klünemann HH, Lourenço CM, Hendriksz CJ, Sedel F, Walterfang M, Kolb SA (2013) Niemann-Pick disease type C symptomatology: an expert-based clinical description. *Orphanet J Rare Dis* 8:166.

Mercer AA, Palarz KJ, Tabatadze N, Woolley CS, Raman IM (2016) Sex differences in cerebellar synaptic transmission and sex-specific responses to autism-linked Gabrb3 mutations in mice. *Elife*.5:e07596.

Meske V, Erz J, Priesnitz T, Ohm TG (2014) The autophagic defect in Niemann-Pick disease type C neurons differs from somatic cells and reduces neuronal viability. *Neurobiol Dis* 64:88-97.

Middleton FA, Strick PL (2001) Cerebellar projections to the prefrontal cortex of the primate. *J Neurosci*.21(2):700-712.

Millard EE, Gale SE, Dudley N, Zhang J, Schaffer JE, Ory DS (2005) The sterol-sensing domain of the Niemann-Pick C1 (NPC1) protein regulates trafficking of low density lipoprotein cholesterol. *J Biol Chem* 280:28581-28590.

Millat G, Baïlo N, Molinero S, Rodriguez C, Chikh K, Vanier MT (2005) Niemann-Pick C disease: use of denaturing high performance liquid chromatography for the detection of NPC1 and NPC2 genetic variations and impact on management of patients and families. *Mol Genet Metab* 86:220-232.

Millat G, Marçais C, Rafi MA, Yamamoto T, Morris JA, Pentchev PG, Ohno K, Wenger DA, Vanier MT (1999) Niemann-Pick C1 disease: the I1061T substitution is a frequent mutant allele in patients of Western European descent and correlates with a classic juvenile phenotype. *Am J Hum Genet* 65:1321-1329.

Miranda RC, Sohrabji F, Toran-Allerand D (1994) Interactions of estrogen with the neurotrophins and their receptors during neural development. *Horm Behav*.28(4):367-375.

Miyawaki S, Yoshida H, Mitsuoka S, Enomoto H, Ikehara S (1986) A mouse model for Niemann-Pick disease. Influencer of genetic background on disease expression in spm/spm mice. *J Hered* 77:379-384.

Mohrmann K, Gerez L, Oorschot V, Klumperman J, van der Sluijs P (2002) Rab4 function in membrane from early endosomes depends on a membrane to cytoplasm cycle. *J Biol Chem* 277:32029-32035.

Morris JA, Zhang D, Coleman KG, Nagle J, Pentchev PG, Carstea ED (1999) The genomic organization and polymorphism analysis of the human Niemann-Pick C1 gene. *Biochem Biophys Res Commun* 261:493-498.

Morris MD, Bhuvaneswaran C, Shio H, Fowler S (1982) Lysosome lipid storage disorder in NCTR-BALB/c mice. I. Description of the disease and genetics. *Am J Pathol* 108:140-149.

Moy SS, Nadler JJ, Perez A, et al (2004) Sociability and preference for social novelty in five inbred strains: an approach to assess autistic-like behavior in mice. *Genes Brain Behav*.3(5):287-302.

Moya-Alvarado G, Tiburcio-Felix R, Ibáñez MR, et al (2023) BDNF/TrkB signaling endosomes in axons coordinate CREB/mTOR activation and protein synthesis in the cell body to induce dendritic growth in cortical neurons. *Elife*.12:e77455.

Muellerleile J, Vnencak M, Ippolito A, et al (2022) Neuroligin-3 Regulates Excitatory Synaptic Transmission and EPSP-Spike Coupling in the Dentate Gyrus In Vivo. *Mol Neurobiol*.59(2):1098-1111.

Mühle C, Huttner HB, Walter S, Reichel M, Canneva F, Lewczuk P, Gulbins E, Kornhuber J (2013) Characterization of acid sphingomyelinase activity in human cerebrospinal fluid. *PLos One* 8:e62912.

Munkacsi AB, Chen FW, Brinkman MA, Higaki K, Gutiérrez GD, Chaudhari J, Layer JV, Tong A, Bard M et al (2011) An “exacerbate-reverse” strategy in yeast identifies histone deacetylase inhibition as a correction for cholesterol and sphingolipid transport defects in human Niemann-Pick type C disease. *J Biol Chem* 286:23842-23851.

Naureckiene S, Sleat DE, Lackland H, Fensom A, Vanier MT, Wattiaux R, Jadot M, Lobel P (2000) Identification of HE1 as the second gene of Niemann-Pick C disease. *Science* 290:2298-2301.

Nguyen H, Ostendorf AP, Satz JS, Westra S, Ross-Barta SE, Campbell KP, Moore SA (2013) Glial scaffold required for cerebellar granule cell migration is dependent on dystroglycan function as a receptor for basement membrane proteins. *Acta Neuropathol Commun* 1:58.

Nielsen GK, Dagnaes-Hansen F, Holm IE, Meaney S, Symula D, Andersen NT, Heegaard CW (2011) Protein replacement therapy partially corrects the cholesterol-storage phenotype in a mouse model of Niemann-Pick type C2 disease. *PLos One* 6:e27287.

Niemann A (1914) Ein unbekanntes Krankheitsbild. *Jahrb Kinderheilkd* 79:1–3.

Nixon RA (2004) Niemann-Pick Type C disease and Alzheimer's disease: the APP-endosome connection fattens up. *Am J Pathol*.164(3):757-761.

Nodera H, Manto M (2014) Cerebellum tunes the excitability of the motor system: evidence from peripheral motor axons. *Cerebellum*.13(6):663-665.

Norman AW, Demel RA, de Kruyff B, van Deenen LL (1972). Studies on the biological properties of polyene antibiotics. Evidence for the direct interaction of filipin with cholesterol. *J Biol Chem* 247:1918:1929.

Nusca S, Canterini S, Palladino G, Bruno F, Mangia F, Erickson RP, Fiorenza MT (2014) A marked paucity of granule cells in the developing cerebellum of the *Npc1-/-* mouse is corrected by a single injection of hydroxypropyl-β-cyclodextrin. *Neurobiol Dis* 70:117-126.

Oddi S, Caporali P, Dragotto J, Totaro A, Maiolati M, Scipioni L, Angelucci CB, Orsini C, Canterini S et al (2019) The endocannabinoid system is affected by cholesterol dyshomeostasis: Insights from a murine model of Niemann Pick type C disease. *Neurobiol Dis* 130:104531.

Ohgami N, Ko DC, Thomas M, Scott MP, Chang CC, Chang TY (2004) Binding between the Niemann-Pick C1 protein and a photoactivatable cholesterol analog requires a functional sterol-sensing domain. *Proc Natl Acad Sci USA* 101:12473-12478.

Ohgane K, Karaki F, Noguchi-Yachide T, Dodo K, Hashimoto Y (2014) Structure-activity relationships of oxysterol-derived pharmacological chaperones for Niemann-Pick type C1 protein. *Bioorg Med Chem Lett* 24:3480-3485.

Ohira K, Funatsu N, Nakamura S, Hayashi M (2004) Expression of BDNF and TrkB receptor subtypes in the postnatal developing Purkinje cells of monkey cerebellum. *Gene Expr Patterns*.4(3):257-261.

Okada K, Tanaka H, Temporin K, et al (2011) Akt/mammalian target of rapamycin signaling pathway regulates neurite outgrowth in cerebellar granule neurons stimulated by methylcobalamin. *Neurosci Lett*.495(3):201-204.

Oliver TG, Grasfeder LL, Carroll AL, et al (2003) Transcriptional profiling of the Sonic hedgehog response: a critical role for N-myc in proliferation of neuronal precursors. *Proc Natl Acad Sci U S A*.100(12):7331-7336.

Olson IR, Hoffman LJ, Jobson KR, Popal HS, Wang Y (2023) Little brain, little minds: The big role of the cerebellum in social development. *Dev Cogn Neurosci*.60:101238.

Ordonez MP, Roberts EA, Kidwell CU, Yuan SH, Plaisted WC, Goldstein LS (2012) Disruption and therapeutic rescue of autophagy in human neuronal model of Niemann Pick type C1. *Hum Mol Genet* 21:2651-2662.

Ory DS (2000) Niemann-Pick type C: a disorder of cellular cholesterol trafficking. *Biochim Biophys Acta* 1529:331-339.

Pacheco CD, Elrick MJ, Lieberman AP (2009) Tau normal function influences Niemann-Pick type C disease pathogenesis in mice and modulates autophagy in NPC1-deficient cells. *Autophagy* 5:548-550.

Pacheco CD, Lieberman AP (2008) The pathogenesis of Niemann-Pick type C disease: a role for autophagy?. *Expert Rev Mol Med* 10:e26

Pak E, Segal RA (2016) Hedgehog Signal Transduction: Key Players, Oncogenic Drivers, and Cancer Therapy. *Dev Cell*.38(4):333-344.

Palay S, Chan-Palay V (1974) Cerebellar cortex. Berlin: *Springer-Verlag*.

Pangrazzi L, Genovesi S, Balasco L, et al (2022) Immune dysfunction in the cerebellum of mice lacking the autism candidate gene Engrailed 2. *J Neuroimmunol*.367:577870.

Paolicelli RC, Bolasco G, Pagani F, et al (2011) Synaptic pruning by microglia is necessary for normal brain development. *Science*.333(6048):1456-1458.

Papandreou A, Gissen P (2016) Diagnostic workup and management of patients with suspected Niemann-Pick type C disease. *Ther Adv Neurol Disord* 9:216-229.

Paridaen JT, Huttner WB (2014) Neurogenesis during development of the vertebrate central nervous system. *EMBO Rep* 15(4):351-364.

Park SW, Park JH, Moon HJ, Shin M, Moon JS, Ko JS (2021) Niemann-Pick disease type C diagnosed using neonatal cholestasis gene panel. *Korean J Gastroenterol* 78:240-244.

Patterson M (2000) Niemann-Pick disease type C. In: GeneReviews. University of Washington, Seattle (WA).

Patterson MC, Hendriksz CJ, Walterfang M, Sedel F, Vanier MT, Wijburg F, NP-C Guidelines Working Group (2012) Recommendations for the diagnosis and management of Niemann-Pick disease type C: an update. *Mol Genet Metab* 106:330-344.

Patterson, MC, Vecchio D, Jacklin E, Abel L, Chadha-Boreham H, Luzy C, Giorgino R, Wraith JE (2010) Long-term miglustat therapy in children with Niemann-Pick disease type C. *J Child Neurol* 25:300-305.

Peake KB, Vance JE (2010) Defective cholesterol trafficking in Niemann-Pick C-deficient cells. *FEBS Lett* 584:2731-2739.

Peça J, Feliciano C, Ting JT, et al (2011) Shank3 mutant mice display autistic-like behaviours and striatal dysfunction. *Nature*.472(7344):437-442.

Pentchev PG, Gal AE, Booth AD, Omodeo-Sale F, Fouks J, Neumeyer BA, Quirk JM, Dawson G, Brady RO (1980) A lysosomal storage disorder in mice characterized by a dual deficiency of sphingomyelinase and glucocerebrosidase. *Biochim Biophys Acta* 619:669-679.

Pérez-Poyato MS, Pineda M (2011) New agents and approaches to treatment in Niemann-Pick type C disease. *Curr Pharm Biotechnol* 12:897-901.

Perlmutter DH (2002) Chemical chaperones: a pharmacological strategy for disorders of protein folding and trafficking. *Pediatr Res* 52:832-836.

Perry M, Konstantinides N, Pinto-Teixeira F, Desplan C (2017) Generation and Evolution of Neural Cell Types and Circuits: Insights from the Drosophila Visual System. *Annu Rev Genet* 51:501-527.

Peter S, Ten Brinke MM, Stedehouder J, et al (2016) Dysfunctional cerebellar Purkinje cells contribute to autism-like behaviour in Shank2-deficient mice. *Nat Commun*.7:12627.

Petrov K, de Almeida Magalhaes T, Salic A (2021) Mechanism and ultrasensitivity in Hedgehog signaling revealed by Patched1 disease mutations. *Proc Natl Acad Sci U S A*.118(6):e2006800118.

Pfeffer SR (2019) NPC intracellular cholesterol transporter 1 (NPC)-mediated cholesterol export from lysosomes. *J Biol Chem* 294:1706-1709.

Pfrieger FW (2003) Role of cholesterol in synapse formation and function. *Biochim Biophys Acta* 1610:271-280.

Pick L (1927) Über die lipoidzellige Splenohepatomegalie Typus Niemann-Pick als Stoffwechselerkrankung. *Med Klinik* 23:1483-1488.

Pierce JE, Thomasson M, Voruz P, Selosse G, Péron J (2023) Explicit and Implicit Emotion Processing in the Cerebellum: A Meta-analysis and Systematic Review. *Cerebellum*.22(5):852-864.

Pineda M, Walterfang M, Patterson MC (2018) Miglustat in Niemann-Pick disease type C patients: a review. *Orphanet J Rare Dis* 13:140.

Pipalia NH, Cosner CC, Huang A, Chatterjee A, Bourbon P, Farley N, Helquist P, Wiest O, Maxfield FR (2011) Histone deacetylase inhibitor treatment dramatically reduces cholesterol accumulation in Niemann-Pick type C1 mutant human fibroblasts. *Proc Natl Acad Sci USA* 108:5620-5625.

Platt FM, Wassif C, Colaco A, Dardis A, Lloyd-Evans E, Bembi B, Porter FD (2014) Disorders of cholesterol metabolism and their unanticipated convergent mechanisms of disease. *Annu Rev Genomics Hum Genet* 15:173-194.

Polo G, Burlina AP, Kolamunnage TB, Zampieri M, Dionisi-Vici C, Strisciuglio P, Zaninotto M, Plebani M, Burlina AB (2017) Diagnosis of sphingolipidoses: a new simultaneous measurement of lysosphingolipids by LC-MS/MS. *Clin Chem Lab Med* 55:403-414.

Portfors CV (2007) Types and functions of ultrasonic vocalizations in laboratory rats and mice. *J Am Assoc Lab Anim Sci*.46(1):28-34.

Pressey SN, Smith DA, Wong AM, Platt FM, Cooper JD (2012) Early glial activation, synaptic changes and axonal pathology in the thalamocortical system of Niemann-Pick type C1 mice. *Neurobiol Dis* 45:1086-1100.

Pu M, Ma Q, Haihambo N, et al (2023) Dynamic causal modeling of cerebello-cerebral connectivity when sequencing trait-implying actions. *Cereb Cortex*.33(10):6366-6381.

Puglisi-Allegra S, Cabib S, Pascucci T, Ventura R, Cali F, Romano V (2000) Dramatic brain aminergic deficit in a genetic mouse model of phenylketonuria. *Neuroreport*.11(6):1361-1364.

Qian H, Cao P, Hu M, Gao S, Yan N, Gong X (2019) Inhibition of tetrameric Patched1 by Sonic Hedgehog through an asymmetric paradigm. *Nat Commun*.10(1):2320.

Quartier A, Courraud J, Thi Ha T, et al (2019) Novel mutations in NLGN3 causing autism spectrum disorder and cognitive impairment. *Hum Mutat*.40(11):2021-2032.

Rahimi-Balaei M, Bergen H, Kong J, Marzban H (2018) Neuronal migration during development of the cerebellum. *Front Cell Neurosci* 12:484.

Ramnani N (2006) The primate cortico-cerebellar system: anatomy and function. *Nat Rev Neurosci* 7:511-522.

Rava A, La Rosa P, Palladino G, et al (2022) The appearance of phagocytic microglia in the postnatal brain of Niemann Pick type C mice is developmentally regulated and underscores shortfalls in fine odor discrimination. *J Cell Physiol*.237(12):4563-4579.

Rea K, Cremers TI, Westerink BH (2005) HPLC conditions are critical for the detection of GABA by microdialysis. *J Neurochem*.94(3):672-679.

Reck-Peterson SL, Redwine WB, Vale RD, Carter AP (2018) The cytoplasmic dynein transport machinery and its many cargoes. *Nat Rev Mol Cell Biol* 19:382-398.

Reith RM, McKenna J, Wu H, et al (2013) Loss of Tsc2 in Purkinje cells is associated with autistic-like behavior in a mouse model of tuberous sclerosis complex. *Neurobiol Dis*.51:93-103.

Ren Y, Guo L, Guo CC (2019) A connectivity-based parcellation improved functional representation of the human cerebellum. *Sci Rep*.9(1):9115.

Ribeiro I, Marcão A, Amaral O, Sà Miranda MC, Vanier MT, Millat G (2001) Niemann-Pick type C: NPC1 mutations associated with severe and mild cellular cholesterol trafficking alterations. *Hum Genet* 109:24-32.

Richter JD, Klann E (2009) Making synaptic plasticity and memory last: mechanisms of translational regulation. *Genes Dev*.23(1):1-11.

Risher WC, Ustunkaya T, Singh Alvarado J, Eroglu C (2014) Rapid Golgi analysis method for efficient and unbiased classification of dendritic spines. *PLoS One*.9(9):e107591.

Roberts B, Casillas C, Alfaro AC, Jägers C, Roelink H (2016) Patched1 and Patched2 inhibit Smoothened non-cell autonomously. *Elife*.5:e17634.

Robinson JM, Karnovsky MJ (1980) Evaluation of the polyene antibiotic filipin as a cytochemical probe for membrane cholesterol. *J Histochem Cytochem* 28:161-168.

Rocha N, Kuijl C, van der Kant R, Janssen L, Houben D, Janssen H, Zwart W, Neefjes J (2009) Cholesterol sensor ORP1L contacts the ER protein VAP to control Rab7-RILP-p150 Glued and late endosome positioning. *J Cell Biol* 185:1209-1225.

Roostaei T, Nazeri A, Sahraian MA, Minagar A (2014) The human cerebellum: a review of physiologic neuroanatomy. *Neurol Clin* 32:859-869.

Rose CF, Verkhratsky A, Parpura V (2013) Astrocyte glutamine synthetase: pivotal in health and disease. *Biochem Soc Trans*.41(6):1518-1524.

Rose S, Melnyk S, Pavliv O, et al (2012) Evidence of oxidative damage and inflammation associated with low glutathione redox status in the autism brain. *Transl Psychiatry*.2(7):e134.

Rosenbaum AI, Maxfield FR (2011) Niemann-Pick type C disease: molecular mechanisms and potential therapeutic approaches. *J Neurochem* 116:789-795.

Rudolph S, Badura A, Lutzu S, et al (2023) Cognitive-Affective Functions of the Cerebellum. *J Neurosci*.43(45):7554-7564.

Runge K, Cardoso C, de Chevigny A (2020) Dendritic Spine Plasticity: Function and Mechanisms. *Front Synaptic Neurosci*.12:36.

Rylaarsdam L, Guemez- Gamboa A (2019) Genetic causes and modifiers of autism spectrum disorder. *Front Cell Neurosci.*13:385.

Saade M, Martí E (2025) Early spinal cord development: from neural tube formation to neurogenesis. *Nat Rev Neurosci* 26(4):195-213.

Saito Y, Suzuki K, Nanba E, Yamamoto T, Ohno K, Murayama S (2022) Niemann-Pick type C disease: accelerated neurofibrillary tangle formation and amyloid deposition associated with apolipoprotein E epsilon 4 homozygosity. *Ann Neurol* 52:351-355.

Salsano E, Umeh C, Rufa A, Pareyson D, Zee DS (2012) Vertical sopranuclear gaze palsy in Niemann-Pick type C disease. *Neurol Sci* 33:1225-1232.

Sanchez-Bezanilla S, Beard DJ, Hood RJ, et al (2022) Growth Hormone Increases BDNF and mTOR Expression in Specific Brain Regions after Photothrombotic Stroke in Mice. *Neural Plast*.2022:9983042.

Sarkar S, Carroll B, Buganim Y, Maetzel D, Ng AH, Cassady JP, Cohen MA, Chakraborty S, Wang H et al (2013) Impaired autophagy in the lipid-storage disorder Niemann-Pick type C1 disease. *Cell Rep* 5:1302-1315.

Sarna JR, Larouche M, Marzban H, Sillitoe RV, Rancourt DE, Hawkes R (2003) Patterned Purkinje cell degeneration in mouse models of Niemann-Pick type C disease. *J Comp Neurol*. 456:279-291.

Scattoni ML, Crawley J, Ricceri L (2009) Ultrasonic vocalizations: a tool for behavioural phenotyping of mouse models of neurodevelopmental disorders. *Neurosci Biobehav Rev*.33(4):508-515.

Scharfman HE, Maclusky NJ (2005) Similarities between actions of estrogen and BDNF in the hippocampus: coincidence or clue?. *Trends in neurosciences*.28(2), 79–85.

Schilling K, Oberdick J, Rossi F, Baader SL (2008) Besides Purkinje cells and granule neurons: an appraisal of the cell biology of the interneurons of the cerebellar cortex. *Histochem Cell Biol* 130:601-615.

Schmahmann JD (2019) The cerebellum and cognition. *Neurosci Lett*.688:62-75.

Schmahmann JD, Sherman JC (1998) The cerebellar cognitive affective syndrome. *Brain*.121 (Pt 4):561-579.

Schmidt S, Kovacs E, Usta D, et al (2023) Cerebellar Mutism Syndrome After Posterior Fossa Tumor Surgery in Children-A Retrospective Single-Center Study. *World Neurosurg*.173:e622-e628.

Schoch S, Deák F, Königstorfer A, Mozhayeva M, Sara Y, Südhof TC, Kavalali ET (2001) SNARE function analyzed in synaptobrevin/VAMP knockout mice. *Science* 294:1117-1122.

Schuchman EH, Wasserstein MP (2015) Types A and B Niemann-Pick disease. *Best Pract Res Clin Endocrinol Metab* 29:237-247.

Schultz ML, Krus KL, Kaushik S, Dang D, Chopra R, Qi L, Shakkottai VG, Cuervo AM, Lieberman AP (2018) Coordinate regulation of mutant NPC1 degradation by selective ER autophagy and MARCH6-dependent ERAD. *Nat Commun* 9:3671.

Scott JA, Schumann CM, Goodlin-Jones BL, Amaral DG (2009) A comprehensive volumetric analysis of the cerebellum in children and adolescents with autism spectrum disorder. *Autism Res.*2:246-257.

Şeker Yilmaz B, Baruteau J, Rahim AA, Gissen P (2020) Clinical and molecular features of early infantile Niemann Pick type C disease. *Int J Mol Sci* 21:5059.

Selak S, Paternain AV, Aller MI, Picó E, Rivera R, Lerma J (2009) A role for SNAP25 in internalization of kainite receptors and synaptic plasticity. *Neuron* 63:357-371.

Sèvin M, Lesca G, Baumann N, Millat G, Lyon-Caen O, Vanier MT, Sedel F (2007) The adult form of Niemann-Pick disease type C. *Brain* 130:120-133.

Sewell GD (1970) Ultrasonic communication in rodents. *Nature*.227(5256):410.

Shadmehr R, Krakauer JW (2008) A computational neuroanatomy for motor control. *Exp Brain Res*.185(3):359-381.

Shammas H, Kuech EM, Rizk S, Das AM, Naim HY (2019) Different Niemann-Pick C1 genotypes generate protein phenotypes that vary in their intracellular processing, trafficking and localization. *Sci Rep* 9:5292.

Shen D, Wang X, Li X, Zhang X, Yao Z, Dibble S, Dong XP, Yu T, Lieberman AP et al (2012) Lipid storage disorders block lysosomal trafficking by inhibiting a TRP channel and lysosomal calcium release. *Nat Commun* 3:731.

Sheng M, Kim E (2000) The Shank family of scaffold proteins. *J Cell Sci* 113:1851-1856.

Shevelkin AV, Ihenatu C, Pletnikov MV (2014) Pre-clinical models of neurodevelopmental disorders: focus on the cerebellum. Rev Neurosci.25(2):177-194.

Shi GD, OuYang YP, Shi JG, Liu Y, Yuan W, Jia LS (2011) PTEN deletion prevents ischemic brain injury by activating the mTOR signaling pathway. *Biochem Biophys Res Commun*.404(4):941-945.

Shulman LM, David NJ, Weiner WJ (1995) Psychosis as the initial manifestation of adult-onset Niemann-Pick disease type C. *Neurology* 45:1739-1743.

Sideris GA, Josephson M (2016) Pulmonary alveolar proteinosis and Niemann Pick disease type B: An unexpected combination. *Respir Med Case Rep* 19:37-39.

Sillitoe RV, Joyner AL (2007) Morphology, molecular codes, and circuitry the three-dimensional complexity of the cerebellum. *Annu Rev Cell Dev Biol* 23:549-577.

Singh M, Meyer EM, Simpkins JW (1995) The effect of ovariectomy and estradiol replacement on brain-derived neurotrophic factor messenger ribonucleic acid expression in cortical and hippocampal brain regions of female Sprague-Dawley rats. *Endocrinology*.136(5), 2320–2324.

Sitarska D, Lugowska A (2019) Laboratory diagnosis of the Niemann-Pick type C disease: an inherited neurodegenerative disorder of cholesterol metabolism. *Metab Brain Dis* 34:1253-1260.

Sleat DE, Wiseman JA, El-Banna M, Price SM, Verot L, Shen MM, Tint GS, Vanier MT, Walkley SU et al (2004) Genetic evidence for nonredundant functional cooperativity between NPC1 and NPC2 in lipid transport. *Proc Natl Acad Sci USA* 101:5886-5891.

Slipczuk L, Bekinschtein P, Katche C, Cammarota M, Izquierdo I, Medina JH (2009) BDNF activates mTOR to regulate GluR1 expression required for memory formation. *PLoS One*.4(6):e6007.

Smith D, Wallom KL, Williams IM, Jeyakumar M, Platt FM (2009) Beneficial effects of anti-inflammatory therapy in a mouse model of Niemann-Pick disease type C1. *Neurobiol Dis* 36:242-251.

Sohrabji F, Lewis DK (2006) Estrogen-BDNF interactions: implications for neurodegenerative diseases. *Frontiers in neuroendocrinology*.27(4), 404–414.

Sokol J, Blanchette-Mackie J, Kruth HS, Dwyer NK, Amende LM, Butler JD, Robinson E, Patel S, Bradi RO et al (1988) Type C Niemann-Pick disease. Lysosomal accumulation and defective intracellular mobilization of low density lipoprotein cholesterol. *J Biol Chem* 263:3411-3417.

Solum DT, Handa RJ (2002) Estrogen regulates the development of brain-derived neurotrophic factor mRNA and protein in the rat hippocampus. *J Neurosci*.22(7):2650-2659.

Sotelo C, Dusart I (2009) Intrinsic versus extrinsic determinants during the development of Purkinje cell dendrites. *Neuroscience* 162:589-600.

Sotelo C, Wassef M (1991) Cerebellar development: afferent organization and Purkinje cell heterogeneity. *Philos Trans R Soc Lond B Biol Sci* 331:307-313.

Spiegel R, Raas-Rothschild A, Reish O, Regev M, Meiner V, Bargal R, Sury V, Meir K, Nadjari M et al (2009) The clinical spectrum of fetal Niemann-Pick type C. *Am J Med Genet A* 149:446-450.

Spisák T, Román V, Papp E, et al (2019) Purkinje cell number-correlated cerebrocerebellar circuit anomaly in the valproate model of autism. *Sci Rep*.9(1):9225.

Steiner P, Higley MJ, Xu W, Czervionke BL, Malenka RC, Sabatini BL (2008) Destabilization of the postsynaptic density by PSD-95 serine 73 phosphorylation inhibits spine growth and synaptic plasticity. *Neuron*.60(5):788-802.

Stoodley CJ (2016) The Cerebellum and Neurodevelopmental Disorders. *Cerebellum*.15(1):34-37.

Stoodley CJ, Limperopoulos C (2016) Structure-function relationships in the developing cerebellum: Evidence from early-life cerebellar injury and neurodevelopmental disorders. *Semin Fetal Neonatal Med*.21(5):356-364.

Stoodley CJ, Schmahmann JD (2010) Evidence for topographic organization in the cerebellum of motor control versus cognitive and affective processing. *Cortex* 46:831-844.

Stoodley CJ, Schmahmann JD (2018) Functional topography of the human cerebellum. *Handb Clin Neurol*.154:59-70.

Storch J, Xu Z (2009) Niemann-Pick C2(NPC2) and intracellular cholesterol trafficking. *Biochim Biophys Acta* 1791:671-678.

Straub I, Witter M, Eshra A, Hoidis M, Byczkowicz N, Maas S, Delvendahl I, Dorgans K, Savier E et al (2020) Gradients in the mammalian cerebellar cortex enable Fourier-like transformation and improve storing capacity. *Elife* 9:e51771.

Sudarov A, Joyner AL (2007) Cerebellum morphogenesis: the foliation pattern is orchestrated by multi-cellular anchoring centers. *Neural Dev*.2:26.

Suzuki T, Sato M (2014) Neurogenesis and neuronal circuit formation in the Drosophila visual center. *Dev Growth Differ* 56(7):491-498.

Sweet ES, Tseng CY, Firestein BL (2011) To branch or not to branch: How PSD-95 regulates dendrites and spines. *Bioarchitecture*.1(2):69-73.

Szejtli J (1998) Introduction and General Overview of Cyclodextrin Chemistry. *Chem Rev* 98:1743-1754.

Takahashi M, Kobayashi T (2009) Cholesterol regulation of rab-mediated sphingolipid endocytosis. *Glycoconj J* 26:705-710.

Takei N, Inamura N, Kawamura M, et al (2004) Brain-derived neurotrophic factor induces mammalian target of rapamycin-dependent local activation of translation machinery and protein synthesis in neuronal dendrites. *J Neurosci*.24(44):9760-9769.

Takikita S, Fukuda T, Mohri I, Yagi T, Suzuki K (2004) Perturbed myelination process of premyelinating oligodendrocyte in Niemann-Pick type C mouse. *J Neuropathol Exp Neurol* 63:660-673.

Tarugi P, Ballarini G, Bembi B, Battisti C, Palmeri S, Panzani F, Di Leo E, Martini C, Federico A et al (2002) Niemann-Pick type C disease: mutations of NPC1 gene and evidence of abnormal expression of some mutant alleles in fibroblasts. *J Lipid Res* 43:1908-1919.

Teegarden S (2012) Behavioral phenotyping in rats and mice. *Mater Methods* 2:122.

Thach WT, Goodkin HP, Keating JG (1992) The cerebellum and the adaptive coordination of movement. *Annu Rev Neurosci*.15:403-442.

Thomas SD, Jha NK, Ojha S, Sadek B (2023) mTOR Signaling Disruption and Its Association with the Development of Autism Spectrum Disorder. *Molecules*.28(4):1889.

Tikoo S, Hernandez-Castillo CR, Chen H, et al (2025) The Evolving Cerebellar and Cerebello-cortical Functional Connectivity Architecture during Infancy. *J Neurosci*.45(11):e1209242025.

Tilot AK, Frazier TW 2nd, Eng C (2015) Balancing Proliferation and Connectivity in PTEN-associated Autism Spectrum Disorder. *Neurotherapeutics*.12(3):609-619.

Tiwari G, Tiwari R, Rai AK (2010) Cyclodextrins in delivery sistems: Applications. *J Pharm Bioallied Sci* 2:72-79.

Tomasoni R, Repetto D, Morini R, Elia C, Gardoni F, Di Luca M, Turco E, Defilippi P, Matteoli M (2013) SNAP-25 regulates spine formation through postsynaptic binding to p140Cap. *Nat Commun* 4:2136.

Torres S, Matìas N, Baulies A, Nuñez S, Alarcon-Vila C, Martinez L, Nuño N, Fernandez A, Caballeria J et al (2017) Mitochondrial GSH replenishment as a potential therapeutic approach for Niemann Pick type C disease. *Redox Biol* 11:60-72.

Tortolani D, Decandia D, Giacovazzo G, et al (2025) Chronic palmitoylethanolamide administration *via* slow-release subcutaneous pellets promotes neuroprotection and mitigates neuroinflammation in the Tg2576 mouse model of Alzheimer's disease. *Front Cell Neurosci*.19:1571428.

Totenhagen JW, Bernstein A, Yoshimaru ES, Erickson RP, Trouard TP (2017) Quantitative magnetic resonance imaging of brain atrophy in a mouse model of Niemann-Pick type C disease. *PLoS One*.12(5):e0178179.

Treiber A, Morand O, Clozel M (2007) The pharmacokinetics and tissue distribution of the glucosylceramide synthase inhibitor miglustat in the rat. *Xenobiotica* 37:298-314.

Trinh MN, Brown MS, Seemann J, Goldstein JL, Lu F (2018) Lysosomal cholesterol export reconstituted from fragments of Niemann-Pick C1. *Elife* 7:e38564.

Truett GE, Heeger P, Mynatt RL, Truett AA, Walker JA, Warman ML (2000) Preparation of PCR-quality mouse genomic DNA with hot sodium hydroxide and tris (HotSHOT). *Biotechniques* 29:52-54.

Tsai SJ (2003) Attention-deficit hyperactivity disorder and brain-derived neurotrophic factor: a speculative hypothesis. *Med Hypotheses*.60(6):849-851.

Tukachinsky H, Lopez LV, Salic A (2010) A mechanism for vertebrate Hedgehog signaling: recruitment to cilia and dissociation of SuFu-Gli protein complexes. *J Cell Biol*.191(2):415-428.

Tulodziecka K, Diaz-Rohrer BB, Farley MM, et al (2016) Remodeling of the postsynaptic plasma membrane during neural development. *Mol Biol Cell*.27(22):3480-3489.

Tyler WJ, Pozzo-Miller LD (2001) BDNF enhances quantal neurotransmitter release and increases the number of docked vesicles at the active zones of hippocampal excitatory synapses. *J Neurosci* 21:4249-4258.

Uchigashima M, Cheung A, Futai K (2021) Neuroligin-3: A Circuit-Specific Synapse Organizer That Shapes Normal Function and Autism Spectrum Disorder-Associated Dysfunction. *Front Mol Neurosci*.14:749164.

Ulu E, Demirci E, Sener EF, et al (2024) Role of Glutamate Receptor-related Biomarkers in the Etiopathogenesis of ADHD. *Clin Psychopharmacol Neurosci*.22(1):79-86.

Valle MS, Garifoli A, Maci T, Perciavalle V (2001) Reticulocerebellar projections to the anterior and posterior lobes of the rat cerebellum. *Neurosci Lett* 314:41-44.

Vallés AS, Barrantes FJ (2021) Dysregulation of Neuronal Nicotinic Acetylcholine Receptor-Cholesterol Crosstalk in Autism Spectrum Disorder. *Front Mol Neurosci*.14:744597. Published 2021 Oct 11.

van der Heijden ME, Gill JS, Sillitoe RV (2021) Abnormal cerebellar development in Autism Spectrum Disorders. *Dev Neurosci.*43:181-190.

van Essen DC, Donahue CJ, Glasser MF (2018) Development and Evolution of Cerebral and Cerebellar Cortex. *Brain Behav Evol* 91:158-169.

Van Overwalle F (2024) Social and emotional learning in the cerebellum. *Nat Rev Neurosci*.25(12):776-791.

Van Overwalle F, Baetens K, Mariën P, Vandekerckhove M (2015) Cerebellar areas dedicated to social cognition? A comparison of meta-analytic and connectivity results. *Soc Neurosci*.10(4):337-344.

Van Overwalle F, De Coninck S, Heleven E, et al (2019) The role of the cerebellum in reconstructing social action sequences: a pilot study. *Soc Cogn Affect Neurosci*.14(5):549-558.

Van Overwalle F, Manto M, Cattaneo Z, et al (2020) Consensus Paper: Cerebellum and Social Cognition. *Cerebellum*.19(6):833-868.

Van Overwalle F, Van de Steen F, van Dun K, Heleven E (2020) Connectivity between the cerebrum and cerebellum during social and non-social sequencing using dynamic causal modelling. *Neuroimage*.206:116326.

Vanier MT (2010) Niemann-Pick C disease: history, current research topics, biological and molecular diagnosis. *Arch Pediatr* 2:41-44.

Vanier MT (2010) Niemann-Pick disease type C. *Orphanet J Rare Dis* 5:16.

Vanier MT (2013) Niemann-Pick diseases. *Handb Clin Neurol* 113:1717-1721.

Vanier MT (2015) Complex lipid trafficking in Niemann-Pick disease type C. *J Inherit Metab Dis* 38:187-199.

Vanier MT, Gissen P, Bauer P, Coll MJ, Burlina A, Hendriksz CJ, Latour P, Goizet C, Welford RW et al (2016) Diagnosis tests for Niemann-Pick disease type C (NP-C): A critical review. *Mol Genet Metab* 118:244-254.

Vanier MT, Latour P (2015) Laboratory diagnosis of Niemann-Pick disease type C: the filipin staining test. *Methods Cell Biol* 126:357-375.

Vanier MT, Millat G (2003) Niemann-Pick disease type C. *Clin Genet* 64:269-281.

Vanier MT, Millat G (2004) Structure and function of the NPC2 protein. *Biochim Biophys Acta* 1685:14-21.

Vanier MT, Rodriguez-Lafrasse C, Rousson R, et al (1991) Type C Niemann-Pick disease: biochemical aspects and phenotypic heterogeneity. *Dev Neurosci*.13(4-5):307-314.

Vanier MT, Suzuki K (1998) Recent advances in elucidating Niemann-Pick C disease. *Brain Pathol* 8:163-174.

Vanier, MT, Pentchev P, Rodriguez-Lafrasse C, Rousson R (1991) Niemann-Pick disease type C: an update. *J Inherit Metab Dis* 14:580-595.

Vargas DL, Nascimbene C, Krishnan C, Zimmerman AW, Pardo CA (2005) Neuroglial activation and neuroinflammation in the brain of patients with autism. *Ann Neurol*.57(1):67-81.

Vázquez MC, Balboa E, Alvarez AR, Zanlungo S (2012) Oxidative stress: a pathogenic mechanism for Niemann-Pick type C disease. *Oxid Med Cell Longev* 2012:205713.

Verkleij AJ, Kruijff B, Gerritsen WF, Demel RA, van Deenen LL, Ververgaert PH (1973) Freeze-etch electron microscopy of erythrocytes, Acholeplasma laidlawii cells and liposomal membranes after the action of filipin and amphotericin B. *Biochim Biophys Acta* 291:577-581.

Verot L, Chick K, Freydière E, Honorè R, Vanier MT, Millat G (2007) Niemann-Pick C disease: functional characterization of three NPC2 mutations and clinical and molecular update on patients with NPC2. *Clin Genet* 71:320-330.

Vihervaara T, Uronen RL, Wohlfahrt G, Björkhem I, Ikonen E, Olkkonen VM (2011) Sterol binding by OSBP-related protein 1L regulates late endosome motility and function. *Cell Mol Life Sci* 68:537-551.

Visentin S, De Nuccio C, Bernardo A, Pepponi R, Ferrante A, Minghetti L, Popoli P (2013) The stimulation of adenosine A2A receptors ameliorates the pathological phenotype of fibroblasts from Niemann-Pick type C patients. *J Neurosci* 33:15388-15393.

Vite CH, Ding W, Bryan C, O'Donnell P, Cullen K, Aleman D, Haskins ME, Van Winkle T (2008) Clinical, electrophysiological, and serum biochemical measures of progressive neurological and hepatic dysfunction in feline Niemann-Pick type C disease. *Pediatr Res* 64:544-549.

Võikar V, Rauvala H, Ikonen E (2002) Cognitive deficit and development of motor impairment in a mouse model of Niemann-Pick type C disease. *Behav Brain Res* 132:1-10.

Völkner C, Pantoom S, Liedtke M, Lukas J, Hermann A, Frech MJ (2022) Assessment of FDA-approved drugs as a therapeutic approach for Niemann-pick disease type C1 using patient-specific IPSC-based model Systems. *Cells* 11:319.

von Ranke FM, Pereira Freitas HM, Mançano AD, Rodrigues RS, Hochhegger B, Escuissato D, Araujo Neto CA, da Silva TK, Marchiori E (2016) Pulmonary involvement in Niemann-Pick disease: a state-of-the-art review. *Lung* 194:511-518.

Voogd J, Glickstein M (1998) The anatomy of the cerebellum. *Trends Cogn Sci* 2:307-313.

Voogd J, Pardoe J, Ruigrok TJ, Apps R (2003) The distribution of climbing and mossy fiber collateral branches from the copula pyramidis and the paramedian lobule: Congruence of climbing fiber cortical zones and pattern of zebrin banding within the rat cerebellum. *J Neurosci* 23:4645-4656.

Voogd J, Schraa-Tam CK, van der Geest JN, De Zeeuw CI (2012) Visuomotor cerebellum in human and nonhuman primates. *Cerebellum*.11(2):392-410.

Walkley SU, Suzuki K (2004) Consequences of NPC1 and NPC2 loss of function in mammalian neurons. *Biochim Biophys Acta* 1685:48-62.

Walterfang M, Patenaude B, Abel LA, Klunemann H, Bowman EA, Fahey MC, Desmond P, Kelso W, Velakoulis D (2013) Subcortical volumetric reductions in adult Niemann-Pick disease type C: a cross-sectional study. *AJNR Am J Neuroradiol* 34:1334-1340.

Wan L, Ai JQ, Yang C, Jiang J, Zhang QL, Luo ZH, Huang RJ, Tu T, Pan A et al (2021) Expression of the excitatory postsynaptic scaffolding protein, Shank3, in human brain: effect of age and Alzheimer's disease. *Front Aging Neurosci* 13:717263.

Wang F, Xu Q, Wang W, Takano T, Nedergaard M (2012) Bergmann glia modulate cerebellar Purkinje cell bistability via Ca2+-dependent K+ uptake. *Proc Natl Acad Sci USA* 109:7911-7916.

Wang H (2014) Lipid rafts: a signaling platform linking cholesterol metabolism to synaptic deficits in autism spectrum disorders. *Front Behav Neurosci*.8:104.

Wang LJ, Wu CC, Lee MJ, Chou MC, Lee SY, Chou WJ (2019) Peripheral Brain-Derived Neurotrophic Factor and Contactin-1 Levels in Patients with Attention-Deficit/Hyperactivity Disorder. *J Clin Med*.8(9):1366.

Wang SS, Kloth AD, Badura A (2014) The cerebellum, sensitive periods, and autism. *Neuron*.83(3):518-532.

Wang W, Kantorovich S, Babayan AH, Hou B, Gall CM, Lynch G (2016) Estrogen's Effects on Excitatory Synaptic Transmission Entail Integrin and TrkB Transactivation and Depend Upon β1-integrin function. *Neuropsychopharmacology*.41(11):2723-2732.

Wang W, Shiraishi R, Kawauchi D (2022) Sonic Hedgehog Signaling in Cerebellar Development and Cancer. *Front Cell Dev Biol*.10:864035.

Wang Y, Zhou Z, Walsh CT, McMahon AP (2009) Selective translocation of intracellular Smoothened to the primary cilium in response to Hedgehog pathway modulation. *Proc Natl Acad Sci U S A*.106(8):2623-2628.

Washbourne P (2015) Synapse assembly and neurodevelopmental disorders. *Neuropsychopharmacology*.40(1):4-15.

Wasserstein MP, Desnick RJ, Schuchman EH, Hossain S, Wallenstein S, Lamm C, McGovern MM (2004) The natural history of type B Niemann-Pick disease: results from a 10-year longitudinal study. *Pediatrics* 114:672-677.

Wassif CA, Cross JL, Iben J, Sanchez-Pulido L, Cougnoux A, Platt FM, Ory DS, Ponting CP, Bailey-Wilson JE et al (2016) High incidence of unrecognized visceral/neurological late-onset Niemann-Pick disease, type C1, predicted by analysis of massively parallel sequencing data sets. *Genet Med* 18:41-48.

Wechsler-Reya RJ, Scott MP (1999) Control of neuronal precursor proliferation in the cerebellum by Sonic Hedgehog. *Neuron*.22(1):103-114

Werling DM, Geschwind DH (2013) Sex differences in autism spectrum disorders. *Curr Opin Neurol*.26(2):146-153.

Wheeler S, Sillence DJ (2020) Niemann-Pick type C disease: cellular pathology and pharmacotherapy. *J Neurochem* 153:674-692.

White JJ, Sillitoe RV (2013) Development of the cerebellum: from gene expression patterns to circuit maps. *Wiley Interdiscip Rev Dev Biol*.2(1):149-164.

Wiegand V, Chang TY, Strauss JF 3rd, Fahrenholz F, Gimpl G (2003) Transport of plasma membrane-derived cholesterol and the function of Niemann-Pick C1 protein. *FASEB J* 17:782-784.

Wilson CW, Chen MH, Chuang PT (2009) Smoothened adopts multiple active and inactive conformations capable of trafficking to the primary cilium. *PLoS One*.4(4):e5182.

Winden KD, Ebrahimi-Fakhari D, Sahin M (2018) Abnormal mTOR Activation in Autism. *Annu Rev Neurosci*.41:1-23.

Wöhr M, Scattoni ML (2013) Behavioural methods used in rodent models of autism spectrum disorders: current standards and new developments. *Behav Brain Res*.251:5-17.

Wolpert DM, Miall RC, Kawato M (1998) Internal models in the cerebellum. *Trends Cogn Sci*.2(9):338-347.

Woś M, Szczepanowska J, Pikuła S, Tylki-Szymańska A, Zabłocki K, Bandorowicz-Pikuła J (2016) Mitochondrial dysfunction in fibroblast derived from patients with Niemann-Pick type C disease. *Arch Biochem Biophys* 593:50-59.

Wraith JE, Guffon N, Rohrbach M, Hwu WL, Korenke GC, Bembi B, Luzy C, Giorgino R, Sedel F (2009) Natural history of Niemann-Pick disease type C in a multicentre observational retrospective cohort study. *Mol Genet Metab* 98:250-254.

Wu HS, Sugihara I, Shinoda Y (1999) Projection patterns of single mossy fivers originating from the lateral nucleus in the rat cerebellar cortex and nuclei. *J Comp Neurol* 411:97-118.

Wu XS, McNeil BD, Xu J, Fan J, Xue L, Melicoff E, Adachi R, Bai L, Wu LG (2009) Ca (2+) and calmodulin initiate all forms of endocytosis during depolarization at a nerve terminal. *Nat Neurosci* 12:1003-1010.

Xie MJ, Ishikawa Y, Yagi H, et al (2019) PIP_3-Phldb2 is crucial for LTP regulating synaptic NMDA and AMPA receptor density and PSD95 turnover. *Sci Rep*.9(1):4305.

Xu H, Yang Y, Tang X, Zhao M, Liang F, Xu P, Hou B, Xing Y, Bao X, et al (2013) Bergmann glia function in granule cell migration during cerebellum development. *Mol Neurobiol* 47:833-844.

Xu S, Benoff B, Liou HL, Lobel P, Stock AM (2007) Structural basis of sterol binding by NPC2, a lysosomal protein deficient in Niemann-Pick type C2 disease. *J Biol Chem* 282:23525-23531.

Xu S, Zhou S, Xia D, Xia J, Chen G, Duan S, Luo J (2010) Defects of synaptic vesicle turnover at excitatory and inhibitory synapses in Niemann-Pick C1-deficient neurons. *Neuroscience* 167:608-620.

Yamashiro K, Hori K, Lai ESK, Aoki R, Shimaoka K, Arimura N, Egusa SF, Sakamoto A, Abe M et al (2020) AUTS2 governs cerebellar development, Purkinje cell maturation, motor function and social communication. *iScience*.23:101820.

Yan S, You ZL, Zhao QY, Peng C, He G, Gou XJ, Lin B (2015) Antidepressant-like effects of Sanyuansan in the mouse forced swim test, tail suspension test, and chronic mild stress model. *Kaohsiung J Med Sci* 31:605-612.

Yan X, Lukas J, Witt M, Wree A, Hübner R, French M, Köhling R, Rolfs A, Luo J (2011) Decreased expression of myelin gene regulatory factor in Niemann-Pick type C1. *Metab Brain Dis* 26:299-306.

Yang Z, Klionsky DJ (2009) An overview of the molecular mechanism of autophagy. *Curr Top Microbiol Immunol* 335:1-32.

Yokoo M, Kubota Y, Motoyama K, Higashi T, Taniyoshi M, Tokumaru H, Nishiyama R, Tabe Y, Mochinaga S et al (2015) 2-Hydroxypropyl-β-Cyclodextrin Acts as a Novel Anticancer Agent. *PloS One* 10:e0141946.

Yoon TY, Munson M (2018) SNARE complex assembly and disassembly. *Curr Biol*.28(8):R397-R401.

Yoshii A, Constantine-Paton M (2010) Postsynaptic BDNF-TrkB signaling in synapse maturation, plasticity, and disease. *Dev Neurobiol*.70(5):304-322.

Yu AC, Hertz L (1982) Uptake of glutamate, GABA, and glutamine into a predominantly GABA-ergic and a predominantly glutamatergic nerve cell population in culture. *J Neurosci Res*.7(1):23-35.

Yu W, Gong JS, Ko M, Garver WS, Yanagisawa K, Michikawa M (2005) Altered cholesterol metabolism in Niemann-Pick type C1 mouse brains affects mitochondrial function. *J Biol Chem* 280:11731-11739.

Yu W, Krook-Magnuson E (2015) Cognitive Collaborations: Bidirectional Functional Connectivity Between the Cerebellum and the Hippocampus. *Front Syst Neurosci*.9:177.

Zervas M, Somers KL, Thrall MA, Walkley SU (2001) Critical role for glycosphingolipids in Niemann-Pick disease type C. *Curr Biol* 11:1283-1287.

Zhan XQ, Yao JJ, Liu DD, Ma Q, Mei YA (2014) Aβ40 modulates GABA(A) receptor α6 subunit expression and rat cerebellar granule neuron maturation through the ERK/mTOR pathway. *J Neurochem*.128(3):350-362.

Zhang J, Liu Q (2015) Cholesterol metabolism and homeostasis in the brain. *Protein Cell* 6:254-264.

Zhang M, Dwyer NK, Love DC, Cooney A, Comly M, Neufeld E, Pentchev PG, Blanchette-Mackie EJ, Hanover JA (2001) Cessation of rapid late endosomal tubulovesicular trafficking in Niemann-Pick type C1 disease. *Proc Natl Acad Sci USA* 98:4466-4471.

Zhang Z, Wang D, Sun T, Xu J, Chiang HC, Shin W, Wu LG (2013) The SNARE proteins SNAP25 and synaptobrevin are involved in endocytosis at hippocampal synapses. *J Neurosci* 33:9169-9175.

Zhou P, Porcionatto M, Pilapi M, Chen Y, Choi Y, Tolias KF, Bikoff JB, Hong EJ, Greenberg ME et al (2007) Polarized signaling endosomes coordinate BDNF-induced chemotaxis of cerebellar precursors. *Neuron* 55:53-68.

Zidovetzki R, Levitan I (2007) Use of cyclodextrins to manipulate plasma membrane cholesterol content: evidence, misconceptions and control strategies. *Biochim Biophys Acta* 1768:1311-1324.

Zuo Y, Lin A, Chang P, Gan WB (2005) Development of long-term dendritic spine stability in diverse regions of cerebral cortex. *Neuron*.46(2):181-189.